Planet formation beyond the solar neighbourhood: a population study of young stars with disks in the harsh environment of Carina

Dominika Itrich

Munich 2023

Planet formation beyond the solar neighbourhood: a population study of young stars with disks in the harsh environment of Carina

Dissertation

at the
Faculty of Physics

of the
Ludwig Maximilians University Munich

submitted by

Dominika Itrich
born in Bydgoszcz, Poland

Munich, 2nd of November 2023

Planetenbildung jenseits der Sonnenumgebung: eine Populationsstudie junger Sterne mit Scheibe in der rauen Umgebung von Carina

Dissertation

an der
Fakultät für Physik

der
Ludwig Maximilians Universität München

vorgelegt von

Dominika Itrich
geboren in Bromberg, Polen

München, den 2. November 2023

Erstgutacher: Prof. Dr. Thomas Preibisch
Zweitgutachter: Prof. Dr. Leonardo Testi
Tag der mündlichen Prüfung: 15. Dezember 2023

Śpieszmy się kochać ludzi tak szybko odchodzą...

Let us hurry to love people they depart so quickly...

— ks. Jan Twardowski

Contents

Acronyms

ADI	Angular Differential Imaging
AGE-PRO	the ALMA survey of Gas Evolution in PROtoplanetary disks
ALICE	Archival legacy investigations of circumstellar environments
ALMA	Atacama Large Millimeter/submillimeter Array
AMBER	Astronomical Multiple BEam Recombiner
AO	Adaptive Optics
BD	Brown Dwarfs
CARMA	Combined Array for Research in Millimeter-wave Astronomy
CHARA	Center for High Angular Resolution Astronomy interferometer
cINN	conditional Invertible Neural Network
CMD	colour-magnitude diagram
CPD	circumplanetary disk
CSO	Caltech Submillimeter Observatory
CTTS	Classical T Tauri Stars
DARTTS-S	Disks Around T Tauri Stars with SPHERE
DECO	the ALMA Disk-Exoplanet C/Onnection
DESTINYS	Disk Evolution Study Through Imaging of Nearby Young Stars
DIGIT	"Dust, Ice, and Gas In Time"
DSHARP	Disk Substructures at High Angular Resolution Project
eDisk	Early Planet Formation in Embedded Disks
ELT	Extremely Large Telescope
EUV	extreme-ultraviolet
FUV	far-ultraviolet
GASPS	GAS in Protoplanetary Systems
GI	Gravitational Instability
GMCs	Giant Molecular Clouds
HR	Hertzsprung-Russell diagram
HSO	Herschel Space Observatory
HST	Hubble Space Telescope
IFU	Integral Field Unit spectroscopy
IOTA	Infrared-Optical Telescope Array
ISI	Infrared Spatial Interferometer
ISM	Interstellar Medium
JOYS	JWST Observations of Young protoStars
JWST	James Webb Space Telescope
KI	Keck Interferometer
MAPS	Molecules with ALMA at Planet-forming Scales

MIDI	MID-infrared Interferometric instrument
MINDS	the MIRI INfrared Disk Survey
MOS	Multi-Object Spectroscopy
MS	Main Sequence
MUSE	Multi Unit Spectroscopic Explorer
NFM	Narrow Field Mode
NOEMA	Northern Extended Millimeter Array
ONC	Orion Nebula Cluster
ORANGES	ORion Alma New GEneration Survey
PACS	Photodetector Array Camera and Spectrometer
PAHs	Polycyclic Aromatic Hydrocarbons
PdBI	Plateau de Bure Interferometer
PDI	Polarization Differential Imaging
PDR	Photo-Dissociation Region
PEACHES	the Perseus ALMA Chemistry Survey
PMS	pre-main sequence star
PPDs	protoplanetary disks
PSF	Point Spread Function
PTI	Palomar Testbed Interferometer
RDI	Reference Differential Imaging
RMSE	root mean square error
SDI	Spectral Differential Imaging
SED	Spectral Energy Distribution
SFR	star forming region
SMA	Submillimeter Array
SODA	Survey of Orion Disks with ALMA
SPIRE	Spectral and Photometric Imaging Receiver
VANDAM	The VLA Nascent Disk and Multiplicity
VLA	Very Large Array
VLMS	Very Low Mass Stars
VLT	Very Large Telescope
VLTI	Very Large Telescope Interferometer
WFM	Wide Field Mode
WTTS	Weak-lined T Tauri Stars
YSO	Young Stellar Object
ZAMS	Zero Age Main Sequence

List of Figures

List of Tables

Abstract

Our knowledge of star and planet formation is based mainly on the nearby star-forming regions (<300 pc). However, most of the stars in our Galaxy form in the massive star-forming regions. The environmental conditions there differ from those which can be seen in the solar neighbourhood. Not only are they more massive, but also usually have higher stellar densities and higher radiation fields. The latter is produced by the most massive OB stars in the regions. The copious amounts of far- and extreme-UV photons (FUV, EUV) can have significant impact on other cluster members in their vicinity. Specifically, the most vulnerable are low-mass stars and their protoplanetary disks. High level of UV radiation can remove the material from outer parts of the protoplanetary disks by the process called external photoevaporation, and as a consequence, the ability of protoplanetary disks to form planets may be significantly diminished, depending on the exact timescale for disk dissipation. Circumstantial evidences suggest that the early evolution of the Sun happened in the neighbourhood of massive star, it is thus very important to understand what is the role of external photoevaporation in early evolution of stars and planetary systems.

This thesis aims to address aforementioned topic in the Carina Nebula Complex, a massive star-forming region hosting almost 100 O-type stars responsible for high level of radiation. Among the most massive clusters in Carina Nebula, we selected Trumpler 14, a very young and compact cluster, and employed integral field spectroscopic observations from MUSE to study the properties of the population of low-mass stars and their protoplanetary disks. The UV radiation emitted by the massive stars is also responsible for the creation of the bright HII region throughout the entire Carina Complex. Spectral analysis of young stellar objects requires careful assessment of nebular contamination and resulted in rigorous quality cuts in the presented catalog. Despite the incomplete sample, this thesis presents the deepest in mass catalog of spectrally characterised stars in the Carina Complex, and in Trumpler 14 in particular. Completeness of the catalog can be significantly improved when applying machine learning methods to the derivation of photospheric parameters ($T_{\rm eff}$, $\log(g)$, and $A_{\rm V}$) for each individual young star in Trumpler 14. As part of a collaborative work within the ECOGAL consortium we successfully tested a neural networks architecture on a set of the well-known Class III sources, and later applied to the MUSE dataset of Trumpler 14. We find the best performance of the

networks in the low-temperature regime. New estimates, when placed on the HR diagram, reveal two populations of stars in Trumpler 14 not clearly distinguishable with the previous method.

The thesis concludes with the search for the signpost of external photoevaporation. Contamination with the nebular emission forced us to re-evaluate the spectral extraction and to develop a new method in order to properly estimate emission line fluxes and upper limits from the individual young stars with disks. Revised measurements show high values of [OI] emission, consistent with predictions from external photoevaporation models. However, moderate resolution of MUSE does not allow to disentangle different components of the line, and with that, different emission mechanisms. Therefore, to comprehensively and conclusively trace the external photoevaporation in the Carina Nebula, a series of future steps have been proposed.

Zusammenfassung

Unser Wissen über Stern- und Planetenentstehung basiert hauptsächlich auf nahegelegenen Sternentstehungsgebieten (<300 pc). Die meisten Sterne in unserer Galaxie entstehen jedoch in massereichen Sternentstehungsgebieten. Die Umweltbedingungen dort unterscheiden sich von denen in der Sonnenumgebung. Sie sind nicht nur massereicher, sondern weisen in der Regel auch höhere Sterndichten und stärkere Strahlungsfelder auf. Letzteres wird von den massereichsten OB-Sternen in der Region erzeugt. Die große Menge an Photonen im Fernen und Extremen UV-Bereich (FUV, EUV) kann erhebliche Auswirkungen auf andere Haufenmitglieder in ihrer Umgebung haben. Besonders anfällig sind massearme Sterne und ihre protoplanetaren Scheiben. Ein hohes Maß an UV-Strahlung kann das Material aus den äußeren Teilen der protoplanetaren Scheiben in einem Prozess der externen Photoevaporation entfernen und damit ihr Planetenbildungspotenzial verringern. Da die frühe Entwicklung der Sonne in der Nähe eines massereichen Sterns stattfand, ist es sehr wichtig zu verstehen, welche Rolle die externe Photoevaporation in frühen Entwicklungsphasen von Sternen und Planeten spielt.

Diese Arbeit befasst sich mit dem oben genannten Thema im Carina-Nebelkomplex, einem massereichen Sternentstehungsgebiet, in dem fast 100 Sterne vom O-Typ zu finden sind, die für eine hohe Strahlungsintensität verantwortlich sind. Unter den massereichsten Haufen im Carina-Nebel haben wir Trumpler 14, einen sehr jungen und kompakten Haufen, ausgewählt, und räumlich aufgelöste, spektroskopische Beobachtungen mit MUSE verwendet, um die Eigenschaften der Population massearmer Sterne zu untersuchen. Da der Carina-Nebel in die HII-Region eingebettet ist, erfordert die Spektralanalyse eine sorgfältige Bewertung der Nebelkontamination und führte zu strengen Qualitätseinschränkungen im vorliegenden Katalog. Trotz der unvollständigen Stichprobe stellt diese Arbeit den massenmäßig umfangreichsten Katalog von spektral charakterisierten Sternen im Carina-Nebel dar. Die Vollständigkeit des Katalogs kann durch die Anwendung von Methoden des maschinellen Lernens auf die spektrale Klassifikation erheblich verbessert werden. Insbesondere haben wir in einer Gemeinschaftsarbeit innerhalb des ECOGAL-Konsortiums eine Architektur neuronaler Netze erfolgreich an einem Satz bekannter Klasse III-Quellen getestet und später auf den MUSE-Datensatz von Trumpler 14 angewendet. Wir finden die beste Leistung der Netze im Niedrigtemperaturbereich. Neue Schätzungen, die in das HR-Diagramm eingefügt werden, zeigen zwei Sternpopulationen in Trumpler 14, die mit der vorherigen Methode nicht klar zu unterscheiden waren.

Zum Abschluss der Arbeit suchen wir nach Indizien für externe Photoevaporation. Die Kontamination mit der Nebelemission führte zu einer erneuten Validierung der zuvor verwendeten Methoden und zu Schätzungen der Emissionslinienflüsse. Die überarbeiteten Messungen zeigen hohe Werte der [OI]-Emission, die mit den Vorhersagen der Modelle für externe Photoevaporation übereinstimmen. Die mäßige spektrale Auflösung von MUSE erlaubt es jedoch nicht, die verschiedenen Komponenten der Linie und damit auch die verschiedenen Emissionsmechanismen voneinander zu trennen. Um externe Photoevaporation im Carina-Nebel umfassend und schlüssig nachzuweisen, wurden daher eine Reihe von weiteren Schritten vorgeschlagen.

Chapter

1 Introduction

The formation of the Sun and its planetary system is one of the most important for humanity among the topics of astronomical research. This chapter aims to give an overview of our current understanding of formation of Sun-like stars and how star and planet formation can be investigated with observations. Following a description of our current understanding of low-mass star formation in Sec. 1.1, I focus on protoplanetary disks in Sec. 1.2. First, on their multi-wavelength observations (Sec. 1.2.1), then how disks evolve (Sec. 1.2.2), and finally how this evolution is tightly connected to accretion onto the central star (Sec. 1.2.3). The environment and its impact on protoplanetary disk evolution is discussed in Sec. 1.3. I conclude this chapter with putting the goals of this thesis into the astrophysical context previously described (Sec. 1.4).

1.1 Low-mass star formation

The question about the formation of the Earth and the Solar System is one of the most important in astronomy. Sun is the highest important star for the humanity so naturally it also attracts the most attention from scientists. Its proximity allows detailed studies including satellites being sent to its proximity and directly measuring solar wind. However, witnessing the formation of the Sun is outside our reach. To understand how our star might have formed, we need to investigate the Sun analogues in their earliest stages of evolution.

Low-mass stars, as they are referred to, are the most common stars in the Milky Way. Hence, with studying large sample of objects we can obtain a comprehensive picture of their properties, as well as their evolution. Consequently, the formation of low-mass stars is better constrained with respect to the very massive stars. Additionally, low-mass stars evolve slowly giving us the opportunity to capture each small step of their evolution, and with great number of measurements, deeply understand the mechanisms driving stellar evolution. For these reasons, here I only focus on the formation of low-mass stars ($\lesssim$2 $M_{\odot}$). In most cases stars do not form in isolation but in groups or clusters and their evolution can be affected by neighbouring stars. Especially, massive stars are the most influencing and this topic is addressed in consecutive sections of this chapter.

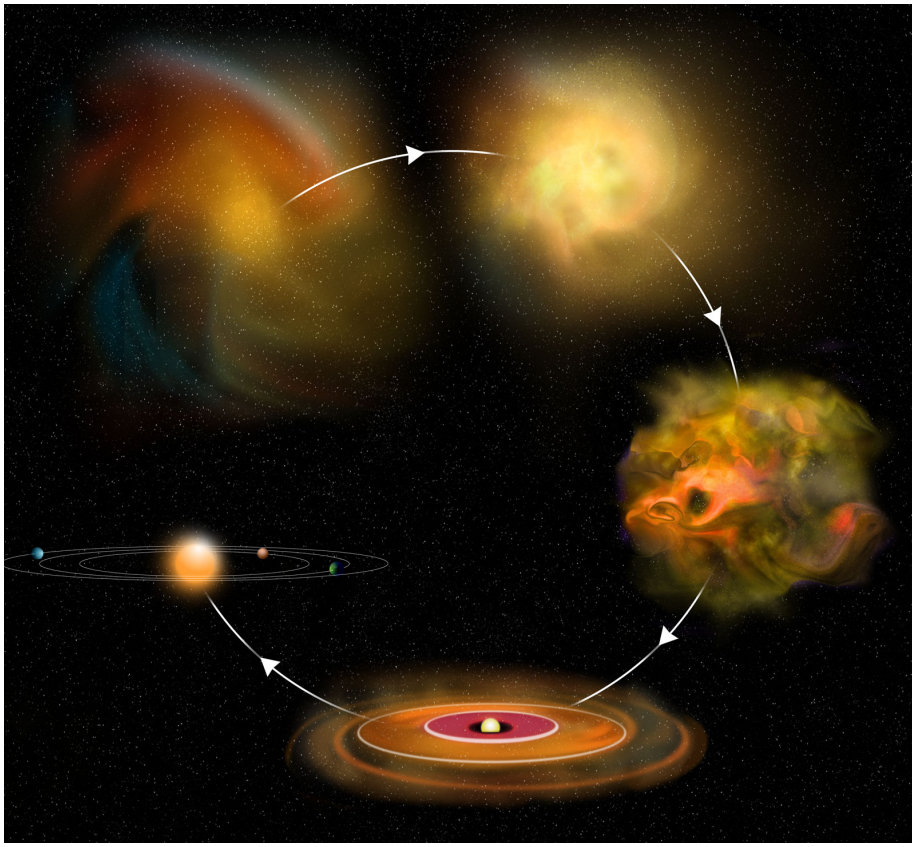

Figure 1.1: Sketch of star formation. From the giant molecular cloud (leftmost) emerges clump, which will be a birthplace for a group of stars. Due to the gravitational collapse dense cores are formed which will continue to accrete the matter through circumstellar disk. This disk is a place where planets are formed (bottom drawing). With time the disk is being cleared from the primordial material and at the end of PMS evolution the new exoplanetary system is revealed. Image credit: Bill Saxton, NRAO/AUI/NSF[1].

1.1.1 From molecular clouds to stars

Molecular clouds are birthplaces of stars (McKee & Ostriker 2007; Kennicutt & Evans 2012). Cold (∼10-40 K), dense (n_{H_2} ∼10^2-10^5 cm^{-3}), and massive ($M \gtrsim 10^4$ $M_\odot$) Giant Molecular Clouds (GMCs) with sizes of 50-100 pc are places where whole stellar clusters are formed (Tacconi et al. 2020, and references therein). A GMC is typically dispersed in 5 to 50 Myr because of protostellar outflows, jets, stellar radiation, and supernova explosions (Elmegreen 2007; Dobbs & Pringle 2013; Kruijssen et al. 2019; Chevance et al. 2023). In the solar neighbourhood (<300 pc) the efficiency of star formation is at the level of ∼3% corresponding to a star formation rate of 7.5×10^{-4} $M_\odot$yr^{-1} (Heiderman et al. 2010; Kennicutt & Evans 2012). In massive clusters or GMCs however, star formation efficiency might be higher (Kennicutt & Evans 2012).

Stars in most cases do not form in isolation and most of the star formation happens in massive clusters emerging from massive GMCs (Miller & Scalo 1978; Adams 2010). Gas and dust overdensities, gravitationally bounded clumps and cores, are seeds of

[1] https://www.nrao.edu/pr/2012/clumpcores

stars. Prestellar cores collapse and evolve into Class 0 protostars, deeply immersed in the natal envelope and invisible for optical observations (Andre et al. 1993, 2000; Ward-Thompson et al. 2007; Kennicutt & Evans 2012). At this stage the envelope is more massive than the stellar component, as indicated by the ratio between submm and bolometric luminosity (Andre et al. 2000). Most of the stellar mass is expected to be acquired by the star in that stage (McKee & Ostriker 2007) which lasts approximately 1-3$\times10^4$ Myr (Andre et al. 2000). Sketch in Figure 1.1 illustrates the first steps of the evolution of low-mass star. When the powerful collimated molecular outflows / jets dissipate the envelope and the protostar develops a circumstellar disk, the system is in the Class I stage. At this point protostar has an age of 1-2$\times10^5$ yr and is observable at NIR wavelengths (Greene et al. 1994; Kenyon & Hartmann 1995). The mass of the stellar component dominates over the envelope, while the accretion disk is of similar mass to the envelope, around $\lesssim$0.1-0.3 $M_\odot$ (e.g., Andre et al. 2000; Williams & Cieza 2011, and references therein).

Further evolution of the system leads to the total clearing of the envelope, widening, weakening, and gradual dissipation of the outflows, and to the disk getting optically thinner (e.g., Kennicutt & Evans 2012). This evolutionary stage is called Class II and the object is usually referred to as a pre-main sequence star (PMS). The Class II stage lasts 2$\pm$1 Myr (Kennicutt & Evans 2012). The dispersion of a disk leaving an (almost) fully-formed planetary system marks the Class III stage. The star is very close to enter the Zero Age Main Sequence (ZAMS). At this point, young star shows very weak or no accretion signs.

1.1.2 Observational classification of young stars

Observational classification of Young Stellar Object (YSO) is not trivial, especially for the youngest objects still deeply embedded in the natal cloud. Historically, the most important classification is done based on the slope of the Spectral Energy Distribution (SED) in IR (see Figure 1.2). Lada & Wilking (1984) and Lada (1987) investigated YSOs in Ophiuchus and found that they can be divided into three classes of objects depending on the slope $\alpha_{\rm IR}$ of the SED between 2 and 25 μm:

$$\alpha_{\rm IR} = \frac{d\log \lambda F_\lambda}{d\log \lambda} = \frac{d\log \nu F_\nu}{d\log \nu} \tag{1.1}$$

The youngest class, Class I, contains objects with $\alpha_{\rm IR} > 0.3$ (Greene et al. 1994). Their SEDs are broader than that of black body and it rises from $\sim$2 μm longward. Greene et al. (1994) introduced additional class of "flat-spectrum sources" intermediate between Class I and II. Their IR spectral index $\alpha_{\rm IR}$ falls in between -0.3 and 0.3. SED of Class II YSO decreases with wavelength with a slope of $-1.6 < \alpha_{\rm IR} < -0.3$ (Greene et al. 1994). The most mature YSOs, Class III, have no or little NIR excess and their SED is black body-like with a slope $\alpha_{\rm IR} < -1.6$. They might still have little MIR excess (Lada 1987). Later on a new, earlier, class of objects was introduced by Andre et al. (1993). Class 0 sources are fully obscured not detectable in NIR. The simplified picture of low-mass star formation with evolutionary classification presented in Sec. 1.1.1 corresponds directly to the above observational categorisation and was its foundation.

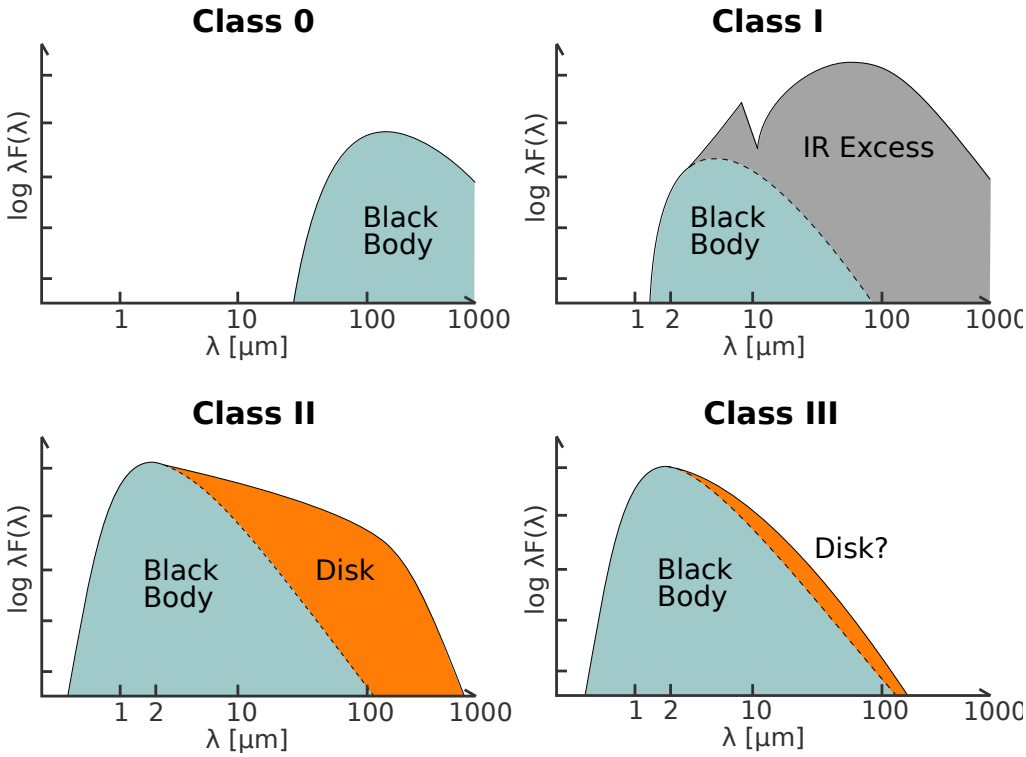

Figure 1.2: Visualisation of the SED for different evolutionary classes of YSOs. With the time, disk's contribution to the whole SED diminishes, while the central object (here drawn as Black Body) becomes more prominent. Credits: Persson (2014).

There exists another classification based on optical spectroscopy. Low-mass stars with $M_* \lesssim 2\ M_\odot$ are referred to as T Tauri stars, while intermediate-mass stars, $2\ M_\odot \lesssim M_* \lesssim 8\ M_\odot$, are called Herbig AeBe stars (Herbig 1960), depending on a spectral type. T Tauri stars are then divided further depending on the strength of Hα emission line. Stars showing strong accretion and the Hα emission with equivalent width above 10 Å are named Classical T Tauri Stars (CTTS). Stars with weaker or no emission are Weak-lined T Tauri Stars (WTTS). The youth of those is identified by their location on Hertzsprung-Russell diagram (HR) or X-ray activity (Feigelson & Montmerle 1999; Williams & Cieza 2011). WTTS can be understood as Class III YSOs, while CTTS as Class II. However, this distinction is not strict as a classification based on a SED can be affected by the orientation of the disk. Edge-on disk will mimic earlier stage of YSO evolution (Robitaille et al. 2006).

1.2 Birthplaces of planets: protoplanetary disks

The circumstellar material around a young star is a cradle of future planetary system. Conditions in circumstellar disk as well as its evolution has a decisive role in shaping this system. On top of that, material present in circumstellar disk is supplied to the star via accretion. The evolution of protoplanetary disks is therefore tidally connected to both the formation and early evolution of planets and the early evolution of the host star. The global picture of low-mass star formation is presented in Section 1.1. Here, I will focus on observational characteristics of protoplanetary disks (Sec. 1.2.1), their evolution and its impact on planet formation (Sec. 1.2.2), and accretion processes from theoretical, as well as an observational, perspective (Sec. 1.2.3).

Our knowledge of protoplanetary disks has grown significantly over the past years mainly due to the significant advancement of instrumentation over all spectral ranges. With new instruments to come and with upgrades of already existing ones, we can expect many new discoveries in the future. Intense development of theoretical models is complementing observational studies and will continue being an essential part of our investigation on the origin of the Solar System. While this thesis focuses on its observational perspective, theoretical studies are of an equal importance.

1.2.1 Direct observations of protoplanetary disks

The existence of protoplanetary disks (PPDs) is known for a long time. First, their presence was inferred from the excess emission in infrared with respect to the stellar Spectral Energy Distribution (SED, Elsasser & Staude 1978). It was quickly realised that SEDs exhibit a variety of morhpologies that lead to definition of YSO/disk classes (Lada & Wilking 1984; Lada 1987; Greene et al. 1994) connected to the first predictions of stellar formation and early evolution (e.g., Strom et al. 1989). Inclination of the disk impacts the observed SED, and therefore might confuse classification based solely on SED: edge-on disk will mimic an SED of a younger object (Robitaille et al. 2006). IRAS observations revealed another class of objects with negligible excess at wavelength below 10 μm but a significant excess emission at longer wavelengths (e.g., Strom et al. 1989; Wolk & Walter 1996; Espaillat et al. 2014). Those disks were named transition disks and the morphology of their spectrum was interpreted as caused by its inner part being cleared, possibly due to the presence of planet(s) or internal photoevaporation (Ercolano & Pascucci 2017). Transitions disks were expected to have an inner cavity, confirmed later by the observations (Andrews et al. 2009).

Observations of PPDs using multiple tracers and across a broad wavelength range, and more importantly, their direct detections, showed that substructures are common. This confirmed their flared structure accompanied by frequent radial and azimuthal substructures. Observations showed that physical and chemical conditions of PPDs vary in all directions: radially, azimuthally, and vertically. Figure 1.3 illustrates this in the simple sketch of protoplanetary disks. Cold dust in the midplane is traced by continuum observations in (sub)mm wavelengths. With temperature increasing vertically and decreasing radially (Kenyon & Hartmann 1987; Calvet et al. 1991), more

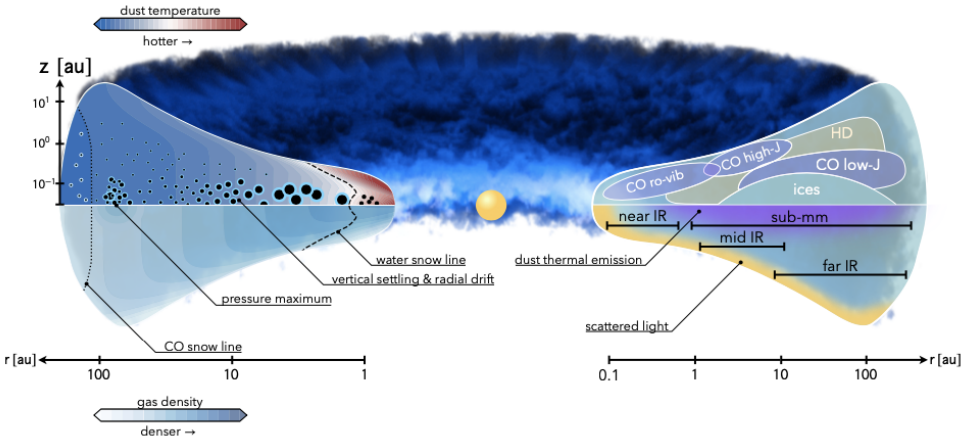

Figure 1.3: Sketch of a protoplanetary disk illustrating its complicated structure. The upper color-scale shows the gradient of dust temperature: it decreases radially and increases vertically. The gas density (lower colour-scale) increases in both, radial and vertical, directions. Larger dust particles (black circles, left side of the image) are located preferentially in the midplane and closer to the central object, while smaller ones occupy higher vertical layers and radial distances. Dashed and dotted lines depict location of water and CO snowlines, respectively. Obtaining this full picture requires observations at different wavelengths involving different tracers (right side of the sketch). Dust thermal emission from midplane can be observed in submm range. Disk surface can be observed in IR in scattered light. Gas content is traced by the molecular emission. Different species are located at different radial extends and emit at different vertical heights. Combining observations from several tracers give better constraint on physical and chemical conditions in the disk. Credits: Testi et al. (2014); Miotello et al. (2023).

molecules are getting unlock from ices exposing to us richness of chemical inventory in disks and material available for planets. Disk upper layers populated by small grains are visible in the scattered stellar light in NIR and optical (Andrews 2020). Advancement in instrumentation opened new possibilities of studying PPDs. Below, I describe what we have learnt from observations taken at different wavelengths and which physical properties and processes can be accessed by those observations.

1.2.1.1 Radio and (sub)mm observations

In radio and (sub)mm range of the spectrum protoplanetary disks are observed in their thermal emission which peaks at this spectral range. This emission traces dust grains with size scaling with wavelength of the observations. Bulk of those grains is located in the cold (∼20 K, e.g. Tazzari et al. 2021) disk midplane. Schematic on Figure 1.3 shows that large grains are gravitationally settled in the midplane while smaller grains can be located at larger vertical extends (e.g., Gräfe et al. 2013; Villenave et al. 2020). Dust vertical distribution depends on how well it is coupled to the gas and that depends on grain size – small grains are bound to the gas, while large particles feel the gas much less.

Continuum observations can be used to infer the disk dust mass and radius, as well as the disk temperature at the location of the emission. An intensity at given frequency ν from a layer of dust with homogeneous temperature and opacity can be described

as (e.g., Miotello et al. 2023):

$$I_\nu = (1 - e^{-\tau_\nu})\ B_\nu(T_{\rm dust}) \tag{1.2}$$

where $T_{\rm dust}$ is a temperature of the dust, $B_\nu(T_{\rm dust})$ is a Planck function of a Black Body with temperature of $T_{\rm dust}$ at given frequency, and τ_ν is a optical depth at this frequency. In the optically thick regime, i.e., $\tau_\nu \gg 1$, exponent in the equation 1.2 becomes negligible and the intensity is simply a Planck function: $I_\nu = B_\nu(T_{\rm dust})$ and gives us a direct information about the temperature of an emitting source. Thermal emission from disk is optically thick in the majority of the spectrum. However, it is expected to become optically thin ($\tau_\nu \ll 1$) at submm wavelengths (Andrews 2020), where observed intensity depends on physical properties of dust grains:

$$I_\nu = \tau_\nu\ B_\nu(T_{\rm dust}) = \Sigma_{\rm dust}\kappa_{\rm abs}\ B_\nu(T_{\rm dust}) \tag{1.3}$$

where $\Sigma_{\rm dust}$ is a dust surface density and $\kappa_{\rm abs}$ is a dust opacity (Miotello et al. 2023). Opacity is commonly assumed to be a power-law of frequency, $\kappa_{\rm abs} \propto \nu^\beta$, analogously to the Rayleigh-Jeans approximation of the Planck spectrum in the submm / radio regime, $B_\nu \propto \nu^2$. It is then convenient to define spectral index α, which connects observed emission with micro-physical parameters of emitting material: $\alpha = \beta + 2$, what then corresponds to $I_\nu \propto \nu^\alpha$.

Constraining spectral index gives some insight into the bulk dust properties, like dust grain size distribution, and is relatively straightforward if multi-wavelength observations are available. Detailed information about dust content of the disk is, however, challenging. Dust optical properties depends on many factors: mineralogy, porosity, shape, abundances of different species, frequency distribution of different grain sizes, local physical conditions. Precise estimation of grain characteristics is a very complex and degenerate problem. A small change in one of the parameters describing grains' properties leads to a large differences in theoretical predictions of opacity values (see, e.g., Draine & Lee 1984; Beckwith et al. 1990; Ossenkopf & Henning 1994; Pollack et al. 1994; Zubko et al. 1996; Min et al. 2003; Kataoka et al. 2014; Birnstiel et al. 2018). Very often, when detailed modelling of dust emission is not possible or feasible, it is a common practice to assume a dust opacity value. Typically adopted values for 1.3 mm emission per dust mass unit range between ∼1 and 2.3 $\rm cm^2 g^{-1}$ (e.g., Ansdell et al. 2016; Tychoniec et al. 2018; van Terwisga et al. 2019; Miotello et al. 2023).

By assuming grain properties (e.g., Pollack et al. 1994; Testi et al. 2014), one can estimate dust mass of the disk based on the measured emission. Hildebrand (1983) as first proposed the way to convert the received flux into dust mass. If the distance to the source, d, is known, as well as some average dust temperature, $T_{\rm dust}$, then based on incident flux F_ν at a frequency ν the dust mass is (Hildebrand 1983):

$$M_{\rm dust} = \frac{F_\nu d^2}{B_\nu(T_{\rm dust})} \times \frac{4}{3}\frac{a}{Q_{{\rm abs},\nu}}\rho \tag{1.4}$$

where the second part on the right hand site is related to the dust properties: radius a (assuming spherical shape), density ρ, and absorption coefficient $Q_{{\rm abs},\nu}$. The latter relates to the absorption mass opacity as: $\kappa_{{\rm abs},\nu} = \frac{\pi a^2}{m} Q_{{\rm abs},\nu}$; m is a mass of the dust

particle. Substituting the term for $Q_{\mathrm{abs},\nu}$ into Eq. 1.4 we get:

$$M_{\mathrm{dust}} = \frac{F_\nu d^2}{B_\nu(T_{\mathrm{dust}})\kappa_{\mathrm{abs},\nu}} \tag{1.5}$$

This simple approximation allows to roughly estimate disk mass based on a single measurement and is therefore very suitable for surveys targeting large number of disks. However, this estimate is highly uncertain due to assumptions on dust temperature, opacity, and optical depth.

Continuum observations also allow to estimate to what extent the dust grains are placed around the star. Dust emission at different wavelengths extend to different distances. Defining the physical disk radius can therefore be challenging. It requires constructing the disk surface density profile based on the multi-wavelength observations or knowledge of submm spectral index (Ricci et al. 2013). Modelling the disk emission in the visibility plane gives the most precise disk parameters (also disk mass and temperature profile, e.g., Isella et al. 2009; Ricci et al. 2014; Tazzari et al. 2016; Hendler et al. 2020) but might not be feasible in large samples of objects. It is a common practice in the literature to model a surface brightness profile instead (e.g., Guilloteau et al. 2011; Tripathi et al. 2017; Andrews et al. 2018; Sanchis et al. 2021). The disk radius is then defined as a radius within which a given percentage of the flux is contained. The most frequently used radius is $R_{68\%}$ containing the 68% of disk emission. More sensitive observation allow, however, to take advantage of deep integrations and use higher percentages, $R_{95\%}$ or $R_{98\%}$, which raises much larger radii and are perhaps better metrics of disk physical radii (Rosotti et al. 2019; Sanchis et al. 2021; Ilee et al. 2022). Several studies found relation between submm disk luminosity and disk radius, which might be understood as a correlation between disk mass and disk size, however, different studies provide different scaling factors indicating that other process, like disk evolution, stellar characteristics, might affect observed relation (Tazzari et al. 2017; Tripathi et al. 2017; Andrews et al. 2018; Zormpas et al. 2022).

First direct interferometric sub(mm) observations of protoplanetary disks offered the angular resolution of a fraction of an arcsecond, e.g., Submillimeter Array (SMA), Combined Array for Research in Millimeter-wave Astronomy (CARMA), Caltech Submillimeter Observatory (CSO), Very Large Array (VLA), or Plateau de Bure Interferometer (PdBI) replaced later by Northern Extended Millimeter Array (NOEMA). Those instruments provided important step forward in our understanding of protoplanetary disk properties allowing first imaging, dust and gas mass estimates, constructing temperature profiles and disk radial extends, and revealing first dust structures (Andrews et al. 2009). The early surveys targeted both Class II disks (Isella et al. 2009) and transition disks (Andrews et al. 2011). However, the true breakthrough came with the iconic image of HL Tau (Fig. 1.4, ALMA Partnership et al. 2015). Long-baseline, multi-wavelength Atacama Large Millimeter/submillimeter Array (ALMA) observations unveiled rings of dust and gaps as narrow as 3.5 au. ALMA gave an improvement in angular resolution of a one order of magnitude and since 2014 hundreds of disks have been observed with high angular

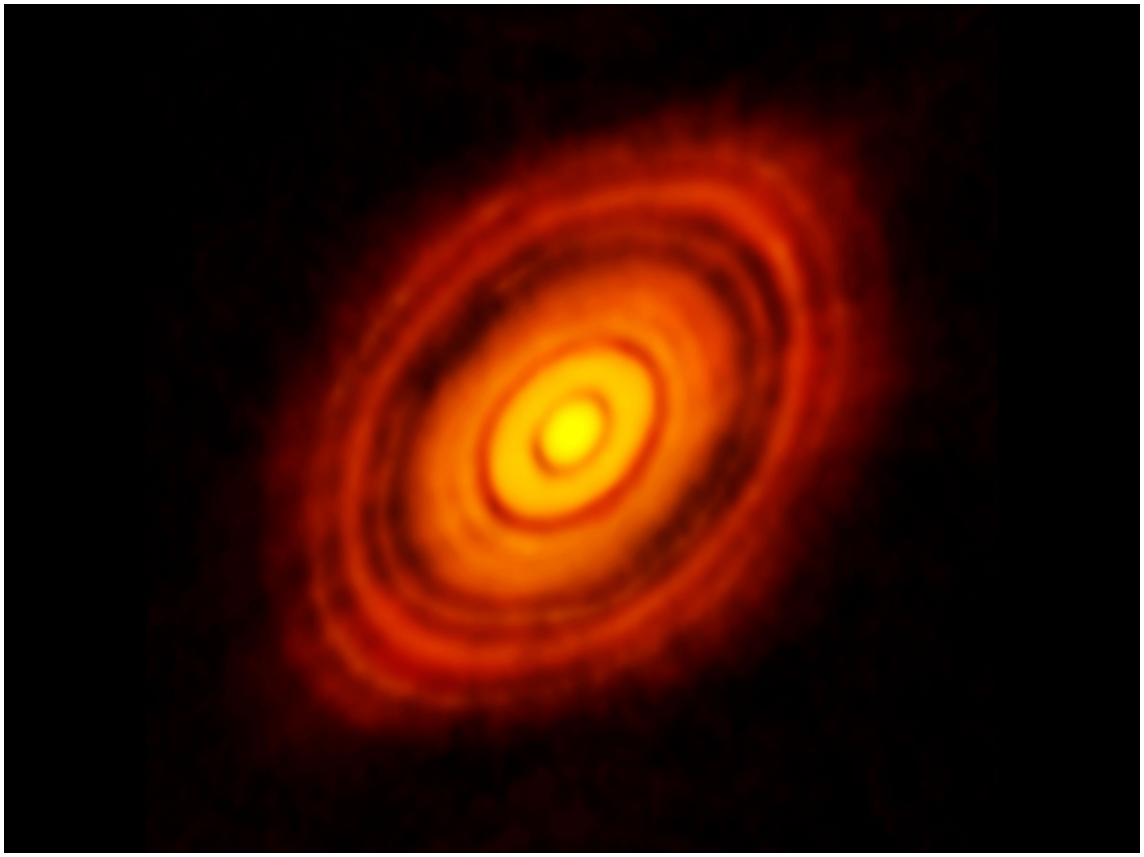

Figure 1.4: Revolutionary image of HL Tauri with ALMA long-baseline campaign revealing for the first time in au-scale substructures in protoplanetary disk, so called "WOW! image"[4]. Image credit: ALMA (NRAO/ESO/NAOJ)[5]; published as part of the press release of the article by ALMA Partnership et al. (2015).

resolution. The first ALMA survey DSHARP[2] showed that substructures are more common in Class II sources than previously thought, while its recent continuator in Class 0/I disks eDisk[3] suggests that those features must form quickly in the transition period between Class I and II since at earlier stages disks appear smooth (Ohashi et al. 2023).

Substructures in form of rings, gaps, spirals, asymmetries, shadows, and crescents were identified in at least 20% of. disks (Bae et al. 2023). Observations suggest that massive disks are more likely to have those substructures. Small, compact disks seem to be smooth, but this behaviour might be an observational bias: most of those objects are observed with low sensitivity and / or low angular resolution (e.g., Long et al. 2019; van der Marel et al. 2021; van der Marel & Mulders 2021; Bae et al. 2023). In some of the disks around very low-mass stars substructures were detected (e.g., Kurtovic et al. 2021). Since substructures might be signposts of the recently formed or still forming planets, it is of a great importance to understand their formation mechanisms and occurrence frequency. This requires statistically large surveys over multiple regions with similar sensitivity and preferably at the same wavelength.

[2] https://almascience.eso.org/almadata/lp/DSHARP/
[3] http://group.asiaa.sinica.edu.tw/almaLP_edisk/index.php

Table 1.1: Protoplanetary disk surveys in different star-forming regions

region	instrument	references	survey
Trapezium	SMA	Mann & Williams (2009)	
Taurus-Auriga	PdBI	Ricci et al. (2010)	
	SMA	Andrews et al. (2013); Akeson & Jensen (2014)	
Taurus	CARMA	Sheehan & Eisner (2017)	
	ALMA	Long et al. (2019)	
ONC	ALMA	Mann et al. (2014); Eisner et al. (2018)	
NGC2024/Orion	SMA	Mann et al. (2015)	
Perseus	VLA	Tobin et al. (2015); Segura-Cox et al. (2016); Tychoniec et al. (2018)	VANDAM
	ALMA	Yang et al. (2021)	PEACHES
Lupus	ALMA	Ansdell et al. (2016, 2018); Lovell et al. (2021); Tazzari et al. (2021)	
Upper Scorpius	ALMA	Barenfeld et al. (2016, 2017)	
OMC	ALMA	Eisner et al. (2016); Otter et al. (2021)	
Chameleon I	ALMA	Pascucci et al. (2016); Long et al. (2018)	
σ Orionis	ALMA	Ansdell et al. (2017)	
IC 348/Perseus	ALMA	Ruíz-Rodríguez et al. (2018)	
Corona Australis	ALMA	Cazzoletti et al. (2019)	
Ophiuchus	ALMA	Cieza et al. (2019); Williams et al. (2019) Testi et al. (2022)	ODISEA
OMC-2	VLA/ALMA	Tobin et al. (2019, 2020)	VANDAM
λ Orionis	ALMA	Ansdell et al. (2020)	
NGC2024/Orion	ALMA	van Terwisga et al. (2020); Haworth et al. (2021)	
OMC-2/3	ALMA	Bouvier et al. (2021)	ORANGES
Lynds 1641 / OMC A	ALMA	Grant et al. (2021)	
Orion A	ALMA	van Terwisga et al. (2022)	SODA

Notes. Surveys are sorted by the year in which a given region was first observed. Observations mainly targeted continuum emission but many of them also traced molecular emission.

The wealth of surveys and submm observations of protoplanetary disks set a foundation of our understanding of those objects. Table 1.1 summarises submm interferometric surveys of several star-forming regions. Surveys of PPDs revealed weak correlation with large scatter between disk and stellar mass (see e.g., Andrews et al. 2013; Manara et al. 2023). This correlation is valid not only for T Tauri stars, but extends also to intermediate mass stars and Very Low Mass Stars (VLMS) / Brown Dwarfs (BD) with the average ratio between disk and stellar mass of $\sim$1% (e.g., Mohanty et al. 2013; Testi et al. 2016; Kurtovic et al. 2021). The relatively most massive disks have mass of $\sim$10% of their host's mass and are expected to be gravitationally unstable. In that case observed substructures might not be only due to the presence of a planet. Measured dust masses of Class II disks appear to be too low with respect to the observed exoplanetary systems. It is very likely that not the whole dust mass is measured due to the lack of sensitivity, or that significant fraction of the mass is locked in large bodies – planetesimals or partially formed planets. Tychoniec et al. (2020) showed that mean disk dust mass decrease with evolutionary stage and that at Class 0 and I disks have comparable amount of solid mass to the known at the time planets. Disk dust masses also seem to decrease on average with the age of the SFR (see e.g., Fig. 5 in Manara et al. 2023). This is a clear signpost of evolution of disk mass with time.

[5]Name chosen at the virtual conference *Five years after HL Tau: a new era in planet formation* hosted by ESO in 2020.

[5]https://www.almaobservatory.org/en/press-releases/revolutionary-alma-image-reveals-planetary-genesis/#fn-6364-2

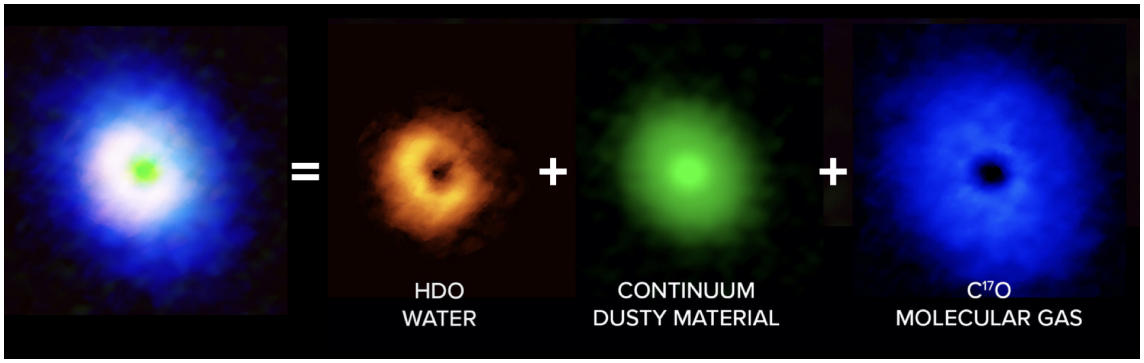

Figure 1.5: Different observables trace different physical and chemical conditions in the disk. Three-colour composite image of the V883 Orionis on the left consists of HDO (red), continuum (green), and $C^{17}O$ (blue) emission. Image adopted from: https://www.eso.org/public/images/eso2302b/. Credits: ALMA (ESO/NAOJ/NRAO), J. Tobin, B. Saxton (NRAO/AUI/NSF)

Dust particles contain the building material needed to form terrestrial planets and cores of gaseous giants. However, a majority of the disk mass is in gas form (∼99%), therefore evolution of the gas impacts the disk evolution at most. Gas in disks is made mostly of hydrogen (atomic and molecular, ∼70%) and helium (∼28%, Bae et al. 2023). Heavier elements contain only 2% of the gas mass with CO, the most frequently detected species in disks, being less abundant than H_2 by a factor of 10^4 (France et al. 2014). Reasons why the most abundant species are not being observed are related to the physical conditions in disks and quantum nature of those species. Typical temperatures in the outer disk of ∼20-40 K are too low to excite H_2 molecule. Energy levels of H_2 are highly separated, on top of that it has no stable dipole moment and only weak quadrupole moment (Field et al. 1966). Similarly, disk temperatures and densities are unfavorable for helium emission. Therefore, to measure disk gas masses one needs to rely on other species that are much less abundant, but still sufficiently bright that are easy to observe in disk conditions (e.g., Miotello et al. 2023; Öberg et al. 2023).

The most commonly detected molecule is ^{12}CO, the main gas-phase carbon carrier in disks. CO is chemically stable with simple interstellar chemistry. ^{12}CO emission is optically thick in most of the cases (Miotello et al. 2023). As that, ^{12}CO can be a good temperature tracer. The main form of CO is also used to trace kinematics of the disk: measure spatially resolved line velocities, deviation from Keplerian rotation, disentangling different emission layers, and investigating structures in the gas with comparison to the dust structures (e.g., Pinte et al. 2023). Other CO isotopologues, ^{13}CO, $C^{18}O$, or $^{13}C^{17}O$, are more optically thin and therefore more adequate for estimates of column densities or disk masses. Disk gas masses are estimated also based on HD (Bergin et al. 2013; Favre et al. 2013; Cleeves et al. 2015; Trapman et al. 2017), CS, or N_2H^+ (Anderson et al. 2022; Trapman et al. 2022). However, this emission is substantially fainter than from CO making observations time expensive. Additionally, fluxes from ionised species depend also on the level of ionised radiation and precise measurement would require additional estimate of ionisation level, e.g. HCO^+ (van 't Hoff et al. 2017; Anderson et al. 2022). Other frequently detected molecules in submm observations consist of CN, HCN, DCN, HCO, C_2H, H_2CO, N_2H^+ (see Öberg et al. 2023, and references therein).

Gas observations give the unique opportunity to infer the vertical structure of the disk. Spatially resolved line emission allows studying morphologies of channel maps (e.g., in a pre-ALMA era: Chapillon et al. 2012). Additionally, very high resolution can reveal butterfly-like patterns tracing upper and lower surfaces of the disk (e.g., MAPS[6] survey, Öberg et al. 2021). Availability of several molecules and / or isotopologues allow constructing temperature profile in not only radial, but also vertical direction (e.g., Law et al. 2021a,b, see also Fig. 1.5). Temperature structure of the disk affects dust dynamics – its migration and vertical settling, chemistry of the disk – location of snowline surfaces for different molecules and possibility of chemical reactions. Chemical inventory and its distribution impacts then composition of planetary embryos and primordial atmospheres.

Resolved emission line observations give the most comprehensive information about protoplanetary disks. Recent years resulted in a large number of ALMA surveys of molecular lines. However, drawing conclusions from the results is not trivial. Interpretation of emission lines observations is highly linked with assumptions put into the modelling (e.g., Woitke et al. 2009; Bruderer et al. 2012; Miotello et al. 2014; Williams & Best 2014). Very complex models are computationally expensive while too simplified ones can lead to incorrect results. Observational surveys included only close, often massive, disks (e.g., Miotello et al. 2017; van Terwisga et al. 2019; Garufi et al. 2020b; Öberg et al. 2021). Deep, high-resolution observations are highly time expensive what results in their rarity. Disk mass measurements revealed some discrepancies. Mass estimates based on gas are different than based on dust suggesting lower than canonical gas-to-dust ratio of 100. Moreover, CO-based masses seem to be too low when compared to other species. For instance, HD-based disk masses are larger by up to two orders of magnitude (e.g., Bergin et al. 2013; Favre et al. 2013; Cleeves et al. 2015; Trapman et al. 2017). Since the discrepancy is not observed to the same extend in warmer disks of Herbig stars (Kama et al. 2020), it has been proposed that carbon is depleted from gas because in cold regions of the disk (midplane, outskirts), carbon and oxygen are locked up in ices and are therefore unobservable in emission (Kama et al. 2016; Powell et al. 2022). Dependence of gas carbon depletion on disk temperature has also been suported by [CI] measurements (Sturm et al. 2022). The amount of carbon in disks with respect to the hydrogen is also not well constrained.

Spectral line surveys targeting large number of PPDs are essential for deep understanding of chemistry in disks and its evolution. Many studies were already done, but we are still lacking a proper statistics. Currently, there are few ALMA Large Programs answering this need. The exoALMA program hunts for planet in 15 disks with high angular resolution observations of few molecular lines. AGE-PRO[7] will homogeneously observe 30 disks spanning wide range of ages to constrain the evolution of disk properties. The carbon depletion and metallicity will be a focus of the the ALMA Disk-Exoplanet C/Onnection (DECO) program observing 80 disks across four star forming regions, range of stellar and disk properties. Those observa-

[6] https://alma-maps.info/
[7] https://www.exoalma.com/

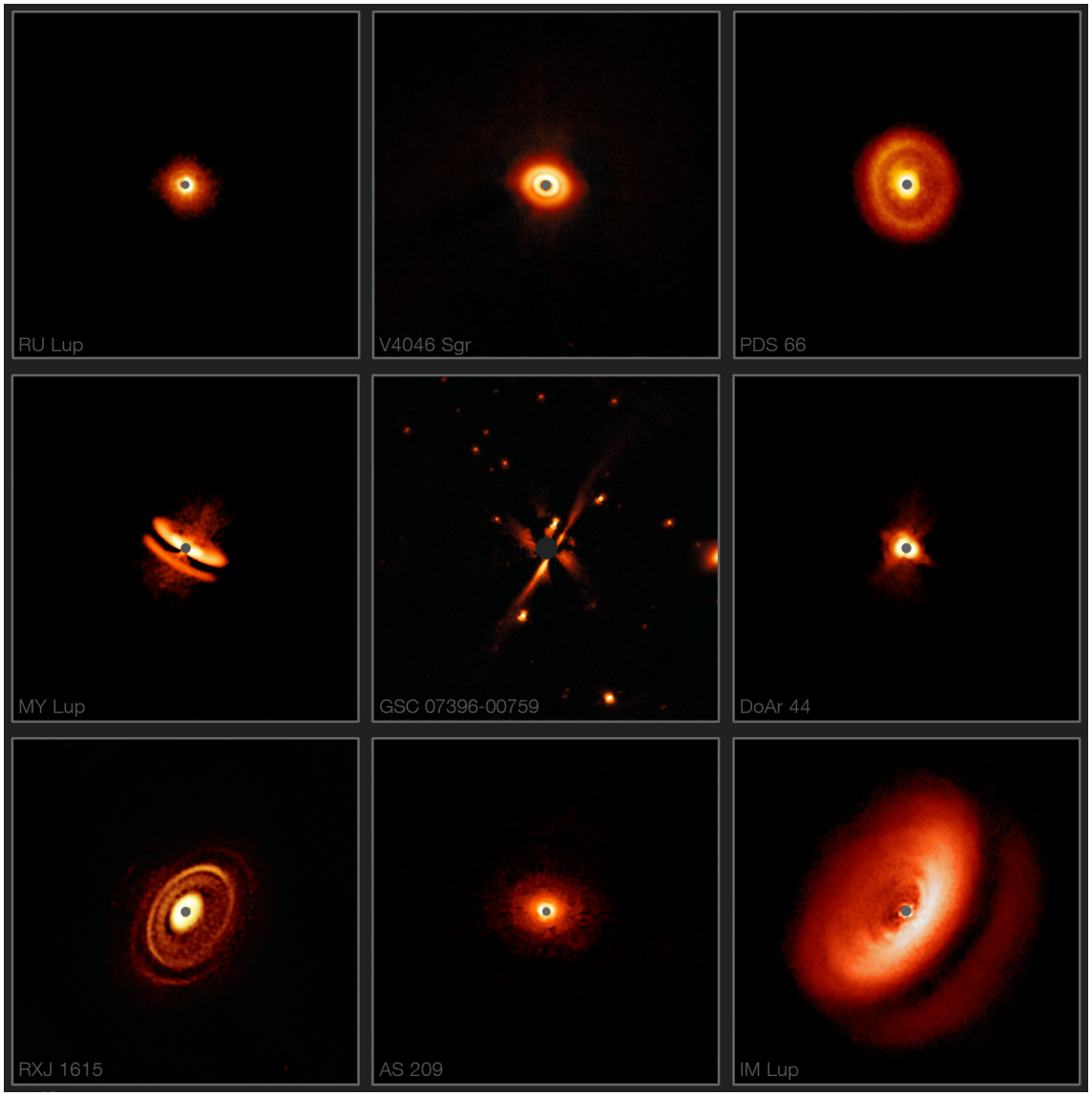

Figure 1.6: Collection of VLT/SHPERE scattered light images of protoplanetary disks. Image credits: ESO / Avenhaus et al. (2018) / Sissa et al. (2018) / DARTTS-S and SHINE collaborations[8].

tions will be essential in expanding our understanding of PPDs as we will be able to start building statistics in different star forming region and start investigating how different environments impact disk chemistry.

1.2.1.2 IR and optical observations of protoplanetary disks

High spectral and spatial resolution observations in (sub)mm regime revealed an extensive collection of substructures in protoplanetary disks. Those features are not only produced by mm-size dust grains or cold molecular gas. High-contrast and high-resolution imaging identified complementarily rich family of features in the stellar light scattered on small, μm-size grains. Figure 1.6 presents a gallery of several PPDs observed in NIR.

[8] https://www.eso.org/public/news/eso1811/

First images of disks were taken by Hubble Space Telescope (HST) and showed proplyds and dark, dusty disks blocking bright nebular background in Orion (O'Dell et al. 1993; O'Dell & Wen 1994; O'Dell & Wong 1996). First scattered light images of disks were observed around binary systems (Roddier et al. 1996) or bright Herbig stars. Grady et al. (1999) presented extended "nebulosity" around AB Aurigae seen in optical HST image, while Fukagawa et al. (2004) investigated the same target in H-band with CIAO at Subaru Telescope. First Adaptive Optics (AO) observations of a disk with ESO/ADONIS targeted HD 100546 (Pantin et al. 2000), followed up by the extensive, multi-instrument study (Grady et al. 2001). Other early scattered light observations with HST consisted of HD 141569 (Weinberger et al. 1999; Mouillet et al. 2001; Clampin et al. 2003), TW Hydrae (Krist et al. 2000), or GG Tauri (McCabe et al. 2002). Edge-on disk were also captured in scattered light, e.g., around PDS 144N with multi-instruments AO polarimetry (Perrin et al. 2006). Studies of single objects were succeded by surveys. The Strategic Explorations of Exoplanets and Disks with Subaru (SEEDS) project performed an imaging of a ∼500 young stars with wide range of masses and ages (Tamura 2009; Thalmann et al. 2009; Hashimoto et al. 2012; Kusakabe et al. 2012; Akiyama et al. 2016; Tamura 2016; Uyama et al. 2017). Another campaign was conducted with VLT/NACO targeting few Herbig Ae stars (Quanz et al. 2011, 2012, 2013b,a; Canovas et al. 2013; Garufi et al. 2014). With VLT/SPHERE coming online new surveys became possible, e.g., Disks Around T Tauri Stars with SPHERE (DARTTS-S, Avenhaus et al. 2018; Garufi et al. 2020a), or Disk Evolution Study Through Imaging of Nearby Young Stars[9] (DESTINYS, e.g., Ginski et al. 2020, 2021). Similar program was run on Gemini Telescope – Gemini-LIGHTS (Large Imaging with GPI Herbig/TTauri Survey, Laws et al. 2020; Rich et al. 2022).

One of the most striking discoveries with imaging technique were detections of protoplanets around famous PDS 70: first, in the polarimetric observations taken by VLT/SPHERE (PDS 70 b, Keppler et al. 2018), and the second in the Hα image from VLT/MUSE tracing accretion onto both protoplanets (PDS 70 c, Haffert et al. 2019). Circumplanetary disks were later claimed around PDS 70 b based on NIR spectrum (Christiaens et al. 2019) and PDS 70 c based on ALMA continuum emission (Benisty et al. 2021). The first and only system with confirmed protoplanets continues being observed with multiple instruments at wide range of wavelengths. Other protoplanetary candidates in protoplanetary disks are still waiting confirmation of their presence.

Imaging of protoplanetary disks in optical and IR wavelengths employs several techniques that allow removal of a stellar signal from the image, e.g., by physically blocking stellar light. All high-contrast imagers and some IFUs are now equipped with coronagraphic mask. However, it limits our investigation to the extend of the disk outside 0.1-0.15″ from the center of the stellar image. Usually, coronagraphy is combined with one of the post-processing techniques of differential imaging.

[9] https://www.christian-ginski.com/home/destinys

In the Reference Differential Imaging (RDI) the signal of the stellar light in the science image is removed using observations of a similar in properties and brightness reference star. That requires assuming that the weather conditions and PSF are the same. The residual image will contain only component from the disk or planet. This technique is particularly applicable for space-based telescopes, since their PSF is more stable than in ground-based telescopes, e.g., Grady et al. (1999, 2001), archival HST project ALICE (Choquet et al. 2014), but also VLT/SPHERE observations (Boccaletti et al. 2021; Wahhaj et al. 2021).

The most frequently used technique is Angular Differential Imaging (ADI). It uses the "pupil-stabilised" mode which makes the instrumental PSF and the stellar image in the center of the field stable. At the same time all off-axis targets exhibit apparent rotation enabling their clear identification. The main problem of the technique is the signal of the planet or disk can be suppressed if the rotation of the field is too small, and that effect can particularly challenging for circumstellar disks (Milli et al. 2012; Perrot et al. 2016; Ginski et al. 2016; de Boer et al. 2016).

The Polarization Differential Imaging (PDI) technique (Kuhn et al. 2001) appears to be particularly successful in imaging of circumstellar disks (Benisty et al. 2023). When the light is scattered off by dust grains, it is partially linearly polarised. The degree of this polarisation depends on scattering angle. The light from the system is split into two orthogonal polarisation directions and recorded simultaneously. The central star exhibits only low level of polarisation and therefore will have a similar image in both polarisations, while disk's image will differ significantly. PDI is applicable to the wide range of instruments, e.g., UKIRT/IRPOL (e.g., Kuhn et al. 2001), VLT/NACO (e.g., Avenhaus et al. 2014b,a), Subaru/HiCIAO (e.g., Akiyama et al. 2016), VLT/SPHERE (e.g., de Boer et al. 2020), Gemini/GPI (e.g., Laws et al. 2020). The technique is challenging to apply to disks with high inclinations, because the assumption that disk polarisation is azimuthal might not hold (Canovas et al. 2015).

High contrast imaging instruments have currently IFU with low spectral resolution ($R \lesssim 100$, Claudi et al. 2008; Larkin et al. 2014; Groff et al. 2015) allowing application of another technique, Spectral Differential Imaging (SDI). Stellar speckle halo scales radially with wavelength, while images of continuum sources do not change. That allows removing stellar light from images leaving the signal from the planet or disk. Shortcomings of this technique are similar to ADI (mainly signal suppression), although here, since images at all wavelengths are taken simultaneously, the change of weather conditions or PSF are not affecting the observations. PDS 70 c was discovered applying SDI to the VLT/MUSE observations (Haffert et al. 2019).

Recent launch of James Webb Space Telescope (JWST) opened new possibilities to look at the PPDs in near and mid-IR. The MIR image of a debris disk of Formalhault was presented by Gáspár et al. (2023), while Lawson et al. (2023) presented NIR coronagraphy of a debris disk AU Mic. Many studies published so far focus on spatially unresolved spectral investigations of MIR chemical inventories of inner parts of protoplanetary disks. The JWST Observations of Young protoStars (JOYS)

program investigates outflows and disks around ∼24 protostars in wide range of masses (Beuther et al. 2023; van Dishoeck et al. 2023). The the MIRI INfrared Disk Survey (MINDS) program targets more evolve sources, ∼50 Class II Herbig Ae, T Tauri, and very low mass stars (Kamp et al. 2023). Early results revealed rich inventory of molecular species: H_2, H_2O, hydrocarbons: C_2H_2, C_4H_2, C_6H_6, CH_4, HCN, CO, CO_2, OH, PAHs, and ice absorption bands (van Dishoeck et al. 2023; Gasman et al. 2023; Tabone et al. 2023). Results of the program include also first detection of $^{13}CO_2$ in space (Grant et al. 2023) and water detection in the inner part of the disk of PDS 70 (Perotti et al. 2023). Water emission in connection with pebble drift was also target of the study of Banzatti et al. (2023). The PDRs4All program extends the legacy of HST in longer wavelengths delivering stunning images Photo-Dissociation Region (PDR) regions and Orion proplyds (Berné et al. 2022; Habart et al. 2023).

Before JWST the access to far- and mid-IR was possible with *Herschel Space Observatory* (HSO). *Herschel* hosted on board FIR IFU instrument, Photodetector Array Camera and Spectrometer (PACS). The angular resolution on PACS was not enough to resolve PPDs, nevertheless, the programs GAS in Protoplanetary Systems (GASPS) and "Dust, Ice, and Gas In Time" (DIGIT) (together with Spectral and Photometric Imaging Receiver (SPIRE)) brought important results. The latter targeted 31 weak-line T Tauri stars and detected circumstellar disks around 15 of them (Cieza et al. 2013). Program also included 30 Class 0/I protostars, which exhibit rich water, OH, CO, [OI], and [CII] emission yelling rotation temperatures of ∼200-400 K for all molecules but hot CO (>1000 K Green et al. 2013). The GAPS program observed ∼250 YSOs focusing mainly on [OI] line at 63 μm (Dent et al. 2013). Strength of this line was correlated with the disk dust mass estimated form submm observations and its detections required a minimum mass of 10^{-5} $M_\odot$. Presence of the line, interpreted as a tracer of a gas disk, was found to be also correlated with the age of the system; there was no detection in associations older than 20 Myr.

The field of direct imaging of disks in optical and IR is now undergoing a huge development resulting in rapidly growing number of disks imaged (∼130, Benisty et al. 2023). However, current facilities limit those studies to the relatively close and bright systems. Disks detected in polarised light are around stars with spectral type between K and A, roughly corresponding to the stellar masses of 0.4-10 $M_\odot$ (Benisty et al. 2023). The limitation on stellar brightness is imposed by the AO. Planned upgrades of existing instruments and AO systems are expected to allow studying disks around lower-mass stars (e.g., VLT/SPHERE+, Boccaletti et al. 2020; Gemini/GPI2, Chilcote et al. 2020; Magellan Clay/MagAO-X Males et al. 2020). Additionally, 30-meter class telescopes will offer significant improvement in spatial resolution with IR AO imagers: ELT/MICADO, ELT/METIS, GMT/IRS, and TMT/IRIS (Benisty et al. 2023).

Access to the very inner regions ($\lesssim$1 au) of protoplanetary disks is possible with optical and IR interferometry. Current facilities offer baselines up to 350 m corresponding to the angular resolution $R \sim \lambda_0/2B \sim$ 2-10 mas (and 0.25-1.5 au at

distance of 150 pc, Millan-Gabet et al. 2007). At wavelength range of ∼1 - 13 μm they allow probing material with T ∼300-1800 K. Among available arrays of telescopes are Palomar Testbed Interferometer (PTI), Infrared-Optical Telescope Array (IOTA), Infrared Spatial Interferometer (ISI), Keck Interferometer (KI), Center for High Angular Resolution Astronomy interferometer (CHARA), and Very Large Telescope Interferometer (VLTI) with MID-infrared Interferometric instrument (MIDI), Astronomical Multiple BEam Recombiner (AMBER), PIONIER, GRAVITY, and MATISSE. Most of them allow combining two telescopes at once, with only PIONIER, GRAVITY, and MATISSE working on four telescopes at once. Due to their complexity and sparse spatial sampling, interferometric observations require modelling of visibilities in order to interpret observed emission. The most frequently assumed model consists of stellar and ring component.

The first ever YSO to be observed with IR interferometry was FU Ori with PTI (Malbet et al. 1998). Those observations confirmed the youth of the object and that it is surrounded by the outbursting circumstellar disk. Then, interferometric observations targeted Herbig stars and found sizes of emitting regions in NIR of 0.6-6 au (Millan-Gabet et al. 1999, 2001), larger than expected (Hillenbrand et al. 1992). It was later established that NIR sizes trace dust sublimation radii and scale with luminosity of the central object (including accretion luminosity), also applicable to the T Tauri stars (Monnier & Millan-Gabet 2002; Muzerolle et al. 2003; Akeson et al. 2005a; Millan-Gabet et al. 2007; Dullemond & Monnier 2010). The corresponding sublimation temperatures range between 1000 and 2000 K. The correlation exhibit some scatter which can be explained by smaller (nano) dust grains (Monnier & Millan-Gabet 2002; Kokoulina et al. 2021), uncertain SED decomposition (Eisner et al. 2005), or evolution of disks and their dispersal (Akeson et al. 2005b). It was also found, that the emitting area changes with wavelength being smaller at shorter wavelength. This finding pinpoints that the inner edge of the disk is not a sharp rim (Eisner et al. 2007; Isella et al. 2008; Kraus et al. 2008; Tannirkulam et al. 2008; Benisty et al. 2010). High spectral resolution interferometric observations (e.g., with VLTI/AMBER) allow extending this study by the investigation of emitting regions of emission lines. Emission of Brγ, popular accretion tracer in NIR, was found to origin from the disk wind from area closer to the star than NIR continuum emission (Caratti o Garatti et al. 2015; Garcia Lopez et al. 2015).

The MIR interferometric observations are sensitive to warm gas and dust with $T \sim 100$ K. The sizes of emitting regions around Herbig stars at those wavelength are of the order of 10 au (Leinert et al. 2004; Millan-Gabet et al. 2007). Those sizes appear to correlate with MIR colours from IRAS suggesting larger degree of flaring of disks. MIR observations give also access to the measurements of dust species: carbon-rich Polycyclic Aromatic Hydrocarbons (PAHs) and oxygen-rich amorphous or crystaline silicates. With recent launch of JWST numerous silicate and ice species has been reported, however this emission is not spatially resolved. Currently, only interferometry is is able to access spatial information about MIR emission.

1.2.2 Evolution of protoplanetary disks

Observations of protoplanetary disks revealed the wealth of their properties (Sec. 1.2.1), which are interpreted as signposts of disks evolution. One of the most important aspects of disk evolution is the transport and removal of angular momentum which manifestations are jets and outflows. Evolution of PPDs is inseparable from the evolution of the central star as indicated by the presence of accretion. Lastly, physical and chemical processes happening in disks directly affect the planets forming there. Understanding how disks evolve is then of high importance for understanding the formation of Solar System. The most common and widely accepted models of PPDs evolution are presented below.

1.2.2.1 Viscous evolution

The early scenario predicting evolution of the disk and considered since then as a "classic model of disk evolution" is a Lynden-Bell & Pringle (1974) realisation of the viscous model of Shakura & Sunyaev (1973). The latter is parameterised by the dimensionless parameter $\alpha \sim (v_\mathrm{t}/c_\mathrm{s})^2$. Using α the kinematic viscosity is $\nu = \alpha c_\mathrm{s} H$, where c_s is a sound speed, v_t is a turbulent velocity, and H is a disk scale height. In this model viscosity is a main carrier of angular momentum and a main driver of disk evolution.

The "self-similar" solution of disk evolution from Lynden-Bell & Pringle (1974) assumes power-law disk exponentially truncated at the characteristic radius R_c. In that framework evolution of disk global properties are also power-laws of time. During the viscous evolution disk spreads out growing in radius but loosing its mass, also mass accretion rate diminishes with time. It is possible to define a typical evolutionary disk timescale:

$$t_\mathrm{disk} = \frac{M_\mathrm{d}(t)}{\dot{M}(t)} = 2(2-\gamma)(t+t_\nu) \tag{1.6}$$

which depends on the slope γ defining the power-law relation between viscosity and disk radius, the viscous time t_ν, which further depends on α. In the framework of protoplanetary disks, α is expected to have values $\sim 10^{-3}$-10^{-4} (Manara et al. 2023), while observations yield wide range of values between $\sim 10^{-4}$ and 10^{-1} (e.g., Hartmann et al. 1998; Ansdell et al. 2018; Rosotti 2023). Another important consequence of self-similar solution is that for age of a the star + disk system significantly larger than viscous time the current mass accretion rate linearly depends on the current disk mass and that relation is independent from viscosity and initial conditions (Hartmann et al. 1998). That correlation was proved observationally by Manara et al. (2016) and later by Mulders et al. (2017).

1.2.2.2 Disk winds evolution

Alternative approach to the disk evolution offer MHD winds scenario. In that context, the angular momentum is not transported as in the viscous scenario but removed from the disk by MHD winds (Blandford & Payne 1982). Winds are launched from the disk

surface by the magnetic field creating an outflow of the material. At large distances from the disk surface those outflows transform into collimated, perpendicular to the disk, bipolar jets. Solving the evolution of disk properties requires some kind of a parameterisation. A recent work of Tabone et al. (2022) proposed a simple approach to the problem. They introduced analogous to the Shakura & Sunyaev (1973) dimensionless parameter, $\alpha_{\rm DW}$, which is a normalised wind torque in a way that allows to define a local accretion rate due to the MHD disk winds in a mirroring way to the local accretion rate due to viscosity. As a consequence, the two mechanisms, viscosity and MHD winds, can be directly compared and ratio of two accretion rates scales with the ratio of the two dimensionless parameters: $\dot{M}_{\rm acc}^{\rm visc}/\dot{M}_{\rm acc}^{\rm DW} \simeq \alpha/\alpha_{\rm DW}$.

In the MHD disk wind scenario disk mass and mass accretion rate evolve exponentially with time scaled by the accretion timescale, equivalent of the viscous timescale: $t_{\rm acc} = (\alpha/\alpha_{\rm DW})t_\nu$. Then, the disk evolutionary timescale is:

$$t_{\rm disk} = \frac{M_{\rm d}(t)}{\dot{M}(t)} = 2t_{\rm acc}(1 + f_{\rm M}) \tag{1.7}$$

where $f_{\rm M}$ is the global mass ejection to mass accretion ratio. This model of disk evolution introduces few important changes with respect to the viscous scenario. First, the initial conditions of disk parameters impact their evolution, specifically the relation between disk mass and mass accretion rate. Secondly, disk radius does not grow with time since angular momentum is not transported outwards to the large radii. Thirdly, disk evolutionary timescale does not become longer as in the viscous case, or in other words, the evolution of the disk does not slow down. Recent population synthesis studies have shown that the MHD disk wind scenario better reproduces spread in disk parameters observed in nearby star-forming regions (Somigliana et al. 2023). However, further observational and theoretical investigation is needed to fully understand mechanisms of disk evolution and explain observed trends and their spreads.

1.2.2.3 Internal photoevaporation from the central star

There are also other processes that take part in dissipation of the disk. One that is more important in later stages of disk evolution is photoevaporation from the central star causing inside-out dispersal. Radiation from the star heats up the disk atmosphere launching thermal winds if the gas temperature becomes higher than the local escape temperature. In order for this process to be destructive, the mass loss rate via photoevaporative winds must exceeds mass accretion rate onto the star (Ercolano & Pascucci 2017). Accretion is very high at the youngest ages of the star but decreases with the evolution, conditions for internal photoevaporation to kick in appear only after few Myr around the Class II / III stage (Ercolano & Pascucci 2017).

To effectively heat up the disk upper layers the radiation needs to have high enough energy. The most efficient to heat up the gas disk are far-ultraviolet photons (FUV, 6 eV$\leq E \leq$ 13.6 eV) and soft X-rays (100 eV$\leq E \leq$2 keV). They have the largest penetration paths, $N_{\rm H} \sim 10^{20}$ - 10^{22} cm^{-2}, which exact values depend on properties

and abundances of the small dust grains and PAHs (Hollenbach & Gorti 2009). The extreme-ultraviolet (EUV, 13.6 eV$\leq E \leq$ 100 eV) radiation is fully absorbed within the $\sim 10^{17}$ cm^{-2} (Hollenbach & Gorti 2009), so might be mostly relevant for the most inner regions of disk (McKee & Ostriker 2007). Hard X-rays ($E \geq$2 keV) can penetrate very deep through the disk and therefore are not efficient driving photoevaporative winds from the most upper layers (Ercolano & Pascucci 2017). Models predict mass loss rates around Sun-like stars of order 10^{-10}-10^{-7} $M_{\odot}$/yr (Alexander et al. 2006; Gorti & Hollenbach 2009; Owen et al. 2012) in same cases depending on the X-ray luminosity of the stars. Young, low-mass stars are strong X-ray emitters but observations show a scatter of 2-3 orders of magnitude in X-ray luminosities (e.g., Feigelson & Montmerle 1999) which then corresponds to the large scatter of mass loss rates and high degeneracies in model predictions.

The transition disks (disks with large inner cavities) are understood as those whose evolution is currently driven by the internal photoevaporation. However, models combining viscous evolution with photoevaporation are able to explain only $\sim$50% of them (Ercolano & Pascucci 2017, and references therein). The others have too high, inconsistent with predictions, accretion rates, suggesting that transition disks might not be a simple evolutionary step between Class II disks and fully cleared out ones but a group of heterogeneous objects with different evolutionary histories. Another evidence in favour of internal photoevaporation are disk winds seen in spectroscopically resolved atomic forbidden emission lines (e.g., [O I] 5577,6300Å, [S II] 4068,6731Å, [Ne II] 12.8μm, Banzatti et al. 2019, Pascucci et al. 2023). However, those winds are hard to distinguish from MHD case (discussed in previous section 1.2.2.2) (Ercolano & Pascucci 2017). Presence of photoevaporation and its properties can impact orbital extends of giant planets (Ercolano & Rosotti 2015), enrich disk midplane, and later atmospheres of giant planets, of refractory elements (Guillot & Hueso 2006; Monga & Desch 2015), and can help explaining formation of Jupiter and Saturn (Ali-Dib 2017).

1.2.2.4 Other processes

If protoplanetary disks are massive enough ($M_{\rm disk} \gtrsim 0.1 M_{*}$) they might be prone to self-gravity (Kratter & Lodato 2016). Manifestations of it are some substructures in the disk, especially spirals. They have been observed in scattered light images (e.g., Grady et al. 2013; Benisty et al. 2015; Wagner et al. 2015; Stolker et al. 2016), molecular emission at submm (e.g., Teague et al. 2018; Paneque-Carreño et al. 2021; Veronesi et al. 2021), but also in thermal dust emission (e.g., Pérez et al. 2016; Dong et al. 2018; Huang et al. 2018). Gravitational Instability (GI) in the form of spiral arms can drive angular momentum transport (Lynden-Bell & Kalnajs 1972). It is the most important consequence as together with angular momentum the accretion of matter is driven onto the star. Also, GI can lead to disk fragmentation and further to the formation of stellar, BD, or planetary companion (Adams et al. 1989; Boss 1997; Nayakshin 2010; Rice et al. 2015; Vigan et al. 2017; Forgan et al. 2018). Even if the instability is not strong enough to brake the disk, the boosted concentrations of dust particles in spiral arms create favorable conditions for dust grains to grow and form planetesimals.

The scenarios presented so far address only gas evolution in the disk. However, dust as a main source of opacity in the disk and material for terrestrial planets and cores of gaseous giants is an important ingredient of disk evolution. While dust grains grow, they become less coupled to the gas and their evolution becomes independent form the gas evolution. At the same time they settle toward the disk midplane (Williams & Cieza 2011). The both processes were observed (Natta et al. 2004b; Andrews & Williams 2005; Wilner et al. 2005; D'Alessio et al. 2006; Furlan et al. 2006; Olofsson et al. 2009; McClure et al. 2010; Ricci et al. 2010, and see Sec. 1.2.1) and ideally should lead to the vertical distribution of dust grains. Turbulence present in the disk however mix dust grains and blurred this ideal picture (Williams & Cieza 2011). Since the disk dust masses on average seem to decrease with cluster time (Testi et al. 2022; Manara et al. 2023), they must be undergoing some evolution possibly leading not only to the dust sublimation close to the stellar surface but also planet formation.

1.2.2.5 Disk evolution and planet formation

Disk substructures, gaps, rings, spirals, arcs, shadows, seen in dust and gas, continuum and scattered light emission (see Sec. 1.2.1), can also be interpreted as the signatures of presence of young planets. That indicates very tide connection between disk evolution and planet formation. The protoplanets were found within the dust gap (in the famous system PDS 70, Keppler et al. 2018; Haffert et al. 2019) as well as inferred from gas kinematics (Pinte et al. 2018), what motivated several planet-hunting campaigns, resulting so far only in planetary candidates (for the criteria for a candidate to be confirmed planet see Pinte et al. 2023).

Timescale of disk evolution sets the time required for planets to form, while disk masses tell us how much material is available for planets. Constraining the two parameters is uncertain as they depend on multiple factors, like characteristics of their host star and environment in which they are formed. Multiple surveys of PPDs found that Class II objects have lower dust mass content than observed in exoplanetary systems. At the same time, stars do not seem to acquire a lot of mass between Class 0/I and Class II stages (Drążkowska et al. 2023, and references therein). Among the others, the most popular explanation is that planet formation must start early on and at the Class II stage dust is mostly locked into larger bodies, like planetesimals or planetary embryos (Tychoniec et al. 2018). The process of planet formation is thought to be highly inefficient, with the ratio between total available dust mass to the final mass of planetary system is $<10\%$ (Drążkowska et al. 2023).

Dust evolution in disks is coupled with gas evolution. Interaction with the gas slows down dust particles leading to their radial drift towards the central star. How strong is this drift depends on grain sizes and leads to radial grain size segregation. If grains drift inwards faster than they grow, it will be impossible to form planetesimals (so called "radial drift barrier", Drążkowska et al. 2023). As dust aggregates grow, they decouple from the gas particles and obtain larger relative velocities, what then leads to collisions between particles. If the velocities are below certain threshold

velocity (1 - 80 m/s depending on disk and grain parameters, e.g., Güttler et al. 2010; Yamamoto et al. 2014; Gundlach & Blum 2015), colliding particles will stick to each others and grow. Above this velocity particles will bounce or fragment, the latter being particularly problematic for larger grains (∼cm-size) stopping them from further growth. This limitation is called "fragmentation barrier". Bouncing particles are small, often still partially coupled to the gas, and their growth is stopped early on due to the "bouncing barrier" (Drążkowska et al. 2023).

In the *Protostars and Planets VI* review, Johansen et al. (2014) listed three possibilities to overcome those three barriers and form planetesimals. If the colliding particles have significantly different masses and collision velocity is very high ($\gtrsim$10 m/s), then only smaller particle will fragment leaving some of its parts on the larger body. That would allow some particles grow beyond bouncing and fragmentation barrier, however this growth was found to be too slow to also overcome radial drift barrier (Estrada et al. 2016). Also porosity can help growing dust aggregates even at large velocities due to their large cross-sections. This scenario have some limitations as icy grains, considered as a main source of porosity, will not survive in the very young and hot disk (Homma & Nakamoto 2018). In the third scenario, self-gravitating pebble clumps can collapse if triggered by the streaming instability, directly leading to planetesimal formation (Youdin & Goodman 2005). This idea is supported by the observations of comets and trans-Neptunian binaries in the Solar System (Nesvorný et al. 2019). Streaming instability leads to formation of large planetesimals (∼100 km, e.g., Simon et al. 2016; Schäfer et al. 2017), but requires mm-size pebbles and local enhancement of dust-to-gas ratio (to the value ∼1 in the midplane, Carrera et al. 2015; Li & Youdin 2021). This is why inferring observationally the location of molecular snowlines is important. Schoonenberg & Ormel (2017) and Drążkowska & Alibert (2017) shown, that the water snowline can support creating the pebble pile-up and further burst of planetesimal formation. The icy, sticky pebbles outside the snowline are moving inwards faster than dry and smaller particles inside the snowline inducing a so called "traffic jam" effect when icy aggregates would be stopped from moving inwards and would therefore boost the concentration of pebbles.

The subsequent process of planet formation incorporates accreting solid material, for cores of giant planets and to build the terrestrial ones, as well as gas, which will become their atmospheres ("core accretion scenario"). Properties of those building block (both dust and gas) determine properties of forming planets and planetary systems. The number of giant planets within the system seem to correlate with metallicity of the host star (Santos et al. 2004; Fischer & Valenti 2005; Fulton et al. 2021). More metal-rich stars have more solids in their disks to build planets. Chemical composition of planets depends on their initial location within the disk and migration history – through how many snowlines they will pass attracting different molecules in gaseous form. Their final mass additionally depends on the speed in which planet is moving inwards and efficiency of accretion. Those processes also vary with time accelerating with growing planetary mass. Additionally, any instabilities within the disk will alter formation paths. The overall process of forming the planetary system is incredibly complicated and dependent on many factors. E.g.,

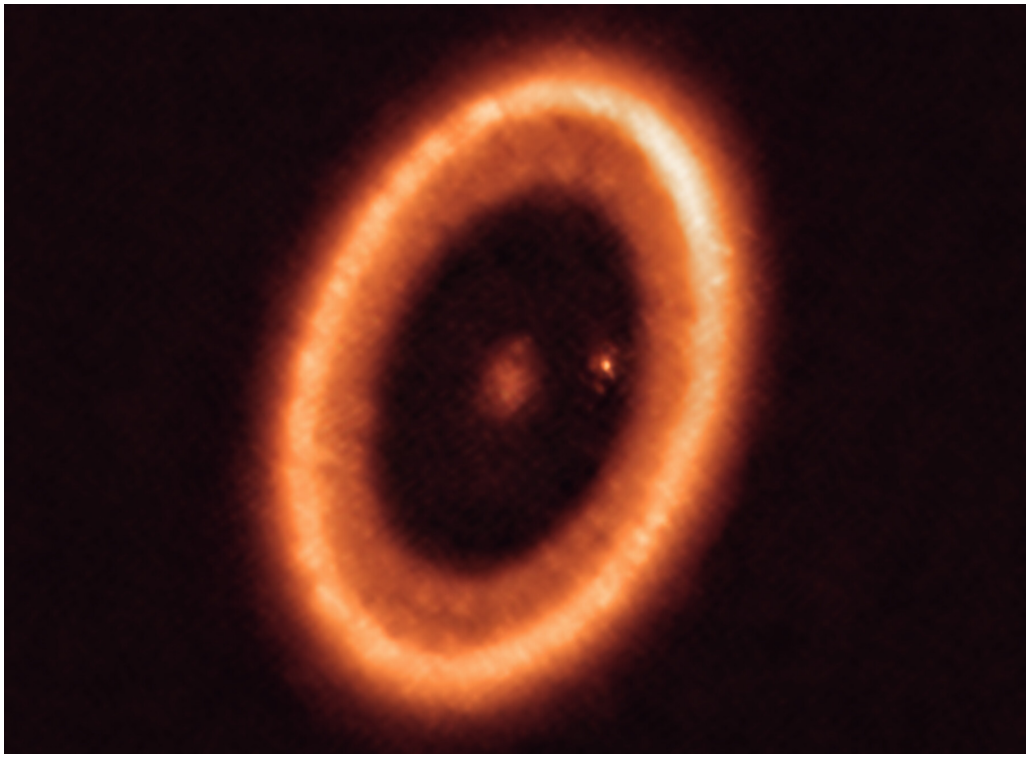

Figure 1.7: Circumplanetary disk around PDS 70 c revealed by high angular resolution ALMA observations. Credit: ALMA (ESO/NAOJ/NRAO)/Benisty et al. (2021)

there is no model that would be able to fully reproduce formation of Solar System in a comprehensive manner (see for overview of available models Drążkowska et al. 2023).

An interesting aspect of planet formation studies which recently became popular is a concept of circumplanetary disk (CPD). Forming planets are supposed to gather material around themselves, similarly to the stars and PPDs, which might or might not be disk-like. CPDs are thought to be places of moon(s) formation in a scaled down version of a star and planets forming in its circumstellar disk. So far, there has been only one detection of CPD with ALMA in the PDS 70 system around planet c (Benisty et al. 2021, see Fig. 1.7), however, more of them could be observed in MIR with future instrument METIS on Extremely Large Telescope (ELT) (Oberg et al. 2023).

1.2.3 Accretion

Young stars grow in mass due to accretion, a process in which material is transferred from the accretion disk onto the star. This process is highly important because it decides about future evolution of the star. Accretion is also a signpost of disk evolution (Hartmann et al. 2016; Miotello et al. 2023). On the other hand, at the first stages of evolution disk gains mass from the surrounding envelope and the remain of the natal molecular cloud. Those stages are also important for stars, as they are supposed to acquire most of the mass at Class 0 stage (McKee & Ostriker 2007, see

also Sec. 1.1.1) and later on decrease their accretion activity. Below, I briefly explain the theoretical view on accretion mechanisms for Class II disks (Sec. 1.2.3.1) and their observational tracers (Sec. 1.2.3.2).

1.2.3.1 Magnetospheric accretion

Material in the disk – gas and dust – is transported inwards by viscosity, turbulence, or other mechanisms (see Sec. 1.2.2). In the vicinity of stellar surface the temperature is very high, disk is heated to ∼1000 K causing sublimation of the dust grains (Hartmann et al. 2016). This dust destruction radius is called sublimation radius and its value is of around 0.1 au. Dust in the inner edge of the disk heats up and re-radiates absorbed energy in NIR. Magnetosphere of the central star truncates disk at few stellar radii. The matter flows onto stellar surface in accretion columns following magnetic field lines and heated to the temperatures of ∼8000 K. When the accreting matter hits the stellar surface it gets heated to the temperatures of $\sim 10^6$ K and radiates this thermal energy in X-rays (Hartmann et al. 2016). However, most of this emission is absorbed and re-radiated in UV excess emission and several emission lines. Excess emission is also observed in optical and IR in photospheric absorption lines which appear shallower than in the MS stars. Sketch in Figure 1.8 illustrates this process: matter travel inwards through the disk, at the truncation radius leaves disk and follows lines of the stellar magnetic field to land on stellar surface heated up to high temperatures (Hartmann et al. 2016). Part of the matter does not land on the stellar surface but is ejected through disk winds or jets / outflows. Ratio between ejected and accreted material defines effectiveness of accretion and usually is close to 0.1 (e.g., Nisini et al. 2018).

The accretion model described above requires stellar magnetic fields strong enough to break the disk before it reaches the stellar surface. Observationally it was shown for low-mass T Tauri stars and brown dwarfs (Hartmann et al. 2016). More massive stars, Herbigs, have weaker magnetic fields. Therefore, this view on accretion mechanism might not apply to them. Since this thesis focuses on low-mass stars, the alternative accretion scenarios will not be discuss further and from now on I will assume magnetospheric accretion scenario as applicable to the topics discussed later here.

1.2.3.2 Observational diagnostics

Accretion shock creates excess emission filling in the photospheric absorption lines and producing additional continuum emission in the UV, optical, and NIR range of the spectrum. Veiling is usually expressed as a ratio between accretion continuum flux, $F_{\mathrm{acc},\lambda}$, and the photospheric emission, $F_{\mathrm{phot},\lambda}$, at the given wavelength (e.g., Fischer et al. 2011; Herczeg & Hillenbrand 2014; Manara et al. 2021):

$$r_\lambda = F_{\mathrm{acc},\lambda}/F_{\mathrm{phot},\lambda} \tag{1.8}$$

The amount of the excess emission can be estimated in UV range, particularly the Balmer jump, which in accreting stars can be higher by a factor of 1.5-3 or higher (Hartmann et al. 2016). Modeling the accretion shocks causing this excess emission

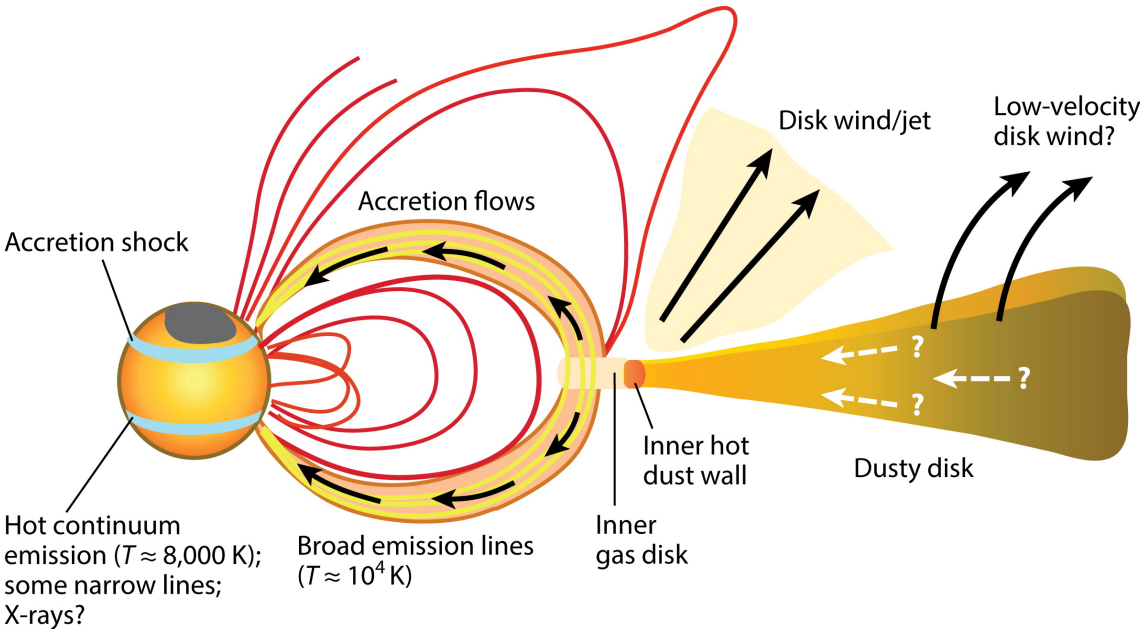

Figure 1.8: Illustration of the magnetospheric accretion onto the young low-mass star. Matter travels inwards through the disk where at the truncation radius continues its journey along the magnetic field lines to fall onto the stellar surface or becomes part of the disk wind or jet. When the disk matter is getting closer to the central star it is heated to high temperatures and re-radiates this energy as NIR excess (dust in the inner edge if the disk), X-ray (accretion shock heating stellar surface), or UV excess with emission lines across electromagnetic spectrum (absorbed and re-radiated X-ray emission). Excess emission from the accretion shock also appears in optical and IR filling in photospheric absorption lines in a phenomenon called veiling. Illustration credit: Hartmann et al. (2016), reproduced with permission from Annual Reviews.

allows obtaining physical characterisation of material landing onto the stellar surface (e.g., Calvet & Gullbring 1998; Lamzin 1998). Very often, good reproduction of observed spectra requires including multiple accretion columns in the model with different densities, temperatures, and filling factors (see e.g., a recent work of Pittman et al. 2022). Excess emission (e.g., Bertout et al. 1988; Gullbring et al. 1998), as well as the veiling (e.g., Basri & Batalha 1990; Hartigan et al. 1995; Stock et al. 2022), can be translated to the accretion luminosity, and if stellar parameters are known, to mass accretion rates. UV excess emission can also be estimated based on U-band photometry (e.g., Gullbring et al. 1998; Romaniello et al. 2004; Rigliaco et al. 2011) as an extension of spectroscopic studies that is specifically fitted to the large surveys.

UV excess emission is difficult to measure in faint or highly extincted stars, like Class 0 YSOs or very low-mass stars. The way to overcome this obstacle is to use emission lines as accretion tracers. Specifically, NIR lines are suitable for veiled objects as the extinction is less uncertain at this spectral range. The empirical relations between line flux / luminosity and accretion luminosity / rate have been established based on sources where measurements of the excess emission were possible (Muzerolle et al. 1998; White & Basri 2003; Natta et al. 2004a; Herczeg & Hillenbrand 2008; Alcalá et al. 2017). This includes also using the width at 10% of the peak of Hα as accretion indicator.

Emission lines identified to scale with measured otherwise accretion consist of a wide range of atomic transitions in optical and IR range of the spectrum. Among the most frequently used lines are hydrogen (Hα, Hβ, Hγ, Hδ, Paβ, Paγ, Paδ, Brγ), helium (at 5876, 6678, 7065, 10830 Å), oxygen (at 7776, 8446 Å), calcium II (K and H lines at 3934, 3968 Å, IR triplet at 8498, 8542, 8662 Å), sodium (doublet at 5889.9 and 5895.9 Å); the list is not exclusive (see e.g., a recent work employing optical spectra from X-Shooter of Alcalá et al. 2017). Relations are linear in the logarithmic scale and are often expressed as:

$$\log\left(L_{\rm acc}\right) = a \cdot \log L_{\rm line} + b \tag{1.9}$$

Similarly like the U-band photometry can be used to infer the UV excess emission, emission lines, especially Hα, can be replaced by the narrow-band filters. The procedure was defined for the HST observations of Magellanic Clouds (Romaniello 1998; Panagia et al. 2000; Romaniello et al. 2004). The excess Hα emission is determined by comparison to the (quasi) R-band magnitudes indicating a photospheric pseudo-continuum near Hα line. Stars with excess emission are expected to have large R-Hα colour (>0.3 mag that corresponds to the equivalent width of Hα of 8 Å for HST filters). Later studies developed also methods of deriving the excess emission from Hα narrow-band filter using V and I-band magnitudes in absence of R-band photometry (De Marchi et al. 2010a; Beccari et al. 2010). The method is particularly successful in studies of distant regions where spectroscopic surveys are limited due to the observational cost and obtaining statistically sound results is challenging.

Magnetospheric accretion model is also supported by the soft X-ray emission observed only from accreting stars (Hartmann et al. 2016). It likely originates from post-shock region and is characterised by the electron densities higher than in the coronal gas ($n_e = 10^{11} - 10^{12}$ cm^{-3} in comparison to $n_e \lesssim 10^{10}$ cm^{-3}) but by the somewhat lower temperatures ($T \sim 10^6$ K and $T \sim 10^7$ K, respectively; e.g., Kastner et al. 2002; Stelzer & Schmitt 2004; Hartmann et al. 2016). However, only a small fraction (few percent) of the total accretion energy is emitted by X-rays (Herczeg & Hillenbrand 2008; Hartmann et al. 2016).

Once the accretion luminosity is estimated, the mass accretion rate, $\dot{M}_{\rm acc}$, can be calculated when stellar parameters, radius R_* and mass M_* are also known:

$$\dot{M}_{\rm acc} = L_{\rm acc} \times \left(1 - \frac{R_*}{R_{\rm in}}\right)^{-1} \frac{R_*}{GM_*} \tag{1.10}$$

where $R_{\rm in}$ is the inner-disk radius; typically $R_{\rm in}$ is assumed to equal $5R_*$ (Gullbring et al. 1998). Mass accretion rates have been measured towards many of young stars across several star-forming regions. The obtained values range between $\sim 10^{-11}$ and $\sim 10^{-6}$ $M_\odot$yr^{-1} (see the recent compilation of Manara et al. 2023, and references therein). The natural expectation, supported by the viscous model, is that accretion rates diminish with age for the same stellar mass. Observations in general show this trend (Hartmann et al. 1998; Sicilia-Aguilar et al. 2010; Manara et al. 2012; Antoniucci et al. 2014) but with large scatter and uncertain relation. The most responsible for this uncertainty are stellar ages very imprecise at those early stages of stellar evolution. Since ages and masses are usually estimated together, there

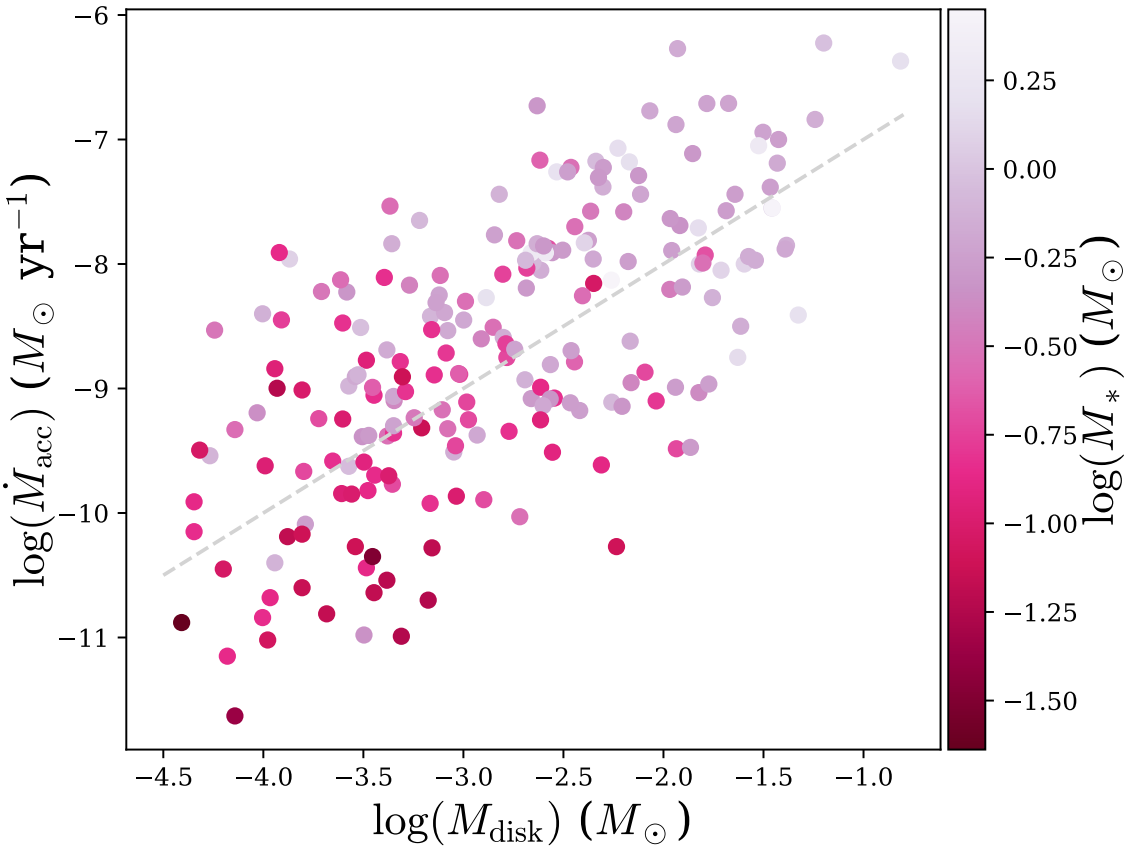

Figure 1.9: Correlations between disk mass (x-axis), mass accretion rate (y-axis), and stellar mass (colour-coded). Disk mass has been estimated from dust continuum emission and multiplied by the gas-to-dust ratio of 100. Lower mass stars tend to have lower mass disks and lower mass accretion rates, however there is a large spread in the correlations. Grey dashed line shows $M_{\rm disk}/\dot{M}_{\rm acc}$ = 1 Myr. Compilation of measurements in different SFR (<300 pc) from Manara et al. (2023), non-detections are not included in this figure.

is a hidden age uncertainty in measurements of mass accretion rates (Hartmann et al. 2016). Recent simulation work of Somigliana et al. (2023) shows that the clear decrease of $\dot{M}_{\rm acc}$ with time in viscous case is replaced by the large scatter in the MHD wind evolution blurring the correlation.

Accretion rates are strongly correlated with stellar mass (see Fig. 1.9). The relation is steeper then linear with the estimated slope between 1.5 and 3.1 with the most frequently assumed proportionality of $\dot{M}_{\rm acc} \propto M_*^2$ (Hartmann et al. 2016, and references therein). Relation exhibits large scatter, ∼0.75 dex (Hartmann et al. 2016), with spread in $\dot{M}_{\rm acc}$ of 1-2 dex (Manara et al. 2023). The correlation holds not only for T Tauri stars but also extends to VLMS and BD. However, it seems that Herbig stars might exhibit steeper relation, especially when looking separately into Herbig Be and Herbig Ae stars (Fairlamb et al. 2015; Hartmann et al. 2016). Steeper relation in Herbigs than in CTTS was assigned to their younger age and possibly more active accretion (Fairlamb et al. 2015).

One of the predictions of the viscous theory is a linear relation in logarithmic scale between mass accretion rate and disk mass (Hartmann et al. 1998; Dullemond et al. 2006). It was proved observationally in a homogeneous and convincing manner only after ALMA became available by Manara et al. (2016). Correlation first seen in Lupus was later confirmed in Chameleon I (Mulders et al. 2017), Upper Scorpius (Manara et al. 2020), and in the BD regime (Sanchis et al. 2020). The correlation seem to follow the line $M_{\rm disk}/\dot{M}_{\rm acc} = 1$ Myr with spread of $\sim$1 dex (Manara et al. 2023). The spread is attributed to different ages of the regions (Lodato et al. 2017), significant radial drift of disk dust that leads to apparent lower disk masses (Sellek et al. 2020), internal photoevaporation (Rosotti et al. 2017), and other environmental effects. The MHD wind scenario, on the other hand, does not predict correlation between the two parameters, unless a specific initial conditions are chosen, but reproduce observed scatter in the correlation very well (Somigliana et al. 2023).

Accretion by its very nature is not a static process and indeed young stars are known to be variable. Although other processes contribute to that behavior (rotating stellar spots, changing extinction), accretion is considered as a dominant factor (Fischer et al. 2023). Accretion variability has a wide range of timescales, from few hours, through weeks and months to years and decades and appears both in photometric and spectroscopic observations (e.g., Hartmann et al. 2016; Fischer et al. 2023). The process is highly irregular, connected to the amount of mass loaded from the disk onto the star, and is thought to be stochastic. In close multiple systems the interaction between different components adds to the complexity. Short-time changes appear on top of the long-scale variations. The shortest changes of hours - days, and at the same time the most frequent, are of low amplitude, <1-2 mag, often accompanied by the change of emission lines morphology (Fischer et al. 2023).

The most famous, and drastic, cases of accretion variability are FU Ori and EX Lup, who gave the name to the classes of objects exhibiting similar behaviours. FUors show great outbursts in optical range of order of several magnitudes that slowly and steadily decay over tens of years or longer (Hartmann & Kenyon 1996; Hartmann et al. 2016; Fischer et al. 2023). Outburst initiates rapid mass accretion (rate of 10^{-5} - 10^{-4} $M_{\odot}{\rm yr}^{-1}$) from the viscously heated disk dominating the spectrum. With such high accretion rates the inner disk reaches midplane temperatures of $\gtrsim 10^5$ K making it impossible for the disk to radiate away excess energy and causing the disk to break through magnetospheric barrier reaching stellar surface close to equator (Fischer et al. 2023, and references therein). Therefore, magnetospheric picture of accretion is not applicable to those objects. Outbursts of EXors are much shorter, of order of few months, with increase of optical brightness of 2.5-5 mag. Those outburst are repetitive, the progenitor had several of them over past hundred years (Hartmann et al. 2016, and references therein). In those states the accretion rates increases to $\sim 10^{-7} M_{\odot}{\rm yr}^{-1}$, emission lines become brighter, some of which were in absorption before, and optical spectrum become hightly veiled. In the quiesence state EXors have spectra of CTTS. The mechanism behind the outburst is thought to be related to instabilities of the inner disk when more material is being accumulated in the

inner parts then accreting to the stellar surface (Hartmann et al. 2016). Increase of emission line fluxes indicate the magnetospheric accretion, this class of objects is therefore driven by different mechanisms than FUors.

1.3 Environment: stars do not form in isolation

Most stars in the Galaxy form in clusters, associations, and groups, and most of the star formation is happening in massive clusters (e.g., Miller & Scalo 1978; Lada & Lada 2003). This suggests, that the picture of isolated star formation (Sec. 1.1) might not be valid and that the environment within the cluster plays an important role in the early evolution of the star and its planetary system. Moreover, there is a strong evidence that the formation of the Solar System was affected by the presence of massive stars in the parental cluster (e.g., Adams 2010). Below, I discuss what kind of environmental effects can affect star formation and protoplanetary disks evolution.

1.3.1 Feedback from massive stars

Massive clusters are dominant hosts of massive stars ($\geq$8 $M_{\odot}$). Those stars evolve much faster than they less massive counterparts. Therefore, when low-mass stars are still in their infancy, massive stars will enter and leave the Main Sequence (MS). Evolution of massive stars is accompanied by the energetic events (stellar winds, strong ionising radiation, supernovae explosion) that can highly affect evolution of other cluster members.

1.3.1.1 External photoevaporation

Strong radiation produced by OB stars is considered as a most impactful on a global scale process that can alter protoplanetary disk evolution (Winter et al. 2018b). Those stars produce immense amount of extreme-ultraviolet (EUV) and far-ultraviolet (FUV) photons which can ionise and heat outer parts of the disk, and because of the weaker gravity experienced there by the disk material, deplete the disk outside-in (Johnstone et al. 1998; Churchwell et al. 1987). This process is called the *external* photoevaporation, in contrast to the one driven by the central star and depleting the disk from inside-out (*internal* photoevaporation Clarke et al. 2001; Ercolano et al. 2008; Owen et al. 2010, 2012; Picogna et al. 2019; Sellek et al. 2022).

Observationally, the first evidence of disks undergoing externally-driven photoevaporation were "proplyds" irradiated protoplanetary disks, captured by HST in the Orion Nebula Cluster (ONC) (O'Dell et al. 1993). Those objects have characteristic elongated shape pointing against the direction towards the source of UV radiation, OB star. Figure 1.10 illustrates a proplyd. An UV radiation heats the disk and launches winds from the disk's surface. Removed material is hit by the forthcoming radiation creating the ionisation front. Measuring the size of ionisation front ($R_{\rm IF}$)

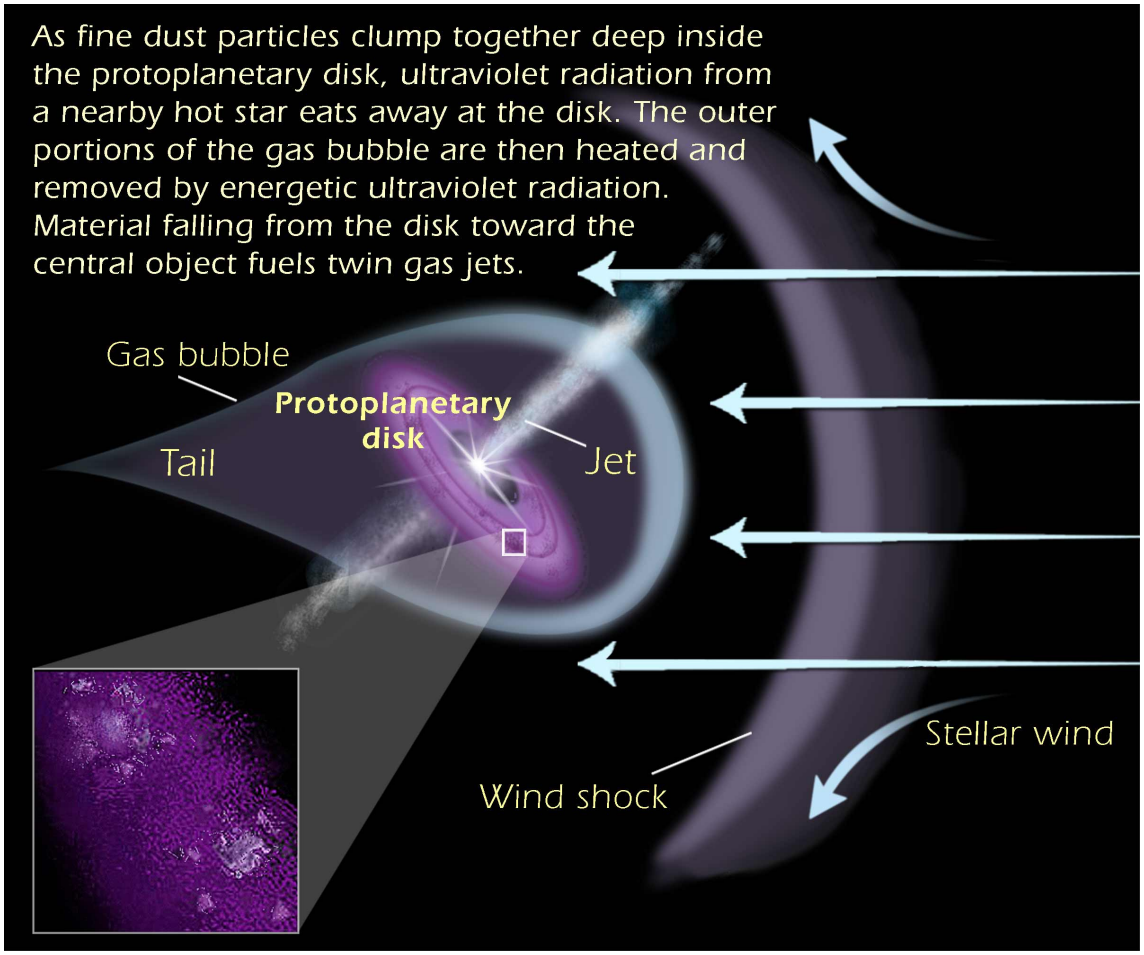

Figure 1.10: Sketch of an irradiated protoplanetary disk, *proplyd*. The disk is surrounded by the cometary-shape cocoon. Tail of this cocoon points in the opposite direction to the source of UV photons. Ionising radiation is depicted by the white arrows. Illustration Credit: NASA, ESA, and A. Feild (STScI)[10].

allows estimations of mass loss rates from the disk due to the external radiation ($\dot{M}_{\rm ext}$, Johnstone et al. 1998; Winter & Haworth 2022):

$$\left(\frac{\dot{M}_{\rm ext}}{10^{-8} M_\odot {\rm yr}^{-1}}\right) = \left(\frac{1}{1200}\right)^{3/2} \left(\frac{R_{\rm IF}}{\rm au}\right)^{3/2} \left(\frac{d}{\rm pc}\right)^{-1} \left(\frac{\Phi}{10^{45} {\rm s}^{-1}}\right)^{1/2} \tag{1.11}$$

where Φ is the number of ionising photons per second emitted by the source at distance d responsible for setting the ionisation front (a massive star). This estimate neglects any extinction between the massive star and the evaporating disk and gives therefore only an upper limit. Measured mass loss rates in NGC 2024 and NGC 1977 are of order of $\sim 10^{-8} - 10^{-7}\ M_\odot {\rm yr}^{-1}$ (Haworth et al. 2021, 2022).

The initial discovery encouraged more observations employing HST and ground-based instrumets in the ONC (e.g., Stauffer et al. 1994; Bally et al. 1998; Johnstone et al. 1998; Ricci et al. 2008; Fang et al. 2016; Haworth et al. 2023), NGC 1977 (Kim et al. 2016), NGC 2024 (Haworth et al. 2021), σOri (Hodapp et al. 2009; Rigliaco

[10] https://hubblesite.org/contents/media/images/2001/13/1044-Image.html

et al. 2009), M16 (Hester et al. 1996), NGC 3603 (Brandner et al. 2000), or Trifid Nebula (Yusef-Zadeh et al. 2005). The search of proplyds was conducted also in more distant regions revealing existence of similar in shape objects, globules, but significantly larger and not necessarily hosting an YSO inside (e.g., Smith et al. 2003; Gahm et al. 2007; Wright et al. 2012; Grenman & Gahm 2014; Reiter et al. 2019).

Proplyds can be studied across the electromagnetic spectrum. Ionisation fronts are traced by many atomic emission lines in optical (e.g., Hα Paα, [OIII], [NeII], [NII]; Henney et al. 2002, Winter & Haworth 2022). Another collection of emission lines can by applied to search of photodissociation. The most frequently used line is [OI] at 6300 Å, which when resolved into several velocity components can directly trace disk wind. In case of phtooevaporation, the line is emitted after the photodissociation of OH (Störzer & Hollenbach 1998; Bally et al. 1998; Ballabio et al. 2023). It was proposed by Haworth & Owen (2020) that CI line can be used as a tracer also in cases where the morphology of the proplyd cannot be inferred. However, confirmation of this hypothesis still needs to be done (Haworth et al. 2022).

Photoevaporation affects also dust content of the disk. By dominantly removal of the gas, the dust-to-gas ratio is enhanced helping building planetesimals (Carrera et al. 2017). Due to external photoevaporation small dust grains will be entrained in the wind (Facchini et al. 2016), while dust remaining in the disk will be heated and will exhibit a radial gradient in the grain sizes (Owen & Altaf 2021). The latter was indeed inferred in one of the ONC disks (Miotello et al. 2012). Additionally, highly irradiated disks are expected to be shrunken and less massive. The correlation of disk mass with the distance to the main source of UV radiation was found in many clusters (e.g., Mann & Williams 2010; Mann et al. 2014; Eisner et al. 2018; Ansdell et al. 2017). The correlation with disk radius remains inconclusive, mostly due to uncertainties of disk sizes and true 3D distances to the OB star. The fraction of NIR excess stars, which traces inner parts of the disk, is lower in highly irradiated environments than in quieter regions with the same age (e.g., Preibisch et al. 2011a; Stolte et al. 2015; Guarcello et al. 2016).

External photoevaporation can have a profound effect on planet formation. Removal of the mass decrease the amount of material available for planet formation. As a result, formed planets might be lower in mass, or there might be fewer planets in the system. At the beginning of protostellar evolution (for ∼0.5 Myr), the star+disk system is effectively protected by the natal cloud (Qiao et al. 2022). If planet formation stars very early (Tychoniec et al. 2020), the seeds of future planets can be already formed when the harsh irradiation reaches the disk. Altered might be only their final mass or physical and chemical properties of their atmospheres. However, a thorough investigation of planet formation in externally photoevaporated disks versus in disks in low-mass star-forming regions in a framework of planet population synthesis models still awaits a proper attention.

1.3.1.2 Stellar winds

Winds of massive stars have the most prominent impact on their surrounding. Through winds, they transfer mass, momentum, and energy to the Interstellar Medium (ISM), and with that they close the cosmic cycle of the matter. Matter given back to the ISM is enriched by chemical elements due to the nuclear processes within the star. Carbon-rich Wolf-Rayet stars and late-type giants produce dust in their winds which is an important ingredient for formation of the next generation of stars (Lamers & Cassinelli 1999).

Stellar winds collide with the medium around producing expanding bubbles and shells. Massive OB stars have mass loss rates of 10^{-5} $M_{\odot}\mathrm{yr}^{-1}$ and loose around half of its mass during MS evolution. For comparison, Sun looses mass due to winds in a rate of $\sim 10^{-14}$ $M_{\odot}\mathrm{yr}^{-1}$, several orders of magnitude less (Maeder & Meynet 2012). Velocity of this wind depends on the stellar mass and can be as high as 3000 km s^{-1} for OB stars (Lamers & Cassinelli 1999). Stars loos less than 1% of their bolometric luminosity, but that energy is enough to heat the the shock front caused by the expanding wind to the temperatures of 10^7 K, much more than due to the radiation field of the star within the bubble ($\sim 10^4$ K, Lamers & Cassinelli 1999). The peak of the mass loss rate through winds during the evolution of massive star depends on their mass and occurs in the MS or post-MS phase and in terms of mass lost can be comparable to the supernova event (Lamers & Cassinelli 1999).

1.3.1.3 Supernovae explosion

Stars more massive than 8 $M_{\odot}$ end their lives in the supernova explosion. In that event they throw out $\sim$60% of their current mass at velocities of several 10^4 km s^{-1} and energies of $\sim 10^{51}$ erg (Tielens 2010). Large volumes of ejected matter contains a hot and low-density gas penetrating and interacting with the surrounding medium (McKee & Ostriker 1977). Shock wave from supernovae injects turbulence to the ISM (Norman & Ferrara 1996), heats it to its hottest phase ($\geq 10^6$ K, McKee & Ostriker 1977), and maintain a pressure equilibrium acting against the dispersion of the cold molecular clouds (McKee & Ostriker 1977; Norman & Ferrara 1996). The interactions with the medium depends on its properties. In the low-density ISM supernova ejecta will expand fast what may lead to distraction of nearby clouds. The transported and transferred energy to the medium may cause evaporating flows removing matter from the clouds. The amount of removed matter depends on the location of the supernova with respect to the cloud. If it is located inside the cloud, it can transfer up to a half of the momentum to the cloud leading to the mass loss up to the half of the gas mass (Iffrig & Hennebelle 2015). Supernova explosion outside the molecular cloud has significantly smaller impact (a factor of 10 in delivered momentum). Iffrig & Hennebelle (2015) found, that supernovae might be particularly effective in removing the intermediate density gas (10 cm^{-3} $\leq n \leq$100 cm^{-3}). Removal of significant portion of the gas from the molecular cloud affects significantly its star formation potential and is being considered as one of the reasons for low efficiency of star formation in the Galaxy.

1.3.2 Close encounters

Dense stellar clusters create favourable conditions for dynamical close interactions between two stars not gravitationally bound. The probability of this event increases with stellar density and is enhanced at early cluster ages (Bate 2018; Andrews 2020). Around 30% of Sun-like stars in an OB association is expected to encounter a flyby at a distance of 100-1000 au within 2 Myr (Pfalzner 2013).

Passing star can strip away material from the circumstellar disk (e.g., Breslau et al. 2014). As a result, the disk will be less massive having lower capacities of forming planetary systems (Clarke & Pringle 1993; Ostriker 1994; Heller 1995; Kobayashi & Ida 2001; Adams 2010). How much of the material is removed depends strongly on the geometry of the interaction (see e.g., Clarke & Pringle 1993). Denser clusters ($>10^{3.5}$ pc^{-2}) are expected to have on average less massive and smaller disks (de Juan Ovelar et al. 2012; Rosotti et al. 2014; Winter et al. 2018a). Additionally, the formation of some of the disk substructures can be triggered by the flyby encounters. They can create spiral arms and tidal bridges (Cuello et al. 2019) or change the inclination of the disk (Xiang-Gruess 2016). However, cluster density is supposed to have a secondary role with respect to the ionising radiation from the massive stars (see Sec. 1.3.1.1, Winter et al. 2018b). Also, close encounters are expected to have smaller effect on protoplanetary disks than companions in multiple systems (Andrews 2020, Sec., 1.3.4) or external photoevaporation (Sec. 1.3.1.1).

1.3.3 Metallicity

Observations of exoplanets show a strong correlation between the frequency of stars hosting a planet and its metallicity (e.g., Santos et al. 2004; Valenti & Fischer 2008). Assuming that the metallicity of the protoplanetary disks is the same as of the hosting star, the trend puts a strong constraint on planet formation models. This correlation is consistent with core-accretion scenarios of giant planet formation in which planetary cores are built from dust grains, thus the ratio between of dust and gas content can predetermine the efficiency of the process. The general trend is qualitatively reproduced by models (e.g., Ida & Lin 2004). At the same time, the gravitational instability models of planet formation fails to explain the observed trend but allows formation of giant planets even in low metallicity environments (Boss 2002).

Similar exercise was performed targeting the inner disk regions traced by the NIR excess. For example, Yasui et al. (2010) investigated few young clusters with low metallicity ([O/H] $\sim$ -0.7). They noticed a rapid decrease of disk fractions in <1 Myr, a time significantly smaller than a typical disk lifetime of $\sim$10 Myr. They suggested a $\sim 10^{Z}$ dependence of disk lifetime on metallicity. Later observations of different low-metallicity star-forming regions report similar behaviour (e.g., Guarcello et al. 2021). Shortened disk lifetimes are also supported by some models (e.g., Nakatani et al. 2018; Gehrig et al. 2023). However, observations of Magellanic Clouds found contradicting evidences of longer and more prominent star formation in low metallicity environments (e.g., De Marchi et al. 2010a, 2011, 2017). To resolve the discrepancy

more dedicated studies are needed targeting other star-forming regions (like, e.g., CMa-ℓ224, Sewiło et al. 2019; Itrich et al. 2023a) or performing in depth analysis combined with modelling including multiple physical processes in play that might blur our interpretation.

1.3.4 Mulitplicity

Stars are born mostly in multiple systems (Offner et al. 2023). The multiplicity fractions depends highly on the mass of the primary companion. Most massive stars (O-type) have multiplicity fraction of almost 100%, while for BDs it is <20%. On top of that, in MS binaries close systems (separation <10 au) are more common than wide ones (>100 au). In particular, BDs have almost no wide companions (Offner et al. 2023). Multiplicity changes also with time. Excess of companions was found with imaging around T Tauri stars in near SFRs with respect to the MS stars (Leinert et al. 1993; Reipurth & Zinnecker 1993; Ghez et al. 1997; Kraus et al. 2011; Tokovinin & Briceño 2020), similarly to some spectroscopic surveys (Jaehnig et al. 2017; Zúñiga-Fernández et al. 2021). Tobin et al. (2022) suggested that Class 0 sources show the primordial multiplicity. The fraction of young wide binaries is lower in the clusters with higher stellar density. E.g., in ONC there is a deficit of wide binaries (Scally et al. 1999; Köhler et al. 2006; Reipurth et al. 2007; Duchêne et al. 2018; Jerabkova et al. 2019), while in Taurus and Chameleaon slight excess was found (Leinert et al. 1993; Reipurth & Zinnecker 1993; Ghez et al. 1997; Köhler & Leinert 1998; Connelley et al. 2008; Kraus et al. 2011; Joncour et al. 2017). That suggests that close encounters can not only disrupt disks (Sec. 1.3.2) but also multiple systems.

Separation between companions is important for their disks properties. Circumstellar disks around wide systems have similar characteristics (mass and radius) like those around single stars. However, close and intermediate multiple system host smaller and less massive disks (Cieza et al. 2009; Cox et al. 2017; Akeson et al. 2019; Manara et al. 2019; Offner et al. 2023). This fact is of high importance as it indicates that stars (initially) in tight system will not form giant planets nor systems with many planets. Moe & Kratter (2021) estimated that the planet occurrence rate is the same for 200 au separation binaries, down to 15% for 10 au system. Truncation of a disk and reducing its mass content can result in very small, undetectable planets with different distribution of orbits than in planetary systems around single stars (Dupuy et al. 2016).

Young binary stars can be surrounded by a circumbinary disk. Not many of them are observed (Czekala et al. 2019) as could be expected from detected circumbinary planets (Martin 2019; Kostov et al. 2020, 2021) and theoretical expectations of close binaries solely impacting their common disk from inside. Offner et al. (2023) suggest, that given the completeness of ALMA observations in close-by SFR, circumbinary disks are truly rare. The reason is not yet fully understood and presence of circumbinary debris disks is only adding to this puzzle. On the other hand, circumbinary

disks in higher order multiples can survive for a longer time due to the combination of internal and external dynamical interaction which might slow down the viscous evolution (Offner et al. 2023, and references therein).

1.3.5 Streamers

Protostars, when emerging from parental molecular cloud, are actively interacting with the surrounding medium. Number of detected "streamers" narrow structures with coherent velocity funneling material to the star or disk, is growing (Pineda et al. 2023). Streamers are most frequently found around the youngest YSOs. Accreting cloud material was found with ALMA in Class 0 objects (Le Gouellec et al. 2019) in dust continuum polarisation, as well as in molecular gas (Cabedo et al. 2021; Murillo et al. 2022; Thieme et al. 2022) and with NOEMA in molecular gas Pineda et al. (2020). The infalling rates onto their disks were found $\sim 10^{-6} M_{\odot} \mathrm{yr}^{-1}$, comparable or higher with their accretion rates onto the stars. Accretion streamer was found also towards HL Tau (Yen et al. 2019; Garufi et al. 2022, see Fig. 1.4), as well as other Class I sources (Segura-Cox et al. 2020; Valdivia-Mena et al. 2022). Infalling rates were similarly found comparable to the accretion. Disks of Class II sources can also be fueled with additional material from the late infall (Akiyama et al. 2019; Alves et al. 2020; Garufi et al. 2022; Gupta et al. 2023).

Supply of the material at later evolutionary stages can significantly alter physical and chemical properties of disks, and consequently, forming there planets. It has been suggested that late infalls can help solving mass-budget problem of protoplanetary disks (e.g., Manara et al. 2018, see also Sec. 1.2.2.5). Similarly, supply of fresh material could explain chemical diversity among meteorites (Nanne et al. 2019). Infalling material can alter disk structure (e.g., Kuznetsova et al. 2022), torque the disk (Thies et al. 2011; Kuffmeier et al. 2021), and even cause FU Ori outbursts (Dullemond et al. 2019). It is therefore highly important to study young objects with context of their surroundings.

1.4 This thesis

The question about the origin of the Solar System drives star and planet-formation studies. Despite the effort, we still do not have a complete and global picture of how stars form. Significant progress has been made in the field thanks to the detailed studies of nearby star-forming regions (Taurus, Lupus, Chamaeleon I, etc.). Those studies, however crucial for our understanding, are missing one puzzle: the role of environment. All star-forming regions in the solar neighbourhood are low-mass and share similar conditions, like metallicity, crowding, overall mass, while most of the star formation is happening in massive complexes. Additionally, there are evidences that massive stars were present in the vicinity of the still forming Sun. These two points motivate the work presented in this thesis: what is the role of the environment in the formation and early evolution of stars and their disks?

The topic itself is very broad and requires exhausting investigation spanning a wide range of conditions. Here, I only focus on a small aspect of the subject: the role of external photoevaporation. It is expected that in regions with high level of UV radiation, the evolution of the protoplanetary disks will be accelerated by removing the disk material from outer parts. First evidences of external photoevaporation were found in Orion Nebula Cluster in the form of proplyds - irradiated protoplanetary disks. Orion however, is not a representative environment for most of the still forming stars. More *harsh* sites are located at larger distances ($\gtrsim$1 kpc), are often highly extincted and crowded, all of which hinders observations. With the advent of highly sensitive instruments mounted on eight-meter class telescopes it is possible to overcome those challenges and reach star formation beyond the solar neighbourhood.

The thesis is structured as follows. Chapter 2 presents the Carina Nebula Complex (CNC), a target of this study. Properties of this star-forming complex make it an ideal laboratory to tackle the scientific question driving this investigation. The appropriate instrumentation is described in Chapter 3. The Integral Field Unit spectroscopy (IFU) technique is the most powerful one in spectroscopic studies of stellar clusters and motivates the use of VLT/MUSE. Chapter includes the details of the observations used here together with the data reduction. Analysis is presented in the Chapter 4 which focuses on stellar properties of Trumpler 14 members. Application of deep observations allows spectroscopic characterisation of low-mass stars, first study of this kind in the CNC. Collecting properties of individual stars gives the insight into attributes of the whole cluster. Analysis of large datasets of stellar spectra requires effective methodology. In Chapter 5 I present the alternative approach to classification of medium-resolution optical spectra of low-mass stars. Characteristics of protoplanetary disks around those stars are acquired through accretion estimates (Chapter 6). Their parameters are examined against the environmental conditions in the Trumpler 14. Summary of the results, as well as suggestions for future investigation, are depicted in Chapter 7.

Chapter 2

Carina Nebula Complex

The content of this chapter is partially based on Itrich et al. (2023b), Sec. 1. Here, I briefly introduce the studied region, Trumpler 14 in the Carina Nebula Complex.

2.1 Physical properties of the Carina Nebula

The Carina Nebula Complex (CNC) is one of the biggest sites of star formation and one of the most massive HII regions in our Galaxy (see Fig. 2.1). It is located in the plane of the Galactic Disk at a distance of 2.35 kpc from the Sun (Shull et al. 2021; Göppl & Preibisch 2022), which makes it the closest analog of a typical environment in which stars form. Most if not all the clusters within the CNC are located at similar distances with very small distance dispersion of 1-2% (Smith 2006; Cantat-Gaudin et al. 2018; Maíz Apellániz et al. 2020; Göppl & Preibisch 2022; Berlanas et al. 2023). Low interstellar extinction towards the region (e.g., Walborn 1995; Hur et al. 2023) makes it an even more suitable target for observational studies of massive clusters in the optical wavelengths. However, it was noticed that the reddening law towards the CNC is anomalous ($R_V = 4$–5, e.g., Smith 2002) combined with the variable intracluster extinction (by ∼9 mag Tapia et al. 2003; Rowles & Froebrich 2009; Preibisch et al. 2012). Additionally, the CNC is located close to the galactic plane, what causes serious problems with contamination of the field stars (both foreground and background).

The CNC contains more than $5{\times}10^4$ stars (Povich et al. 2019) with a total mass of $\sim 37000\ M_\odot$ (Preibisch et al. 2011a) immersed in a massive HII region. While part of the CNC population is spread over a wide area characterised by a low stellar density regime, most of the young stars are located in a number of star clusters, with Trumpler (Tr) 14, 15, and 16 being the most massive ones. These clusters host the greatest concentrations of O-type stars, which are expected to highly influence the evolution of their low-mass neighbours. There are at least 74 O-type stars in the CNC (Smith 2006; Berlanas et al. 2023), including some of the most massive stars known: prototypical O2 (HD 93129A in Tr 14) and O3 (in Tr 14 and Tr 16) stars, luminous blue variable η Carinae (in Tr 16), as well as several Wolf-Rayet stars (Walborn 1973; Walborn et al. 2002; Smith 2006).

[1] https://www.eso.org/public/images/eso1208a/

Figure 2.1: Composite image of Carina Nebula Complex taken with the VLT/HAWK-I. The image reveals beautiful gaseous structures in the region. The bright star in the lower left corner is the ηCar. Illustration Credit: ESO/T. Preibisch[1].

Current observational campaigns of Carina focused mostly on massive or intermediate-mass stars. Photometric studies included optical, near infrared (NIR), and X-ray observations. More than 100 stars in Tr 14 and Tr 16 were observed by Feinstein et al. (1973) down to G-type stars which allowed the authors to obtain distance values to the clusters close to the most recent ones. DeGioia-Eastwood et al. (2001a) investigated over 500 stars in Tr 14 and Tr 16 with optical photometry detecting stars down to $\sim$1 $M_{\odot}$. Tapia et al. (2003) presented the optical and NIR photometry of 4150 stars in Carina with mass limit of 2 $M_{\odot}$. Multi-wavelength observations (optical + NIR) were also analysed by Beccari et al. (2015) who built spectral energy distributions (SEDs) of 356 stars, obtained their stellar parameters (down to $\lesssim$0.4 $M_{\odot}$) and estimated their mass accretion rates. Optical photometry of stars in Tr 14, Tr 16, and Collinder 232 was analysed by Carraro et al. (2004) down to $\sim$1 $M_{\odot}$. Hur et al. (2012) showed visual CCD photometry of the two most massive clusters in CNC and investigated their stellar content together with IMF with the limit of 1.5 $M_{\odot}$. They recently extended this catalog by deep photometry of 135 000 stars down to 0.2 $M_{\odot}$ in I-band assuming the CNC age of 7 Myr (Hur et al. 2023).

NIR photometry of massive and intermediate-mass stars was published by Ascenso et al. (2007) together with a study of the mass function. Povich et al. (2011) investigated mid-IR excess of $\sim$1400 young stars in Carina based on *Spitzer* observations. Extensive, wide-field, and deep NIR photometry of CNC from Vista and HAWK-I of more than 600 000 sources down to $\lesssim$0.1 $M_{\odot}$ was published by Preibisch et al. (2011a,b, 2014). Later, Zeidler et al. (2016) investigated their NIR excess. These

surveys were often cross-matched with the deep X-ray imaging of the Chandra Carina Complex Project (CCCP, Broos et al. 2011; Townsley et al. 2011), which identified ∼14 000 sources and help confirming the youth of low-mass Carina stars. The survey was preceded by study of Tr 16 with Chandra by Albacete-Colombo et al. (2008) and XMM-Newton observations of early-type stars Antokhin et al. (2008).

Individual, high-mass members of Carina were classified first photometrically (Walborn 1973; Massey & Johnson 1993; Walborn 1995), then spectroscopically (Levato & Malaroda 1982; Morrell et al. 1988; Walborn et al. 2002; Vaidya et al. 2015; Maíz Apellániz et al. 2016; Preibisch et al. 2021; Berlanas et al. 2023). The first spectroscopic properties of massive, intermediate-mass, and solar-like stars in Tr 14 and Tr 16 were obtained in the *Gaia*-ESO survey by (Damiani et al. 2017), who used high-resolution (R∼17 000) observations from FLAMES/Giraffe spectrometer at the ESO Very Large Telescope (VLT) to characterise more than 1000 stars and to portray characteristics of those two clusters.

2.2 Trumpler 14 cluster

Tr 14 is the most compact and youngest among the three main clusters in the CNC. Figure 2.2 shows the three-colour image composed of HST observations. Its structure was recognised to consist of a dense core (r of 0.5′–0.9′ corresponding to 0.3–0.6 pc at the distance of 2.35 kpc) and an extended halo population of possibly slightly older age (4′–7.8′ corresponding to 2.7–5.2 pc Tapia et al. 2003; Ascenso et al. 2007; Kharchenko et al. 2013). The core is collocated with the brightest concentration of stars on the image. The surrounding gaseous and dusty structures of HII region illustrate the challenge of analysing the stellar emission.

Its age was estimated to be ∼1 Myr (Penny et al. 1993; Vazquez et al. 1996; DeGioia-Eastwood et al. 2001a; Carraro et al. 2004); 2 Myr younger than Tr 16 (Walborn 1995; Smith & Brooks 2008). It contains ∼20 O-type (Shull et al. 2021; Berlanas et al. 2023) and several tens B-type stars. As a result, its ultraviolet luminosity is ∼20 times higher than Θ^1Ori C in the Orion Nebula (Smith 2006; Smith & Brooks 2008). High UV field, high cluster density and mass, young age, and low reddening towards the cluster make Tr 14 a perfect target to investigate the role of environment on star formation.

2.3 Missing piece of the puzzle: low-mass stars

The photometric and spectroscopic works listed in the previous sections are not a comprehensive list of all studies of the CNC. However, up to date no spectroscopic survey targeting stars below 1 $M_\odot$ was conducted in Carina leaving the most important part of the region uncharacterised. In this thesis I present a first catalog of spectroscopically characterised young, low-mass stars in Tumpler 14 in the CNC

[2] https://hubblesite.org/contents/media/images/2001/13/1044-Image.html

Figure 2.2: *Hubble* view on Trumpler 14. Illustration Credit: NASA, ESA, and J. Maíz Apellániz (Institute of Astrophysics of Andalusia, Spain); Acknowledgment: N. Smith (University of Arizona)[2].

(Chapter 4). The developed method shows that distant, crowded regions can be observed and well characterised with highly sensitive Integral Field Unit (IFU) instruments (Chapter 3). Presented here work fills the gap so far present in the all investigations of Carina Nebula Cluster.

Chapter 3

Observational technique

3.1 Integral Field Spectroscopy

Traditional spectroscopic observations employing slit spectrographs can target usually only single object. This can be mitigated by the Multi-Object Spectroscopy (MOS) that allows obtaining spectra for many sources at once. It is done by placing multiple fibers within telescope's field of view or creating a mask with microslits; each for a different object. While powerful for moderately crowded regions, both techniques present some limitations for studying very dense fields or large-scale structures. An answer to the need of access to the spatially resolved kinematics of the whole regions is Integral Field Unit spectroscopy (IFU).

The IFU technique was first proposed by Courtes (1982). The idea behind IFU is to divide a projected image of the sky into subfields, and disperse their light separately, as if each of them was a single exposure. Figure 3.1 illustrates three main ways to perform IFU spectroscopy (Allington-Smith 2005). The first one uses an array of lenslets to focus light from each subfield of an image and then disperse it on the detector. In the second case, the focused light from each subfield is reformatted into a pseudo-slit by a set of fibres and dispersed later on. The third technique employs a set of mirrors to slice an input image into a pseudo-slit. The latter approach to extract spatially-dependent spectrum minimises the waste of unused detector's pixels.

There are many advantages in using IFU technique. The spectra of the sampled region are obtained without repetition of the telescope pointing. The spectral resolution of the spectrograph does not depend on the seeing, there are also no slit losses related to the slit width. Pointing is much easier than in the case of slit spectrograph, as the exact position of the source can be determined after the observations are taken from its position on the image extracted from the datacube (Allington-Smith 2005). It is also possible to unambiguously study emission from the extended objects. IFU has also some disadvantages. It requires a complicated and sophisticated apparatus, the spectral resolution of IFU instruments is usually low or moderate, and the data reduction is very complex making the use of IFU data challenging.

Figure 3.2 visualises the 3D spectral cube, an output of the reduction of IFU observations. The image of the astronomical object changes with the wavelength, revealing different physical and chemical processes lying behind the observed emission. At the same time, we can investigate how those processes depend on physical location

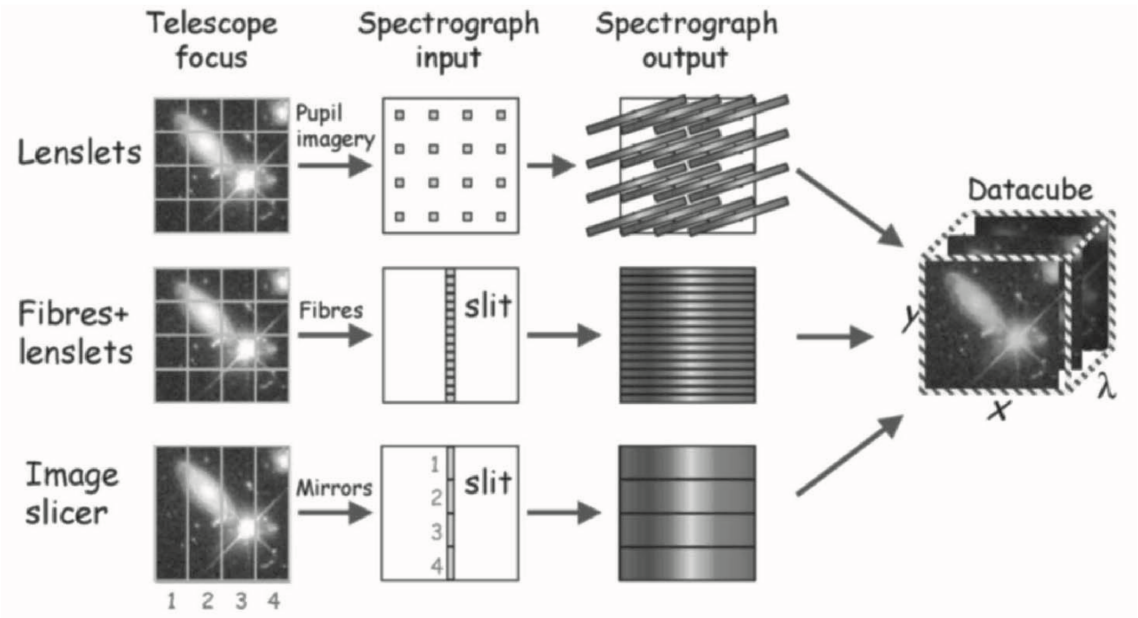

Figure 3.1: Image credit: Allington-Smith (2005), reproduced with permission from Springer Nature.

in the observed region by accessing the spectrum in every pixel of our image. Currently, there are several IFU spectrograph working in the optical or infrared regime, e.g., MUSE, KMOS, ERIS at the VLT, GMOS, NIFS at the Gemini Telescopes, or NIRspec and MIRI/MRS at the JWST, and more will be installed at the 30 meter class telescopes, e.g., HARMONI at the ELT (Allington-Smith et al. 2002; McGregor et al. 2003; Bacon et al. 2010; Sharples et al. 2013; Rieke et al. 2015; Thatte et al. 2021; Böker et al. 2022; Davies et al. 2023). IFU instruments opened new possibilities in astronomy. They moved and are still moving astronomy forward by giving scientists access to the previously unavailable information about the Universe and enabling new, unexpected discoveries. The scientific gain significantly overcomes the complexity of data reduction and justifies the complexity of an instrument.

3.2 MUSE: the Multi Unit Spectroscopic Explorer

The Multi Unit Spectroscopic Explorer (MUSE) is a second generation IFU instrument mounted on the Nasmyth B focus at the Very Large Telescope (VLT) in Paranal, Chile (Bacon et al. 2010). Figure 3.3 shows MUSE placed at the telescope UT4. Its design is based on the image-slicing technique. MUSE is composed of 24 identical units of IFU spectrographs with CCD detectors covering together a field of view of $1' \times 1'$ with spatial sampling of $0.2''$ in Wide Field Mode (WFM) or a field of view of $7.4'' \times 7.4''$ with sampling of $0.025''$ in Narrow Field Mode (NFM). MUSE covers the wavelength range of 4800–9300 Å with a spectral resolution $R \sim 4000$ (sampling of 1.25 Å). The limiting magnitude for 1 hr integration time in WFM is ∼22 mag in V-band.

[1] https://www.eso.org/public/images/eso1518c/

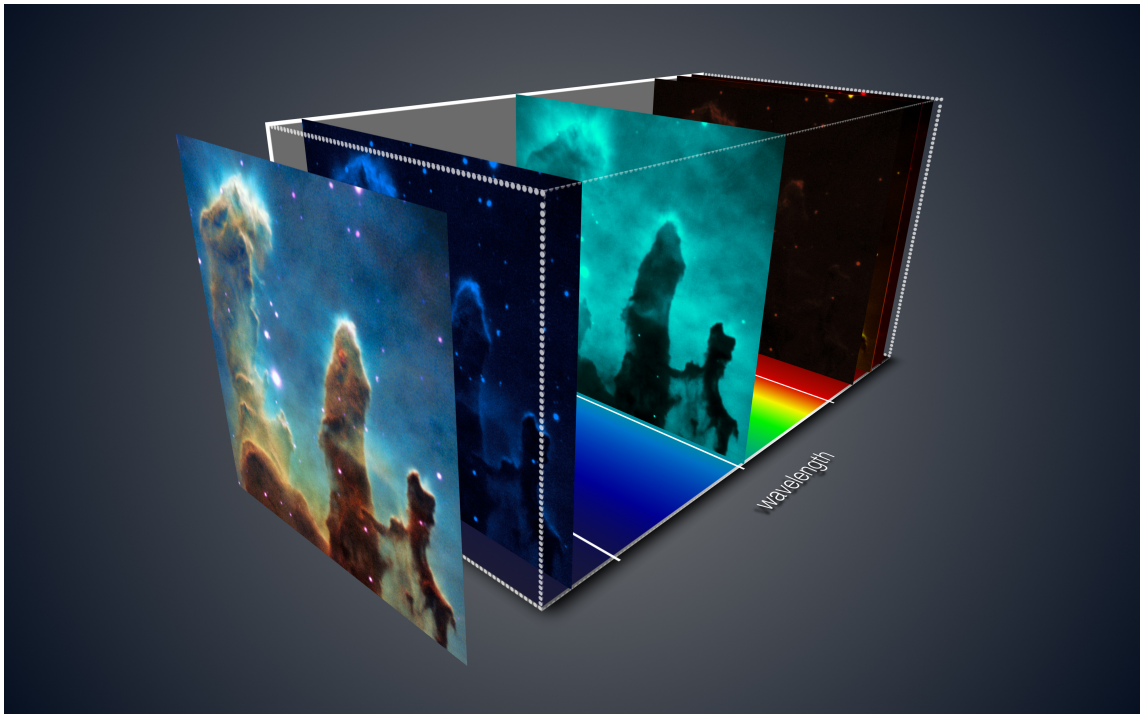

Figure 3.2: Visualisation of the 3D IFU datacube. Image of the targeted region varies across wavelength range revealing different physical and chemical processes at play. Image credit: ESO[1]; published as part of the press release of the article *The Pillars of Creation revisited with MUSE: gas kinematics and high-mass stellar feedback traced by optical spectroscopy* by McLeod et al. (2015).

A great advantage of MUSE is that it can utilise the Ground Atmospheric Layer Adaptive Corrector for Spectroscopic Imaging (GALACSI, Ströbele et al. 2012), a part of the ESO Adaptive Optics Facility (AOF) (Arsenault et al. 2008; Oberti et al. 2018). GALACSI relies on the 4-Laser Guide Star Facility (4LGSF) and the Natural Guide Star (NGS) to sense the wavefront aberrations caused by the atmospheric turbulence. The wavefront correction is enabled by the Deformable Secondary Mirror (DSM). GALACSI provides a tomographic AO correction in NFM and ground layer AO correction in WFM. While AO-assisted observations are optional for WFM, the usage of AO in NFM is mandatory due to the very small field of view. Employment of AO significantly sharpens astronomical images and enhances detectability of faint objects (Ströbele et al. 2012).

The unprecedented combination of MUSE's assets, i.e. an optical IFU with moderate spectral resolution, the large field of view combined with dense spatial sampling, the high sensitivity, and the possibility to enhance instrument's capabilities by AO, make it a one of the most demanded ESO instruments[2]. MUSE has been so far used for a very broad range of astrophysical topics, starting with the extragalactic studies (e.g., Williams et al. 2022; Azevedo et al. 2023; Holoien et al. 2023), through stellar clusters (e.g., Husser et al. 2016; Fang et al. 2021), surroundings of young stars (e.g., Xie et al. 2021; Kirwan et al. 2023), and accreting protoplanets (Haffert et al. 2019; Xie et al.

[2]Telescope at which MUSE is mounted, UT4, is regularly the most over-subscribed ESO telescope during call for proposals, see e.g., https://www.eso.org/sci/observing/phase1/p111/pressure.html

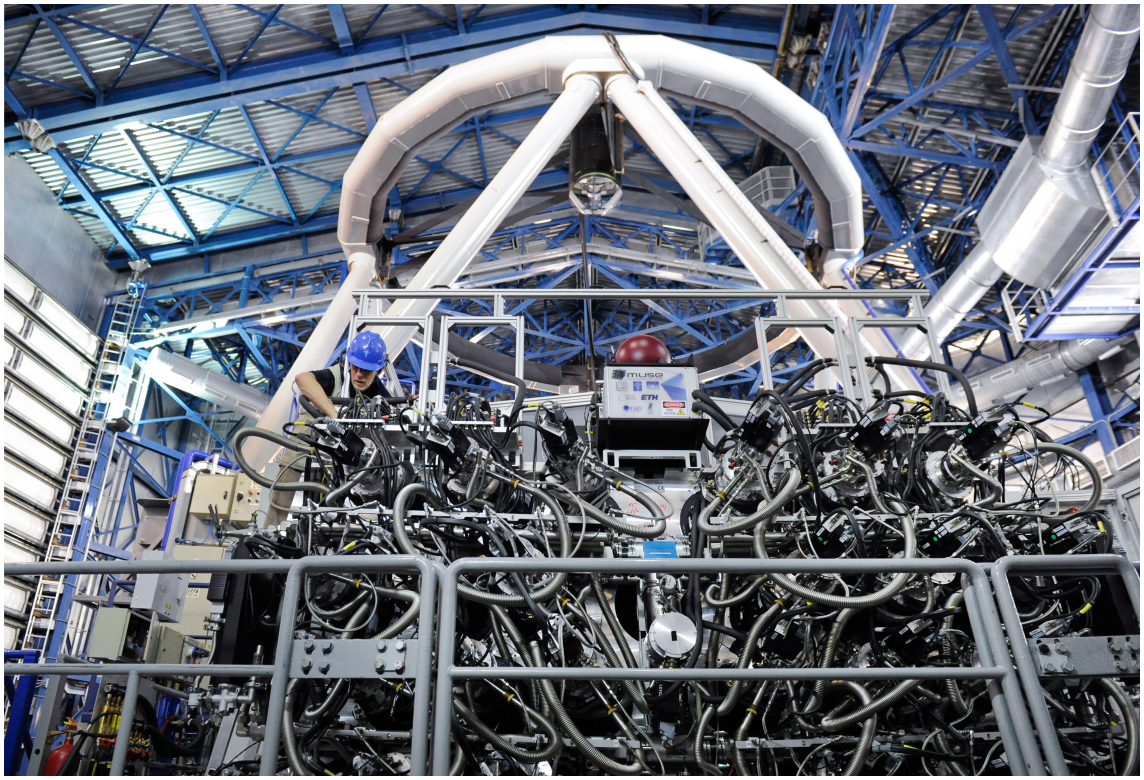

Figure 3.3: MUSE instrument mounted at the Nasmyth focus of the UT4 (Yepun) of VLT. Image credit: ESO[3].

2020), to the Solar System bodies (e.g., Kwon et al. 2023). This list of works and science cases where MUSE was used is highly incomplete but already shows in which areas the application of MUSE is the most suitable. Kinematic studies of low-redshift galaxies (e.g., Kolcu et al. 2023), measurement of turbulence in HII regions (García-Vázquez et al. 2023), or their ionisation (McLeod et al. 2015) prove, that MUSE is ideal for targeting distant, faint, and crowded regions, perhaps immersed into spatially variable emission from the surrounding gas, where the spatial and spectral information about the emission is crucial. Therefore, MUSE, with large field of view, is a perfect instrument to perform a survey of low-mass stars in the Carina massive star-forming region and disentangle the stellar component of the emission from that of the nebular gas. In the next section, I describe the observational setup and successful strategy that allowed this study.

[3] https://www.eso.org/public/images/ann15041a/

3.3 MUSE observations of Trumpler 14

The content of this section is partially based on Itrich et al. (2023b), Sec. 2.1.

Observations of Trumpler 14 (hereafter Tr 14) were carried out in 2016 with the VLT/MUSE under the programme ID 097.C-0137 (PI: A. Mc Leod). To cover the largest possible area with a single pointing, a WFM without adaptive optics was chosen for these observations. A wide region around Tr 14 including the core of the cluster and the surrounding nebula, was covered with 22 pointings with small spatial overlaps between individual pointings (see Figure 3.4). Each of the pointings was observed three times with a 90° rotation dither pattern to better remove instrument artefacts. The goal of the project was to capture the cluster members, faint and bright, and also to study the kinematics of the gas in the pillar-like structures north-east and south-west from Tr 14. Therefore, the whole region was observed with two integration times: 13 min ("long") and 5 sec ("short") exposure. Deep exposures cause saturation of the images of the brightest and most massive stars, but allow detection and spectroscopic characterisation of faint and low-mass stars (see Chapter 4). Here, we are interested in how low-mass stars are impacted by the presence in the cluster of the massive ones, therefore we only use "long" integrations in our study.

In Table 3.1 we list the average seeing conditions and the ESO quality grade for long exposures used in this work. We also indicate the name of the standard star used for flux calibration of each set. Due to the bad atmospheric conditions some observations were repeated. We checked all datasets and used those, which were graded A to B by the Observatory, i.e. those, which were taken with observing conditions in line with the requested during the design of observations.

Observations were reduced using the dedicated ESO pipeline v. 2.8.3 (Weilbacher et al. 2020) embedded in the EsoReflex environment (Freudling et al. 2013). The pipeline provides bias and overscan subtracted, flat-field and illumination corrected, wavelength and flux calibrated IFU cubes. Calibrated exposures (3 per pointing) were combined into the 3D data cubes, one per field, that were used for the analysis presented here.

In addition to the 3D data cubes, the ESO pipeline allows extraction of photometric images, among other ones, in the standard Johnson-Cousins bands. We extracted I, R, and V-band images. The first ones were used as reference to guide the selection of bona-fide sources for the extraction of spectra from the IFU cubes. All of the images were later used to extract aperture photometry and obtain optical colour-magnitude diagram (CMD).

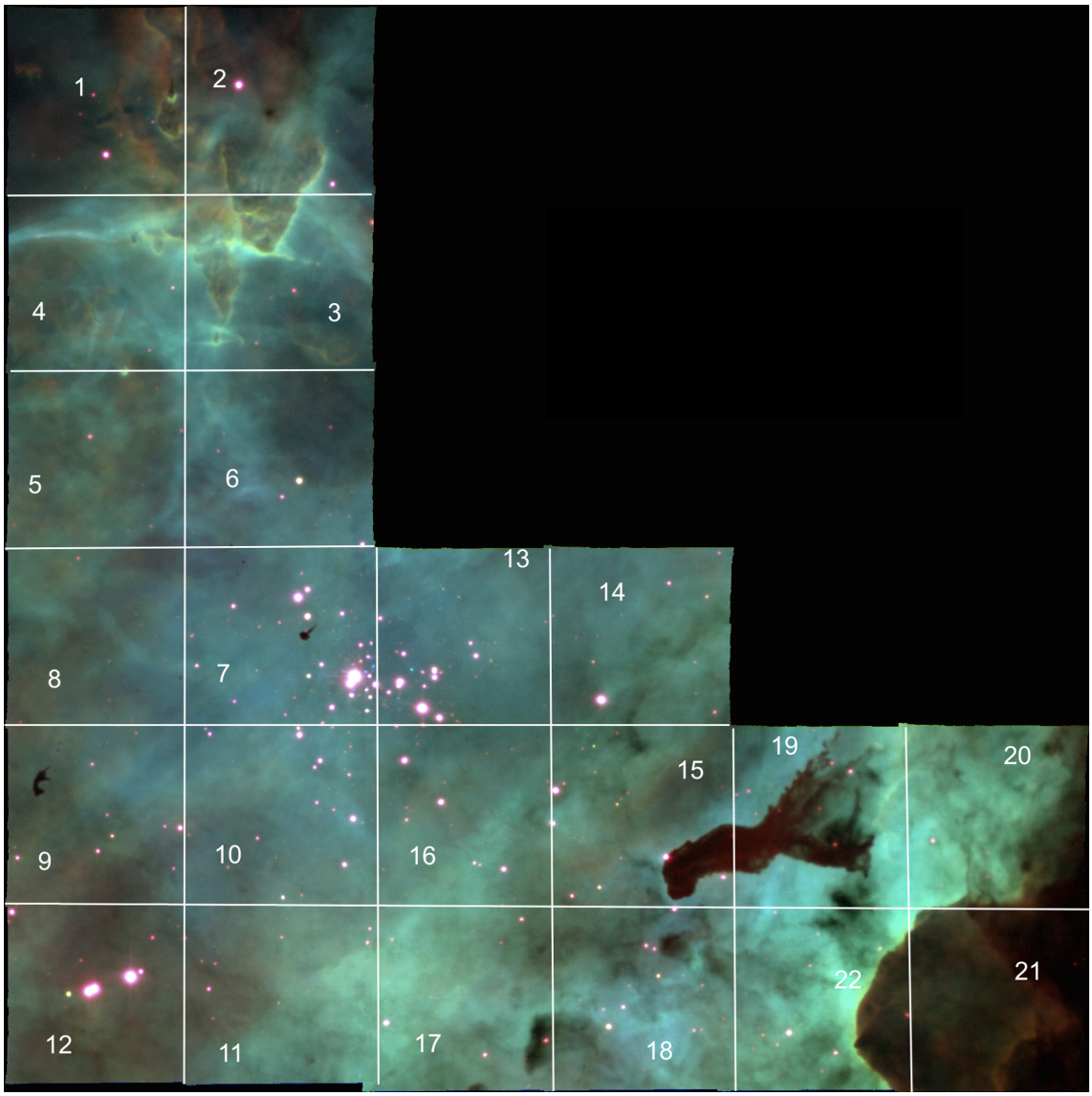

Figure 3.4: MUSE pointings around Trumpler 14 with overlaid field identification numbers used throughout the thesis. Image credit: Anna F. Mc Leod.

Table 3.1: Observational log

pointing	coordinates (h:m:s d:m:s)	date	seeing (″)	grade	calibration standard
1	10:44:08.4 -59:29:39.9	28.02.2016	0.75	A	GD108
2	10:44:00.7 -59:29:39.6	25.02.2016	0.92	B	GD71
3	10:44:00.7 -59:30:39.3	25.02.2016	0.85	B	GD71
4	10:44:08.3 -59:30:39.7	25.02.2016	0.86	B	GD71
5	10:44:08.3 -59:31:39.0	25.02.2016	0.92	A	GD153
6	10:44:00.6 -59:31:38.6	28.02.2016	0.90	B	GD71
7	10:44:00.6 -59:32:38.4	25.02.2016	1.24	B	GD108
8	10:44:08.2 -59:32:38.8	02.03.2016	0.89	A	GD108
9	10:44:08.2 -59:33:38.1	30.03.2016	1.01	A	GD108
10	10:44:00.5 -59:33:37.7	30.03.2016	1.07	A	GD108
11	10:44:00.5 -59:34:37.3	28.03.2016	1.10	A	GD108
12	10:44:08.1 -59:34:37.8	27.03.2016	1.58	B	GD108
13	10:43:52.9 -59:32:37.8	04.04.2016	0.53	A	GD108
14	10:43:45.3 -59:32:37.3	04.04.2016	0.50	A	GD108
15	10:43:45.3 -59:33:36.8	17.04.2016	0.68	B	GD108
16	10:43:52.9 -59:33:37.2	30.03.2016	1.48	B	GD108
17	10:43:52.9 -59:34:36.9	30.03.2016	1.38	B	GD108
18	10:43:45.2 -59:34:36.4	01.04.2016	0.79	A	GD108
19	10:43:37.7 -59:33:36.2	01.03.2016	1.47	B	LTT3218
20	10:43:30.0 -59:33:35.7	02.03.2016	1.33	A	GD108
21	10:43:30.0 -59:34:35.3	02.03.2016	0.99	A	GD108
22	10:43:37.6 -59:34:35.9	02.03.2016	1.15	A	GD108

Notes. Each of the pointings were observed three times with a 90^o dither pattern, listed seeing is a mean value for each Observational Block (OB). OB's grades refer to: A – fully within constraints, OB completed; B – mostly within constraints, some constraint is ∼10% violated, OB completed; C - out of constraints, OB must be repeated.

Chapter

The population of young low-mass stars in Trumpler 14

4

This chapter describes the analysis of the observations of Trumpler 14 introduced in Chapter 3 and discuss results of this investigation. The work presented here is based on Itrich et al. (2023b) and has been accepted for publication in Astronomy & Astrophysics. As a leading author I carried out all of the data analysis and writing of this article.

Massive star-forming regions are thought to be the most common birth environments in the Galaxy and the only birth places of very massive stars. Their presence in the stellar cluster alters the conditions within the cluster impacting at the same time the evolution of other cluster members. In principle, copious amounts of ultraviolet radiation produced by massive stars can remove material from outer parts of the protoplanetary disks around low- and intermediate-mass stars in the process of external photoevaporation, effectively reducing the planet-formation capabilities of those disks. Here, we present deep VLT/MUSE observations of low-mass stars in Trumpler 14, one of the most massive, young, and compact clusters in the Carina Nebula Complex. We provide spectral and stellar properties of 717 sources and based on the distribution of stellar ages derive the cluster age of ∼1 Myr. The majority of the stars in our sample have masses $\leqslant 1\ M_{\odot}$, what makes our spectroscopic catalogue the most deep to date in term of masses, and proves that detailed investigations of low-mass stars are possible in the massive but distant regions. Spectroscopic studies of low-mass members of the whole Carina Nebula Complex are missing. Our work provides an important step forward towards filling this gap and set the stage for follow-up investigation of accretion properties in Trumpler 14.

4.1 Introduction

Star formation takes place in both, low-mass and massive complexes of molecular clouds. The latter is considered to be a more common star-forming environment in the Galaxy (e.g., Miller & Scalo 1978; Lada & Lada 2003; Winter et al. 2018c). Those giant regions form hot and massive OB stars, which can significantly affect the formation and evolution of less massive cluster members. Copious amounts of ionising far- (FUV) and extreme-ultraviolet (EUV) photons, as well as an enormous

Based on observations collected at the European Southern Observatory under ESO programme 097.C-0137.

volume of ejected mass via outflows or strong stellar winds, can create a so-called *negative* feedback. By injecting large amounts of energy into the surrounding medium, massive stars ionise and disperse the natal molecular cloud producing expanding HII regions (e.g., Freyer et al. 2003; Krumholz et al. 2011; Winter et al. 2018c) and remove the matter from circumstellar disks that could otherwise be used to form a planetary system (e.g., Adams et al. 2004; Anderson et al. 2013; Facchini et al. 2016; Eisner et al. 2018; Winter & Haworth 2022). On the other hand, expanding shock and ionisation fronts can also compress molecular clouds and in that way trigger the formation of new stars (*positive* feedback, e.g., Gritschneder et al. 2010; Haworth & Harries 2012). There is a strong evidence that the formation of the Solar System took place in such a large cluster and was heavily influenced by close-by massive stars (e.g., Adams 2010; Pfalzner et al. 2015). It is therefore of great importance to understand how the presence of massive stars in the cluster influences the intrinsic star formation, particularly of low-mass stars, as well as the initial mass function (IMF), star formation efficiency, or the planet formation capacity.

Despite the importance of understanding the global picture of star formation, a substantial part of the investigation was so far focused on nearby (<300 pc), and therefore low-mass, star-forming regions (Manara et al. 2023). While they are very important to construct and test a theory of formation of Sun-like stars, those studies neglect the role of the cluster environment. The closest massive region, the Orion Nebula, although providing excellent first examples of photoevaporating disks ("proplyds", O'Dell et al. 1993), might not be representative of the most extreme environments where most of the stars in the Galaxy are forming (Smith 2006).

The greatest problem of studying massive star-forming regions is that they are all relatively far away from us (>1 kpc) and usually suffer from high extinction. These two factors significantly hinder the characterisation (and even detection) of individual members of these complexes, especially those less massive and fainter. Since the stellar content of any cluster is dominated by low-mass stars, lack of those objects can essentially impact results of studies of massive star-forming regions, as well as their interpretation. Moreover, low-mass stars are more vulnerable to the harsh environment than the massive ones (see e.g., Whitworth & Zinnecker 2004; Almendros-Abad et al. 2023). Environmental conditions like high UV radiation impacts also the capability of protoplanetary disks around young stars to form planets (e.g., Throop & Bally 2005; Anderson et al. 2013; Facchini et al. 2016; Winter et al. 2018c; Parker 2020; Winter et al. 2020; Qiao et al. 2023).

Another observational problem that often accompanies the studies of massive regions is a bright and variable emission from the surrounding HII region. Assessment of this emission in most cases cannot be done globally but requires the knowledge of the local variation of this emission. This issue is particularly profound when studying emission lines from the young stars, e.g., tracing accretion, winds, or jets. Stellar spectrum is contaminated with the nebular emission what can lead to potentially incorrect conclusions. Due to that reason, fiber-fed spectroscopy is not a good approach to study star-forming regions. A significantly more efficient way to obtain local and wavelength-dependent sky emission is to employ integral field spectroscopy

(IFU) instruments. Current instrumentation offers several IFU spectrographs with medium to high spectral and spatial resolution (e.g., ERIS, MUSE, KMOS at the Very Large Telescopes, or GMOS, NIFS at the Gemini Telescopes, Allington-Smith et al. 2002; McGregor et al. 2003; Bacon et al. 2010; Sharples et al. 2013; Davies et al. 2023). They allow obtaining position-dependent spectra of sources of interest as well as surrounding background and with that characterising faint objects in distant regions.

The Carina Nebula Complex (CNC) is one of the biggest sites of star formation and one of the most massive HII regions in our Galaxy (for details see Chapter 2). The $>5\times10^4$ stars (Povich et al. 2019) with a total mass of $\sim 37000\ M_\odot$ (Preibisch et al. 2011a) constitute the CNC stellar population. There are at least 74 O-type stars in the CNC (Smith 2006; Berlanas et al. 2023) producing copious amounts of FUV radiation ($10^4 - 10^5\ G_0$, Smith 2006; Smith & Brooks 2008). Those properties makes the CNC ideal laboratory to investigate the role of external photoevaporation. Additionally, the whole complex is located at the distance of 2.35 kpc (Shull et al. 2021; Göppl & Preibisch 2022) with relatively low extinction (Walborn 1995; Hur et al. 2023). However, up to date no spectroscopic survey targeting stars below 1 $M_\odot$ was conducted in the Carina Nebula leaving the most important part of the region uncharacterised. The aim of this work is to fill this gap and provide a spectroscopic catalogue of low-mass stars in one of the main clusters in the Carina Nebula, Trumpler 14. High UV field, high cluster density and mass, young age, and low reddening towards the cluster make Tr 14 a perfect target to investigate the role of environment on star formation.

Here, we present the optical photometry and spectroscopy of young, low-mass stars in Tr 14. We define the methodology to detect those faint sources, extract their spectra, assess contamination from the sky emission, and conduct the spectral classification. Subsequently, we describe how the stellar properties are obtained. We conclude our work with a more global outlook on the Tr 14's properties. This study will be followed up by the detailed characterisation of accretion properties of the young stars presented here.

4.2 Data

4.2.1 Observations and data reduction

Observations were carried out in 2016 with the Multi Unit Spectroscopic Explorer (MUSE), a second generation integral field unit (IFU) instrument on the VLT in Paranal, Chile (Bacon et al. 2010), under the programme ID 097.C-0137 (PI: A.F. Mc Leod). The details of observational strategy and data reduction are provided in Chapter 3.

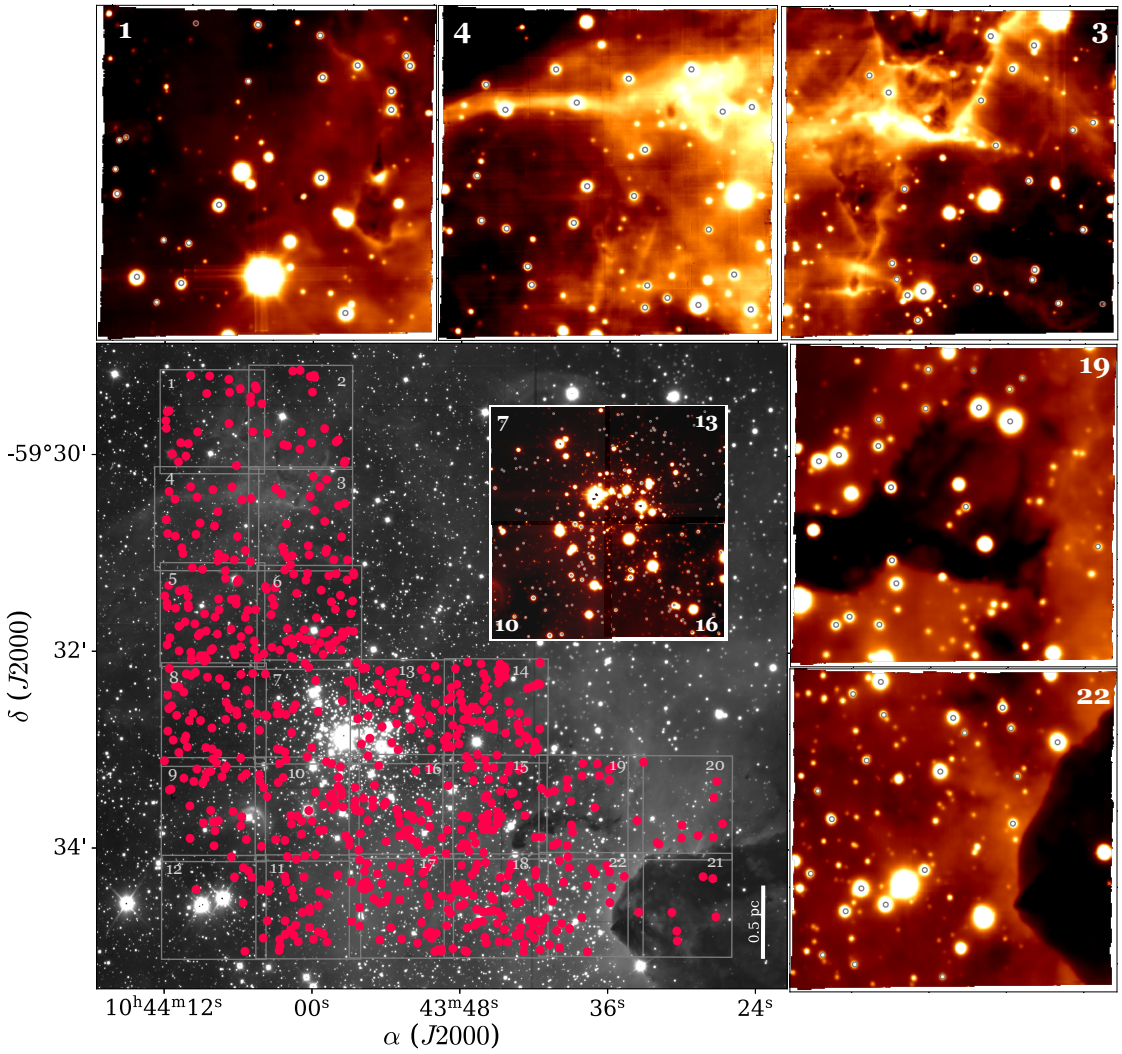

Figure 4.1: Trumpler 14 cluster studied in this work. Grey sky image from HAWK-I H-band observations (Preibisch et al. 2011a,b) shows the whole region with the light grey grid of MUSE pointings and stars studied in this work marked as red circles. The five panels above and on the right show selected MUSE I-band images. The panel inside consists a mosaic of four MUSE pointing of the Tr 14 center. Their numbers are indicated in the panels. Positions of the stars on MUSE images are marked with empty grey circles. The bar on the lower right corner of the HAWK-I image indicates the projected distance of 0.5 pc at the assumed distance of 2.35 kpc towards Tr 14 (Göppl & Preibisch 2022).

4.2.2 Identification of sources and extraction of spectra

In addition to producing the 3D data cubes, the ESO pipeline allows the user to extract photometric images, among other ones, in the standard Johnson-Cousins bands. We use these images as reference to guide the selection of bona-fide sources for the extraction of spectra from the IFU cubes. We use `SExtractor` (Source–Extractor[1], Bertin, E. & Arnouts, S. 1996) to perform the source identification on the photometric images. `SExtractor` is a free software designed to perform aperture photometry on astronomical images, suited also for crowded regions. It estimates and subtracts the background emission assuming its smooth variation. We tested

[1] https://sextractor.readthedocs.io/

the background estimation varying the size of the mesh cell and found that the size of 16 pixels gives the best performance in terms of recovering large gaseous features on the sky and at the same time not creating artificial ones. The same pixel size is used throughout the aperture photometry and extraction of the spectra. We in fact anticipate here that the latter is done by performing aperture photometry on each individual slice of the MUSE cube at the position of the bona-fide sources identified on the I-band images.

We first perform the identification of the sources on the I-band images, which we use as the reference. We employed a fixed aperture size of 5 pixels in diameter and the background mesh size of 16 pixels. Hence using the `SExtractor` we create a catalogue which includes for each source the X and Y position in the MUSE CCD reference frame together with I-band aperture magnitudes. Based on "identification" image, we run the `SExtractor` in double image mode on all photometric images obtaining magnitudes from other bands, namely R and V. This is possible as all the images have identical dimensions being all extracted from the same IFU cube. With that we create the initial photometric catalogue of 5428 objects with I-band magnitude measurements.

We used the same approach to extract spectra from the MUSE cubes of each source detected in the I-band images. Upfront, we slice MUSE datacubes with `MissFITS`[2] (Marmo & Bertin 2008) into individual images, one per spectral element. Then, we run `SExtractor` on each slice and estimate flux for each source within the same aperture as for photometric images. Measured fluxes per spectral element are then combined into a single spectrum for each target. In the same way we extract wavelength-dependent flux uncertainties and sky spectra. Both are later used to evaluate goodness of stellar spectra.

4.2.2.1 Coordinates correction

We transform astrometric coordinates of stars extracted from the MUSE cubes to the coordinate system of the recently released *Gaia* DR3 catalogue (Gaia Collaboration et al. 2022). We first perform a match between the catalogues with a large separation limit (1-2″), separately for each MUSE pointing. We estimate median offsets of right ascension and declination for every pointing and adopt them as coordinate corrections. Absolute corrections range between 1.46″ and 5.75″ for right ascension, and between 0.08″ and 2.98″ for declination. We list corrections and show distributions of offset for each pointing in Appendix A.1. We apply the corrections to coordinates of our stars and list them in Table 4.1.

Consecutively, we match our catalogue with corrected coordinates once again with *Gaia* (Gaia Collaboration et al. 2016, 2022). We find 1902 counterparts within the separation of 0.5″. In Appendix A.1 we show the distribution of separations between *Gaia* and MUSE and argue the selection of the separation limit. Based on this distribution we also find that the accuracy of astrometry of our stars is of ∼0.1″.

[2] https://www.astromatic.net/software/missfits/

4.2.2.2 Identification of spurious sources

Before analysing the sample we remove from the catalogue spurious sources, which may be due to low signal to noise, confusion near the very bright stars, and contamination from the structures in the nebular emission.

Due to different atmospheric conditions the sensitivity of different pointings is uneven. Additionally, some images contain bright stars whose luminosity dominates at the images making the detection of the faint sources in their vicinity challenging. We first use flags issued by `SExtractor` on photometric measurements to exclude potentially incorrect magnitudes. Those flags mark cases when neighbouring source likely bias estimation, when the light from the object has been deblended, when the position of the object is too close to the edge of the image, when one or more pixels were saturated, or when the photometry process was corrupted[3]. With this approach, we remove 21% of the sources from the catalogue. We additionally only accept stars with the photometric uncertainty in I-band of less than 0.1 mag. We remove photometric measurements not fulfilling those criteria in other bands. This procedure leaves 3082 sources in our catalogue.

The Carina Nebula is an HII region, remarkably bright in some atomic lines (Hα, Hβ, OI, HeI, etc.). In particular, small, compact gas concentrations can mimic light from the stars having stellar-like point spread function (PSF). We performed visual inspection of the I-band images comparing them to the other broad-band MUSE images, as well as to the HAWK-I H-band image (Preibisch et al. 2011a,b), identifying all possible "spurious" detections that are not present in other images; we flag them accordingly and remove from the catalogue.

We pay particular attention to the images affected by the presence of nearby saturated stars. Their light is spread on the pixels around their PSF on the CCD detector. This artificially changes the local background making the measurement of the stellar flux falling on those regions unreliable. Additionally, we identify elongated spikes near those bright stars, due to the diffraction pattern of the secondary mirror support. Combined, those effects significantly hinder the analysis of fainter stars in the closest neighbourhood of the bright ones. Based on visual inspection, we identify stars where light is not separated spatially on I-band MUSE images from the bright stars, flagged them as „illuminated" and remove from the final photometry catalogue leaving 2727 stars.

4.2.2.3 Detections in overlapping pointings

Edges of some neighbouring pointings overlap causing double detection of the same stars in our photometry catalogue. After correcting coordinates, we defined a threshold separation of 0.5″within which we looked for stars present in two (or more) pointings. We find 55 pairs of doubly observed targets. We exclude from the cata-

[3]The full description of `SExtractor` flags is available on the website at https://sextractor.readthedocs.io/en/latest/Flagging.html#flags-def

logue those sources that have worse signal-to-noise ratio (snr) of spectrum around 7500 Å. We show comparisons of spectra between two detection in the Appendix A.2.

4.2.2.4 Background emission

All the images of Carina Nebula, as an HII region, suffer from bright and highly variable background emission. The presence of a strong background with flux variations of the order of one stellar PSF makes the estimation of the local background in the vicinity of the stars very uncertain. Hence, the aperture photometry from which the stellar spectra are built, can be very imprecise and unreliable. During the stellar flux extraction (Sec. 4.2.2), background emission was estimated by `SExtractor` assuming it is varying smoothly across the field. To make sure that the photometry is robust, we estimate the local background variation for each star in our catalogue based on the standard deviation (std) of the background estimates for stars within a radius of 20″. We adopt the threshold of 3σ, where σ is the standard deviation, and remove all photometric measurements where the stellar flux is below the threshold. In Appendix A.3 we discuss the applied definition in depth. The final number of stars with well defined and reliable I-band magnitudes is 804 (Figure 4.1).

4.2.2.5 Magnitude correction

To check the flux calibration we compare the MUSE photometry with the optical photometry from the Wide Field Imager (WFI) at the MPG/ESO 2.2m telescope published by Beccari et al. (2015). The catalogues were matched adopting a 0.5″maximum separation radius between the stars from the two catalogs. We find 613 common stars in the two catalogs. We perform the comparison of magnitudes for each field and band separately. For the I-band the corrections vary between 0.16 and 1.28 mag depending on the MUSE pointing with the mean value of 0.55 mag. This is mainly due to the fact that each MUSE field was observed in very different weather conditions. All corrections are provided in Appendix A.4. We discard B-band magnitudes as highly uncertain for our faint stars. We provide in the Table 4.1 the photometry of the sources extracted from the MUSE images with the magnitudes corrected to match the WFI ones.

As a next step, we investigate the distribution of the magnitudes. We show the observed luminosity function for I, R, and V-bands from MUSE observations in Appendix A.4. The distribution of I-band magnitudes peaks at ∼18 mag and falls to ∼21 mag. If we adopt the cluster age of 1 Myr (Smith & Brooks 2008), the distance to the cluster of 2.35 kpc (Göppl & Preibisch 2022), and extinction of 2.3 mag (see Sec. 4.3), those magnitudes will correspond to the stellar masses of ∼0.8 and ∼0.14 $M_\odot$ according to the theoretical evolutionary models of Baraffe et al. (2015). Even though we do not correct luminosity function for completeness, those rough mass estimates show depth of our catalogue.

4.2.2.6 Cross-match with other photometry catalogs

To complete our catalogue with information from other wavelength ranges, in addition to the *Gaia* DR3 and WFI, we cross-match the MUSE catalogue with VISTA (Preibisch et al. 2014), HAWK-I (Preibisch et al. 2011a,b), *Spitzer* (Povich et al. 2011), and *Chandra* (Preibisch et al. 2011b; Townsley et al. 2011) observations. For consistency, we define the same maximum separation of 0.5″ for all the catalogues. In Appendix A.1 we explain the use of this separation limit. We find 658, 766, 26, and 309 stars in common between MUSE and VISTA, HAWK-I, *Spitzer*, and *Chandra*, respectively. We present in Table 4.1 the example of the catalogue together with flags indicating the presence of the counterpart in any other catalogue. The full content of the catalogue is available online.

We emphasise that we adopt a very conservative approach and apply severe photometric quality thresholds and checks to select only bona-fide stars with high quality spectra. In doing so we are aware that a number of real stars which have not passed our photometric quality criteria might have been removed from the final catalogue. In fact, a large number of these stars do have a counterpart in one or more of the catalogues used to complement the MUSE photometry. Among discarded sources are 841 *Gaia*, 212 WFI, 913 VISTA, 1809 HAWK-I, 2 *Spitzer*, and 120 *Chandra* counterparts. We are aware that within this limitation our catalogue is not complete in terms of cluster members. We report the list of probable members with uncertain photometry due to the background contamination in Table A.3 and assess the completeness in the next section.

4.2.3 Completeness of the catalog

The goal of this work is to have a high quality spectroscopic sample of low-mass members of Tr 14. In order to achieve this goal we apply a number of quality cuts to the photometric catalogue (Sec. 4.2.2.4), which can affect the interpretation of our results.

To better understand the limitations of our work, we estimate the completeness by comparison to the photometric catalogue from HAWK-I (Preibisch et al. 2011a,b). Figure 4.2 shows distribution of J-band magnitudes observed by HAWK-I in the exact same region as covered by our MUSE pointings (dark berry histogram). The stars in common between the two catalogues are shown in violet. With the grey line we show the ratio between the stars retrieved in our catalogue and the number of stars observed by HAWK-I per magnitude bin of 0.5 mag. The ratio gives us a rough estimate of the completeness of our catalogue. The upper panel shows only those stars for which three sigma level of background variation did not exceed I-band flux measured with MUSE. Their J-band magnitudes range from 12.5 to 19.0 mag, corresponding at the low-mass end to 0.065 $M_{\odot}$ at 1 Myr (Baraffe et al. 2015). Assuming that the HAWK-I catalogue is complete down to ∼21 mag in J-band (Preibisch et al. 2011a), we can adopt this ratio as the rough estimate of the completeness of our catalogue. Based on this assumption, we reach 50% level of completeness at ∼15.5 mag corresponding to 0.8 $M_{\odot}$ at 1 Myr. The 30% completeness

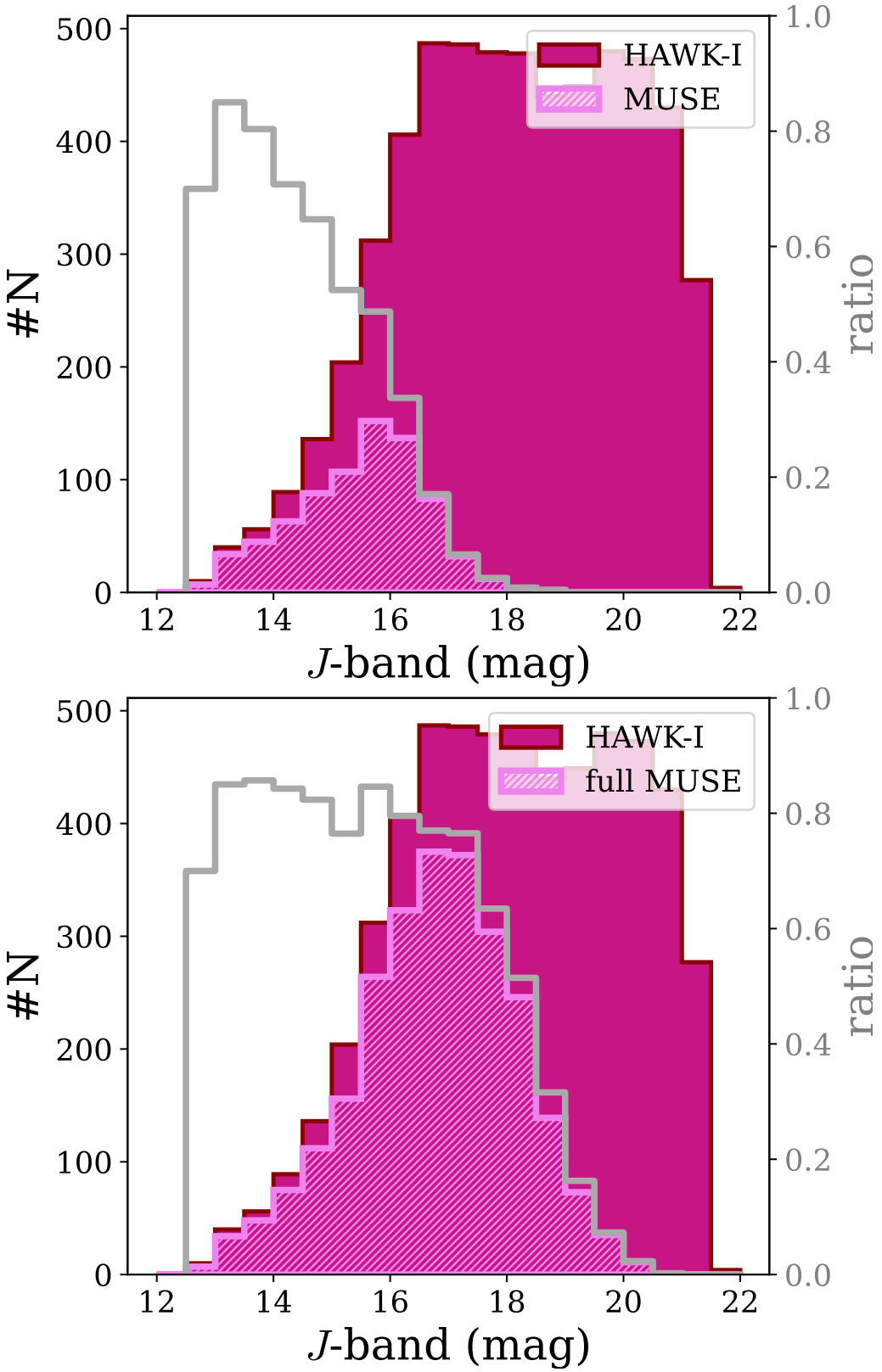

Figure 4.2: The distribution of J-band magnitudes from HAWK-I in the MUSE field (Preibisch et al. 2011a,b). The dark berry histogram shows all HAWK-I measurements taken in the same area that was covered by MUSE. The violet distribution presents point source detections from Sec. 2.2.6, (upper panel) and in combination with the one excluded due to the high background variation and foreground stars (lower panel). In both panels, the grey line shows completeness of our catalogue defined as a ratio of the number of stars in a given magnitude bin (0.5 mag wide) in our catalogue and in the HAWK-I catalogue.

Table 4.1: Catalogue of low-mass in Trumpler 14 stars analysed with MUSE observations.

ID	coordinates (h:m:s d:m:s)	I-band (mag)	R-band (mag)	V-band (mag)	$\mathrm{snr}_{I,\mathrm{bkg}}$	$\mathrm{snr}_{R,\mathrm{bkg}}$	$\mathrm{snr}_{V,\mathrm{bkg}}$	possible_frg_bkg	gaia_flag	wfi_flag	VISTA_flag	hawki_flag	spitzer_flag	chandra_flag	NIR excess	SpT	T_{eff} (K)	A_V (mag)	r_{7500}	$\log(L_{\mathrm{bol}}/L_\odot)$	$M_{\star,\mathrm{PARSEC}}$ ($M_\odot$)	$M_{\star,\mathrm{BT2000}}$ ($M_\odot$)	$\mathrm{Age}_{\mathrm{PARSEC}}$ (Myr)	$\mathrm{Age}_{\mathrm{BT2000}}$ (Myr)
F01N009	10:44:09.93 -59:29:11.72	20.49±0.12	–	–	3.96	–	–	False	None	False	True	True	False	False	True	M5.0$^{+1.6}_{-2.7}$	3125$^{+160}_{-160}$	2.70$^{+1.22}_{-1.22}$	0.08$^{+0.56}_{-0.07}$	-1.05$^{+0.51}_{-0.45}$	0.38	0.18	6.2	2.3
F01N010	10:44:08.38 -59:29:12.03	17.37±0.09	18.11±0.09	19.01±0.08	17.26	4.18	5.00	False	Good	True	True	True	False	False	False	K4.0$^{+0.6}_{-0.6}$	4561$^{+98}_{-98}$	1.20$^{+0.41}_{-0.41}$	0.00$^{+0.56}_{-0.00}$	-0.32$^{+0.34}_{-0.36}$	1.02	0.99	13.0	19.8

Notes. The first column gives IDs of the detected sources, the second one lists coordinates. The third, fourth, and fifth columns give apparent magnitudes in I, R, and V-band, respectively. The sixth, seventh, and eighth columns provide signal-to-noise of the flux with respect to the background variation in a given band, as indicated by the lower script (see Sec. 4.2.2.4 for details). The ninth marks possible foreground or background stars (see Sec. 4.3.1 for definitions). The next five columns flag matches with other catalogs: *Gaia* (Gaia Collaboration et al. 2022), WFI (Beccari et al. 2015), VISTA (Preibisch et al. 2014), HAWK-I (Preibisch et al. 2011a,b), *Spitzer* (Povich et al. 2011), and *Chandra* (Preibisch et al. 2011a; Townsley et al. 2011). The following indicates if the star has an NIR excess as defined by Zeidler et al. (2016). In the consecutive nine columns are given stellar parameters: spectral type, effective temperature, visual extinction, constant veiling at 7500 Å, bolometric luminosity, and stellar mass and stellar age estimated from PARSEC (Bressan et al. 2012) and Baraffe et al. (2015) / Siess et al. (2000) tracks, as indicated by the subscript. A full version of this table will be available at the CDS upon publication. The first few rows are shown as an example.

level is achieved at ∼16.5 mag corresponding to ∼0.4 $M_\odot$ at 1 Myr. As we indeed see later in Sec. 4.3.2 or 4.4.2, our deep observations allow us to detect and characterise very low-mass stars in Tr 14. However, due to our conservative approach to the background emission (Sec. 4.2.2.4), the final sample is highly incomplete in the low end of mass spectrum.

In the lower panel of Figure 4.2 we include the "full MUSE" sample consisting the one with robust I-band MUSE photometry and the one discarded due to the highly variable background emission. Here, flagged or uncertain MUSE photometry sources (Sec. 4.2.2.2) were not included. We see immediately that with our approach we removed mostly faint, low-mass objects. The "full" catalogue extends to the ∼21 J-band magnitude (0.018 $M_\odot$ at 1 Myr adopting the evolutionary models of Baraffe et al. 2015) and reaches 50% level of completeness at ∼18.5 mag, corresponding to 0.085 $M_\odot$ at 1 Myr. The 30% completeness level is achieved at ∼19 mag (0.065 $M_\odot$).

The significant difference between the two distributions ("MUSE" sample with robust I-band photometry and "full MUSE" sample affected by the background emission) shows the possible impact of the adopted procedure on the final results and the estimated global properties of Tr 14. Since the deep NIR photometric observations can contain significant fraction of contamination from background sources, especially in the faint end (see the discussion in Sec. 3.3 in Preibisch et al. (2011a) and in Sec. 2.3 in Preibisch et al. (2011b)), we do not correct our analysis for the incompleteness. We assume that our study is complete at the level of 50% for stars more massive than 0.8 $M_\odot$ and at the level of 30% for stars more massive than 0.4 $M_\odot$.

4.3 Stellar population

4.3.1 Identification of foreground stars

To exclude possible contamination from foreground and background stars we use accurate *Gaia* astrometry for our sources. We first perform a number of quality checks on the matched objects. We first exclude all stars that have goodness of fit parameter RUWE > 1.4 (Lindegren 2018), astrometric_gof_al > 5 (Lindegren et al. 2021), parallax over error lower than 5, and uncertainty of the proper motion above 20%. We flag them as object with poor *Gaia* astrometry, `gaia_flag`='poor'. We find 175 good objects out of the 794 *Gaia* counterparts. None of them is flagged as a non-single star or a duplicated object, reassuring us about the good quality of the astrometry. All of them have 5- or 6-parameter solution. We select fore- and background stars based on parallaxes corrected for bias, as described in Lindegren et al. (2021). This correction is possible only for stars with G-band magnitude between 5 and 21, and for the effective wavenumber (for 5-parameter solution) or the pseudocolour (for 6-parameter solution) between 1.24 and 1.72 $\mu\mathrm{m}^{-1}$. Wavenumbers are calculated using calibrated BP/RP spectra, while pseudocolour is an approximate colour of the source based on its astrometric solution utilising the chromaticity of the instrument.

We illustrate the distribution of corrected parallaxes of stars with good *Gaia* astrometry in Figure 4.3. The Gaussian profile fit to the distribution is centred at $\varpi = 0.43$ mas and has a width of $\sigma = 0.04$ mas. The centroid parallax corresponds to the distance of 2.35 kpc, in very good agreement to the findings of Göppl & Preibisch (2022). We follow their procedure to identify fore- and background stars. We define the background stars as those, whose 3σ extend of the parallax value (i.e. parallax value plus its error) is smaller than the ϖ_{min} ($\varpi + 3\sigma_{\varpi} < \varpi_{\mathrm{min}}$), while foreground stars as those with 3σ extend (i.e. parallax value minus its error) higher than ϖ_{max} ($\varpi - 3\sigma_{\varpi} > \varpi_{\mathrm{max}}$). We adopt as ϖ_{min} and ϖ_{max} values corresponding to range of parallaxes defined by the width of the Gaussian distribution (0.43±0.04 mas), further corresponding to the distance range of (2.61 kpc, 2.13 kpc). Out of 175 'good' *Gaia* counterparts we identify 0 background stars and 24 foreground stars. However, if we take into account all possible *Gaia* matches with corrected and positive parallaxes and possibly high astrometry uncertainties (784 stars), then for the same parallax ranges we find 35 possible foreground stars and 10 possible background stars. We remove from our catalogue 24 foreground stars with robust astrometry and flag remaining 21 stars as possibly contaminated (fore- or background) stars (`possible_frg_bkg`). Summarising, we find 794 *Gaia* counterparts, including 175 with good astrometry; 24 of them are foreground stars. At the end our catalogue contains 780 sources.

4.3.2 Colour–magnitude diagram

We first present the colour-magnitude diagrams (CMDs) based on corrected MUSE photometry. Figure 4.4 shows two CMDs based on (V-I) and (R-I) colours from MUSE, exclusively, and one based on I-band magnitude from MUSE and J-band

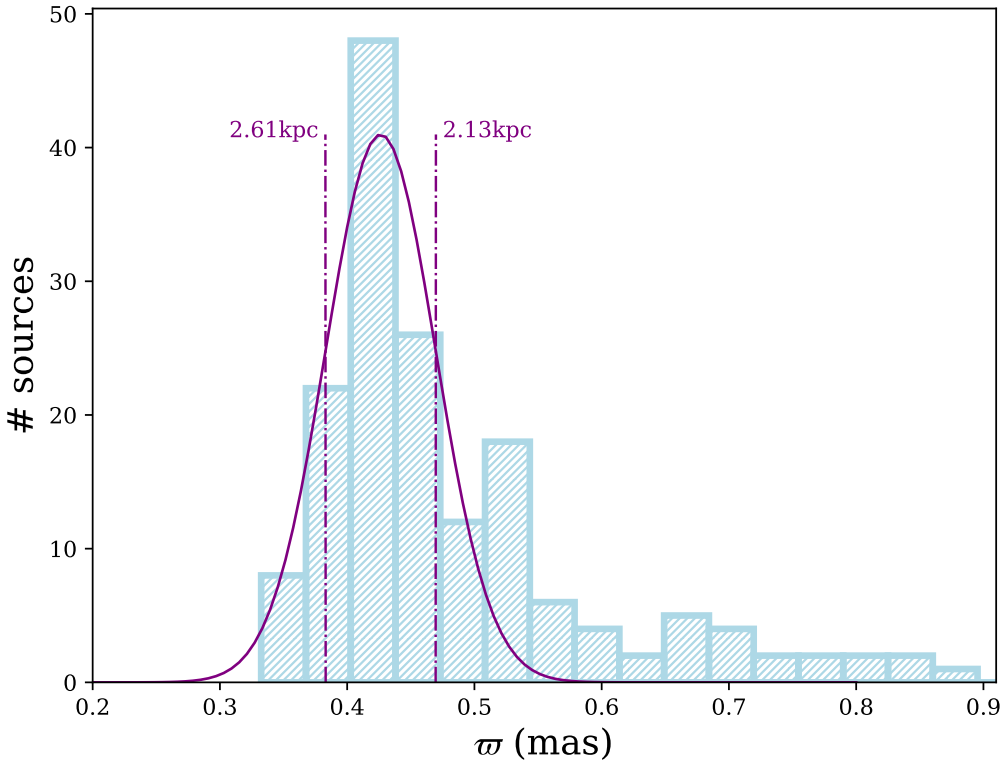

Figure 4.3: Distribution of corrected parallaxes (light blue histograms) with fitted normal distribution (purple line). Dashed-dotted lines mark 1σ width of the fitted distribution and applied ranges for excluding fore- and background stars.

magnitudes from HAWK-I or VISTA. We also plot PARSEC v1.2S[4] theoretical isochrones with black solid lines (Bressan et al. 2012; Chen et al. 2014) reddened by A_V=2.6 mag, best matching our observations (see also Sec. 4.3.4), using extinction law of Cardelli et al. (1989) and R_V=4.4 (Hur et al. 2012). We apply a distance modulus of 11.86 mag, equivalent of the distance to Tr 14 (Göppl & Preibisch 2022). We show tracks for 0.3, 0.7, 1, and 3 $M_\odot$ stars with dotted lines. Our observational CMDs already demonstrate that, despite very conservative quality control, our MUSE data allows us to sample stars in Tr 14 with robust I-band photometry down to $\sim 0.3\ M_\odot$. We note, however, that due to the decrease of snr at shorter wavelengths, number of robust R and V-band magnitudes is smaller than in I-band, and at the same time the number of very low-mass stars detected in those bands reduced.

Ascenso et al. (2007) used high resolution near-IR data to study the core of Trumpler 14. Based on their photometry they found a global visual extinction towards Tr 14 of A_V=2.6±0.3 mag and a sparse foreground population with A_V of 1.4 mag. Additionally to the isochrones reddened by the visual extinction matching our observations, we show also in Fig. 4.4 the location of the Zero Age Main Sequence (ZAMS, grey solid line) reddened by the visual extinction of a sparse population (1.4 mag). The authors suggested that this population of older stars comes from the nearby young clusters. In our CMDs we see indication of two separate populations, one concentrated around 1 Myr isochrone, and the other following ZAMS. We note

[4] http://stev.oapd.inaf.it/cmd

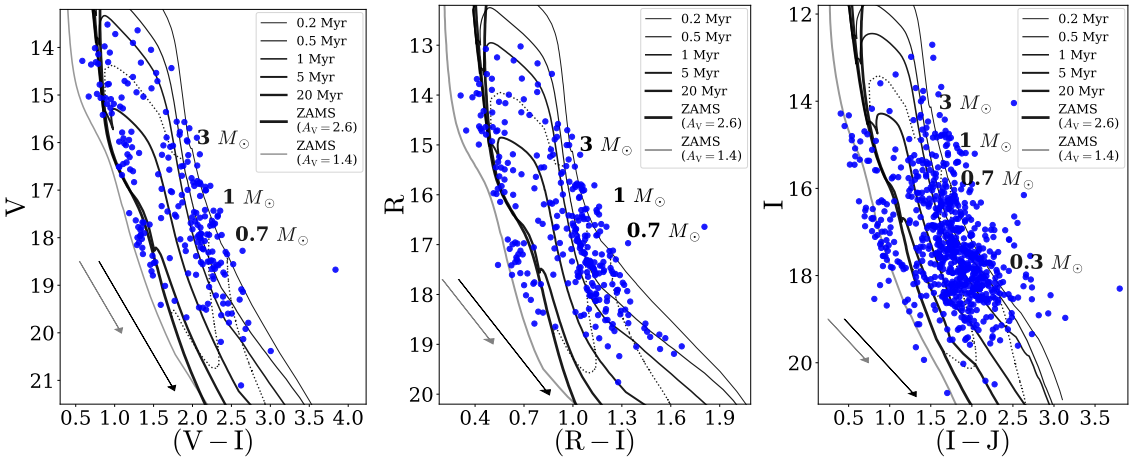

Figure 4.4: Colour–magnitude diagrams from MUSE broad-band filters images in V and I (right panel), R and I magnitudes (middle panel), and I and J magnitudes (left panel). J-band magnitudes are from VISTA and HAWK-I instruments. Shown are only data points with I-band magnitudes above 3σ. Solid lines show PARSEC isochrones from 0.2 to 20 Myr and ZAMS, dotted lines show isomasses of 0.3, 0.7, 1, and 3 $M_\odot$, as labeled (Bressan et al. 2012). Isochrones were reddened by the average extinction $A_V = 2.6$ mag measured from MUSE spectra (see Sec. 4.3.4). Additionally, we plot the ZAMS reddened by A_V=1.4 mag with grey lines.

similar, two-population CMDs of more massive stars in the work of Carraro et al. (2004) (see their Fig. 5). We will examine this feature with spectral classification in the following sections.

4.3.3 Spectral classification

The goal of this paper is to characterise the low-mass members of Trumpler 14 and provide a catalogue of their stellar parameters. As shown in Fig. 4.4, our dataset samples a wide range of stellar masses and colours, and thus spectral types. Hence, we split the procedure of spectral classification into two cases and give the detailed description in the forthcoming sections. We note that our procedure is comparable to the one adopted by Fang et al. (2021) in the study of the Trapezium cluster.

We base the spectral classification on Class III templates observed with VLT/X-Shooter and published by Manara et al. (2013, 2017). The list of templates is provided in Appendix A.5. Those sources where previously studied in the literature and their spectral types are well known. We note here that they all have a negligible extinction A_V<0.3 mag. We will refer to the Class III templates as "templates" later in the text. We degraded the templates spectra (with natal resolution of $R \sim 7500$–18200) to the MUSE resolution convolving them with a Gaussian kernel and then re-sampled on the common for the both instruments spectral range (∼5500–9350 Å). The comparison between the spectra is done in the aforementioned range after normalising to the flux at 7500 Å, f_{750}.

4.3.3.1 M-type stars

The spectra of M-type stars have a characteristic shape in the optical range due to the presence of TiO and VO absorption bands. The depth of those features changes with the spectral sub-type and increases with later stellar types.

In this work, only spectra that have sufficient signal-to-noise (snr>10) are used and classified. From the whole sample of spectra we pre-select those, that might be of M-type based on spectral indices from Riddick et al. (2007), Jeffries et al. (2007) and Oliveira et al. (2003) (TiO feature at 7140 Å) and Herczeg & Hillenbrand (2014) (TiO 7140, 7700, 8465 Å). We require that at least half of the indices suggest an M-type spectrum. We remove from the spectra prominent emission and absorption lines to prevent confusion in the fitting to the templates. Spectral classification is performed together with the estimation of the visual extinction, A_V, and veiling at 7500 Å, r_{750}. We veil and redden templates using the Cardelli extinction law (Cardelli et al. 1989) and a pre-defined grids of A_V and r_{750} values. The extinction is sampled with a step of 0.1 mag between 0.0 and 7.0 mag, while the veiling is assumed to change between 0.0 and 1.9 with a step of 0.02. The average extinction towards Tr 14 was found to be 2.6±0.3 mag (Ascenso et al. 2007), thus we do not expect huge variation of A_V for cluster members. The adopted sampling of the extinction and veiling is smaller than the typical uncertainty of these parameters assessed later.

We minimise the value of a reduced χ^2-like metric, defined as

$$\chi^2_{\rm red} = \frac{1}{N} \sum_i \frac{(O-T)^2_i}{err^2_i} \tag{4.1}$$

to find the best combination of spectral type, A_V, and r_{750}. The O is the observed spectrum, T is the fitted template, err defines the extracted uncertainty of the observed spectrum per spectral bin i, and N is the number of degrees of freedom (number of all spectral bins subtracted by three free parameters). Figure 4.5 shows an example of the result from the fitting procedure, whereas in the Appendix A.6 we show the corresponding $\chi^2_{\rm red}$ maps. We notice that the worst fits usually have marginal values of A_V and r_{750}. In total, we classify 269 M-type stars.

To asses the uncertainty of the estimated parameters, we run the fitting again keeping each time one of the parameters fixed at the best value. We draw the 1–σ curves on the $\chi^2_{\rm red}$ maps between each two parameters. Examples are shown in Fig. A.8. The maximum and minimum values within 1σ from the best fit of two parameters are indicated by the extreme points of the 1–σ curve. With this procedure we get two pairs of uncertainties for each parameter. We combine them taking the minimum. The lower and upper uncertainties are reported together with the best-fit values in the Table 4.1. The uncertainties of the spectral types obtained in this way are on average 2-3 sub-classes, also confirmed by the visual goodness of the fit to the spectra. We note that due to the uneven sampling of spectral types, the $\chi^2_{\rm red}$ maps do not represent the true $\chi^2_{\rm red}$. We also emphasise that our method of error assessment introduces a bias towards the values close to the borders of the adopted ranges and causes underestimation of the uncertainty on that side. Therefore, uncertainties for parameter values close to the border should be treated with caution.

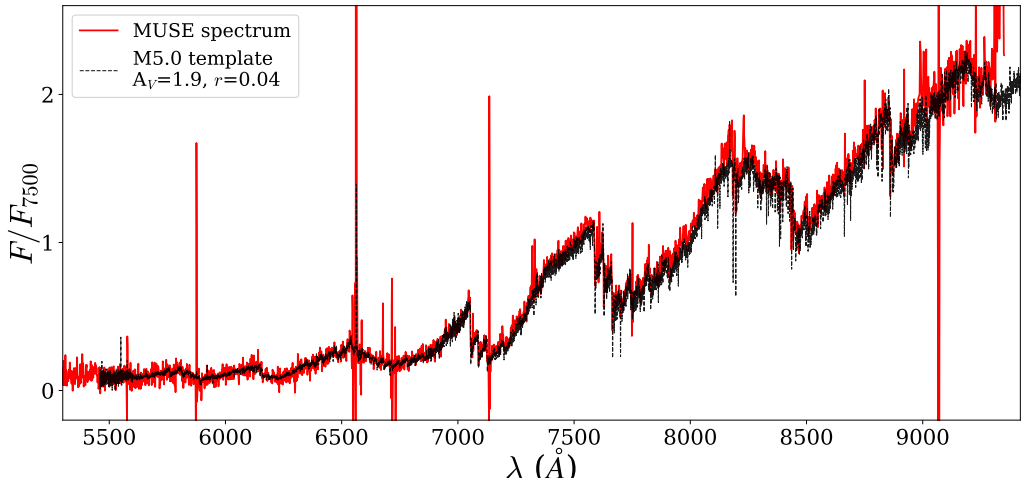

Figure 4.5: Example of a MUSE spectrum (red solid line) of an M-type star and the matching spectral template (black dashed line). Both spectra are normalised at 7500 Å.

4.3.3.2 K and late G-type stars

The prominent TiO and VO bands in the spectra of M-type stars fade away in mid-K-type stars, while the overall shape of the spectrum flattens. We identify hotter stars in our sample based on the equivalent widths (EWs) of selected absorption lines; we list them in Table A.6. We first calibrate the change of the EWs as a function of spectral type using the Class III templates (Sec. 4.3.3) assuming a linear correlation. For each line we adopt a single value of the uncertainty of our calibration based on the fit's uncertainty. Additionally, for late K-type stars we use the spectral index TiO (7140 Å) identified by Oliveira et al. (2003) and Jeffries et al. (2007) and add it to a pool of previous estimates. The final spectral type is assigned as a weighted mean of types from single EWs and indices. Similarly, the uncertainty of the spectral type is a weighted mean of the uncertainties assigned to all of the indices. A single index error is the root of the sum of the squared uncertainties on individual EW measurements and EW calibrations. The resulting values are listed in Table 4.1.

Once the spectral type is assigned, we perform an estimation of the extinction and veiling following the same approach used to classify the M-type stars (see Sec. 4.3.3.1). We fit to observed spectra the templates closest to the estimated spectral types varying A_V and r_{750}. The best values are those, for which the value of pseudo-χ^2_{red}, $\chi^2_{red,ps} = \chi^2_{red}/\min(\chi^2_{red})$, is minimum. The uncertainties of A_V and r_{750} are estimated based on $\chi^2_{red,ps}$ maps, similar to the procedure described in Sec. 4.3.3.1. Example of a MUSE spectrum of a K-type star with the matched template is shown in Fig. 4.6. We find 14 early M-, 339 K-, and 95 late G-type stars.

We note that the non-homogeneous sampling of the templates can cause an error on the estimates of stellar parameters that is hard to estimate properly (see the examples of χ^2_{red} maps in Appendix A.6). That applies not only to the spectral types, but also for extinction and veiling. However, for the lowest mass stars in our sample, the low snr dominates over any other source of uncertainty. For this reason, we do not interpolate between spectral types of templates to create a homogeneous grid. K-

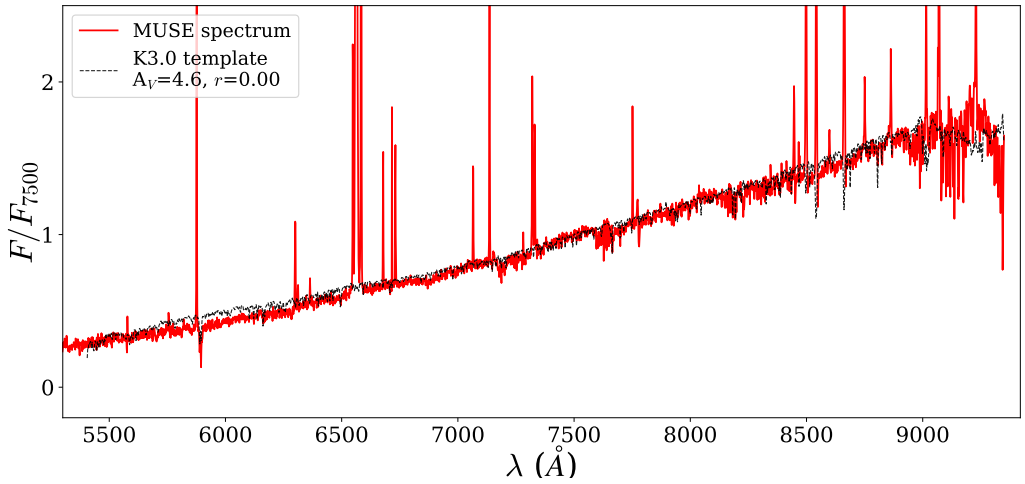

Figure 4.6: Example of the MUSE spectrum (red solid line) of the K-type star and matching spectral template (black dashed line). Both spectra are normalised at 7500 Å.

and G-type stars have on average smaller uncertainties of the spectral classification than M-type stars, since for these stellar types the estimate is based on absorption lines and is independent of the density of the grid sampling. A possible source of large error is the assumption of a linear correlation between the spectral types and EWs. Those relations are usually quadratic (e.g., CaI Herczeg & Hillenbrand 2014) or higher-order polynomial (e.g., Oliveira et al. 2003; Riddick et al. 2007). Overall, our estimations of spectral type are accurate within 2-3 sub-classes.

4.3.4 Extinction corrected colour-magnitude diagrams

As described in Sec. 4.3.2, the MUSE data presented here allow us to sample the stellar population in Tr 14 down to very low-mass stars. The observed CMDs shown in Fig. 4.4 indicate the presence of two populations. Here, after the accurate determination of the stellar parameters using the MUSE spectra (see previous Section) we reevaluate this using the extinction values derived for each individual star.

Based on measurements toward individual stars, we estimate the visual extinction towards the Tr 14. The medium value of A_V is 2.60 mag. In Fig. 4.7 we show the distribution of visual extinctions estimated in the previous sections. The distribution has a Gaussian-like shape, the fitted profile raises a centroid of 2.49 mag, consistent with the findings of Ascenso et al. (2007) and slightly lower with respect to the value reported by Beccari et al. (2015). Our distribution of A_V is quite broad with Gaussian width of 1.04 mag. On average, the uncertainties of individual A_V estimates are ~ 0.5 mag. We conclude that our measurements are in line with the literature values within uncertainties.

We use the estimated A_V to correct the observed magnitudes. We show de-reddened colour-magnitude diagrams in Fig. 4.8 together with the isochrones from the PARSEC v1.2S models (Bressan et al. 2012). The previously seen two populations are no longer apparent when the new extinction correction is applied, as expected for

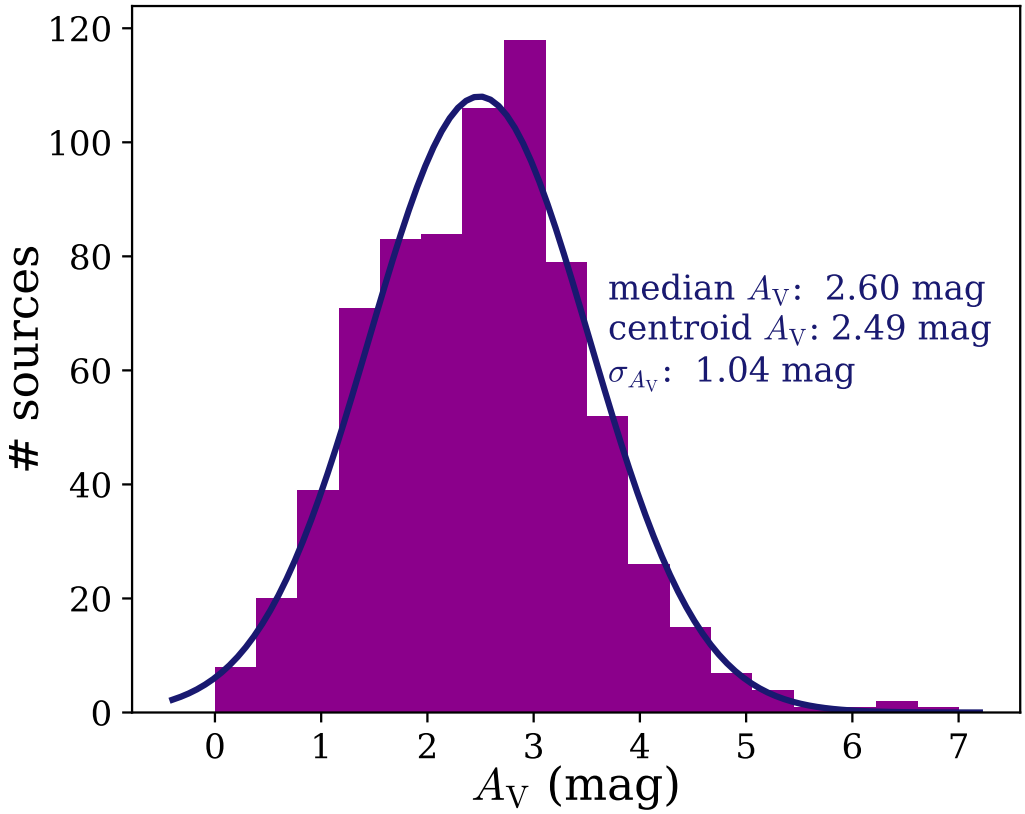

Figure 4.7: Distribution of A_V estimated for Tr 14 stars. Additionally, we fitted the Gaussian function to estimate the centroid of the distribution. Centroid, width of the distribution and median value in our sample is indicated in the upper right part of the figure.

differently obscured populations (Ascenso et al. 2007). This reassures us about the correctness of our procedure. The large scatter of points remains, we will discuss possible reasons in the following sections.

4.4 Physical parameters of the stars

4.4.1 Effective temperature and stellar luminosity

We derive the effective temperatures ($T_{\rm eff}$) of our stars based on their spectral types. For M-type stars we use the SpT – $T_{\rm eff}$ scale from Luhman et al. (2003) and for earlier types, we apply the scaling from Kenyon & Hartmann (1995) and interpolate linearly between the sub-classes. Newer scales, like e.g., from Herczeg & Hillenbrand (2014), agree well for low-temperature stars (types later K5). The scale adopted here deviates for the hotter stars up to 380 K in case of K0 stars in comparison to Herczeg & Hillenbrand (2014).

It has been shown in the literature that the J-band photometry is most suitable in deriving bolometric correction for young stars. The spectral energy distribution in these objects can be strongly affected by the presence of NIR excess due to the ongoing mass accretion from a protoplanetary disk or intrinsic differential extinction.

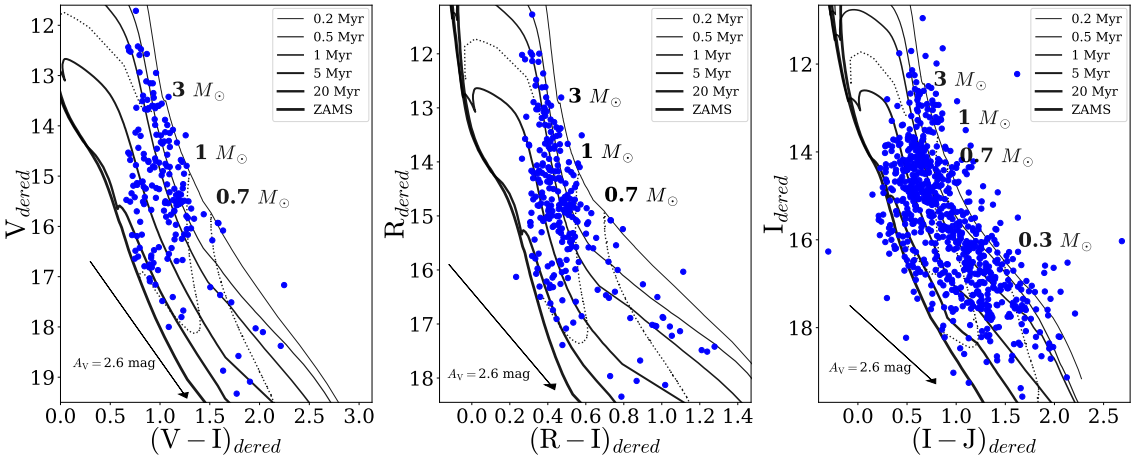

Figure 4.8: Colour–magnitude diagrams from MUSE broad-band filters images in V and I (left panel), R and I magnitudes (middle panel), and I and J magnitudes (right panel) corrected for individual extinction. J-band magnitudes are from the VISTA and HAWK-I observations. Reddening vectors in the lower left corners show reddening by a median value of A_V estimated for Tr 14. Solid lines show isochrones from 0.2 to 20 Myr (and ZAMS), dotted lines show isomasses of 0.3, 0.7, 1, and 3 $M_\odot$, as labeled (Bressan et al. 2012).

Such effects can not be fully avoided but are minimised using the J-band filter (e.g., Kenyon & Hartmann 1995; Luhman 1999). Our bolometric luminosities are hence calculated using the J-band photometry from VISTA (Preibisch et al. 2014) and HAWK-I (Preibisch et al. 2011a,b). Whenever magnitudes from both catalogues are available for a given star, we choose the one with smaller uncertainty. We first calculate the bolometric magnitude ($M_{\rm bol}$) dereddening the observed magnitudes by individual visual extinction determined from our spectral classification (Sec. 4.3.3) and estimating its value in J-band using extinction law from Cardelli et al. (1989), subtracting distance modulus and adding bolometric correction with colours, as indicated by the equation:

$$M_{\rm bol} = J - A_{\rm J} - {\rm DM} + ({\rm BC}_V + (V-K) - (H-K) - (J-H)) \qquad (4.2)$$

Values of the corrections and colours were taken from Kenyon & Hartmann (1995). Finally, to obtain the bolometric luminosity in $L_\odot$, we subtract from the previously estimated $M_{\rm bol}$ the solar bolometric magnitude $M_{\rm bol,\odot} = 4.74$ (Cox 2000):

$$\log\left(L_{\rm bol}/L_\odot\right) = -0.4 \cdot (M_{\rm bol} - M_{\rm bol,\odot}) \qquad (4.3)$$

The $L_{\rm bol}$ values thus calculated are listed in Table 4.1. There is only ∼1% of spectroscopically classified stars in our catalogue which were not matched with any source from the NIR catalogues and therefore do not have estimated stellar parameters. This might be due to the fact that NIR catalogues are not 100% complete.

The uncertainty of the stellar luminosity in our estimations is mostly driven by two factors: uncertainty of J-band photometry adopted from the VISTA and HAWK-I catalogs, and uncertainty of the extinction measured by us while performing the spectral classification of the each star (Sec. 4.3.3). The latter has significantly

greater impact: typical uncertainty of the J-band magnitudes used in this work is ∼0.03-0.05 mag, while the average A_V error is ∼ 0.5 mag, corresponding to $\Delta A_J \sim 0.16$ mag.

4.4.2 HR diagram and stellar parameters

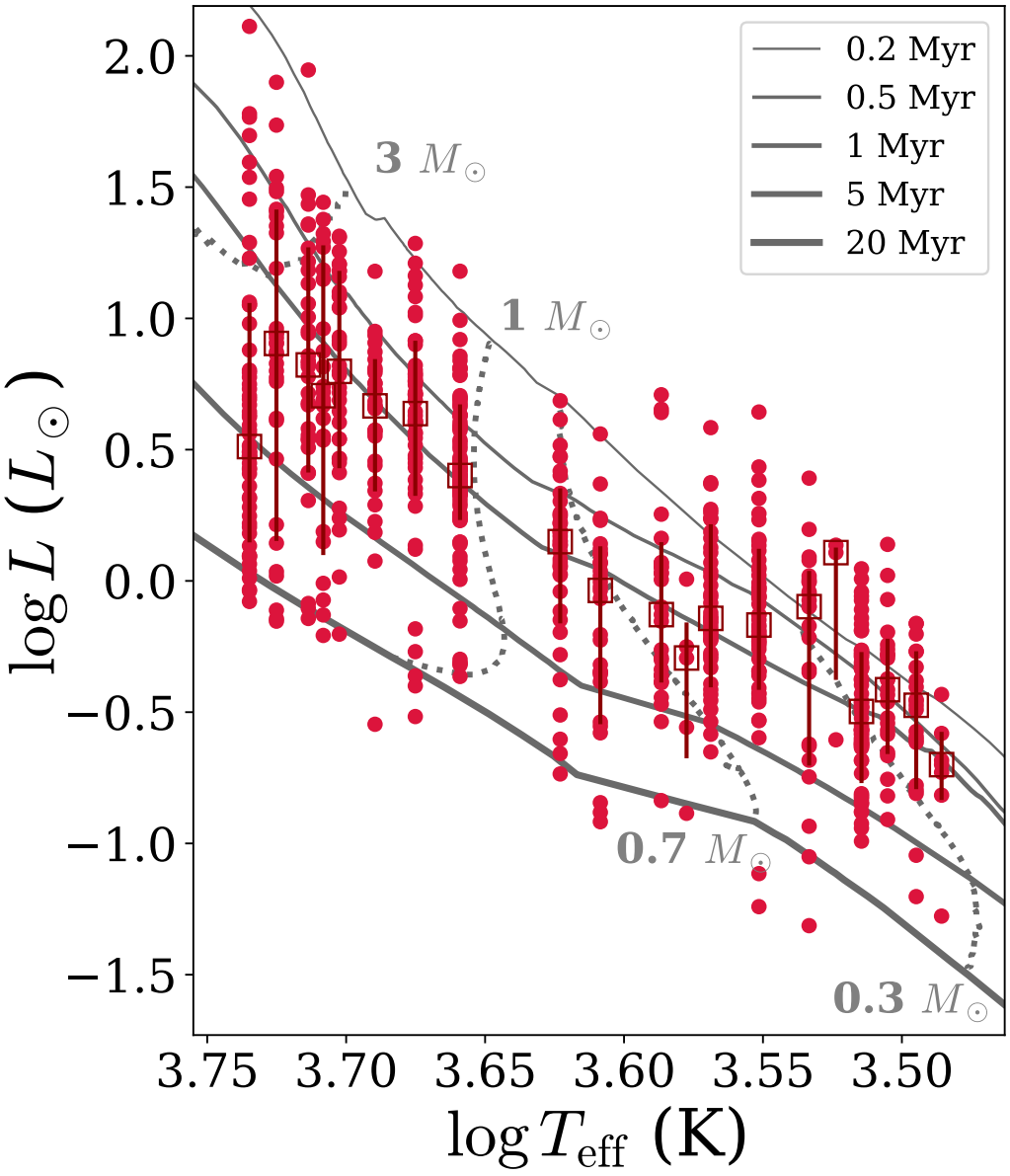

Figure 4.9: HR diagram for low-mass stars of Tr 14. Filled circles show data points, empty squares are median values of the bolometric luminosity for each spectral subclass with errorbars indicating 1-σ percentiles. Theoretical tracks from Bressan et al. (2012) are shown as solid black lines. Grey dotted lines show tracks for 0.3, 0.7, 1, and 3 $M_\odot$ stars.

In Figure 4.9 we show the bolometric luminosity as function of effective temperature. The stars detected with MUSE are shown with filled circles. The open squares represent the median luminosities for each spectral type. We show on the HR diagram the PARSEC v1.2S theoretical isochrones (Bressan et al. 2012). We assign the stellar masses and ages by performing linear interpolation between the tracks

and isochrones. The resulting values are listed in Tab. 4.1. For stars more luminous than predicted by the lowest age isochrone we assign the boundary value of 0.1 Myr as a stellar age.

The HR diagram (Fig. 4.9) shows the presence of a large spread of luminosities for sources with the same spectral type. Depending on the spectral type, the spread ranges from 0.5 to 2.0 dex. Possible explanations of this behavior are two-fold: observational and physical. Observational reasons for the spread cover uncertainties in estimations of stellar luminosity and / or effective temperature, as well as contamination from foreground sources. As we discussed in Sec. 4.4.1, the main source of luminosity uncertainty is the extinction, closely linked to the uncertainty of the spectral type (and thus $T_{\rm eff}$) and veiling. On average, the luminosity values are uncertain by ∼0.3 dex, temperatures by 300 K, and veiling by 0.1-0.3. Given the large distance to Tr 14 (2.35±0.05 kpc, Göppl & Preibisch 2022), we expect a significant contamination by foreground stars. In Sec. 4.3.1 we therefore used the *Gaia* DR3 catalogue to minimise this effect and remove objects in the foreground of Carina Nebula. However, the limited number of good astrometric measurements does not allow to identify all non-cluster members. It is then not trivial to estimate the contribution of foreground contamination to our results. This effect, combined with uncertainties in our measurements, can explain a large part of the observed luminosity spread in our HR diagram.

The physical sources of the luminosity spread include intrinsic age spread, variability, binarity, dispersion in distance, and accretion history. Episodic but vigorous accretion of low-mass objects at the very early stages of their formation (Class 0 – Class I) can leave its imprint on their evolution for the next few Myr (Baraffe et al. 2009). If most of the accreting kinetic energy is radiated away, the structure of the stars will be more compact (i.e., stellar radius will be smaller) than of the non-accreting star of the same age and mass. Short, intense and numerous accretion episodes do not leave enough time for the object to relax to a larger radius for the newly acquired mass. As a result, object has lower luminosity and seems to be older than non-accreting of the same $T_{\rm eff}$. Baraffe et al. (2009) found that episodic accretion at early stages of stellar evolution can well reproduce luminosity spread equivalent to an age spread of ∼10 Myr observed in Orion Molecular Cloud (Peterson et al. 2008). Moreover, the intrinsic spread of accretion rates in the cluster might add to the luminosity spread. In their estimates, Hartmann (2001) adopted arbitrarily an error of 0.1 in $\log L$ due to accretion (ignoring the effect of disk inclination). We use the J-band photometry to minimise the excess luminosity caused by the accretion (following Kenyon & Hartmann 1995). We also included veiling in our spectral classification. However, we made a very simplistic approach, where the veiling is independent of the wavelength.

Another physical process, that has a great impact on the luminosity of young stars is the photometric variability and to lesser extend, accretion variability. Usually, photometric variability is relatively small (e.g., ∼0.2 mag in J, H, K_s bands, see Carpenter et al. 2001) and has a timescale of less than a few days. It is very often assigned to the rotational modulation of cool or hot spots. Variability related to

accretion can span wide range of amplitudes and timescales. Typically, changes in brightness are lower than 1-2 mag and last few days (Fischer et al. 2023). However, some extreme cases were also spotted. For example, Claes et al. (2022) recently reported change by $\gtrsim$1.4 dex on accretion rate of XX Cha measured on UV excess and by $\sim$0.5 dex measured on lines (including Paβ in J-band) over a period of 11 years. Previous studies of accretion variability from photometry (e.g., Venuti et al. 2014) or spectroscopy (Costigan et al. 2012, 2014) recorded variability $<$0.5 dex at different-time scales (years, days, and minutes). If behaviour of XX Cha is more common for young stars than thought so far, it could explain a significant fraction of observed luminosity spread. The authors note also high photometric variability of the star in optical bands ($>$ 2 mag in B-band to $\sim$ 0.5 mag in I-band). Hartmann (2001) in their Taurus study adopted a variability of 0.1 mag to explain an observed luminosity scatter. While not negligible, this value alone cannot explain our observations.

A different source of uncertainty, which impact is difficult to predict, is the inclination of the accretion disk: stars with edge-on disks will appear significantly redder than face-on ones. For instance, Alcalá et al. (2014) suggested highly inclined disks as an explanation of the sub-luminosity of four young stars in Lupus. After correction for disk obscuration by a factor of 4–25 (corresponding to 0.4–1.4 dex) their accretion properties were well in line with those from other sources in the region.

Unresolved multiplicity has potentially a large impact on luminosity distribution, especially for young clusters, where the multiplicity fraction is observed to be higher than among the more evolved field stars (Duchêne & Kraus 2013; Zurlo et al. 2023). Multiplicity also scales with stellar mass, from $\sim$25% for M-type stars to almost 100% for OB stars (Duchêne & Kraus 2013; Zurlo et al. 2023). Zagaria et al. (2022) noted, that at lest 20% of all stellar systems in Lupus, Chameleon I and Upper Scorpius with measured disk masses and accretion rates are multiples. They all also have higher observed accretion rates than isolated stars. Similarly, Zurlo et al. (2020) found the fraction of binaries in Ophiuchus with separations from 9 to 1200 au to be 18%, whereas in Coronae Australis that number was estimated to be 36.2$\pm$8.8% (separations between 17 and 780 au, Köhler et al. 2008) and in Taurus is 37.4$\pm$4.6% (the same separation range, Leinert et al. 1993). Unresolved multiples appear brighter with respect to the single stars in the HR diagram mimicking younger age. Hartmann (2001) estimated this potential shift of luminosities to be $\sim$ 0.2 $\log(L_\odot)$.

The individual distances to the cluster members might also add to the observed spread. Here, we use the distance estimate of 2.35 ± 0.05 kpc based on *Gaia* EDR3 catalogue (Göppl & Preibisch 2022) for all sources in the field. We expect to include in that way both members of the Tr 14 and young stars from the dispersed population of CNC. Tr 14 has a compact core of radius of $\sim$0.6–0.7 pc with extended halo up to $\sim$3.4–5.3 pc (Ascenso et al. 2007; Kharchenko et al. 2013), much less than the distance uncertainty of 50 pc (note, that Ascenso et al. (2007) assumed distance of 2.8 kpc to Tr 14, here we re-scaled their results to 2.35 kpc). This error corresponds to an uncertainty of 0.05 dex in luminosity and cannot explain the scatter of estimated

values. Similarly, the dispersion in distances to the different clusters in Carina of 2% (Göppl & Preibisch 2022) is too small to explain observed scatter. Therefore, we neglect any impact from the distance spread on the luminosity dispersion.

Summarising, we conclude that the luminosity spread is mostly caused by large uncertainties of photospheric parameters, contamination of non-cluster members, accretion and photospheric variability, and unresolved multiplicity. Other parameters, like internal spread of stellar ages, accretion properties, individual distances might play a role, but their impact is smaller.

4.4.3 Age of Trumpler 14

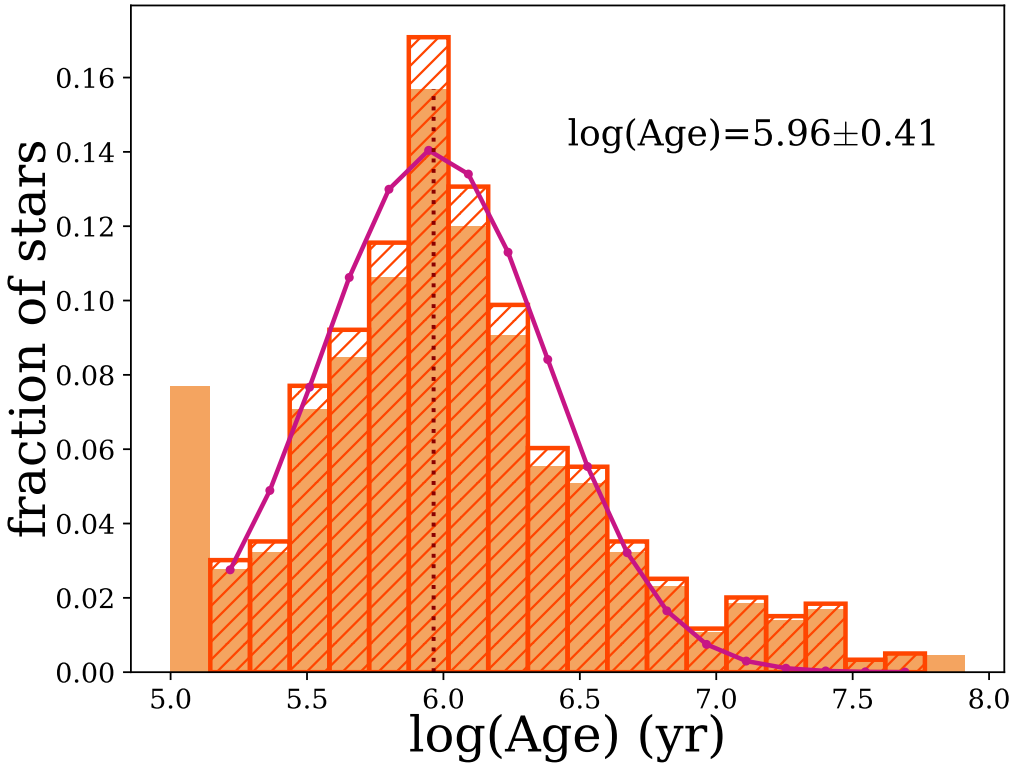

Figure 4.10: Fraction of stellar ages derived from HR diagram for stars with $\log(T_{\rm eff}) < 3.73$. Filled orange histogram shows distribution for the whole sample, while hatched red histogram represents the fraction distribution after removing the extreme bars with respect to the total number of stars within the new age range. The normal fit to the probability density distribution converted into the fraction distribution for the visual purposes is shown as a dark violet curve with mean value of $\log(\text{age}) = 5.96 \pm 0.41$ corresponding to the $0.9^{+1.4}_{-0.6}$ Myr.

The YSOs plotted in Fig. 4.9 concentrate near the 1 Myr isochrone strongly suggesting a young age of the cluster. Here, we look more closely into the distribution of stellar ages in Tr 14.

Figure 4.10 presents the distribution of fraction of the stars within each age bin in logarithmic scale. Only measurements for stars with $\log(T_{\rm eff})$ <3.73 are included in the distribution. Ages were estimated based on PARSEC evolutionary tracks (Bressan et al. 2012, see Sec. 4.4.2). The lowest stellar ages provided by the models

are 0.1 Myr. Some of our sources lay above this isochrone on HR diagram. Since we do not extrapolate stellar parameters beyond theoretical models, those sources have a fixed age of 0.1 Myr causing an artificial overdensity in the first bin of the age distribution in Fig. 4.10. Therefore, to estimate the cluster age, we excluded from this analysis the boundary bars. We fit the lognormal profile to the remaining distribution, as shown in Fig. 4.10. The fit peaks at the logarithm of 5.96±0.03, which we interpret as a cluster age, with the width of 0.41±0.02, which we adopt as an uncertainty. In linear scale that corresponds to the age of Tr 14 of $0.9^{+1.4}_{-0.6}$ Myr.

We check how conclusion on the cluster age is impacted when using different set of models. Therefore, we employ tracks from Baraffe et al. (2015) for low-mass stars (spectral types later than K5), and since they are limited to the solar-mass stars, for hotter stars we employ tracks from Siess et al. (2000). We present HR diagram, stellar properties, and comparison between those two set of tracks in Appendix A.7. Those stellar parameters (M_* and age) are also listed in Table 4.1 and A.3. Use of different models changes values of parameters for individual stars, but do not affect our conclusion on cluster age. We perform the same exercise as described above for a distribution of stellar ages based on Baraffe et al. (2015) / Siess et al. (2000) evolutionary tracks. The normal fit indicates cluster age of $\log(\text{age}) = 6.16 \pm 0.31$, corresponding to $1.4^{+1.5}_{-0.7}$ Myr, consistent within errors to the previous estimate. Stellar, and hence cluster, ages around 1 Myr are difficult to infer precisely. We adopt that the age of Tr 14 is ∼1 Myr. This is a robust result (given uncertainties related to differences in models and internal uncertainties of observations) since the estimate is not affected by the choice of evolutionary tracks.

The large spread in the HR diagram seen in Tr 14 lead in the past to conclusions of long, continuous star formation over last 10 Myr (DeGioia-Eastwood et al. 2001b; Povich et al. 2019), 1–6 Myr (Tapia et al. 2003), or 5 Myr (Ascenso et al. 2007). While comparing different clusters in Carina, Damiani et al. (2017) stated that Tr 14 is younger than Trumpler 16, similarly to Smith & Brooks (2008) who found the age difference of 1-2 Myr between these two clusters. More precise estimates indicate a Trumpler 14's age of 2±1 Myr (Preibisch et al. 2011b). Rochau et al. (2011) found a recent (1.0±0.5 Myr) starburst-like event and hint of the presence of an older (3 Myr) population in Tr 14, which might be part of the dispersed population of CNC. Overall, our estimate is in line with general findings in literature. Our measurements also show a large spread of isochronal ages, which is a direct consequence of the luminosity spread. In the previous section (4.4.2) we listed several possible sources responsible for the spread in luminosity within the stellar population of Tr 14, with the uncertainty of the parameters estimated during spectral classification expected to have the strongest impact. It is important to note, that the aforementioned studies were mostly focused on massive and intermediate-mass stars ($\gtrsim 1 M_\odot$), while here we do not analyse stars hotter than ∼5500 K.

Additionally to the spread, Fig. 4.9 shows also decrease in median luminosities toward hotter stars and deviation from ∼1 Myr isochrone with the last temperature bin above $\log(T_{\rm eff})$ ∼3.73 exhibiting significant drop in luminosity. This behaviour can be caused by our selection bias as we focus on low-mass objects and do not

identify in this work stars with spectral classes earlier than G8. This might result in the apparent 'older' population of hotter stars. Hartmann (2003) noted a similar trend in Taurus star-forming region. Stars colder than 4350 K (corresponding to the masses below $\sim$1 $M_{\odot}$) had an age distribution strongly pointing to the values <2 Myr, while hotter stars exhibited flat distribution spanning up to 22 Myr (Hartmann 2003, see their Fig. 1). If we divide the age distributions into the same $T_{\rm eff}$ ranges, we do not see such a strong behavior, both sub-samples peak around 1 Myr, although we note that the youngest stars ($\leqslant$0.15 Myr) are among those with $T_{\rm eff}$<4350 K. Hartmann (2003) argued, that the flat distribution of hotter Taurus members is due to the highly inaccurate positions of birth line for the more massive stars, as well as non-member contamination. Similarly, Fang et al. (2017) showed that cluster ages are higher when derived from luminosities and temperatures of hotter stars. The behaviour hold for different theoretical models and different young clusters. This effect can also impact our results.

Our observations span prominent, dense and compact cluster core (r $\sim$0.5′–0.9′, Ascenso et al. 2007; Kharchenko et al. 2013) and extended area around. The widely dispersed population of Carina Nebula Complex members (Feigelson et al. 2011; Zeidler et al. 2016) is mixed in our observations with the Tr 14 members causing the apparent age spread. We investigate that possibility below.

In Fig. 4.11 we mark the "core" area with radius 0.9′ and compare it to the location of our sources. We do not detect many sources in the most central area due to the spectral contamination. We investigate whether the stars inside the core have different properties than the population at larger radii from the cluster center. Figure 4.12 shows de-reddened CMDs where sources inside (left panel) and outside (right panel) the radius of 0.9′ are marked with red hexagons. The core population of Tr 14 is mostly concentrated around 1 Myr isochrone. Although the extended, "halo", population exhibits larger spread in colours and ages, most of the stars are also located around 1 Myr isochrone. There are more faint stars in the latter group which are affected by the higher observational uncertainties. It is likely that the "halo" population is a mixture of young Tr 14 members and the older widely distributed population of the whole Carina Nebula Complex. Since the widely distributed population of young stars in the CNC exhibits a range of ages between <1 Myr and $\sim$8 Myr (Preibisch et al. 2011a), it is not possible with the available data to distinguish between Tr 14 members in the outer parts of the cluster and stars from the distributed population.

We additionally check the spatial distribution of young stars using the Li I 6708 Å absorption line. In the Figures 4.11 and 4.12 the stars where Lithium was detected are marked with blue crosses. We do not find any specific concentration in the cluster of those stars but they all follow the <10 Myr isochrones, as expected for Lithium-bearing stars. We note similar behaviour for NIR excess or X-ray emitting sources (see Appendix A.8). We conclude that in our dataset, where the most central core part is saturated and we can not characterise most of the stars located there, the true, young members of Tr 14 are distributed evenly across the cluster. However, our

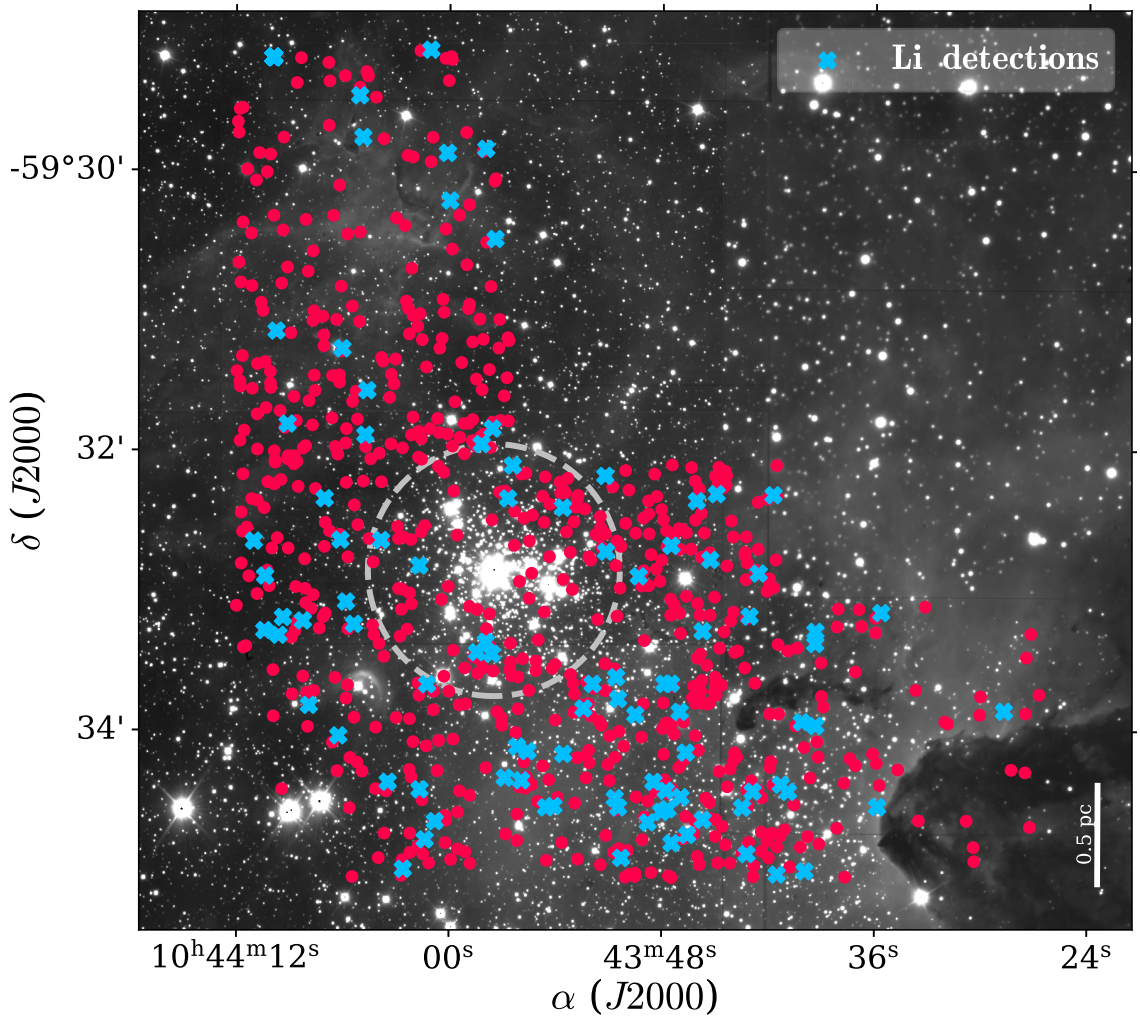

Figure 4.11: Locations of the Li 6708 Å detections in the MUSE field blue crosses). All stars studied here are marked with red dots, as in Fig. 4.1. The dashed circle with radius of 0.9′ shows the core of the Tr 14, as defined by Kharchenko et al. (2013). The background image in grey scale is the *H*-band image from HAWK-I (Preibisch et al. 2011a,b).

sample contains also number of stars from the widely distributed Carina population. We are not able to distinguish between the true and apparent Tr 14 members nor to confirm the cluster membership of older stars.

4.4.4 Mass distribution

Whether the environment can affect the initial mass function (IMF) of the stellar cluster was investigated in multiple studies. For example, Damian et al. (2021) studied low-mass stars in eight young clusters (∼2-3 Myr) observed in J and K-band spanning wide range of FUV radiation levels, cluster densities, and galactocentric distances. Their log-normal IMFs (Chabrier 2003) agreed well within each other peaking within the range 0.2–0.4 $M_{\odot}$ and not revealing any dependence on any of the three environmental properties. On the other hand, De Marchi et al. (2010b) suggested that the present-day characteristic mass of the IMF is significantly correlated with the dynamical age of the cluster.

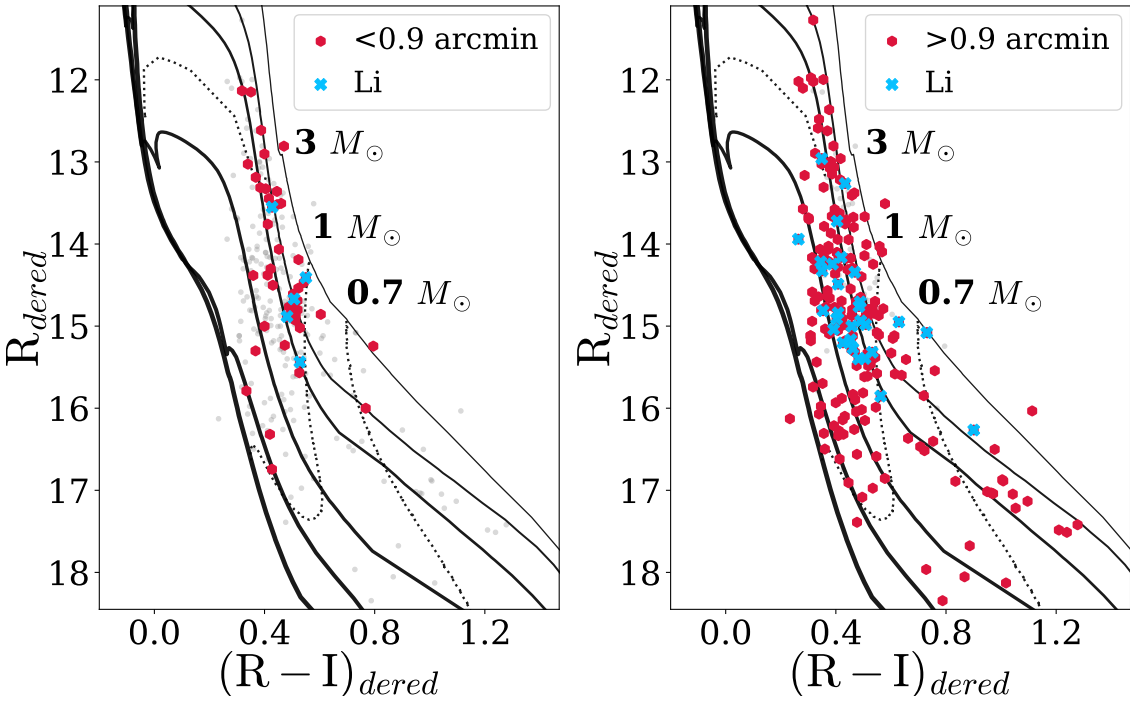

Figure 4.12: Colour-magnitude diagrams for de-reddened R and I-band magnitudes from MUSE. Red hexagons mark stars within the core of Tr 14 (left, 0.9′, Kharchenko et al. (2013)) or outside (right). The blue crosses indicate location of the Lithium-bearing stars on the CMDs within and outside the core radius, respectively. Plotted are the same tracks as in Fig. 4.8.

There is no study dedicated to investigate the impact of high FUV field on the IMF in the Carina Nebula. Only Rochau et al. (2011) tried to look at the mass function in the closest vicinity of the massive stars in Tr 14, but they could not draw any binding conclusions on their impact onto neighbouring stars. Similarly, Rainot et al. (2022) studied low-mass companions in the vicinity of seven O-type stars with VLT/SPHERE in K-band. Despite the found differences between their IMF and the one from Rochau et al. (2011) or Chabrier (2003), they could not robustly confirm if the presence of the massive stars impacts their neighbouring companions or if the noticed differences are due to the observational bias. Former IMF studies in Tr 14 (e.g., Ascenso et al. 2007; Hur et al. 2012) were also based mostly on NIR photometry, up to date there is no study employing spectroscopy in Tr 14 to investigate the stellar mass distribution.

Our work focuses on low-mass stars with spectral type later than G8. Figure 4.13 presents the distribution of stellar masses estimated based on MUSE observations in Tr 14 for stars with $\log(T_{\rm eff})$ below 3.73. The shown masses range from 0.17 to 2.08 $M_\odot$. The presented distribution is not an IMF as we did not correct for the photometric incompleteness. As we discussed in Sec. 4.2.3, completeness of our catalogue is affected by crowdness in the cluster core, presence of bright stars, and highly variable nebular emission. According to the J-band magnitudes distribution in Fig. 4.2, we reach 50% completeness level at 15.5 mag corresponding to 0.8 $M_\odot$ at 1 Myr (Bressan et al. 2012; Baraffe et al. 2015). However, if we include detections excluded from our catalogue due to the variable background emission, the 50% completeness level is already achieved at 18.5 mag (equivalent of 0.1 $M_\odot$), demonstrating

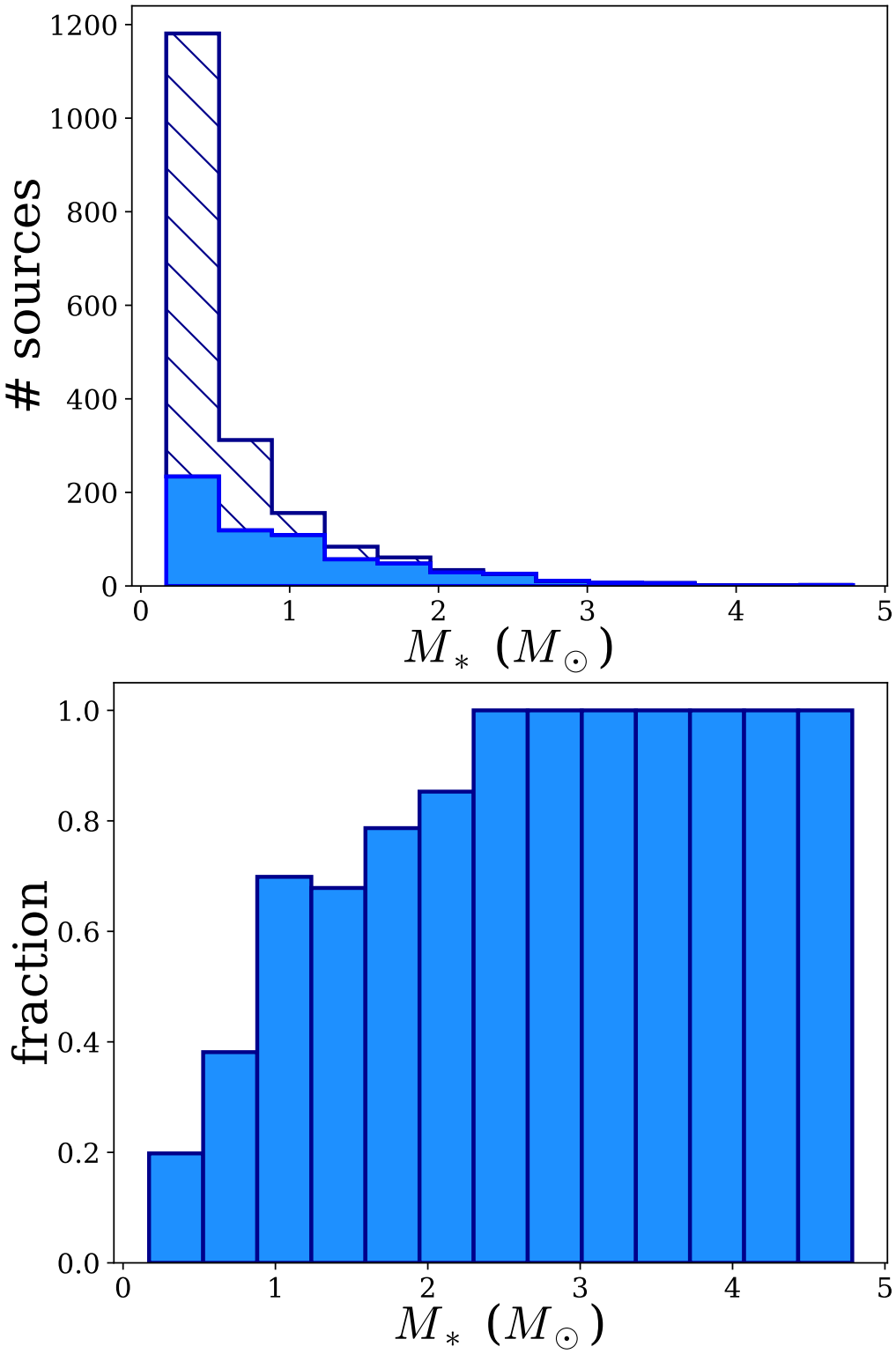

Figure 4.13: Distribution of stellar masses in Tr 14 for stars with $\log(T_{\rm eff}) < 3.73$. Top: filled histograms presents distribution of masses for stars analysed in this paper. On top of it (hatched histogram) we display the distribution of the probable members with uncertain photometry removed from the analysis due to the high variability of the background emission. As expected, most of the removed stars are faint, low-mass objects. Bottom: fraction of stars in the final spectroscopic catalogue within each mass bin relative to the combined catalogues of final sample and probable members with uncertain photometry due to the variable background emission. Bins are the same as in the upper panel.

the depth and value of our MUSE data. In the second panel of Fig. 4.13 we show the fraction of stars in mass bins in the final (clean) catalogue in comparison to the sample without applying the background cut (Sec. 4.2.2.4). In the mass range below $\sim$0.8 $M_{\odot}$ more than 50% detections are missing due to our conservative approach to the background contamination. At the same time, none of the stars with masses $\gtrsim$2.3 $M_{\odot}$ is removed due to the high background variation. In Table A.3 we list targets with uncertain photometry and their stellar parameters, where available. Removing the lowest-mass stars from our catalogue prevents us from constructing an IMF estimate and identifying the characteristic mass of the Tr 14 population. More than half of the stars with masses <0.8 $M_{\odot}$ are removed from the final catalog due the highly variable background (Fig. 4.13) but the proper completeness analysis is beyond the goal of this work. We note however, that when using combined set of Baraffe et al. (2015) and Siess et al. (2000) evolutionary tracks, the distribution of masses is similar, although stellar masses extend only up to 4.1 $M_{\odot}$. While the global picture of stellar mass distribution in Tr 14 is not affected by the choice of evolutionary models, the individual values can be different even by a factor of few, especially for the least massive objects. This illustrate how challenging it is to derive accurate properties of young, low-mass stars.

The (in)variance of the IMF in the high FUV environment is also outside the scope of this paper. Future work addressing this problem needs first to resolve the completeness issue. Including more massive stars will allow investigating the slope of the mass function in the high-mass end. More sophisticated approach to the estimation of the background emission may allow including significantly more low-mass stars and with that testing the breaking point of the Kroupa-like IMF or characteristic mass of log-normal IMF. High-spatial-resolution observations (e.g., with adaptive optics) of the very center of Tr 14 can help resolving the inner core region. Brown dwarfs and very low-mass members of Tr 14 can only be well spectroscopically characterised by the NIR IFU instruments, like VLT/KMOS, VLT/ERIS, JWST/NIRspec, or future ELT/HARMONI.

4.5 Summary and conclusions

In this work, we presented the first optical spectroscopic study of low-mass stars in Tr 14 based on IFU observations from VLT/MUSE. We identified targets and extracted photometry and spectra using `SExtractor`. We excluded from the catalogue all sources with uncertain photometry. Specifically, the most significant cut (of 1868 sources) was related to the highly variable in spatial dimension emission of the HII region in Carina Nebula. At the end, our catalogue consists of 780 stars. We make available both catalogs, with robust and uncertain photometry for possible future follow-up studies.

Most of our sources have photometric measurements from NIR (99%) and optical (76%) catalogs, and almost 40% were detected in X-rays. We performed the spectral classification using spectra of Class III stars from Manara et al. (2013, 2017) as templates. Together with spectral type we estimated visual reddening and constant

veiling of 717 stars. We converted the spectral types to the effective temperatures and used J-band photometry to calculate bolometric luminosities. We placed our stars in the HR diagram and by the comparison to the theoretical evolutionary tracks (Bressan et al. 2012) we estimated the stellar masses and ages. Based on the distribution of stellar ages we estimate the cluster age of ∼1 Myr. This result is maintained even when using different evolutionary models (Siess et al. 2000; Baraffe et al. 2015). Majority of our stars (51%) have mass below 1 $M_{\odot}$, while the least massive object has estimated mass of 0.17 $M_{\odot}$.

Massive star-forming regions represent the most common environment in which the stars form in the Galaxy. This environment differs from those seen in the solar neighbourhood and therefore necessitates for extension of the studies of the more distant regions. Those examinations are however challenging due to the large distance to the cluster, often high extinction, and high stellar crowding. This is particularly difficult for spectroscopic observations. Here, we presented that those kind of explorations are feasible with IFU spectrographs like VLT/MUSE. Low-mass stars are the most common in the Galaxy but at the same time the most vulnerable to the environmental conditions. Presented here stellar characteristics of the few hundreds of low-mass stars provide a step into the better understanding of formation and early evolution of low-mass stars in the massive cluster. This study set up a base for the follow-up investigation of the protoplanetary disk population response to the high FUV field in the cluster that will be presented in the consecutive paper. (Chapter 6)

Chapter

Alternative method of spectral classification

5

This chapter is based on work carried out in collaboration lead by Da Eun Kang. The first part (Sec. 5.2) has been published by Kang et al. (2023b) and was included in the PhD thesis of Kang (2023). The second part (Sec. 5.3) is a work in preparation (Kang et al. 2023c) that will be submitted to A&A later this year. My contribution to the projects encompassed preparation of the sample of Class III templates and adapting original spectra to the purpose of the project; preparation the MUSE / Trumpler 14 sample: selection of the sources, dividing the sample into subgroups, preparation of the spectra and of the catalog of stellar parameters; preparation of list of spectral regions important for standard spectral classification or containing emission lines; preparation and application of the procedure of veiling and reddening the spectra; writing parts of the manuscripts. Here, I report the main results of the collaboration and give a brief overview of the method used.

5.1 Neural networks

The (artificial) neural networks are one of the machine learning techniques. Their structure mimic the way biological neurons transmit the information to each others what gave them their name. The NN are composed of multiple layers: input, output, and several hidden layers where the data are processed. Each layer is connected through an 'artificial neuron' which have an associated weight. During the training, the network fine-tunes those weights trying to reproduce the expected output based on a given input. Once the network learns, it can process large amount of data at the very high speed (with short computation time) and is therefore an efficient machine for image, speech, and language processing.

The volume of astronomical data is increasing exponentially with the time (Smith & Geach 2023) creating a difficulty to analyse them thoroughly with the 'classical', human-supervised methods. This creates a need to develop more efficient approaches for data analysis. Additionally, there might be correlations hidden in the datasets that might be very hard to discover using traditional ways of analysing the data. Machine learning techniques can offer a solution to both issues. Specifically, artificial neural networks are being commonly applied to the wide range of problems. They have been used to estimate a photometric redshift (Tagliaferri et al. 2003), classify the galaxies on photometric images (Hayat et al. 2021), characterise properties of

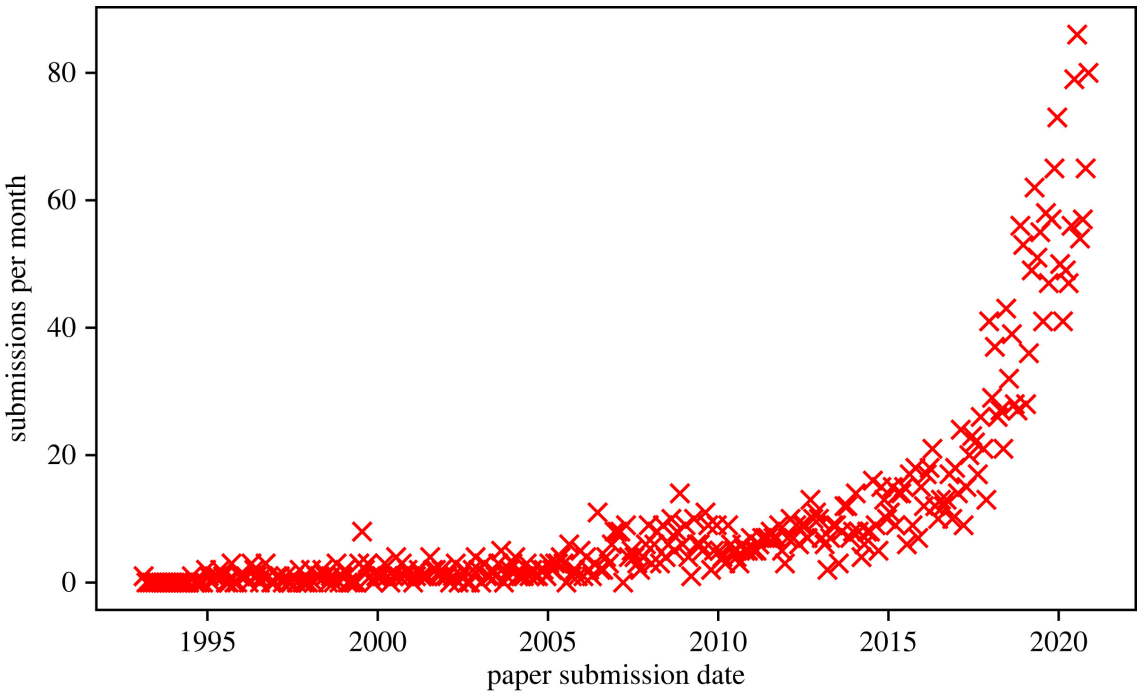

Figure 5.1: Number of submitted to `arXiv` astronomical papers employing machine learning techniques per month. This inlcudes any manusripts with keywords: 'ML', 'machine learning', 'AI', 'artificial intelligence', 'deep learning', or 'neural networks'. Credits: Smith & Geach (2023).

exoplanets (Haldemann et al. 2023), young stellar clusters (Ksoll et al. 2020), or study emission lines in HII regions (Kang et al. 2022). The number of astronomical papers using machine learning techniques exploded recently (see Fig. 5.1, Smith & Geach 2023) and it is expected that this trend will remain.

In Kang et al. (2023b) and Kang et al. (2023c) we use a conditional Invertible Neural Network (cINN) architecture (Ardizzone et al. 2018, 2019) named GLOW (Kingma & Dhariwal 2018). This deep learning technique is well-suited for solving inverse problems like recovering the physical properties from a set of observables. In order to do so, the cINN approach introduces a set of unobservable, latent variables with a known, prescribed prior distribution to the problem. The invertibility of the cINN architecture is achieved by chaining the conditional affine coupling layers (11-16 in our case) which perform transformations on the halves of the input that are easily invertible. Advantage of use of the cINN architecture is the treatment of observations as condition allowing for they arbitrarily large size.

5.2 Validation of the method

The main goal of the project is to classify and derive photospheric parameters of young, low-mass PMS stars from medium- to low-resolution optical spectroscopy. Our target instrument is MUSE which can provide hundreds of stellar spectra within single pointing and therefore can be applied to the surveys studies.

We employ the cINN architecture (Sec. 5.1) and train it on three Phoenix libraries of theoretical spectra: the NextGen, Dusty, and BT-Settl (Allard et al. 2012; Husser et al. 2013; Baraffe et al. 2015). Those libraries have different ranges of applicability of stellar parameters, as well as different treatment of internal physics (see Allard et al. 2012, for details and discussion on model differences). The networks resulting from the three training sets are later referred to as NextGen-Net, Dusty-Net, and Settl-Net, respectively. The employment of theoretical spectra instead of the observed ones is due to the insufficient number of available well-characterised and with high snr spectra (the required size for training set is few tens of thousands data points).

With the application goal in mind (low-mass PMS stars observed with moderate spectral resolution), we do not use the full range of available stellar models. We restricted our training set (at maximum) to the $2600 \leq T_{\rm eff} \leq 7000$ K, $2.5 \leq \log g \leq 5.0$, and $0 \leq A_{\rm V} \leq 10$ mag, which well reflects parameters of stars we want to classify. The Dusty models are dedicated to the brown dwarfs and low-mass stars, therefore their temperature range is limited to the 4000 K. Since the model spectra have higher resolution, we convolved them to the MUSE resolution using a Gaussian kernel and resampled to match the MUSE wavelength coverage. The spectra are normalised to the total flux in the MUSE spectral range. We create three samples of ∼16 000 synthetic spectra, one for each library. Spectra span the previously defined ranges of $T_{\rm eff}$, $\log g$, and $A_{\rm V}$ sampled randomly across the parameter space. That required interpolation between available spectra in the library. We interpolated linearly first between temperatures in logarithmic scale, then between surface gravities. Extinction was added afterwords with randomly selected $A_{\rm V}$. We adopt the Cardelli et al. (1989) extinction law and $R_{\rm V} = 4.4$, characteristic for Carina (Hur et al. 2012). For each library, the 80% of extracted spectra were used as a training set corresponding to the 3×13 107 test models; the rest are used for validation. Validation tests showed that cINN has learnt well the physics hidden in the models and can be applied to the observations (see for details of validation test Sec. 5 in Kang et al. 2023b).

The trained and validated networks were applied to the 36 spectra of well-known Class III stars observed with VLT/X-Shooter and characterised by Manara et al. (2013); Stelzer et al. (2013); Manara et al. (2017). Those spectra were used in Chapter 4 as templates for spectral classification and additionally exhibit low to zero extinction, they have been dereddened before analysis. Since they have high signal-to-noise ratio and their parameters are robust, we first use them to check the performance of the cINN before applying to the Trumpler 14 dataset. All three networks were applied to Class III stars and all predict very well the effective temperature within the applicable range. Also surface gravities agree with the literature values but with larger scatter. This is expected as the MUSE spectral resolution is not high enough to allow accurate measurements of gravity. $A_{\rm V}$ values deviate for coolest stars in all three networks (<3400 K). The $A_{\rm V}$ discrepancy is maximum 3 mag for Settl-Net and Dusty-Net, the NextGen-Net gives predictions different by $\lesssim$3.3 mag in that temperature range and has an average relative error at least 1 mag larger than the other networks. Discrepancies in $A_{\rm V}$ might be partially due to the fact,

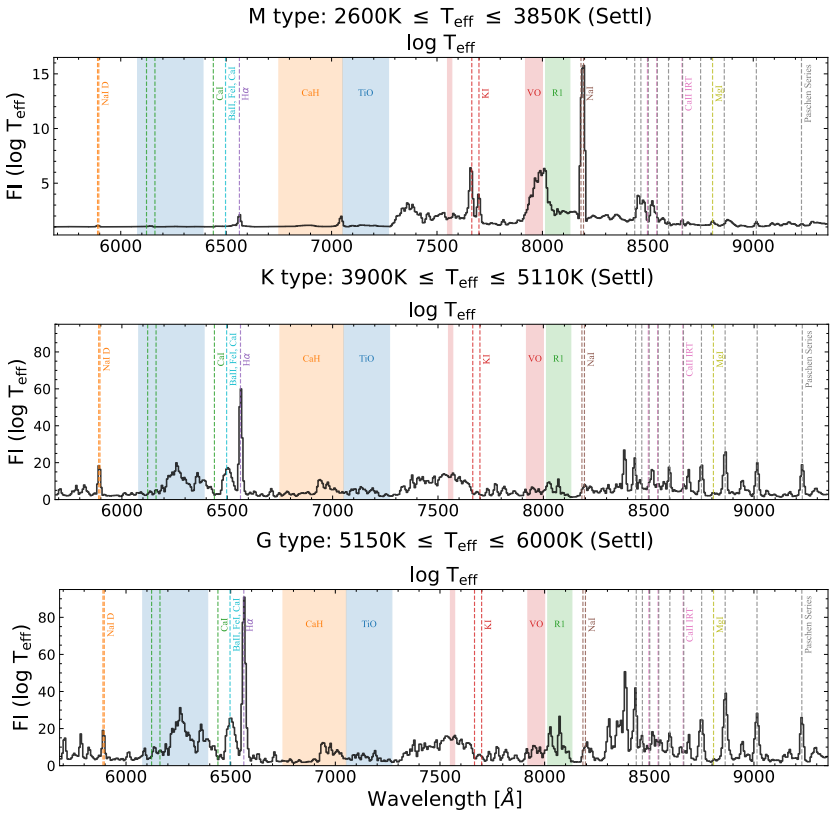

Figure 5.2: Feature importance for deriving $T_{\rm eff}$ by cINN as a function of wavelength. The whole sample is divided into three temperature groups corresponding to the M-type (**top panel**), K-type (**middle panel**), and late G-type stars (**bottom panel**). Colour shaded areas mark lines and molecular bands most frequently used for spectral classification. Reproduced from Kang et al. (2023b).

that Class III stars have close to zero extinction, which is a border condition in the training parameter space. The overall goodness of performance is confirmed also by re-simulated spectra using stellar parameters estimated by cINN.

We tested which of the 3 spectral libraries gives the best performance of the cINN. We found out that the Settle-Net gives overall the best results and reaches the peak of performance for M6.5-K1.0 (2935-5000 K) stars. The NextGen-Net performs acceptably for M4.5-K1.0 (3200-5000 K) stars. The Dusty-Net, as expected from the design of the models, has the best performance from the 3 models for cool stars (<4000 K) and this performance is significantly better for stars $T_{\rm eff}\lesssim$3000 K. Overall, the networks provide reliable predictions for all stars within an error of 5–10%, especially for temperature and surface gravity. Predicted extinction has similar accuracy for stars with $T_{\rm eff}$>3200 K. Deviation for extinction estimation for cooler stars we interpret as a result of simulation gap, the differences between theoretical models and observations. The simulation gap appears to be the largest for Dusty models, while the smallest - for BT-Settl ones, being the one more argument favouring this set of theoretical spectra above others.

Particularly interesting finding of the study is the consistency between cINN and traditional classification in terms of the use of spectral features. Traditionally, spectral classification is performed measuring the depth of spectral absorption lines or molecular bands. We wanted to understand which parts of the spectrum cINN considers as important for assessing the three parameters: $T_{\rm eff}$, $\log g$, $A_{\rm V}$, and whether those features agree with those used in traditional classification. Since spectral bins are not necessarily independent from each other, instead of analysing the importance of each of them, we grouped each 10 of them together with the step of 5 bins. The group width corresponds to 12.5 Å. Then, we were randomly changing flux values in each group consecutively. We run the classification again and assessed the so-called permutation feature importance, a quantity that measure how much the results differ from the original assessment (Breiman 2001; Fisher et al. 2019). The higher the value, the more important is the spectral window for derivation of a given parameter. Since in our sample of stars the spectral features that were used for classification (Itrich et al. 2023b) change with $T_{\rm eff}$, we divided the whole sample into three temperature ranges: <3900 K, between 3900 and 5150 K, and >5150 K, and evaluate importance of features separately for all model sets. Figure 5.2 shows comparison of feature importance (IF) for estimating $T_{\rm eff}$ in different temperature ranges for BT-Settl models. The most important line in case of M-type stars is the NaI doublet 8183, 8195 Å, then the VO molecular band at $\sim$ 7950 Å, and KI lines at 7665, 7699 Å. For K-type stars the dominant role has Hα, followed by lines from Paschen series and NaI. Similar behaviour is seen for the hottest stars. These results show that the features on which our networks rely to determine parameters vary depending on the intrinsic parameters of the object. The largest change occurs at ∼3900 K, as expected. The relatively low importance of molecular bands for the coolest objects might be however a bit surprising. On the other hand, the gravity-sensitive lines were captured by the network (e.g., NaI, KI Riddick et al. 2007; Herczeg & Hillenbrand 2014; Manara et al. 2017). This confirms that even though we do not exactly know how cINN learns the hidden rules from the training data, but is very close to our physical knowledge.

5.3 Application to the Trumpler 14 in Carina

Having well-tested and well-performing neural networks (Sec. 5.2, Kang et al. 2023b), we can now apply them to the MUSE observations of Trumpler 14 presented in Chapter 3 and analysed in Chapter 4. However, the Class III stars to which we applied the networks so far have very high signal-to-noise ratios, low $A_{\rm V}$, and no veiling, which is not the case for spectra used here. Trumpler 14 is located ∼10 times further away than Class III stars, what corresponds to the 10^2 weaker flux from the same star. Thanks to the deep integration times, we were able to characterise stars down to ∼0.2 $M_{\odot}$ in Itrich et al. (2023b). Nevertheless, extracted spectra are of low snr. That obliges us to consider the observational error in the cINN estimates. We apply therefore a so-called Noise-Net from Kang et al. (2023a). Since the spectral classification of Trumpler 14 stars was performed estimating simultaneously also $A_{\rm V}$ and veiling, to have consistent results and be able to compare with the classical approach, we need to add this parameter to the networks. We follow the same

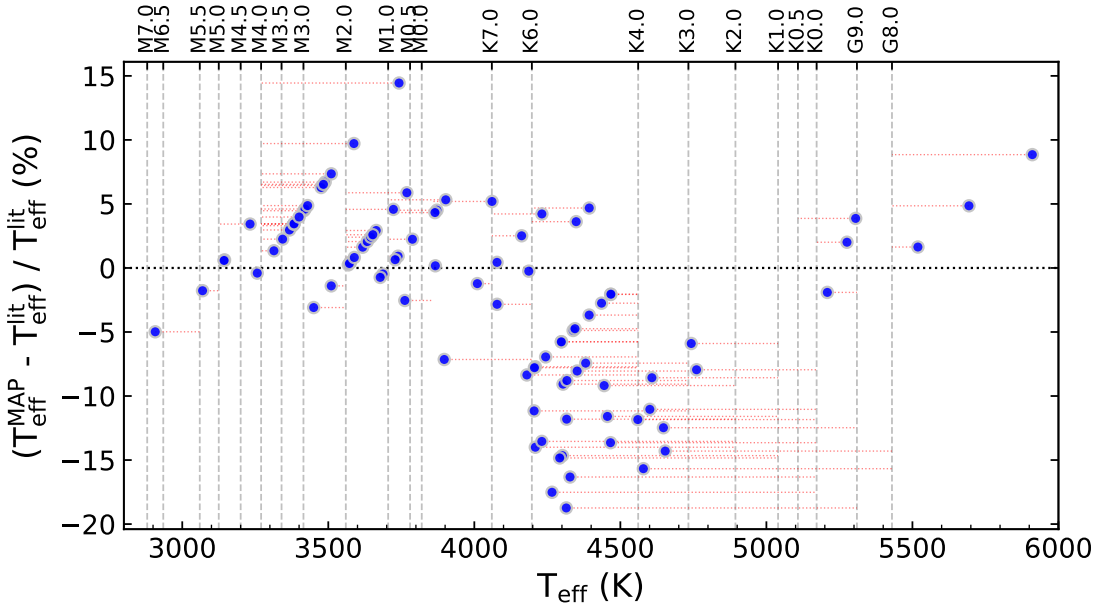

Figure 5.3: Relative differences in estimated effective temperatures between cINN ("MAP", blue circles) and Itrich et al. (2023b, "lit", red dotted lines) as a function of temperature. Grey dashed vertical lines connect the temperature with the corresponding spectral types of template stars used to fit those stars. Shown is only "best" group.

prescription as in Itrich et al. (2023b): veiling is defined by the ratio between excess emission and the photospheric flux at 750 nm, $r_{750} = f_{\rm exc,750}/f_{\rm phot,750}$. The possible r_{750} vales fall within the range 0-2. The last modification to the networks is training dataset. We applied a hybrid approach combining BT-Settl and Dusty libraries. In the parameter space covering by Dusty, we randomly select a spectrum from both libraries and then feed it to cINN. We make sure that both libraries are equally represented in the training dataset. We add a flag indicating which library is a sources of the spectrum: 0 – BT-Settl, and 1 – Dusty.

We validate the performance of the networks separately for different groups of sources sharing similar snr. The "best" group consists of 100 the best classified stars analysed in Chapter 4. The "good" stars are all others characterised sources. The "normal" are those targets that due to the variable background emission were excluded from the "clean" catalog, but the information about their uncertain properties is given in Table A.3. The "bad" sources were not classified in Chapter 4 but were detected with `SExtractor`. We expect the best performance for the "best" stars, and in general high level of consistency for "best" and "good" groups. Prevalence of the cINN over the traditional classification method will become apparent if the stars from the "bad" group are characterised at the same level of robustness as the "good" ones.

We first compare estimated parameters by cINN with those obtained in Chapter 4. We perform the comparison separately for "best" "good", and "normal" stars. In general, measured stellar parameters are very similar, especially for extinction. The main difference with the work presented in Sec. 5.2 is the larger scatter and deviation from perfect 1:1 relation. This is a direct result of the worse quality of spectra. As

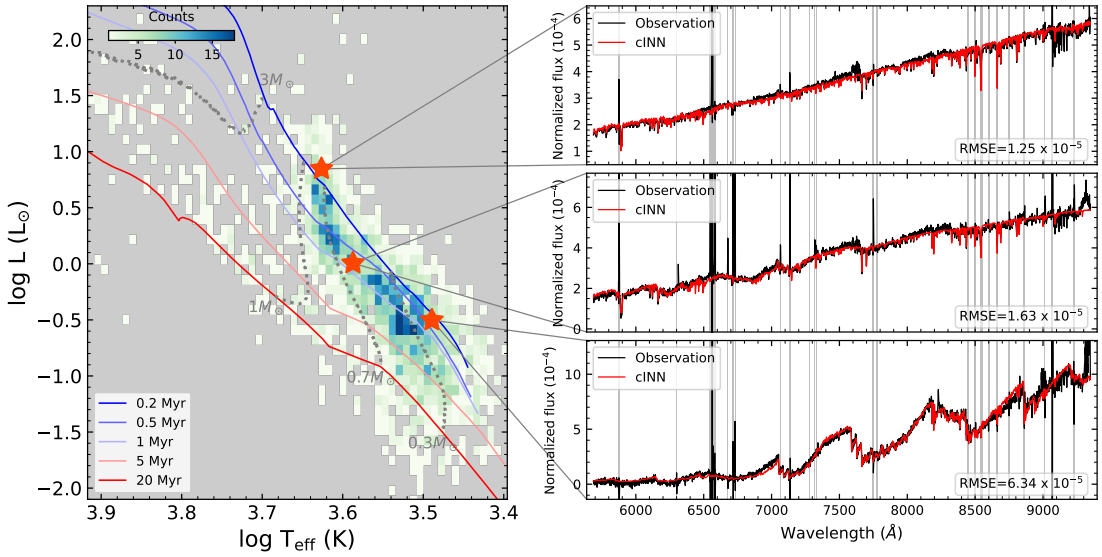

Figure 5.4: HR diagram for the whole Trumpler 14 sample. Colorbar shows the number density within each bin. $T_{\rm eff}$ are estimated by cINN, while estimates of luminosities combine J-band photometry from VLT/HAWK-I (Preibisch et al. 2011a,b) and cINN estimates of $T_{\rm eff}$and $A_{\rm V}$. Overlaid evolutionary tracks are from Bressan et al. (2012), as in Itrich et al. (2023b) and Figure 4.9. Objects mark with red stars on the HR diagrams are highlighted on the right. Black line present observed spectrum, while red – resimulated theoretical spectrum matching estimated by cINN parameters.

expected, the smallest differences between estimates are found for the "best" sample. The "normal" group reaches better agreement for temperature and surface gravity than the "good"stars. Note that $\log g$, which was not estimated in Chapter 4, for a "literature" reference is adopted from the corresponding template Class III star. Scatter in veiling measurements is similar in both groups.

The smallest relative discrepancies are in $T_{\rm eff}$ estimates. The best agreement is reached in the low-temperature regime, while hotter stars (4200 – 5100) are found to be cooler by cINN. The root mean square error is overall almost 3 times higher for the latter temperature range. Figure 5.3 shows the relative difference of temperature estimates as a function of temperature. The differences in the middle temperature range and at the high end can be explained by the lack of templates used for spectral classification (Chapter 4, Itrich et al. 2023b) and shows the advantage of using the continues or densely sampled grid. That, however, cannot fully explain the differences in the 4200 – 5100 K temperature range. Those stars have high snr, therefore misclassification (in either of methods) is not due to the high noisiness of the spectra. So far, the reason behind the discrepancies remains unclear to us.

To further investigate the results, we use cINN estimates of $T_{\rm eff}$ and $A_{\rm V}$ and J-band photometry from HAWK-I and Vista catalogs (Preibisch et al. 2011a,b, 2014, see Chapter 4 for details) to calculate the bolometric luminosities. Then, we place our new measurement on the HR diagram (Figure 5.4, left panel). The first important finding is that stars are concentrated around 0.5–1 Myr isochrones (Bressan et al. 2012) confirming the cluster age estimate from Chapter 4. Secondly, since the estimates were not limited by the sampling of the spectral type references, there

is a smooth distribution of $T_{\rm eff}$ and $L_{\rm bol}$. Thirdly, the population of older stars clearly visible in the colour-magnitude diagrams in Fig. 4.4 and not recovered in the "observational" HR diagram (Fig. 4.9), is well visible here.

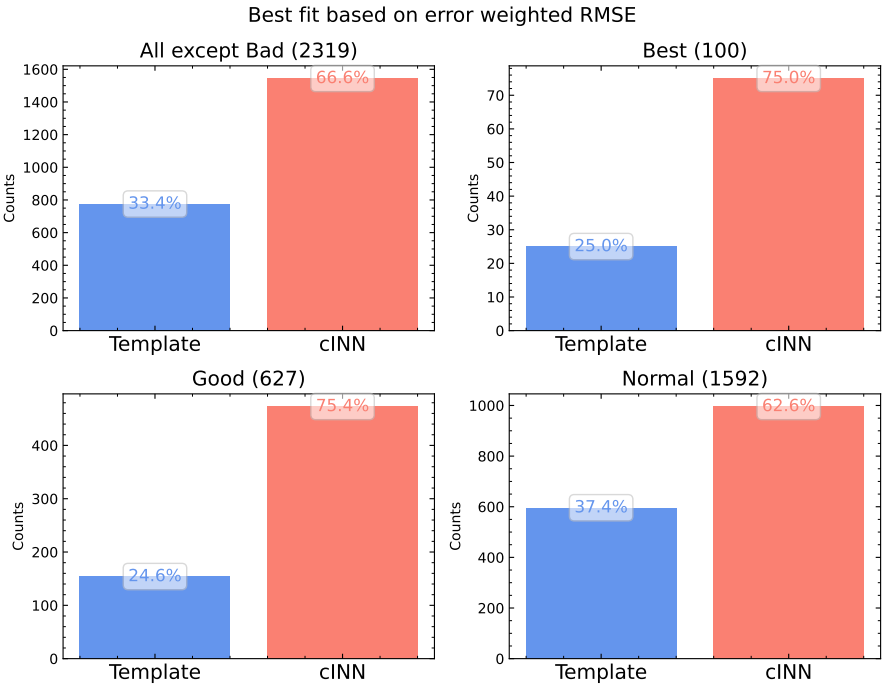

Figure 5.5: Comparison of the number of sources for which the template-based method (in blue) or cINN-based method (in red) gives more accurate estimates based on the value of RMSE. The upper left panel compiles all cases for which both estimates are available, the upper right – only the "best" ones, the lower left – the "good" stars, and the lower right – the "normal" sources. In all cases the preference is given to the cINN, although the differences between the methods are not large.

To show that the estimated parameters well represents the observed spectra, we present for three stars the re-simulated spectra (red) using cINN estimates on top of the observed (black) in the right panel of Figure 5.4. In all three cases, the re-simulated spectrum match the observed one, even though in the top panel the difference in estimated temperatures is large (∼660 K) and in the bottom panel the star was not classified in Chapter 4. The middle panel shows the case where both estimates agree with each others very well (temperature difference of ∼7 K). It might be puzzling that both, consistent and contradictive results seem to reproduce the spectra similarly well. One of the possible explanations is the different spectral normalisation procedure. In Chapter 4 spectra are normalised to the flux at 7500 Å, while here spectra are normalised to the total flux. It was already suggested that the different wavelengths to which the shape of the spectrum is referred might change the spectral classification results (e.g., Herczeg & Hillenbrand 2014; Manara et al. 2017). Testing whether the cINN will perform differently depending on the normalisation will be investigated in the future.

To better understand which method gives better results, or in other words, more closely reproduces observed spectrum, we compare the root mean square error (RMSE) calculated between the observed spectra and re-simulated ones for cINN,

and between the observed and Class III template. The smaller the RMSE, the better is the estimate. Overall, both methods give similar quality fits with on average a small error (of the order of few percents). The RMSE is the smallest applying both methods for the "best" and "good" stars and increases for "normal" and "bad" samples (in the latter only cINN method is available). For the entire sample, the median residual of cINN-based estimates is 5.12% and that employing template spectra is 5.33%.

We then check for each star, which method gives better value of RMSE and illustrate the results with histograms (Fig. 5.5). For all spectral qualities the preferred method is cINN-based (60-75%). Taking into account, that this comparison does not include stars not classified in Chapter 4, the main result of this work is highly positive. The cINN is able to reproduce human-based classification but often with smaller uncertainty and is able to classify cases which are challenging for traditional methods. By using the cINN we can derive a good and homogenous set of photosperic parameters for stars with $T_{\rm eff} \lesssim 4200$ K based on medium-resolution spectra. The performence of the cINN for hotter stars is under investigation. The derived homogenous sample includes a set of spectra that were difficult to classify in Chapter 4. In the temperature range 3000 – 4200 K (the lower limit is set by the lowest $T_{\rm eff}$ estimated in Chapter 4) the number of identified stars increase from 355 for the "clean" catalog in Chapter 4 to 1650 for cINN, an increase almost by a factor of 5. This demonstrate that effectiveness of networks is high. Moreover, once trained, neural networks are highly time-efficient. With this work we show that cINN can be successfully applied to the large datasets of cool stars observed with medium to low spectral resolution.

We see, however, the way to further develop our method. For instance, the deviation of tempetarature estimations for hotter stars (>4200 K) seems systematic and requires better understanding in order to have a cINN identifying stars over a wide range of temperatures what will make our method more general. Our application of the veiling is very simplistic assuming a constant value accross the spectrum, improvement of the method requires also to include more realistic approach. The ultimate goal is to construnct networks estimating stellar parameters, i.e., $T_{\rm eff}$, M_*, age, L_*. That requires including in the parameter space absolute flux values which were so far normalised. We built the method to apply it to young, accreting, stars. We noticed that emission lines present in the spectra of young stars confuse the cINN, thereofore we masked those spectral regions in analysis and in training. To measure accretion luminosities or accretion rates from those stars, we need to include those lines and train the networks accordingly. Those developments will be subjects of future investigation.

Chapter

Is photoevaporation affecting disks in Trumpler 14?

6

This chapter utilise data presented in Chapter 3. Work described here is a result of collaboration with Giuseppe Milazzo, a MSc student from University of Bologna, who has carried out a considerable number of tests of the new method of spectra extraction, which development was a collaborative work. The method is applied to the whole dataset and is part of the work in preparation (Itrich et al. in prep.), indented for submission to Astronomy & Astrophysics later this year.

Thorough classification of the stars is essential in characterisation of their protoplanetary disks. With the MUSE dataset, we have access to several emission lines which are used as accretion tracers (e.g., Alcalá et al. 2017). However, a bright and spatially variable nebular emission from the HII region contaminates stellar spectra in most of those tracers (e.g., Hα, Hβ, HeI), as well as of tracers of photoevaporation (ionised atomic forbidden emission, e.g., [OI], [NII]). After a series of tests we realised that the spectra extraction approach from Chapter 4 is not sufficient for accurate line measurements. `SExtractor` estimates background emission assuming its smooth change across the field and might not account for rapid local changes in nebular emission (see images extracted from MUSE observations in the Fig. 4.1).

Motivated by the above, we decided to test another method of spectra extraction. Instead of modelling background emission with `SExtractor`, we estimated it based on the emission within the annulus around the position of the star, a method well known in aperture photometry. The only difference with respect to photometry is due to the IFU cubes, which require performing the aperture photometry in each spectral channel and resulting with the "sky spectrum". We used aperture with radius of 3 pixels instead of 5 (Chapter 4) and apply aperture correction. The latter is estimated based on the isolated stars in the image and analysis of their curve of growth. We found that beyond radius of 10 pixels the stellar brightness do not increase anymore marking the reference for aperture correction. For each field we define one, wavelength-dependent correction being a median of those estimated using a set of isolated stars.

Comparison between newly extracted spectra and those from Chapter 4 show increase of the total flux of the spectrum probably due to the application of the aperture correction. This does not affect the estimation of $T_{\rm eff}$ and $A_{\rm V}$ from Chapters 4

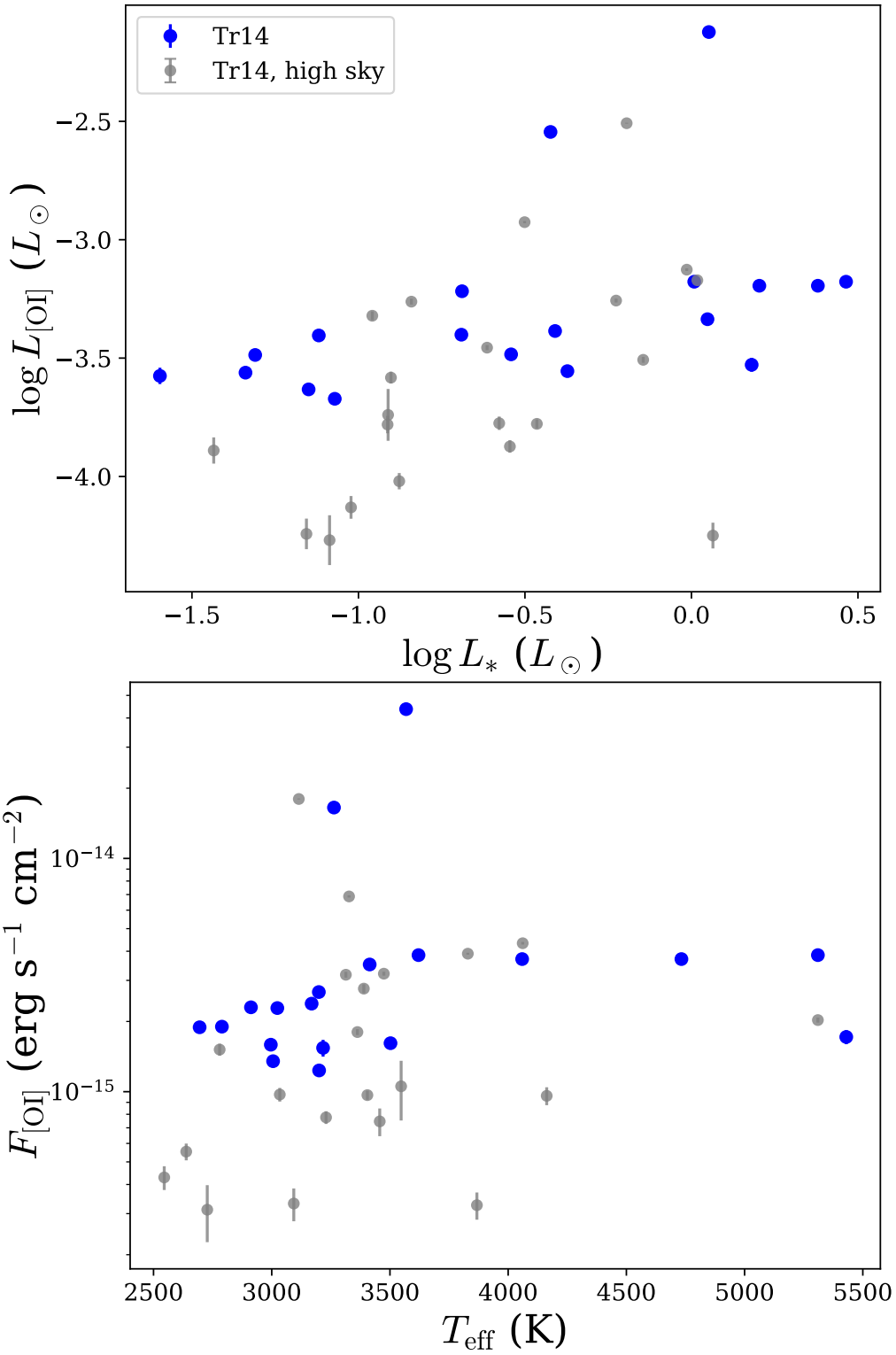

Figure 6.1: Upper panel: Luminosity of [OI] 6300 Å line versus stellar luminosity. Dark blue circles represent robust measurements, while grey – uncertain due to the high nebular emission what is illustrated by they larger errorbars (see text for details). Luminosities are extinction corrected. [OI] estimates exhibit increasing trend with L_*. **Lower panel:** [OI] 6300 Å line flux versus effective temperature. [OI] line is detected mostly towards the cooler stars.

and 5. We then test our method on the emission of [OI] line at 6300 Å. The line in high-resolution studies is resolved into multiple velocity components tracing inner microjets or disk winds (Hollenbach & Gorti 2009; Simon et al. 2016). The latter might be caused by either internal photoevaporation (Hollenbach & Gorti 2009; Ercolano & Owen 2016) or combination of the internal and external photoevaporation (Ballabio et al. 2023). With the MUSE resolution we are not able to resolve different velocity components, but we can put meaningful upper limits on the low-velocity components tracing disk winds, and compare them with other measurements, as well as with the theoretical predictions.

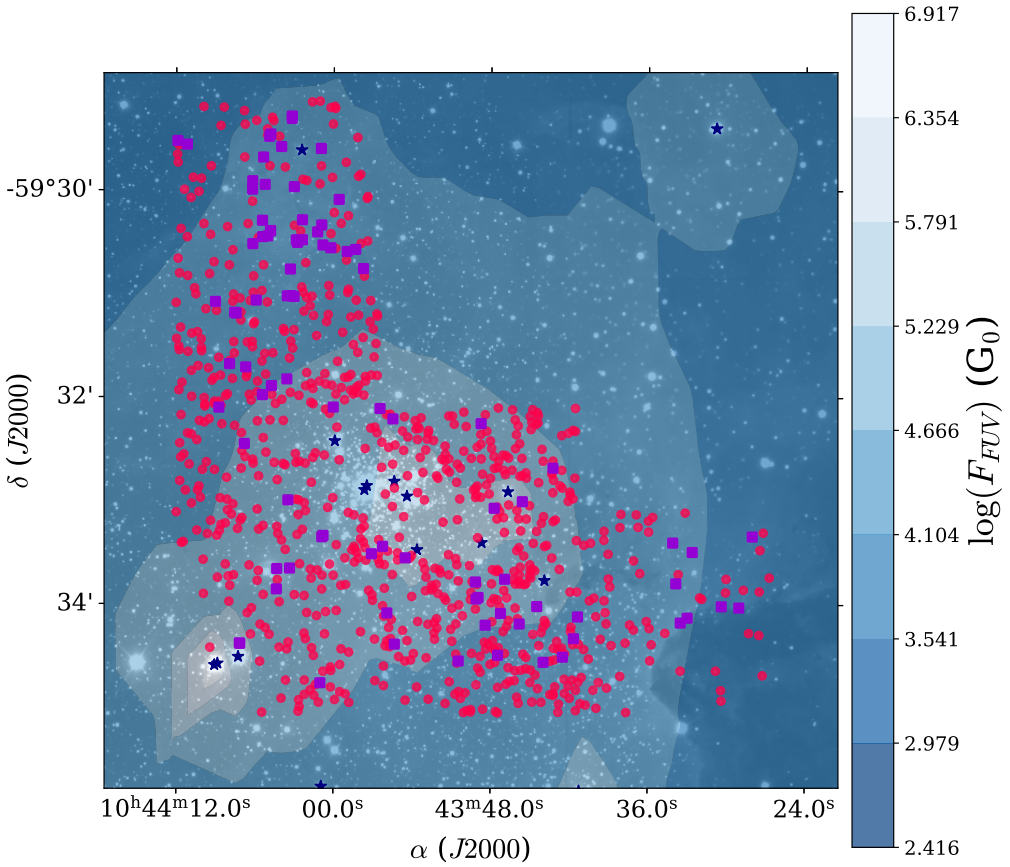

Figure 6.2: Distribution of the intrinsic FUV field in Trumpler 14 estimated based on properties of the O-type stars (dark blue stars). Estimate is done assuming projected distances as a real ones and lack of intracluster extinction, therefore it can be treated as an upper limit of FUV field. We also overplotted positions of the final sample from Chapter 4 for comparison.

We estimate line flux integrating the flux within the spectral range close to the line. We estimated two uncertainties of the measurement: one indicating the noise of the stellar spectrum, and the other indicating the uncertainty of "sky" estimation. The latter is affecting more than a half of detections. We consider only those measurements which have both detection level and flux estimate $>3\sigma$. In Figure 6.1 we show [OI] luminosities versus L_* and [OI] line flux versus $T_{\rm eff}$. We corrected lines for extinction using values estimated in Chapter 5 for stars <4200 K, and in Chapter 4 for hotter stars. Blue circles mark robust measurements, while the grey dots are affected by the relatively uncertain estimate of nebular emission ($<3\sigma$).

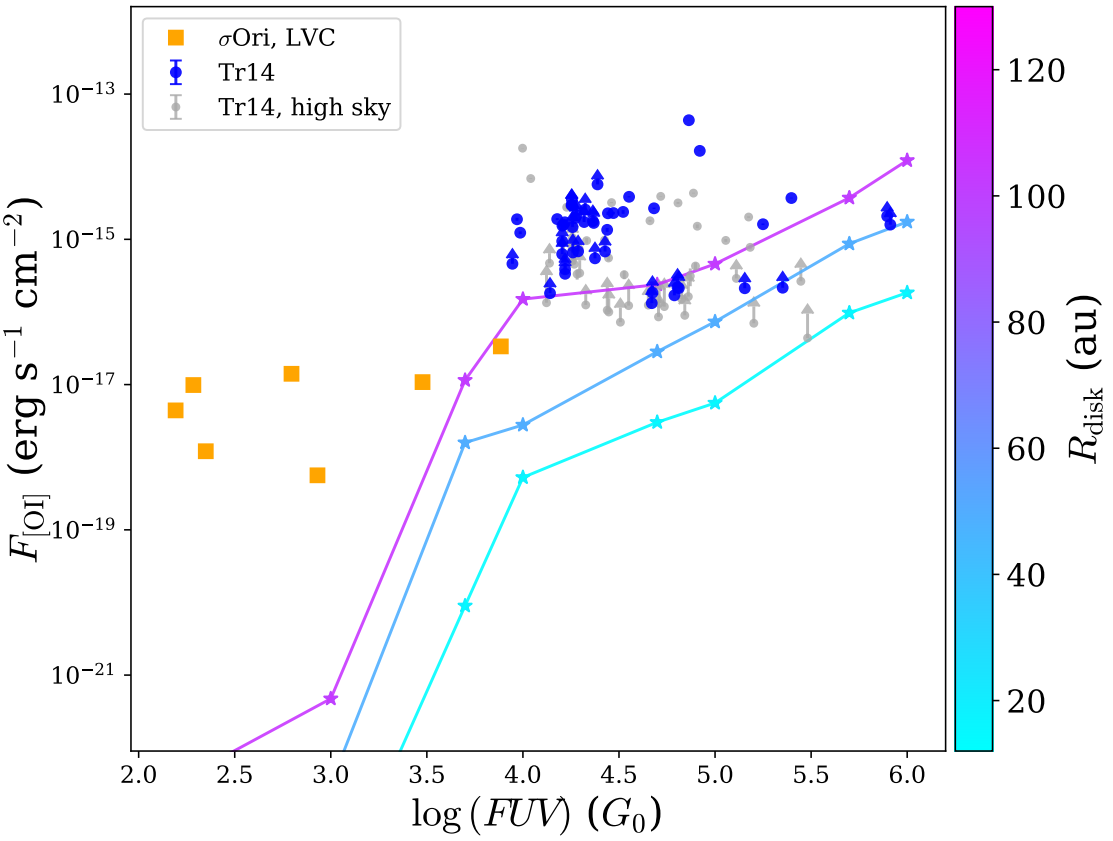

Figure 6.3: The [OI] line flux as a function of FUV field in G_0 ($G_0 = 1.6 \cdot 10^{-3}$ erg s^{-1} cm^{-2}, Habing 1968). Our measurements are presented with dark blue circles, while the uncertain measurements due to the nebular emission – with grey ("high sky"). Lower limits mark cases where A_V estimates were not available. Tr14 values are compared with those from σOri (orange squares, Natta et al. 2014) and theoretical models predicting [OI] 6300 Å emission from disks with different radii due to the external photoevaporation (colour-scale: light blue – 20 au, blue – 50 au, violet – 100 au; Ballabio et al. 2023).

Figure shows trend of increasing oxygen luminosity with the luminosity of the star seen previously in the literature for both velocity components (high and low, e.g., Nisini et al. 2018). The trend with the $T_{\rm eff}$ is however less prominent.

As it was mentioned before, the whole Carina Complex is characterised by the high FUV field. The level of radiation was estimated by the Roccatagliata et al. (2013) with FIR dust emission observed by *Herschel*. Their results indicate FUV$\sim 10^4$ G_0 in the center of Tr 14, which is probably a lower limit. Here, to estimate the FUV flux felt by each star in our sample, we sum the integrated flux in FUV range emitted by each O-type star in the region and scaled to the projected distances to each of our targets. We assume the same distance to all stars of 2.35 kpc (Göppl & Preibisch 2022) and no extinction within the cluster. Therefore, our estimates might actually be the upper limits of the real FUV flux received. Figure 6.2 shows how the FUV flux is distributed aorund the Trumpler 14. The overplotted on the HAWK-I image (Preibisch et al. 2011a) contours indicate interpolated values by the

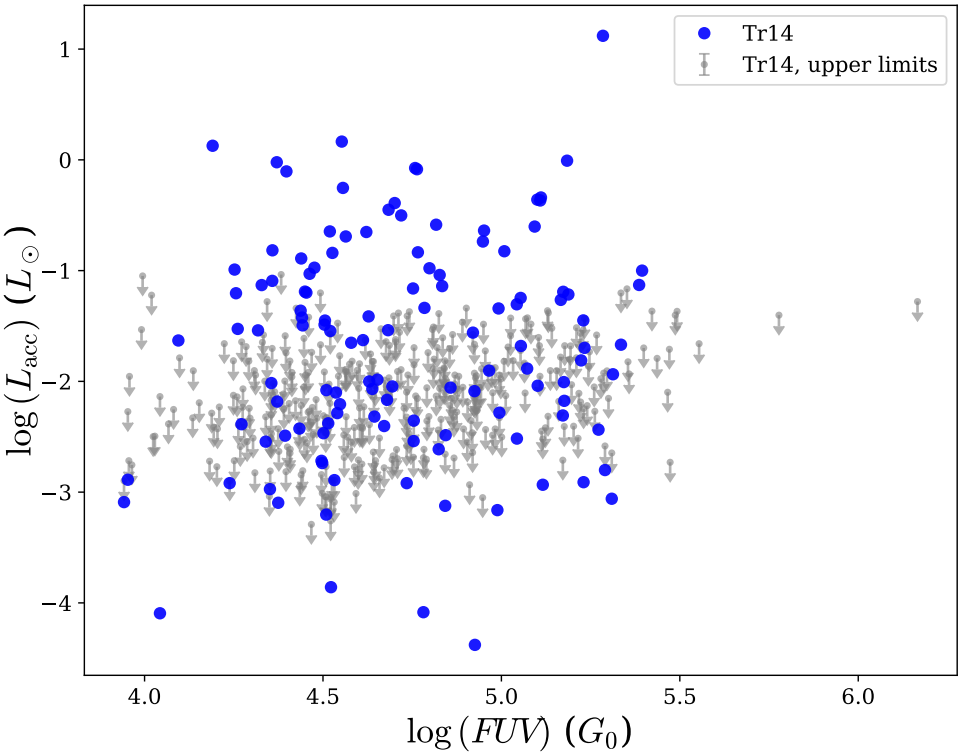

Figure 6.4: Accretion luminosity as a function of FUV field. Accretion estimates are based on CaII IRT emission lines (blue circles). This emission usually tracers strong accretors, thus is not detected in most of our stars. We place upper limits (grey arrows) for the rest of the sample.

randomly sampled locations within the shown area. The FUV flux in the cluster center reaches values well above 10^6 G_0, higher than estimates from FIR observations (Roccatagliata et al. 2013).

We estimate FUV fluxes for all our stars that have [OI] detections and plot the latter against the former (Fig. 6.3). Lower limits mark cases for which we do not have stellar properties and therefore it was not possible to correct those measurements for extinction. For a meaningful comparison we added to the figure measurements from the σOri cluster (Natta et al. 2014) scaled to the distance to Tr 14. Note, that those observations were done with higher spectral resolution and plotted are only values for low-velocity components (LVC). Our measurements raise higher values of [OI] emission than in σOri. Our stars are also affected by the higher FUV field, the possible explanation might be that they are undergoing externally-driven photoevaporation. This hypothesis is in agreement with the theoretical predictions from Ballabio et al. (2023). Our measurements seem to be consistent with models of large disks (100 au). This poses an interesting question whether the lack of smaller disks is related to their fast dispersion and to resulting weaker [OI] emission falling below our detection capabilities. Shown models do not account for internal photoevaporation but present significant increase of expected [OI] emission above $\sim 10^{3.5}$ G_0, conditions present in Tr 14. However, to be able to confirm that those sources are being photoevaporated, we need to be able to separate different components of the emission line, which will be our goal for the future investigation (Sec. 7.2.4).

We also investigate whether accretion properties are altered by the different level of FUV radiation. To avoid possible contamination from the sky, we focus on CaII IRT emission lines. Because the calcium triplet is located close to the Paschen series of hydrogen lines, we adopt different procedure of flux measurements. We first fit Gaussian profiles to the hydrogen lines that are not blended with CaII IRT. We predict the amplitude of the blended hydrogen lines assuming its linear increase with wavelength. The width of the line is assumed to be constant. Then we subtract the Gaussian profiles of the blended hydrogen lines from the spectra and only then we measure the calcium lines again fitting Gaussian profiles. Measured lines are afterwords corrected for extinction. We then translate luminosities of all three lines per star to accretion luminosities using empirical relations from Alcalá et al. (2017). The final accretion luminosity is a median of the three. We show our results in Figure 6.4.

CaII IRT traces high accretors (Yamashita et al. 2020) and indeed some of our sources have accretion luminosity close to the solar value or higher. It is then not surprising that not all of our sources exhibit this emission. Only ∼10% of stars presented in the Figure 6.4 are emitting those lines. This limits our possibilities to test whether accretion properties change with FUV field. In Fig. 6.4 we do not see a clear trend. It is however interesting to note, that high accretors are only detected in the lower end of FUV field values. The question posed by this section remains open. This study requires further investigation, in particular employment of other emission lines (e.g., HeI) will be crucial to increase the sample size and obtain global view of protoplanetary disk population in Trumpler 14.

Chapter

7 Conclusions and future prospects

7.1 Summary

The motivation behind this thesis was the investigation of the role of external photoevaporation in star formation and evolution and planet formation. External photoevaporation, a process of removal of material from the outer parts of the protoplanetary disks due to the high UV radiation originating in massive OB stars, is considered to be the most important environmental effect altering disk evolution in our Galaxy (Winter et al. 2018c). This process could also affect a very young Solar System as the Sun formed in the neighbourhood of massive stars.

The best way to unambiguously assess the importance of external photoevaporation is to study its impact on stars located in environments characterised by the presence of many massive stars. This thesis focused on the Carina Nebula Complex (CNC) and its Trumpler 14 cluster. Tr 14 is one of the most massive, young, and dense clusters of CNC. The level of FUV radiation ($\sim 10^4$ - 10^7 G_0) is $\sim$2 orders of magnitude higher than in any cluster in Orion. Tr 14 is therefore a perfect laboratory to study external photoevaporation. However, observations of Tr 14 are challenging due to the distance to the region (2.35 kpc), the presence of bright and spatially variable nebular emission from HII region, and of multiple massive and bright stars in the cluster hindering the detection and characterisation of their faint neighbours. A way to overcome those difficulties and to obtain a census of low-mass stars members is to use highly sensitive instruments with large field-of-view. The IFU technique is ideal to perform effective spectroscopic investigations under such conditions. All of those requirements are met by the Multi Unit Spectroscopic Explorer (MUSE), an optical, moderate-resolution spectrograph which was successfully employed here (Chapter 3).

Trumpler 14 was observed with MUSE in 2016 (programme ID: 097.C-0137, PI: A.F. Mc Leod). The observations covered the cluster center and the north and south-west outskirts in 22 pointings. Deep integrations allowed for the first time a spectroscopic characterisation of the low-mass stars (<1 $M_\odot$) in Carina. In Chapter 4 the catalog of young, low-mass stars in Trumpler 14 was constructed. The spectra were classified using as templates X-Shooter observations of Class III stars from Manara et al. (2013, 2017). Spectral parameters (spectral type, $T_{\rm eff}$, $A_{\rm V}$, r_{750}) were then combined with J-band photometry to estimate the bolometric luminosity. Stellar characteristics (M_*,

age) were obtained by comparison to the theoretical evolutionary PARSEC tracks (Bressan et al. 2012). The good quality of the spectra allowed the characterisation of stars down to 0.2 $M_{\odot}$ but with a significant loss of completeness below 0.8 $M_{\odot}$. The completeness of our catalog was mostly affected by the highly variable nebular emission hindering precise and reliable estimation of stellar photometric brightness, as well as fluxes of the spectra. For that reason, >1800 detections were removed from the catalog when applying rigorous quality control parameters, leaving only 780 robustly characterised stars. This shows the potential of the instrument and the analysed dataset, but urges for a more sophisticated methodology.

The MUSE/Tr 14 dataset with only 22 pointings is already large. This is due to the instrumet large FOV ($1'\times1'$) which at the distance to Carina corresponds to 0.68×0.68 pc. Within such an area and with the stellar density of 2×10^3 pc^{-2} (Ascenso et al. 2007), single MUSE cube contains spectra of hundreds of stars. Analysis of the whole sample by classifying each individual spectrum is very time consuming. MUSE is being applied to more stellar clusters, similarly a medium-resolution spectroscopic survey instruments that are planned for the future (e.g.,Integral Field Spectrograph at Wide-field Spectroscopic Telescope, WST). Those facts motivate the search for more efficient methods of spectral analysis. Machine learning techniques are becoming more and more popular in astronomy. Specifically, neural networks which allow for accounting for an observational uncertainty, are gaining popularity. Chapter 5 presents a way to employ an cINN architecture which, when trained on theoretical spectra and applied to well known Class III stars, accurately predicts stellar parameters. Similarly, the network performs well on the MUSE spectra of Tr 14 stars giving similarly accurate parameters as the "traditional" method. Additionally, new method works well also on lower-snr spectra allowing classification of ∼5 times more stars in the temperature range of 3000 – 4200 K. Those promising results are of key importance for statistical studies based on very large samples, which will be necessary to build a global picture of star and planet formation.

7.2 Future prospects

7.2.1 Intermediate-mass and massive stars in Trumpler 14

The analysis of the MUSE dataset (see Chapter 4) was focused on low-mass stars. Therefore, only long exposures were used in the investigation. However, the dataset also includes short exposures which were designed to avoid saturation of bright stars. They can be used to extract their spectra and perform classification similarly to what was done for G-type stars (Section 4.3.3.2 or in Hernández et al. 2004). Complementing short exposures with the deep ones will allow sampling the massive end of the IMF by including G, F, A, B, and O-type stars. Building a complete IMF will allow to compare it with other clusters in the Milky Way, as well as in the Magellanic Clouds, and to test its universalism. Only by sampling the IMF towards the bothe low and high mass end it is possible to obtain the full census of Trumpler 14 members and full description of cluster properties.

7.2.2 When planets don't planet: role of the harsh cluster environment in shaping future planetary systems

The universality of the Initial Mass Function (IMF) has been a long-standing question. Whether the IMF depends on the environmental conditions or not has profound implications on our understanding of star formation. Several studies addressed this question investigating star-forming regions. Damian et al. (2021) studied the low-mass populations ($\sim 0.05 - 2.5\ M_{\odot}$) of several young clusters (1-5 Myr) spanning different environmental conditions. They constructed their IMFs and tested whether the parameters that describe the mass distributions show any correlation with the environmental conditions which included high FUV field. They found that all the IMFs are comparable within the uncertainties, indicating an independency of the IMF from the environment. However, this study is based on NIR photometry alone and still requires spectroscopic confirmation. Another way in which star formation might be impacted by the massive stars was proposed by Whitworth & Zinnecker (2004). They suggested that strong radiation from OB stars can strip the outer layers of the core from a forming protostar and cause formation of a star with reduced mass, namely a free-floating brown dwarf or planetary-mass object (Fang et al. 2016). Almendros-Abad et al. (2023) have found brown dwarfs located closer to the OB stars than other cluster members, which might be a result of the violent impact that massive stars have on their surroundings. Recent JWST/NIRCam observations in Orion revealed a presence of hundreds of free-floating brown dwarf and planetary-mass object candidates. The most striking discovery was Jupiter-Mass Binary Objects (JuMBOs), whose formation mechanism might highlight the importance of the environment (McCaughrean & Pearson 2023; Pearson & McCaughrean 2023).

The deepest spectroscopic studies of Trumpler 14 to date are optical IFU observations from VLT/MUSE presented in Chapter 4. Due to the high level of nebular emission from HII region, the study is highly incomplete at the low mass end of the sample

(<0.8 $M_{\odot}$), so neither the construction of the IMF nor an examination of the effect of external photoevaporation on star formation are possible. The highly sensitive JWST Near Infrared Spectrograph (NIRSpec) observations can fill this gap and provide spectroscopy of the very low-mass stars that were detected with multi-band NIR VLT/HAWK-I photometry (Preibisch et al. 2011a,b) but due to their faintness lack spectroscopic follow-up observations and thus their cluster membership requires confirmation.

Not only the lowest mass members of a cluster are the most vulnerable to the harsh conditions in the region, but also their protoplanetary disks are expected to be affected the most (Winter et al. 2020). There are no direct observations of disks at (sub)mm wavelengths in Trumpler 14. An indirect way to study disks is to detect the IR excess coming from the inner part of the disk (e.g., Lada & Wilking 1984; Lada 1987; Greene et al. 1994). Among all the sources detected in Trumpler 14 with HAWK-I, 10% exhibit the NIR excess (Preibisch et al. 2011b). To confirm their youth and membership it is needed to (1) obtain their spectral classification and (2) measure accretion from the disks onto the stars.

(1) Very low-mass stars and brown dwarfs have very characteristic spectra in the NIR, exhibiting several molecular bands whose depth depends on the temperature of the source (e.g., H_2O, CH_4, NH_3, CO, CO_2; Oppenheimer et al. 1998; Geballe et al. 2002; Testi 2009; Cushing et al. 2005; Kirkpatrick 2005; Almendros-Abad et al. 2022). Those features are present across the whole NIR range with some of the most prominent bands at 1.9, 2.2, 3.3 μm. Robust spectral classification requires observations with a wide wavelength range ($1.7 - 5.0$ μm), like the one offered by JWST/NIRSpec. Obtaining statistically significant results demands the sample size of ∼300 objects (Alexander et al. 2023). To classify the whole sample consistently, it is possible to employ a neural network based approach to simultaneously asses their stellar parameters, including effective temperature, surface gravity, and extinction, which then will be translated into masses and ages (Baraffe et al. 2015; Chabrier et al. 2023). Neural networks have been demonstrated to perform effectively on medium-resolution spectra ($R \sim 3000$) and accurately estimate stellar parameters (see Chapter 5, Kang et al. 2023b,c). The advantage of using machine learning methods is a short computation time even when applied to large datasets like few hundreds of medium-resolution spectra spanning wide wavelength range.

(2) Measuring the accretion rates provides the opportunity to investigate the evolution of protoplanetary disks. In the magnetospheric accretion scenario, the accretion shock creates excess emission measurable across the spectrum (e.g., Hartmann et al. 2016). The amount of the excess emission can be accurately estimated in the UV range (Balmer jump). However, UV excess emission cannot be measured in highly extinguished and cool, very low-mass stars. For those extremely faint in UV objects, emission lines, for which empirical relations with the accretion luminosity have been derived, can be used instead. Specifically, NIR lines are suitable for the coolest objects which are too faint in the optical range to obtain precise estimates, like our targets. Relations between the accretion luminosity and luminosity of hydrogen lines have long been established and applied to a wide range of stellar masses, also in

the substellar regime (e.g., Natta et al. 2004a; Alcalá et al. 2017; Fiorellino et al. 2021). However, the Brα line at 4.0523 μm has not yet been extensively used (Komarova & Fischer 2020). JWST with NIRSpec and NIRCam now offers a possibility to regularly measure accretion from highly extinguished objects but the empirical relation between the Brα line and the accretion luminosity (Komarova & Fischer 2020) needs to be confirmed. With ∼300 objects and simultaneous measurements of other hydrogen emission lines (e.g., Brγ, Paα), the proposed observations will allow to verify the existing relations at a statistically significant level. The ratio of the intensity of two lines widely separated in wavelength (Brα and Brγ) will give us an estimate of the level of extinction from the emitting region. Accretion luminosities acquired from several emission lines will then be combined with previously estimated stellar parameters to derive the corresponding mass accretion rates.

Accretion rates correlate with both stellar and disk masses (see e.g., a recent review of Manara et al. 2023). More massive stars tend to have higher mass accretion rates. At the same time, more evolved stars exhibit weaker accretion (Hartmann et al. 1998; Antoniucci et al. 2014). In the substellar regime the relation between stellar mass and accretion rate is observed to be steeper than in the solar-type stars (e.g., Manara et al. 2017). Trumpler 14 is a very young cluster with an age of ∼1 Myr. Therefore, in a typical low-mass star-forming region we would expect mass accretion rate values to be on a higher end. However, in Tr 14 the early evolution of cluster members, as well as their circumstellar disks, is impacted by the high level of UV radiation ($L_{\rm FUV}$ ∼$10^7 L_\odot$) which might significantly change their properties.

How the cluster environment changes the evolution of planet-forming disks and consequently their planet-formation potential is of key importance for a global picture of star and planet formation. Only by going to the extreme environments like the one in Carina it is possible to unambiguously assess the role of environment which could also play an important factor in formation of the Earth and the Solar System (Adams 2010). The full picture cannot be obtained without investigating the lowest mass members of the cluster.

7.2.3 Mdisk - Mdot in high G0: Impact of external photoevaporation on disk masses in Trumpler 14

The formation and early evolution of planets is highly influenced by the evolution and dispersion of their birthplaces – protoplanetary disks. The environment in which the young star is immersed can significantly alter the evolution of planet-forming disks. Specifically, a large loss of the disk mass due to photoevaporation, as well as an increase of the disk temperature due to the external irradiation can prevent formation of Jovian planets (Winter & Haworth 2022). To understand the role of external photoevaporation in the protoplanetary disk evolution, it is important to test the $\dot{M}_{\rm acc}$−$M_{\rm disk}$ relation in the highly irradiated environment of Carina Nebula.

The impact of O-type stars on protoplanetary disks has been investigated in the ONC (Mann et al. 2014) and the σOri cluster (Ansdell et al. 2017). Disk dust masses were found to increase with distance from the source of UV radiation, indicating that dust in disks closer to massive stars is being depleted by their intense radiation. Additionally, Ansdell et al. (2017) detected disks in gas emission only for objects more than 1.5 pc away from the cluster center. Typically, gas emission is more extended than dust, which makes it less tightly bound to the star and possibly more vulnerable to external photoevaporation (e.g., Boyden & Eisner 2020). While the ONC's ionising budget is dominated by a single O star (Θ^1Ori C, Simón-Díaz et al. 2006), clusters in the CNC contain a dozen of them. Specifically, Tr 14 hosts 20 O-type stars (Shull et al. 2021) with a total luminosity ∼20 times greater than that of the ONC (Smith 2006; Smith & Brooks 2008) and a similar cluster age to ONC (∼1 - 2 Myr, Hur et al. 2012). In effect, the FUV flux in Tr 14 (∼10^4 - 10^7 G_0)is significantly higher than in the ONC (∼$10^3 - 10^4$ G_0, Anderson et al. 2013). Carina, as a more representative region of the environment in which planets form in our Galaxy (e.g., Lee & Hopkins 2020), is an ideal case study to investigate the impact of an extreme environment on the evolution of protoplanetary disks (see also Chapter 2).

Over the last decade ALMA has been revolutionising the field of star formation providing highly sensitive and detailed observations of protoplanetary disks. Extensive surveys of nearby star-forming regions allowed to confirm the $\dot{M}_{\rm acc}-M_{\rm disk}$ relation predicted by the viscous theory (Hartmann et al. 1998; Manara et al. 2016, Sec. 1.2.2.1), and extend already well-known $\dot{M}_{\rm acc}-M_*$ relation (e.g., Hillenbrand et al. 1992; Natta et al. 2006; Alcalá et al. 2017). The correlation between $\dot{M}_{\rm acc}$ and $M_{\rm disk}$ is also expected in MHD winds scenario (Tabone et al. 2022). However, this correlation was not observationally tested in the environments where external photoevaporation is expected to play a major role in disk evolution. Since the disk masses are supposed to be lower on average in high FUV environments, the observed $\dot{M}_{\rm acc}-M_{\rm disk}$ correlation will be shifted towards smaller $M_{\rm disk}$ values (Somigliana et al. 2020). Models of external photoevaporation also predict a rapid decrease of disk radius at ∼1 Myr when the disk is exposed to the FUV flux of 5000 G_0 (Winter & Haworth 2022). On the other hand, if the disks are primarily shielded from the radiation for 0.5−1 Myr by the dusty envelope, their mass reservoir will not be depleted and their initial ability to form planets will remain intact (Qiao et al. 2022, 2023). It is then of a profound importance to understand how external photoevaporation impacts $\dot{M}_{\rm acc}-M_{\rm disk}$ relation.

Until now, there were only two attempts to observe disks in CNC with ALMA. The first imaging campaign of millimetre emission from YSOs, which extended from the cluster center to its outskirts, was reported by Mesa-Delgado et al. (2016). They used ALMA 1.3 mm continuum observations to detect disks in the two evaporating gas globules associated with mid-infrared sources and classified as intermediate mass Herbig AeBe stars (Povich et al. 2011). High angular resolution ($0.03'' \times 0.02''$) and a sensitivity of ∼60 μJy allowed to resolve those two disks and estimate their masses (∼0.05 and ∼0.03 $M_\odot$, respectively). However, they did not detect any other disk above the threshold of 4σ (corresponding to less than 0.01 $M_\odot$) in the core of

Tr 14, hinting at the devastating effect of strong UV radiation onto the disk masses. Recently, the detection of two embedded YSOs on the outskirts of Tr 14 associated with the protostellar jets HH 901 / 902 was reported by Cortes-Rangel et al. (2020) with estimated total masses of $\sim$0.1 $M_{\odot}$.

To study how strong interstellar radiation affects the evolution of disks around low-mass stars in Carina, it is needed to measure the 1.3 mm continuum emission from a sample of 29 young stars distributed around Tr 14. The best candidates are young, highly accreting, pre-main sequence stars with disks. To maximise the chances of their detection, the sample targets strongly accreting solar-mass stars that are most likely to survive strong UV radiation in the young ($\sim$1 Myr) cluster.

The combination of ALMA and ESO data (Chapters 3 and 4) will allow investigation of the $\dot{M}_{\rm acc}$- $M_{\rm disk}$relation (see e.g., Manara et al. 2016). Comparison with similar samples of low-mass stars in nearby star-forming regions with similar ages (e.g., Taurus, Lupus, Chameleon I, Ophiuchus, ONC Andrews et al. 2013; Ansdell et al. 2016; Pascucci et al. 2016; Williams et al. 2019; Mann et al. 2014) will provide assessment, whether disks in Tr 14 are altered by the environment or not. If the role of external photoevaporation is dominant, the disk masses will be lower for similarly high accretion rates like in low-mass regions.

7.2.4 Finding external photoevaporation where it cannot be seen - Carina Nebula and Trumpler 14

There is now overwhelming evidence that planets form in circumstellar disks of material around young stars (e.g., Benisty et al. 2021). The distribution of material in these disks is key for the planet formation process and resulting planetary architectures (e.g., Mordasini et al. 2009). It is therefore important to understand how the distribution of material in disks evolves over time. For example, the inner regions of disks are cleared internally by winds driven by the host star (Pascucci et al. 2023). Furthermore, since most stars form in large clusters containing massive stars (Lada & Lada 2003), the majority of disks are also expected to be irradiated by significant environmental UV radiation, which drives an "external" photoevaporative wind from the outer parts of the disk (e.g., O'Dell et al. 1993; Winter & Haworth 2022). However, distinguishing and quantifying these external contributions to disk dispersal have so far been completely overlooked. The studies of internally driven disk winds are for relatively nearby systems (<400 pc), which are all in weak, $<10^2$ G_0, UV environments (Pascucci et al. 2023). Conversely, externally driven winds are predominantly studied using spatially resolved observations of the cometary shaped wind that results in regions like the Orion Nebula Cluster, so similarly neglect any inner winds (O'Dell et al. 1993). Furthermore, by relying on spatially resolved observations of proplyds, the study of external photoevaporation is limited by the spatial resolution to the star-forming regions within around 400 pc (i.e., the ONC, NGC 1977, NGC 2024, O'Dell et al. 1993; Kim et al. 2016; Haworth et al. 2021).

High spectral resolution observations are absolutely vital to distinguish between externally and internally driven wind components, especially in distant clusters where morphological diagnostics of external photoevaporation cannot be spatially resolved. For example, with X-Shooter observations of the low-mass stars in Trumpler 14 and with focus on the most frequently used optical diagnostics of disk winds (e.g., [OI] 5577, 6300Å, [SII] 4068, 4076, 6716, 6731Å, [NII] 6543, 6548Å, Hollenbach & Gorti 2009) it will be possible to investigate the main source of the observed emission. In particular, the most important will be the analysis of the [OI] 6300 Å line, studied in depth for proplyds. The line was found to have typically two velocity components: low (LVC) and high (HVC). The HVC arises in protostellar winds or inner microjets with typical velocities of 100-200 km/s (Hollenbach & Gorti 2009; Simon et al. 2016). The LVC is connected to disk winds driven magnetically (MHD) or thermally (photoevaporative, Simon et al. 2016). This component is usually slightly blue-shifted (∼-5 km/s), with broad wings (up to ±60 km/s), probably due to the Keplerian rotation. Both components were found to scale with accretion luminosity (e.g., Hartigan et al. 1995; White & Hillenbrand 2004; Nisini et al. 2018). However, models of internal photoevaporation underestimate the highest values of [OI] emission (e.g., Hollenbach & Gorti 2009; Ercolano & Owen 2016), which might be enhanced by external mechanisms.

The bulk of the MUSE measurements of [OI] line in Tr14 (Chapter 6) lie above the empirical relation between $L_{\rm acc}$ and [OI] luminosity (Nisini et al. 2018) and theoretical prediction for internally-driven [OI] emission (Ercolano & Owen 2016) suggesting additional mechanism in play. Models addressing the effect of external photoevaporation on protoplanetary disks (Ballabio et al. 2023) predict that only in the environment with very high FUV field ($>10^4 - 10^5\ G_0$) [OI] LVC line fluxes can be enhanced in a way allowing to test the impact of external photoevaporation. Tr 14 observations reproduce this prediction in contradiction to Orion data due to the FUV field higher by one order of magnitude. However, the spectral resolution of MUSE (∼60 km/s at 6300Å) does not allow to distinguish between slow and fast winds (LVC and HVC). Also its angular sampling of $0.2''$ at the distance to Carina is not enough to spatially resolve the emission, as it was done for proplyds in the Orion Bar (Haworth et al. 2023). Testing the currently developed models requires higher resolution observations. The suggested here observations can provide a clear observational test whether external photoevaporation is the main mechanism altering disk properties in Tr 14.

7.2.5 Impact of the environment on the protoplanetary disks population in Trumpler 16 with MUSE

As it was already discussed several times, the impact of external photoevaporation on protoplanetary disks evolution should be addressed in a massive cluster, where the UV field produced by young OB stars exceeds the one in the ONC and is affecting thousands of young protoplanetary disks. Models predict that in these

harsh environments protoplanetary disks can be dissipated on very short timescales ($\tau_{\rm FUV} < 1$ Myr for 1 $M_\odot$ star, Winter et al. 2020), which would have catastrophic consequences on their planet formation capacity.

MUSE observations of the Tr 14 cluster in Carina (Chapter 3) proves the effectiveness of this instrument to conduct this type of study. Thanks to the IFU technique the background emission from the HII region can be accurately estimated for every object in the cluster. The MUSE spectrum covers multiple emission lines connected with accretion (like Hα, Hβ, HeI, or CaII IRT) which used together give the most robust estimation of accretion luminosity, and when combined with stellar parameters, of mass accretion rates. However, Tr 14 is a dense cluster (central number density of $7{\times}10^3$ pc^{-3}, central surface density of $2{\times}10^3$ pc^{-2}, Ascenso et al. 2007), and thus tidal truncation of disks probably contributes to their disruption, even though external photoevaporation is expected to be dominant mechanism (Winter et al. 2018c; Concha-Ramírez et al. 2021). As the local density exceeds $\gtrsim$10^4 pc^{-3} / 100 pc^{-2}, like in Tr 14, the dispersion process is significantly accelerated (Concha-Ramírez et al. 2021). Specifically, for regions with FUV above $\sim$3000 G_0 and central density $\gtrsim$10^4 pc^{-3} all disks will be dispersed in $\sim$3 Myr (Winter et al. 2018c). To investigate in a more direct way the effect of photoevaporation, it is necessary to observe an environment with similar FUV field and lower stellar density. An ideal case meeting those conditions is Tr16, cluster also located in the Carina Complex.

Tr16 and Tr14 share some properties, but differ in others, critical in comparing the effects of photoevaportation and dynamical truncation. Similar are total mass ($\sim 4 \times 10^3$ $M_\odot$), number of O-type stars ($\sim$20), and distance from the Sun (2.35 kpc, Shull et al. 2021; Göppl & Preibisch 2022). Tr16 is slightly older (by 1-2 Myr, Smith & Brooks 2008; Preibisch et al. 2011a) and displays a higher intrinsic FUV luminosity ($\log L_{\rm FUV} = 6.8$ $L_\odot$ in comparison to $\log L_{\rm FUV} = 6.3$ $L_\odot$ in Tr 14, Smith 2006), but has a lower stellar density (by a factor of 4 according to the clusters parameters in Cantat-Gaudin & Anders 2020). Only looking at a clusters with high FUV field but low stellar density like Tr16 we can disentangle the role of external photoevaporation in shaping protoplanetary disks evolution. Comparing with the cases of Orion and nearby star-forming regions will provide a quantitative assessment of the expected environmental impact on disk evolution.

The Tr14 MUSE data have shown that it is possible to effectively and efficiently derive spectroscopically photospheric parameters (Chapter 4), as well as luminosities of emission lines related to accretion for young stars in distant star-forming regions (Chapter 6). We have recently applied the similar, successful observational strategy to the Tr16 cluster (Programme ID 110.23YL). The entire cluster was covered with 27 pointings. The main project objectives are:

- To derive the photospheric properties of the stellar population in Tr16 following the procedure used for Tr 14 in Chapter 4 by combining the MUSE data with Class III spectral templates from Manara et al. (2013, 2017), cross-matching

with NIR catalogues (VISTA, HAWK-I, Preibisch et al. 2011a,b, 2014), estimating stellar parameters from evolutionary tracks (e.g., Siess et al. 2000; Bressan et al. 2012; Baraffe et al. 2015).

- To measure mass accretion rates using stellar properties and emission line luminosities (Hα, Hβ, HeI, CaII IRT) converted to accretion luminosities with calibrated empirical relations (e.g., Alcalá et al. 2017).

- To measure the distribution of accretion properties against the distance from massive O-type stars and FUV flux, compare it to the distribution in Tr 14 to constrain the relative importance of external photoevaporation and dynamical disruption of disks

The observing program has been fully completed. With this new, extensive dataset we will compare accretion properties (luminosities, mass rates) to the values obtained in other star-forming regions to find evidence for systematic differences in correlations linking accretion, stellar and disk parameters (e.g., $\dot{M}_{\rm acc}-M_{\rm disk}$ relation, Manara et al. 2016). Verification of the latter requires follow-up observations with ALMA to measure disk masses of accreting stars (see Sec. 7.2.3). Obtaining an unbiased spectroscopic sample requires employment of the IFU technique. VLT/MUSE instrument has proofed to be a perfect tool for studying distant sites of star formation and is being currently applied to many others young clusters.

Appendix

Appendix for Chapter 4

A

A.1 Coordinates correction and cross-match with photometric catalogs

We corrected MUSE coordinates using *Gaia* DR3 catalogue (Gaia Collaboration et al. 2022). The applied corrections are median differences in right ascension and declination between MUSE and *Gaia*. We show distribution of those differences per each pointing in the Figure A.1. Corrections, which need to be added to the original MUSE coordinates, are listed in Table A.1. They range in absolute values between 1.46″ and 5.75″ for right ascension, and between 0.08″ and 2.98″ for declination with typical standard deviation of 0.15″ for right ascension and 0.08″ for declination.

After correcting MUSE coordinates we matched again our sources with *Gaia* to examine the goodness of our astrometry and define the best matching radius between different catalogs. Based on the bimodal distribution of separations between corrected MUSE and *Gaia* coordinates in Figure A.2, we found that the best separation radius for cross-matching is 0.5″. Within it we find all true counterparts and do not include false matches with larger separations. False matches are caused by the crowding, especially large in the cluster center. The same distribution shows that the uncertainty of our astrometry is ∼0.1″.

A.2 Targets detected in more than one pointing

The pointing of observations were designed to overlap. Therefore, some stars are detected multiple times in several pointings. After coordinates correction we identify those targets performing coordinate matching within the catalogue. We define the same separation limit of 0.5″, below which we assume that the two detections correspond to the same object. We find separations in the range from 0.09″ to 0.26″ with median of 0.20″ corresponding to the size of one pixel. In Table A.2 we list all the pairs of double detections.

In most of the cases the I-band magnitudes of both detections are consistent within the uncertainties. That reassures us about the overall good inter-frame calibration. We choose a signal-to-noise ratio in the vicinity of 7500 Å (snr_{750}) as a measure of the quality and use in the analysis the spectrum with higher snr_{750}. In Figure A.4 we show few examples of comparisons between the spectra of the two doubles.

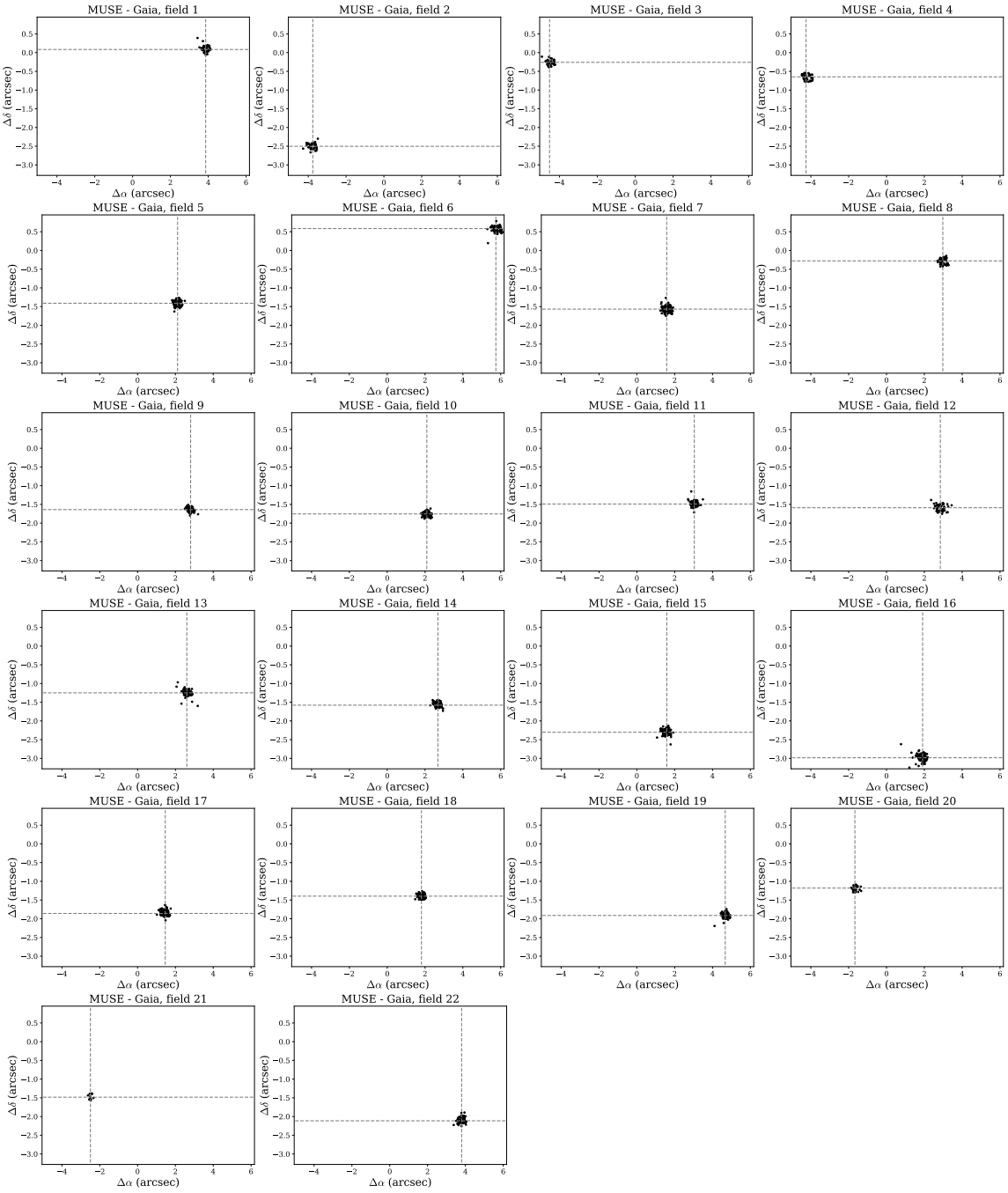

Figure A.1: Distribution of differences in right ascensions and declinations from MUSE and *Gaia* DR3 at each field.

Corresponding snr_{750} are indicated in the legend for each panel. The difference between the spectra is particularly visible in the case of late-type stars. There, the blue part of the spectrum is very vulnerable to the quality of the spectrum. In general, we see no trend between the chosen spectra and weather conditions, although there is a slight preference towards better seeing. We also note that stars located very close to the detector's edge were not detected by the `SExtractor`.

Table A.1: Applied coordinate offsets.

pointing	$\Delta\alpha$ ($''$)	$\Delta\delta$ ($''$)
1	-3.86 ± 0.15	-0.08 ± 0.08
2	3.76 ± 0.19	2.50 ± 0.08
3	4.53 ± 0.15	0.26 ± 0.07
4	4.25 ± 0.17	0.65 ± 0.07
5	-2.12 ± 0.15	1.41 ± 0.08
6	-5.75 ± 0.16	-0.59 ± 0.07
7	-1.58 ± 0.14	1.57 ± 0.07
8	-2.98 ± 0.15	0.28 ± 0.07
9	-2.80 ± 0.14	1.64 ± 0.06
10	-2.09 ± 0.13	1.75 ± 0.06
11	-3.04 ± 0.14	1.49 ± 0.08
12	-2.85 ± 0.21	1.59 ± 0.09
13	-2.60 ± 0.14	1.25 ± 0.06
14	-2.68 ± 0.15	1.58 ± 0.06
15	-1.58 ± 0.15	2.30 ± 0.07
16	-1.91 ± 0.18	2.98 ± 0.08
17	-1.46 ± 0.16	1.86 ± 0.07
18	-1.81 ± 0.12	1.40 ± 0.05
19	-4.67 ± 0.15	1.91 ± 0.07
20	1.67 ± 0.13	1.18 ± 0.06
21	2.49 ± 0.08	1.48 ± 0.06
22	-3.80 ± 0.14	2.11 ± 0.07

Notes. Corrections calculated as a median difference between the *Gaia* and MUSE coordinates. Corrections were added to MUSE coordinates.

A.3 Assessment of the background variability

`SExtractor` provides estimates of stellar fluxes, magnitudes, and sky emission at the positions of the stars. It assumes smooth variation of the sky emission across the whole image. The tool does not provide uncertainty of the background estimation. Since some parts of the cluster covered by our observations are very crowded and sky emission exhibits prominent gaseous structures, local variation of the sky emission might not be smooth. Therefore, we employ another strategy to assess the quality of stellar magnitudes and spectra.

We look at the variation of the background emission estimated for each target by `SExtractor` within the defined area around each star. We checked that the circle with the radius of $20''$ is a large area enough to cover satisfactory number of neighbouring sources, and at the same time, small enough to cover only "local" area. Left panel of Figure A.5 shows how many neighbouring sources for each star is within the radius $20''$. The distribution peaks at 40-50 neighbours giving a satisfactory large statistics. We calculate the standard deviation (std) of the sky emission within this area for every star in our catalogue. Right panel of the Fig. A.5 shows the distribution of the

Table A.2: Double detected sources.

Selected double			Discarded double			
ID	snr_{750}	I-band (mag)	ID	snr_{750}	I-band (mag)	separation ($''$)
2_14	17.02	19.87 ± 0.02	1_2	12.36	19.95 ± 0.02	0.22
1_29	63.08	17.808 ± 0.002	2_33	62.55	17.784 ± 0.003	0.20
1_35	79.62	17.121 ± 0.001	2_39	44.84	17.694 ± 0.003	0.22
1_55	6.53	21.09 ± 0.05	2_66	3.64	21.07 ± 0.06	0.26
1_62	13.81	20.04 ± 0.02	2_69	10.24	20.06 ± 0.02	0.20
1_90	8.61	20.65 ± 0.03	2_135	7.14	20.61 ± 0.04	0.17
2_162	77.77	16.459 ± 0.001	1_118	71.39	16.763 ± 0.001	0.25
2_177	8.00	20.43 ± 0.03	1_140	7.90	20.27 ± 0.02	0.18
3_4	6.80	20.70 ± 0.05	4_2	5.09	20.53 ± 0.04	0.22
3_84	5.18	20.75 ± 0.05	4_45	4.27	20.78 ± 0.05	0.20
3_184	15.78	19.39 ± 0.02	4_116	14.32	19.39 ± 0.01	0.22
7_12	18.22	19.69 ± 0.08	10_280	11.33	19.77 ± 0.03	0.26
8_23	27.06	19.34 ± 0.01	7_33	20.22	19.46 ± 0.06	0.20
13_140	51.00	17.94 ± 0.01	7_164	21.99	18.41 ± 0.02	0.17
7_222	20.56	19.72 ± 0.08	8_122	8.48	19.75 ± 0.01	0.25
8_127	23.12	19.11 ± 0.01	7_237	15.69	19.12 ± 0.05	0.18
8_182	53.25	18.544 ± 0.004	7_376	35.47	18.62 ± 0.03	0.22
8_1	6.40	20.79 ± 0.03	9_7	5.29	20.75 ± 0.04	0.26
10_48	10.51	20.41 ± 0.05	9_19	8.79	19.98 ± 0.02	0.26
10_86	47.456	18.16 ± 0.01	9_43	42.22	18.235 ± 0.004	0.22
10_100	15.94	19.60 ± 0.03	9_54	14.83	19.56 ± 0.01	0.26
10_126	18.29	19.45 ± 0.02	9_67	16.14	19.45 ± 0.01	0.26
10_232	73.77	17.308 ± 0.003	9_144	65.14	17.383 ± 0.002	0.17
10_266	15.93	19.66 ± 0.03	9_180	11.07	19.65 ± 0.01	0.25
16_39	50.09	17.51 ± 0.01	10_22	42.31	17.560 ± 0.004	0.15
16_43	73.70	16.008 ± 0.002	10_27	73.43	15.965 ± 0.001	0.24
16_68	34.34	18.12 ± 0.01	10_65	28.41	18.01 ± 0.01	0.25
10_72	79.62	17.696 ± 0.005	16_79	35.85	17.84 ± 0.01	0.18
10_87	80.83	17.716 ± 0.005	16_89	46.28	17.77 ± 0.01	0.20
16_98	20.65	18.99 ± 0.02	10_102	19.55	18.96 ± 0.01	0.25
10_140	50.56	18.02 ± 0.01	16_149	40.08	18.07 ± 0.01	0.24
10_165	92.15	16.245 ± 0.001	16_183	73.15	16.267 ± 0.002	0.25
10_255	28.86	18.721 ± 0.012	16_256	25.06	18.72 ± 0.02	0.18
12_67	89.56	14.873 ± 0.001	11_76	85.15	14.9120 ± 0.0002	0.20
11_104	7.77	20.37 ±0.03	17_99	5.86	20.47 ± 0.06	0.18
13_3	28.83	18.50 ± 0.01	16_284	27.22	18.11 ± 0.01	0.21
13_4	6.61	20.65 ± 0.07	16_286	5.07	20.41 ± 0.09	0.23
16_6	96.93	16.546 ± 0.002	13_6	88.40	16.39 ± 0.001	0.22
13_29	11.36	20.26 ± 0.05	14_53	10.03	20.36 ± 0.03	0.24
14_140	11.75	19.98 ± 0.02	13_144	10.61	20.12 ± 0.04	0.19
14_301	16.92	19.78 ± 0.02	13_361	8.05	19.28 ± 0.02	0.14
16_2	69.07	16.325 ± 0.002	15_5	47.33	16.138 ± 0.001	0.15
16_57	13.90	19.47 ± 0.04	15_59	5.67	19.49 ± 0.03	0.18
16_241	45.60	18.11 ± 0.01	15_350	23.01	17.86 ± 0.01	0.09
16_270	14.70	19.66 ± 0.04	15_429	4.96	19.39 ± 0.02	0.15
18_138	11.89	20.08 ± 0.03	17_87	10.84	20.02 ± 0.04	0.21
18_177	37.29	18.65 ± 0.01	17_112	24.83	18.57 ± 0.01	0.15
18_246	10.48	20.34 ± 0.04	22_142	6.51	20.10 ± 0.06	0.23
20_23	6.83	20.42 ± 0.05	19_24	5.19	20.36 ± 0.09	0.17
20_35	23.49	19.61 ± 0.02	19_33	10.86	19.54 ± 0.04	0.22
20_65	16.53	19.69 ± 0.02	19_60	11.32	19.59 ± 0.05	0.16
20_80	15.67	19.55 ± 0.02	19_76	11.60	19.54 ± 0.04	0.16
19_84	53.84	17.62 ± 0.01	20_95	51.17	17.623 ± 0.004	0.24
20_113	68.79	17.776 ± 0.004	19_100	40.30	17.82 ± 0.01	0.13
21_22	6.49	20.42 ± 0.02	22_14	6.15	20.38 ± 0.08	0.19

Notes. Table is separated into two part: left part lists ID, snr at 750 nm, and I-band magnitude for measurements used in the analysis, while right part lists the same properties of the discarded measurements. Magnitudes are corrected to match those from WFI catalogue (Beccari et al. 2015). Additionally, last column shows separation between the two measurements. One MUSE pixel has width of $0.2''$.

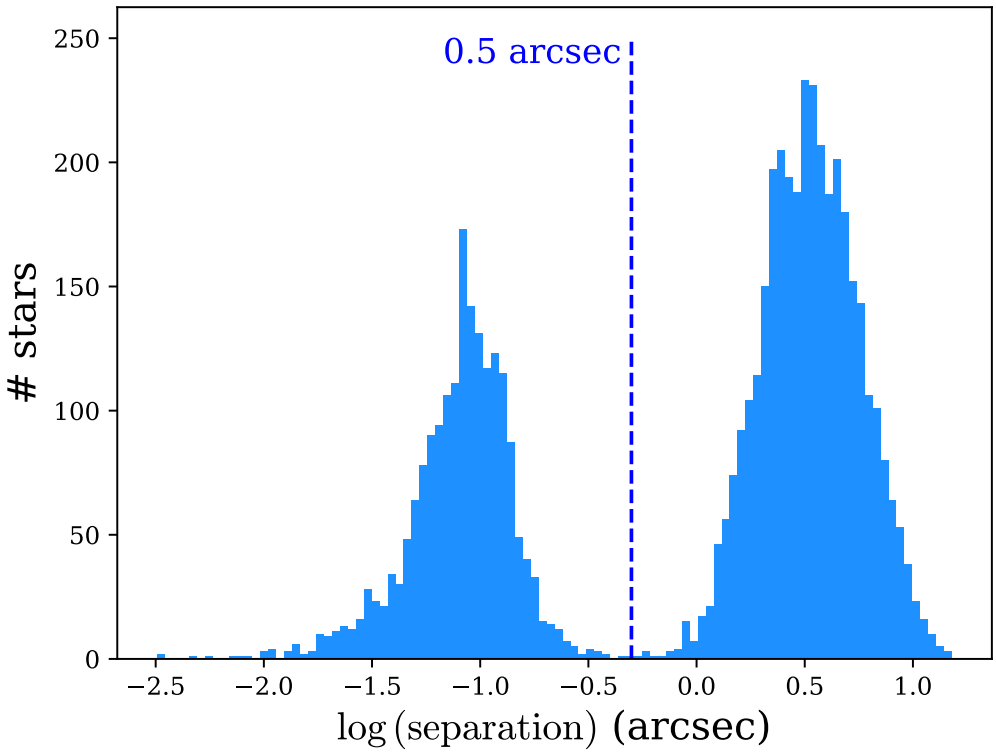

Figure A.2: Separations in arcsec between MUSE and *Gaia* DR3 stars in logarithmic scale. MUSE catalogue here contains data points as of Sec. 4.2.2.1, before removing uncertain photometry. Overplotted is the threshold separation of 0.5″ used in this work.

std measured in flux units of erg s^{-1} cm^{-2} Å^{-1}. We use such defined variability to select a robust photometry: we discard measurement of the stellar flux that is below the threshold of three sigma (here σ=std). We initially perform this exercise in I-band, as the presence of this magnitude is our definition of detection, and repeat for R and V-bands. Since our stars have late spectroscopic types, they appear fainter in bluer bands, therefore, there are fewer photometric measurements in R and V-bands than in the I-band. That can be noticed in our CMDs in Fig. 4.4 and 4.8. We note that our approach is very conservative: spectra of some of the removed targets from the final catalogue have high enough snr for spectral classification. For this reason, we list in Table A.3 sources removed due to the uncertain photometry in I-band caused by the high background variation. We include in the Table uncertain photometry from all bands. The columns "snr$_{I,\mathrm{bkg}}$", "snr$_{R,\mathrm{bkg}}$" and "snr$_{V,\mathrm{bkg}}$" show ratios between stellar flux and background variation in a given band, and therefore can be used as indicators of photometric certainty.

A.4 MUSE photometry

The MUSE I, R, and V-band images in flux units were produced by collapsing the 3D MUSE cubes within the corresponding wavelength range and applying the filter transmission curve embedded in the ESO reduction pipeline (Weilbacher et al. 2020). We performed the aperture photometry with `SExtractor` extracting stellar fluxes from the images and converting them to magnitudes using Vega zero points

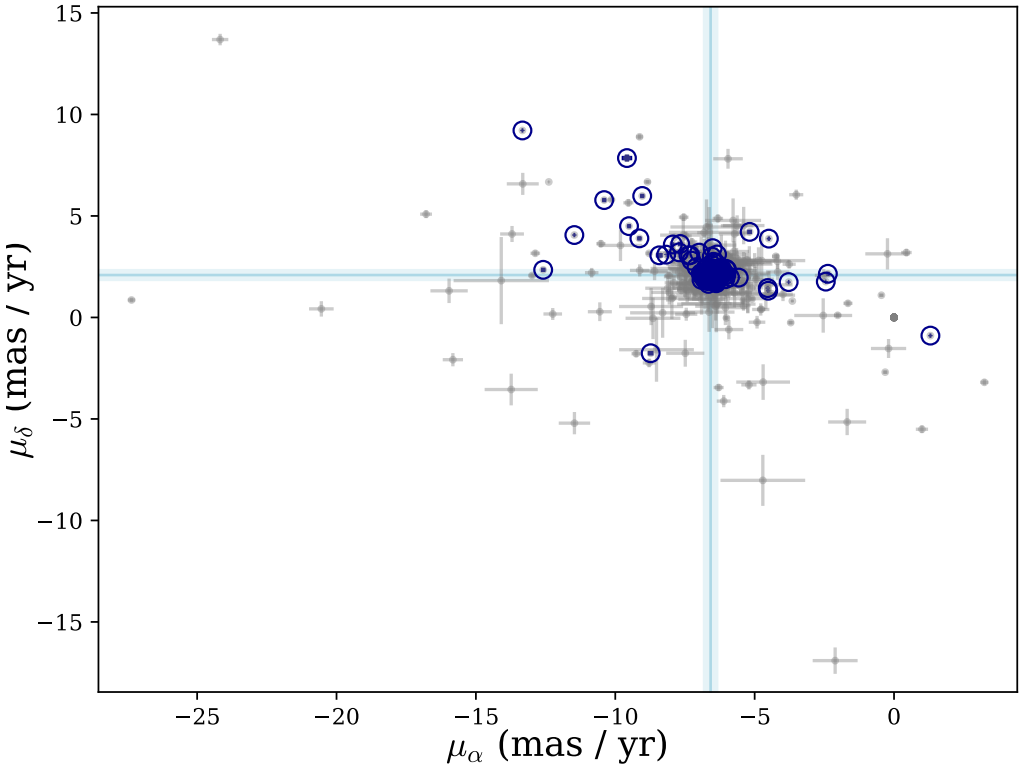

Figure A.3: Proper motions of *Gaia* counterparts. We show points with available proper motion measurements (grey dots) and with good astrometry (dark blue circles) (see Sec. 4.2.2.6 for details). Uncertainties of the latter points are smaller than the symbol sizes. Foreground and possibly contaminated stars are excluded. For reference, we also mark group proper motions from Berlanas et al. (2023) derived from *Gaia* EDR3 astrometry of OB stars in Tr 14.

written in the headers by the pipeline. Even though our observations were flux calibrated using standard stars, we found that our magnitudes deviate from those measured with Wide Field Imager by Beccari et al. (2015) (described below). As those measurements are well calibrated, we correct MUSE magnitudes so they match those from WFI. We define a correction as a difference between MUSE and WFI magnitudes and subtract it from MUSE photometry. Corrections for each field and each band are listed in the Table A.4. In I-band they range from 0.29 mag in field No. 5 to 1.27 mag in field No. 15. We also check whether a colour term is present in MUSE photometry. Fig. A.6 shows an example of this examination with the result of no colour term between I and R-bands.

The highest values of corrections are in fields No. 15, 12, and 19 ($\gtrsim$ 1.0 mag). Pointings No. 12 and 19 have the worst seeing from all used observations, which may explain the difference in the estimated flux. No. 12 suffers additionally from the presence of two very bright stars in the center of the field, whose brightness impact all neighbouring stars in the image, possibly to a larger extent than assumed in this work. No. 15 is one of the most crowded pointings, although it does not cover the very center of the Tr 14. The presence of few bright stars and prominent extincted feature in the lower right corner of the field might be another explanation of the large magnitude difference. If, as the result, the background estimation from

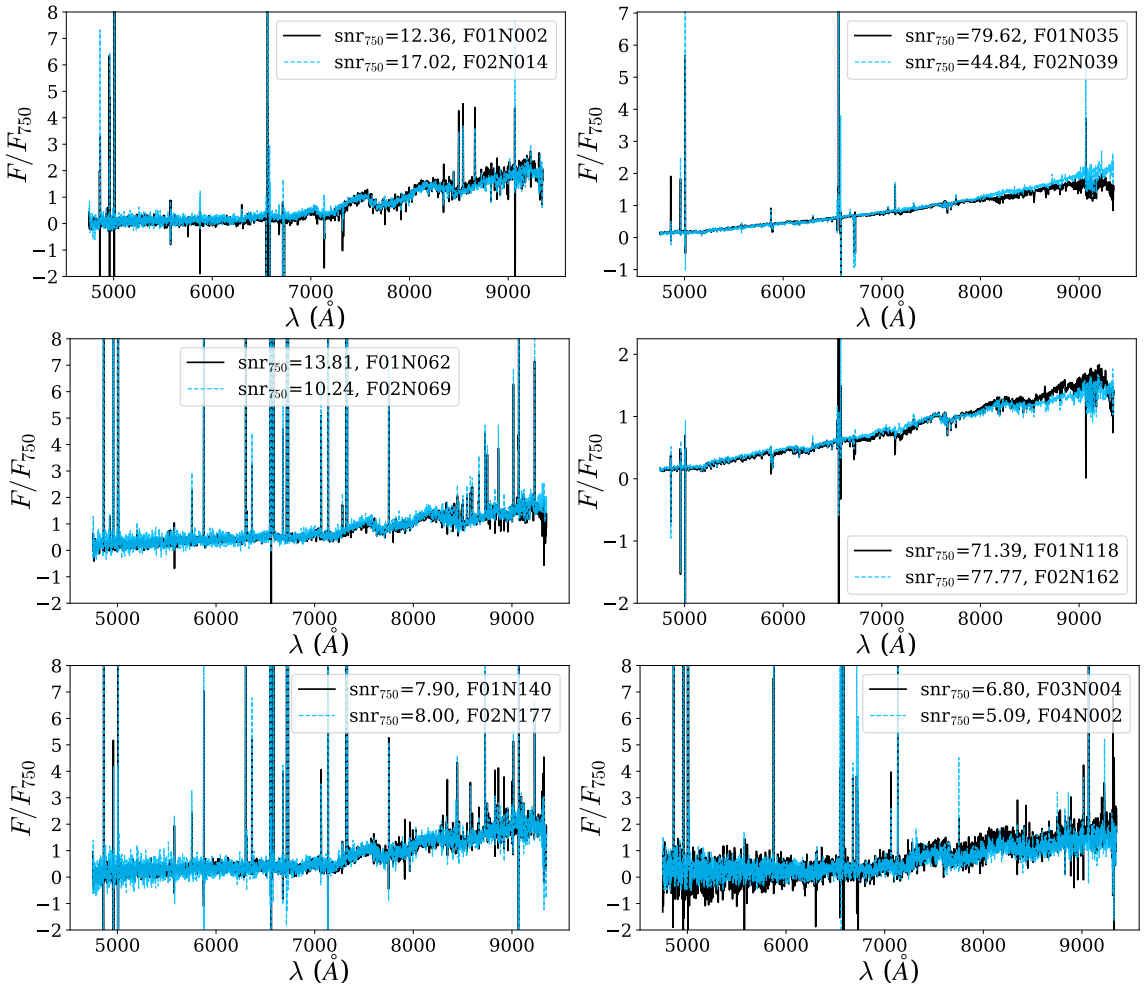

Figure A.4: Examples of spectra of stars observed twice. Spectra were normalised to the flux at 7500 Å. Label indicates source identifier and its snr around 7500 Å used to decide which spectrum to keep for the analysis.

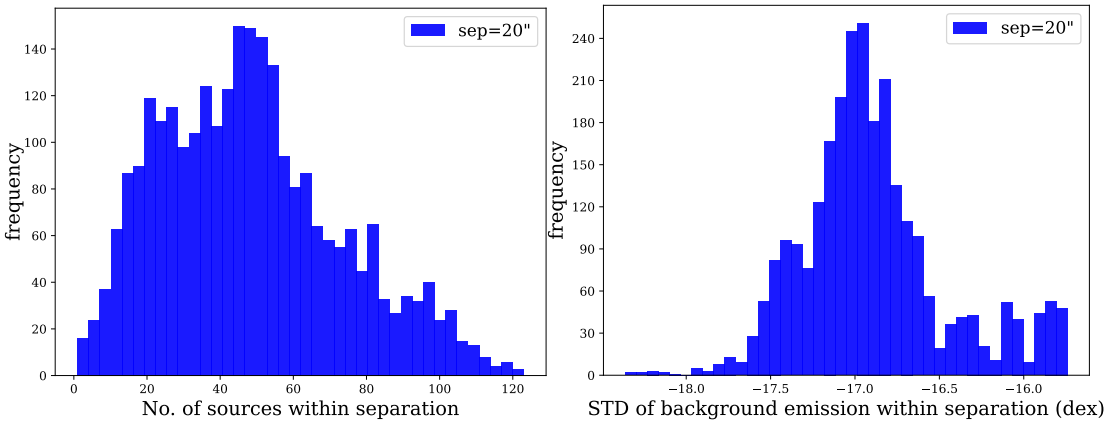

Figure A.5: Left: distribution of number of sources within a separation of 20″ from a given star. Right: distribution of the standard deviation (std) of background emission estimated in I-band from the individual measurements within 20″ from the given star.

the `SExtractor` is incorrect, that would lead to the uncertain stellar photometry. Weather conditions were moderate (thin clouds) which might also have affected the observations.

Table A.3: Parameters of stars removed from the catalogue due to the high background variation.

ID	coordinates (h:m:s d:m:s)	I-band (mag)	R-band (mag)	V-band (mag)	$\mathrm{snr}_{I,\mathrm{bkg}}$	$\mathrm{snr}_{R,\mathrm{bkg}}$	$\mathrm{snr}_{V,\mathrm{bkg}}$	possible_frg_bkg	gaia_flag	wfi_flag	VISTA_flag	hawki_flag	spitzer_flag	chandra_flag	NIR excess	SpT	T_{eff} (K)	A_V (mag)	r_{7500}	$\log(L_{\mathrm{bol}}/L_\odot)$	$M_{*,\mathrm{PARSEC}}$ $(M_\odot)$	$\mathrm{Age}_{\mathrm{PARSEC}}$ (Myr)	$M_{*,\mathrm{BHAC}}$ $(M_\odot)$	$\mathrm{Age}_{\mathrm{BHAC}}$ (Myr)
F01N008	10:44:07.40 -59:29:11.60	19.29±0.01	20.80±0.04	22.01±0.04	2.42	0.36	0.37	False	Poor	True	True	True	False	False	False	M3.0$^{+0.0}_{-0.0}$	3415$^{+9}_{-58}$	0.00$^{+0.03}_{-0.00}$	0.02$^{+0.00}_{-0.00}$	-1.09$^{+0.11}_{-0.22}$	0.60	0.33	23.6	6.8
F01N011	10:44:11.86 -59:29:12.11	20.94±0.03	–	–	1.10	–	–	False	None	False	True	True	False	False	True	M4.0$^{+1.5}_{-1.5}$	3270$^{+248}_{-95}$	3.50$^{+1.02}_{-0.05}$	0.00$^{+0.58}_{-0.00}$	-0.99$^{+0.32}_{-1.19}$	0.48	0.23	8.9	2.3

Notes. The first column gives IDs of the detected sources, the second – coordinates. The third, fourth, and fifth columns give apparent magnitudes in I, R, and V-band, respectively. The sixth, seventh, and eighth columns – signal-to-noise of the flux with respect to the background variation in a given band, as indicated by the lower script (see Sec. 4.2.2.4 for details). The ninth marks possible foreground or background stars (see Sec. 4.3.1 for definitions). The next five columns flag matches with other catalogs: *Gaia* (Gaia Collaboration et al. 2022), WFI (Beccari et al. 2015), VISTA (Preibisch et al. 2014), HAWK-I (Preibisch et al. 2011a,b), *Spitzer* (Povich et al. 2011), and *chndra* (Preibisch et al. 2011a; Townsley et al. 2011). The following indicates if the star has an NIR excess as defined by Zeidler et al. (2016). In the consecutive nine columns are given stellar parameters: spectral type, effective temperature, visual extinction, constant veiling at 7500 Å, bolometric luminosity, and stellar mass and stellar age estimated from PARSEC (Bressan et al. 2012) and Baraffe et al. (2015) / Siess et al. (2000) tracks, as indicated by the subscript. A full version of this table will be available at the CDS upon publication. The first few rows are shown as an example.

The uncertainty of magnitude corrections, measured as a standard deviation of magnitude differences, is ∼0.1 mag for most of the pointings. It also usually increases towards bluer bands. However, smaller number of available magnitudes in bluer bands due to the high background variability can cause underestimation of those uncertainties. Overall, the offset of the MUSE magnitudes seem to be relatively constant within the pointing. We add linearly correction uncertainties to the magnitude uncertainties of our sources and report them in the catalogues (Tab. 4.1 & A.3).

We show the resulting distributions of the corrected MUSE magnitudes in Figure A.7. The distribution of I-band magnitudes peaks at 18.01 mag, R-band – 17.60 mag, and V-band – 17.58 mag. The number of magnitudes in each band decreases bluewards from 780 in I-band, through 294 in R-band, to 223 in V-band.

A.5 Spectral templates

Here, we list all Class III stars and their properties used in spectral classification as spectral templates (Table A.5). Spectral types for those stars later than K5 were obtained based on depth of molecular absorption bands (TiO, VO and CaH) and few photospheric lines (e.g., NaI, CaI, MgI, etc.) present in optical part of the spectra (Manara et al. 2013). Earlier K-type stars were identified using the spectral indices introduced by Herczeg & Hillenbrand (2014), while G-type stars were identified based on the difference at 5150 Å of continuum estimated between 4600 and 5400 Å, and 4900 and 5150 Å (Herczeg & Hillenbrand 2014). Effective temperatures (T_{eff}) were derived from spectral types using relations from Luhman et al. (2003) for M-type objects and Kenyon & Hartmann (1995) for K- and G-type stars. Most of the templates have none or negligible extinction ($A_{\mathrm{V}} < 0.5$ mag, Manara et al. 2017);

Table A.4: Photometric corrections.

#	I (mag)	R (mag)	V (mag)
1	0.47 ± 0.09	0.57 ± 0.08	0.58 ± 0.08
2	0.43 ± 0.11	0.42 ± 0.12	0.41 ± 0.15
3	0.36 ± 0.12	0.34 ± 0.18	0.37 ± 0.21
4	0.52 ± 0.06	0.58 ± 0.07	0.55 ± 0.07
5	0.29 ± 0.22	0.26 ± 0.12	0.22 ± 0.18
6	0.43 ± 0.14	0.47 ± 0.11	0.46 ± 0.11
7	0.44 ± 0.07	0.52 ± 0.11	0.56 ± 0.14
8	0.37 ± 0.25	0.42 ± 0.25	0.42 ± 0.17
9	0.49 ± 0.15	0.58 ± 0.14	0.62 ± 0.13
10	0.46 ± 0.11	0.53 ± 0.08	0.55 ± 0.06
11	0.44 ± 0.18	0.48 ± 0.36	0.48 ± 0.41
12	1.07 ± 0.05	1.18 ± 0.05	1.17 ± 0.08
13	0.37 ± 0.27	0.42 ± 0.31	0.41 ± 0.15
14	0.47 ± 0.08	0.54 ± 0.10	0.49 ± 0.13
15	1.27 ± 0.09	1.33 ± 0.06	1.31 ± 0.06
16	0.77 ± 0.11	0.86 ± 0.14	0.91 ± 0.15
17	0.65 ± 0.10	0.74 ± 0.13	0.75 ± 0.21
18	0.16 ± 0.19	0.20 ± 0.10	0.18 ± 0.09
19	0.93 ± 0.37	1.01 ± 0.02	1.05 ± 0.02
20	0.50 ± 0.03	0.58 ± 0.04	0.62 ± 0.06
21	0.54 ± 0.02	0.61 ± 0.05	0.65 ± 0.12
22	0.62 ± 0.27	0.72 ± 0.36	0.75 ± 0.06

Notes. Corrections are defined as mean differences between MUSE and WFI (Beccari et al. 2015) magnitudes. Provided uncertainties are standard deviations of the difference between MUSE and WFI magnitudes.

spectra were dereddened before analysis assuming the extinction law from Cardelli et al. (1989) and $R_V = 3.1$. All the details of the data reduction, calibration, and spectral classification are provided in the original papers.

A.6 Spectral classification

In this Appendix, we list spectral indices used for spectral classification of K- and late G-type stars, as well as we explain more in detail estimation of uncertainties based on $\chi^2_{\rm red}$ maps.

Indices were defined, calibrated, and tested on Class III spectra listed in the Table A.5. Each spectral index is defined as an equivalent width of a given line or a line ratio of the two. Table A.6 shows our indices together with their weights. The final spectral type is a weighted average of indices. Indices with values outside the applicable range of spectral types (indicating type earlier than G8 or later than M0)

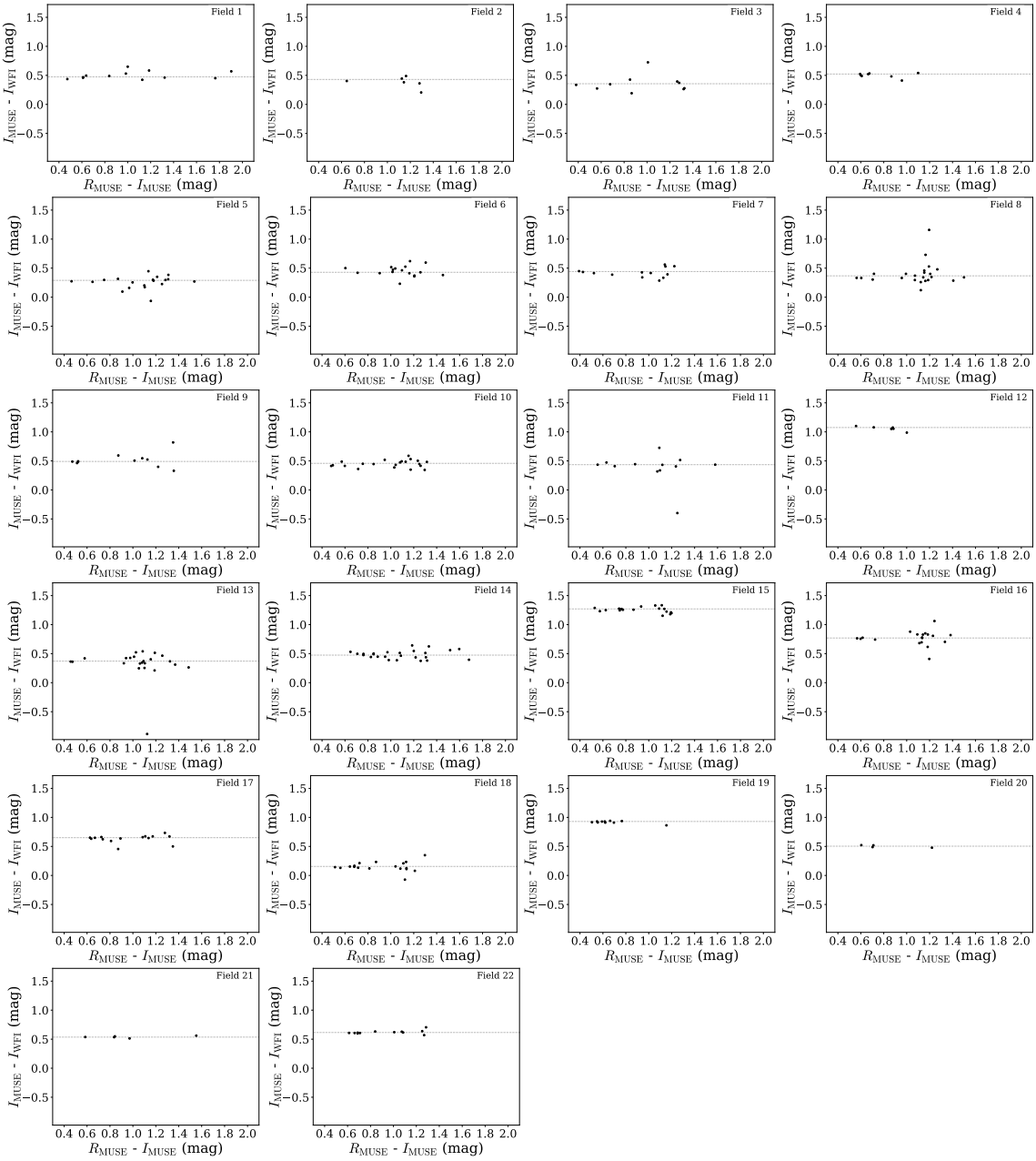

Figure A.6: Differences between MUSE and WFI (Beccari et al. 2015) I-band photometry as a function of MUSE colour $R - I$. Every panel represents separate field, as indicated in the upper right corner. Grey dashed line shows mean difference between I-band magnitudes applied to MUSE photometry as magnitude correction.

were excluded from the average to avoid extrapolation. We required at least 3 valid indices to estimate the spectral type. Additionally, we included in our list the index from Oliveira et al. (2003); Jeffries et al. (2007), TiO 7140Å. It is applicable only to the stars with spectral type later than K5.

Extinction and veiling at 7500Å, as well as spectral type for M-type stars, were estimated based on $\chi^2_{\rm red}$ maps. Figure A.8 shows the examples of such maps for an M-type star, and Figure A.9 for an K-type star. At each time, we examine the distribution of $\chi^2_{\rm red}$ in relation to a given two out of three variables in our problem

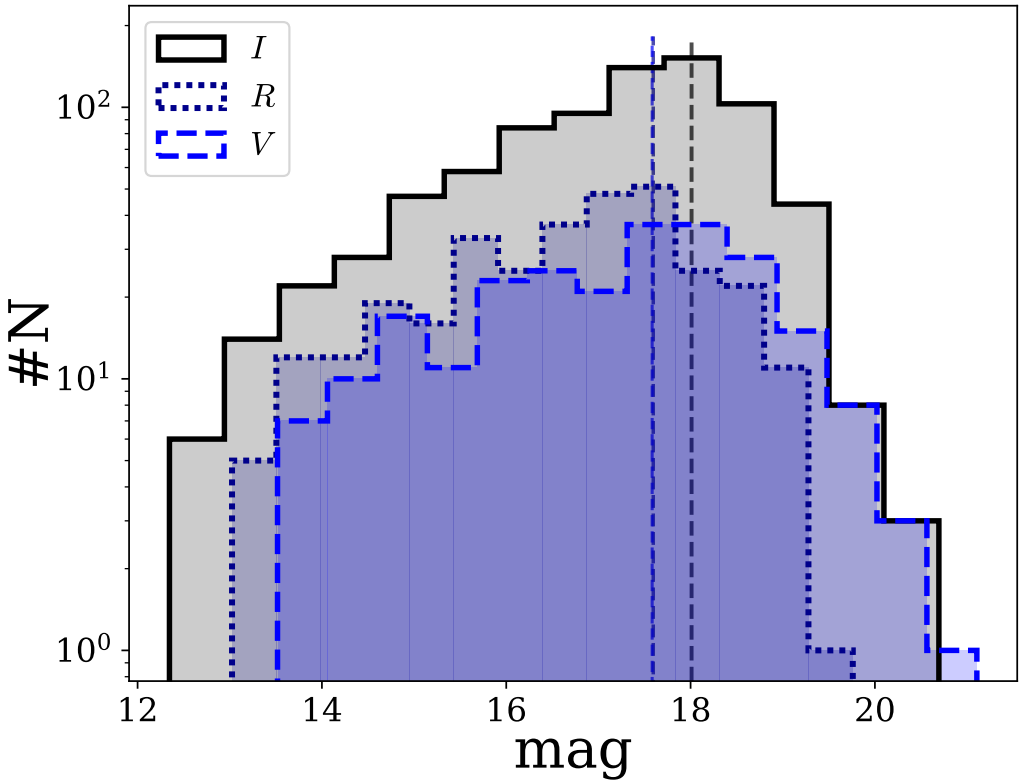

Figure A.7: Distribution of corrected MUSE magnitudes. Colours indicate different photometric bands as stated in the upper left corner of the figure. Dashed lines show the turn-over point of the distributions located at: 18.01 mag (I-band), 17.60 mag (R-band), 17.58 mag (V-band).

(spectral type, SpT; visual extinction, A_V, and constant veiling at 7500 Å, r_{750}). Hence, for M-type stars, there are three χ^2_{red} maps for each star. For K-type stars, where uncertainties of the spectral type are assigned differently, there is only one χ^2_{red} map constructed based on the Class III template closest with the SpT to the SpT of a given star. The best set of parameters' values is indicated by the minimum value of the χ^2_{red}. The 1-sigma contours drawn on top of the distributions are the basis for the uncertainty estimates. We adopt the projections of the contours onto the axis as the uncertainties of the given parameters. Fig. A.8 and A.9 show 1-sigma contours, and additionally also 2-, and 3-sigma ones, for reference.

Estimating uncertainties based on our χ^2_{red} distributions is itself prone to the uncertainty. The sampling of spectral templates used for classification is not even causing discontinuous, step-like shape of 1-sigma contours. We do not propagate errors outside the range of adopted values for our parameters. As a result, when the best value is close to the edge if this range, one of the uncertainties will be underestimated. We observe high degeneracy between veiling and extinction, as well as high uncertainty of the value of the veiling, especially in hotter stars. Therefore, our veiling estimates might be inaccurate and we recommend to treat them as the rough indications of the presence of the veiling and its prominence.

Table A.5: Properties of Class III stars used as spectral templates.

Object	SpT	$T_{\rm eff}$ (K)	Reference
RXJ1508.6-4423	G8.0	5520	2
RXJ1526.0-4501	G9.0	5410	2
HBC407	K0.0	5200	2
RXJ1515.8-3331	K0.5	5050	2
PZ99J160550.5-253313	K1.0	5000	2
RXJ0457.5+2014	K1.0	5000	2
RXJ0438.6+1546	K2.0	4900	2
RXJ1547.7-4018	K3.0	4730	2
RXJ1538.6-3916	K4.0	4590	2
RXJ1540.7-3756	K6.0	4205	2
RXJ1543.1-3920	K6.0	4205	2
SO879	K7.0	4060	1
TWA6	K7.0	4060	1
Tyc7760283_1	M0.0	3850	1
TWA14	M0.5	3780	1
RXJ1121.3-3447_app2	M1.0	3705	1
RXJ1121.3-3447_app1	M1.0	3705	1
CD_29_8887A	M2.0	3560	1
Sz122	M2.0	3560	1
TWA15_app2	M3.0	3415	1
TWA7	M3.0	3415	1
TWA15_app1	M3.5	3340	1
Sz94	M4.0	3270	1
Sz121	M4.0	3270	1
SO797	M4.5	3200	1
SO641	M5.0	3125	1
Par_Lup3_2	M5.0	3125	1
SO925	M5.5	3060	1
SO999	M5.5	3060	1
Sz107	M5.5	3060	1
Par_Lup3_1	M6.5	2935	1
LM717	M6.5	2935	2
J11195652-7504529	M7.0	2880	2
LM601	M7.5	2795	2
CHSM17173	M8.0	2710	2
TWA26	M9.0	2400	1
DENIS1245	M9.5	2330	1

Notes. References: (1) Manara et al. (2013); (2) Manara et al. (2017).

A.7 Stellar parameters

Selection of stellar evolutionary models impact values of derived stellar parameters. In Section 4.4.2 we constructed HR diagram and employed PARSEC v1.2S tracks (Bressan et al. 2012) to estimated masses and ages of Tr 14 members. Here, we

Table A.6: Indices used for spectral classification of K- and late G-type stars.

Index	weight	G8	G9	K0	K1	K2	K3	K4	K5	K6	K7	M0	Uncertainty	Source
NaI 5890Å	2.0	1.424	1.971	2.519	3.066	3.613	4.160	4.708	5.255	5.802	6.349	6.896	0.112	This work
CaI 6162Å	1.0	0.850	1.029	1.207	1.386	1.564	1.743	1.921	2.099	2.278	2.456	2.635	0.033	This work
CaI 6103Å	1.0	0.323	0.358	0.393	0.428	0.463	0.498	0.533	0.567	0.602	0.637	0.672	0.018	This work
NaI 8183Å	1.0	0.279	0.325	0.372	0.418	0.465	0.511	0.558	0.604	0.651	0.697	0.743	0.008	This work
NaI 8195Å	1.0	0.357	0.412	0.468	0.523	0.578	0.634	0.689	0.744	0.800	0.855	0.910	0.016	This work
CaI 8690Å	2.0	0.315	0.358	0.401	0.444	0.487	0.530	0.573	0.616	0.659	–	–	0.016	This work
MgI 8806Å	1.75	0.665	0.713	0.761	0.809	0.857	0.905	0.954	1.002	1.050	–	–	0.029	This work
MgII 8824Å	2.25	0.230	0.263	0.296	0.329	0.362	0.395	0.428	0.460	0.493	0.526	0.559	0.010	This work
KI 7665Å/7699Å	1.0	2.531	2.442	2.354	2.265	2.177	2.088	2.000	1.912	1.823	1.735	1.646	0.111	This work
CaII 8663Å/CaI 8690Å	1.75	3.639	3.447	3.256	3.065	2.873	2.682	2.490	2.299	2.108	1.916	1.725	0.189	This work
MgI 8806Å/MgII 8824Å	1.25	2.834	2.722	2.611	2.499	2.387	2.276	2.164	2.052	1.941	1.829	1.717	0.137	This work
TiO 7140Å	1.5	–	–	–	–	–	–	–	-2	-1.5	-1	0	0.1	Jeffries et al. (2007) Oliveira et al. (2003)

Notes. Indices listed here are equivalent widths and their ratios, as indicated by the index name. Values were obtained from linear fitting of equivalent widths to spectral types. Listed uncertainties represent the uncertainty of this fit. The final spectral type is a weighted average of corresponding spectral types to each index and their weights. Indices and weights were calibrated on the Class III spectra listed in the Tab. A.5.

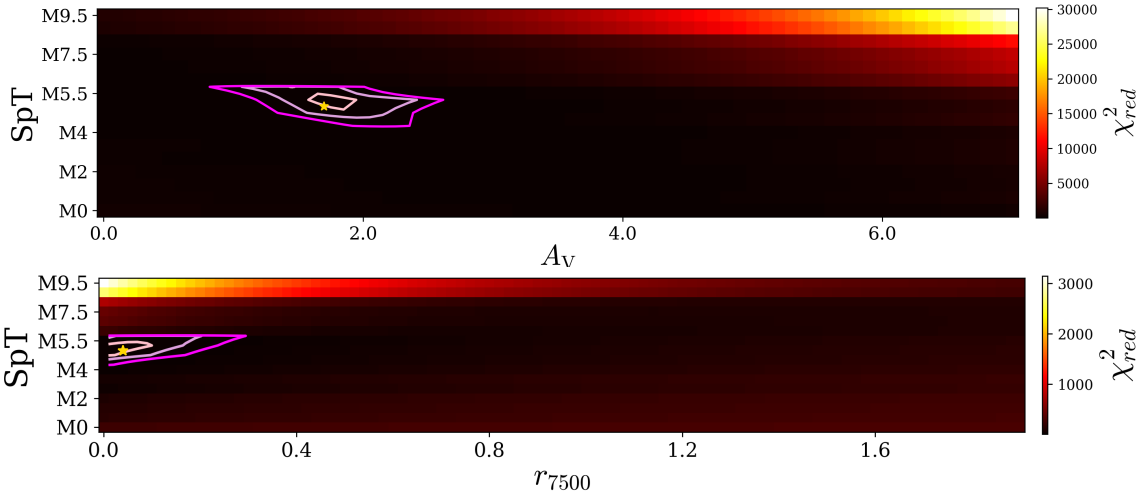

Figure A.8: The $\chi^2_{\rm red}$ maps corresponding to the fit presented in Fig. 4.5. Top: $\chi^2_{\rm red}$ as a function of spectral type and visual extinction. Bottom: $\chi^2_{\rm red}$ as a function of spectral type and veiling. The yellow star marks the best-fit position in the parameter space. Contours represent 1, 2, and 3σ levels.

investigate how the choice of tracks impact our results on cluster properties. We use tracks developed for young stars from Siess et al. (2000) and Baraffe et al. (2015). The latter are dedicated to low- and very-low mass stars and therefore do not cover star more massive than $\sim$1 $M_\odot$. Thus, we combine them with tracks from Siess et al. (2000) and define a border of spectral type K5 between usage of the two models. Neither model explores ages below 0.5 Myr. We restricted the comparison up to 30 Myr, as we do not expect true Tr 14 members to be that old.

We present HR diagram in Figure A.10. Comparison with HR diagram using PARSEC tracks in Figure 4.9 shows differences in stellar masses at the lower end. Figure A.11 compares mass distributions of the two sets of tracks. Distribution of PARSEC masses is shifted with respect to the Baraffe et al. (2015) / Siess et al. (2000) ones.

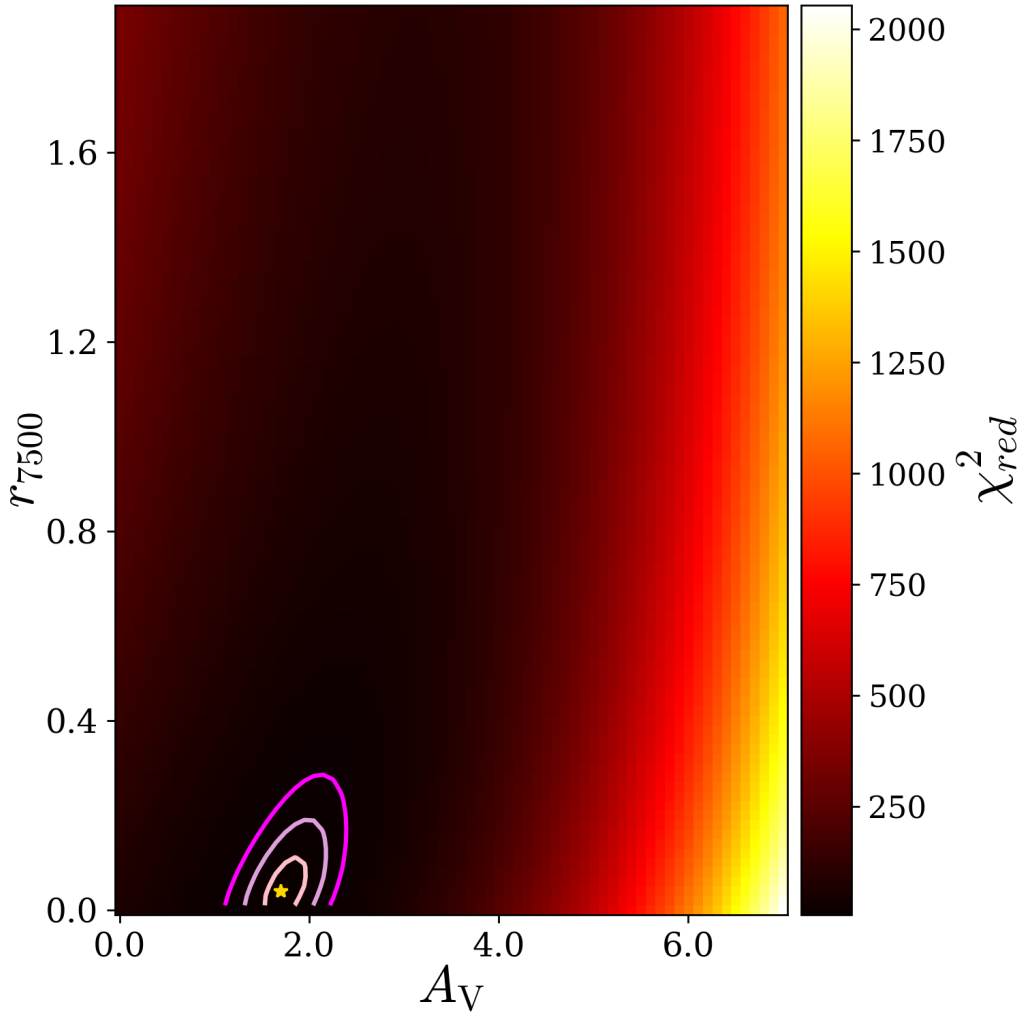

Figure A.8: (Cont.) The $\chi^2_{\rm red}$ as a function of veiling and extinction. The yellow star marks the best-fit position in the parameter space. Contours represent 1, 2, and 3σ levels.

Differences are the most prominent between PARSEC and Baraffe et al. (2015) models up to a factor of ∼2. Masses from PARSEC and Siess et al. (2000) seem to be consistent with some spread.

The PARSEC models span wider range of stellar ages at the lower end, down to 0.1 Myr, while Baraffe et al. (2015) and Siess et al. (2000) stop at 0.5 Myr. Therefore, the age distribution from Baraffe et al. (2015) / Siess et al. (2000) set are affected by the artificial overdensity at the edge of the distribution (Figure A.12). That feature motivated removal of histogram bars at the borders from the analysis. As we highlighted in Section 4.4.3, the same method of estimating the cluster age applied to two sets of evolutionary models yields the same within uncertainties cluster age of 1 Myr. We show corresponding distribution in Figure A.13. Individual measurements are affected by the uncorrelated differences between PARSEC and Baraffe et al. (2015), up to a factor of ∼3. However, Siess et al. (2000) isochrones seem to be offset by a constant factor of 2 towards younger ages.

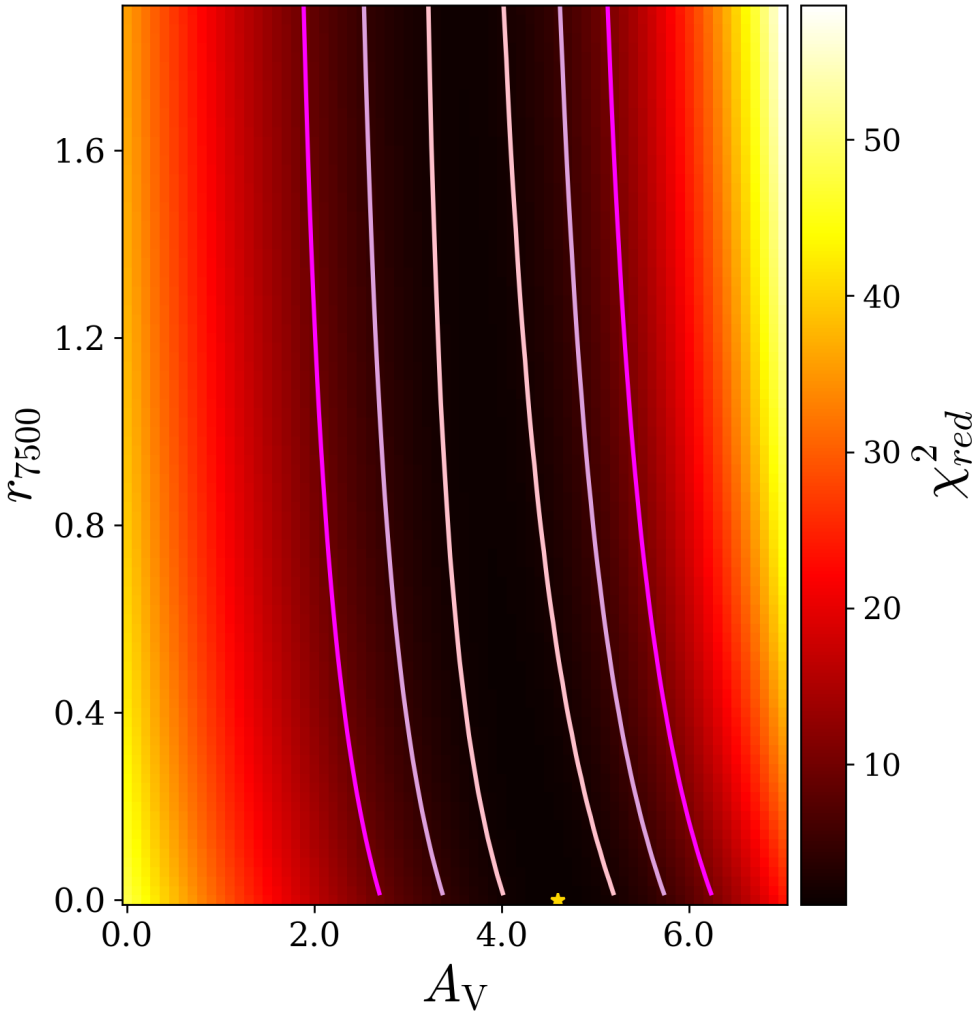

Figure A.9: The χ^2_{red} map as a function of veiling and extinction corresponding to the fit presented in Fig. 4.6. The yellow star marks the best-fit position in the parameter space. Contours represent 1, 2, and 3σ levels.

We have chosen PARSEC models for the analysis because they allow homogeneous treatment of all stars in our sample spamming wide range of masses. We note however, that individual estimates of stellar parameters are uncertain by an unknown value. The short comparison here between two sets of tracks showed that values of both masses and ages can differ by a factor of few depending on a chosen tracks. This significantly exceeds any possible estimates of errors of those parameters done accounting for observational uncertainties and tabulation of spectral templates used here. Therefore, in Tables 4.1 and A.3 we only report estimated values as true uncertainties are impossible to asses.

A.8 Young stars in Trumpler 14

Here, we complete the discussion in Section 4.4.3 showing the distribution of NIR excess and X-ray sources on the CMD (Fig. A.14) and the sky (Fig. A.15). To define NIR excess stars, we collect the NIR photometry from Preibisch et al. (2011a) and

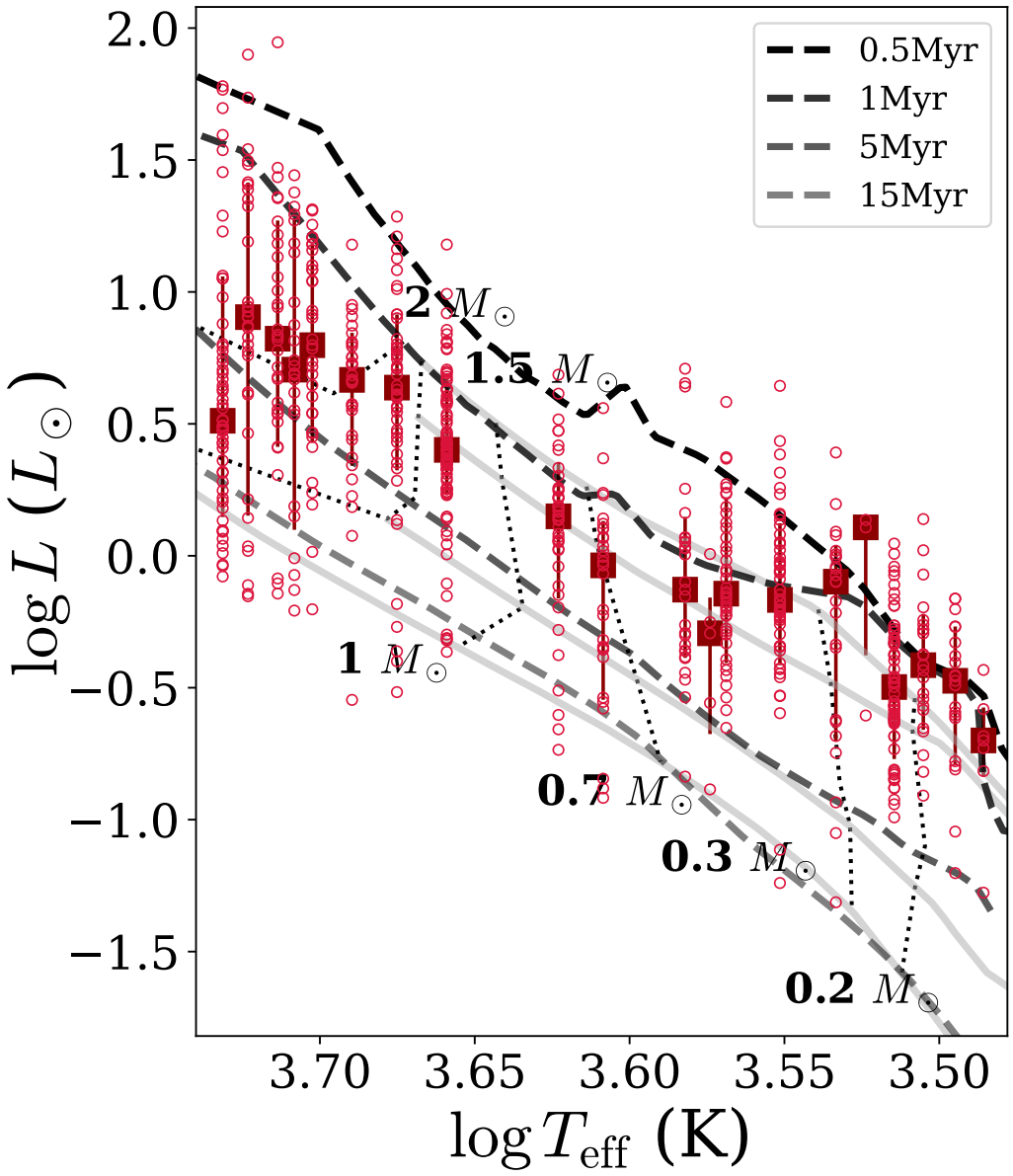

Figure A.10: HR diagram for low-mass stars of Tr 14. Empty circles show data points, open squares are median values of the bolometric luminosity for each spectral subclass with errorbars indicating 1-σ percentiles. Theoretical tracks from Baraffe et al. (2015) are shown as solid grey lines, whereas tracks from Siess et al. (2000) are plotted as dashed lines. Dotted lines show tracks for various masses of stars.

Preibisch et al. (2014), and follow the definition of the NIR excess of Zeidler et al. (2016). Whenever photometry from the both catalogues is available, we choose the one with better signal-to-noise ratio. X-ray detections originate in the *chndra* Carina Complex Project (CCCP, Townsley et al. 2011). NIR excess is often interpreted as a signpost of the inner circumstellar disk, while strong X-ray emission is expected from low-mass stars. The distributions of both characteristics confirm, that the core of Tr 14 consists mainly of young stars (∼1 Myr), while the extended, halo population has more diverse ages, including the very young stars. There is no strong correlation between any of those characteristics and location in the cluster for stars from the extended population.

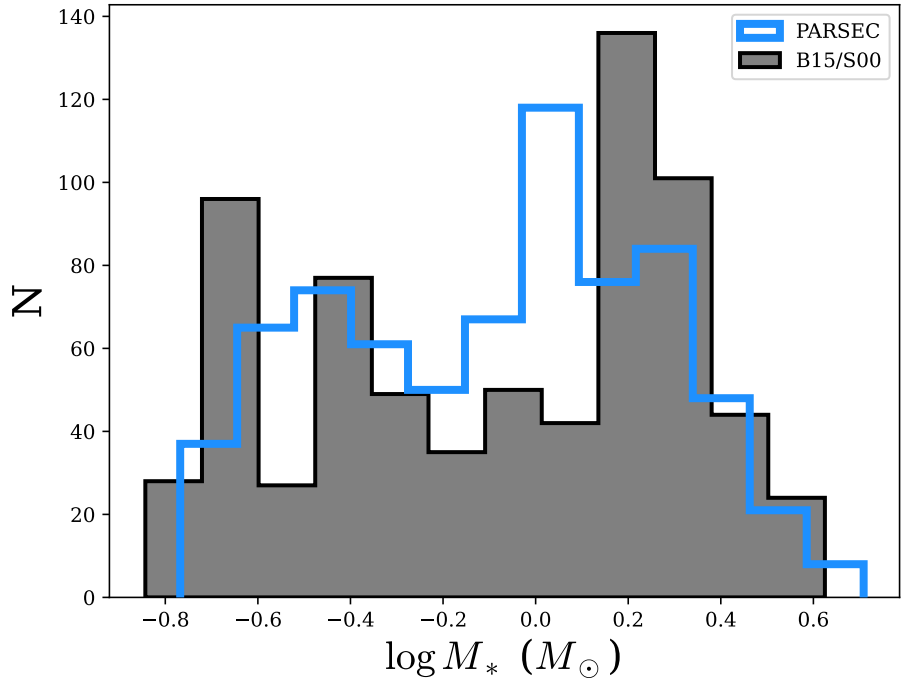

Figure A.11: Distribution of all stellar masses from the final catalog in logarithmic scale. Black histogram filled with grey shows masses estimated based on evolutionary tracks from Baraffe et al. (2015) and Siess et al. (2000), while blue open histogram shows stellar masses based on PARSEC models (Bressan et al. 2012).

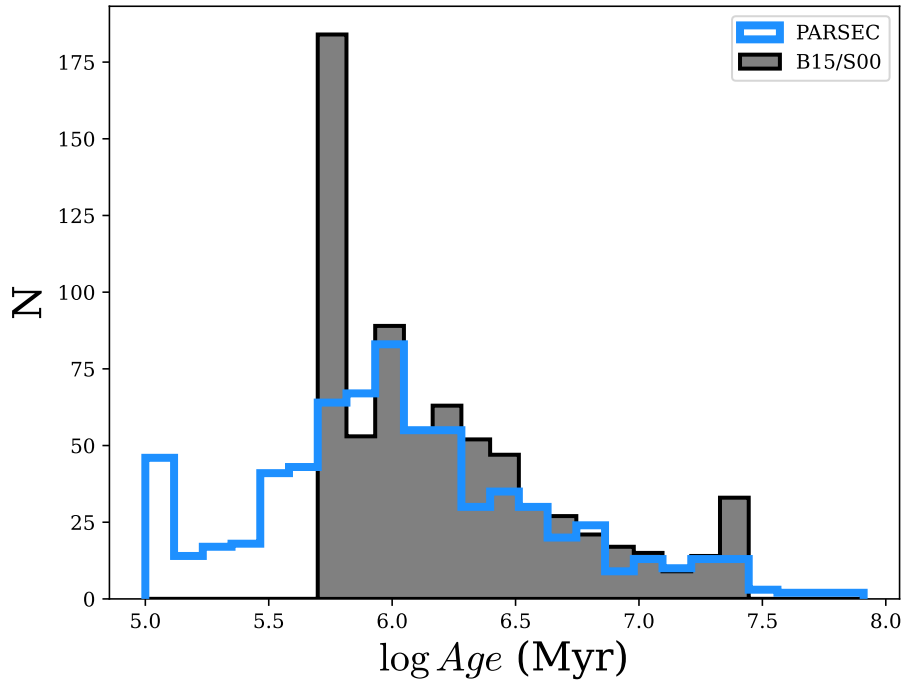

Figure A.12: Distribution of all stellar ages from the final catalog. Black histogram filled with grey shows ages estimated based on evolutionary tracks from Baraffe et al. (2015) and Siess et al. (2000), while blue open histogram shows stellar ages based on PARSEC models (Bressan et al. 2012). PARSEC models span ages down to 0.1 Myr, while the other two – to 0.5 Myr. Both histograms have the same bins fixed to the distribution of PARSEC ages.

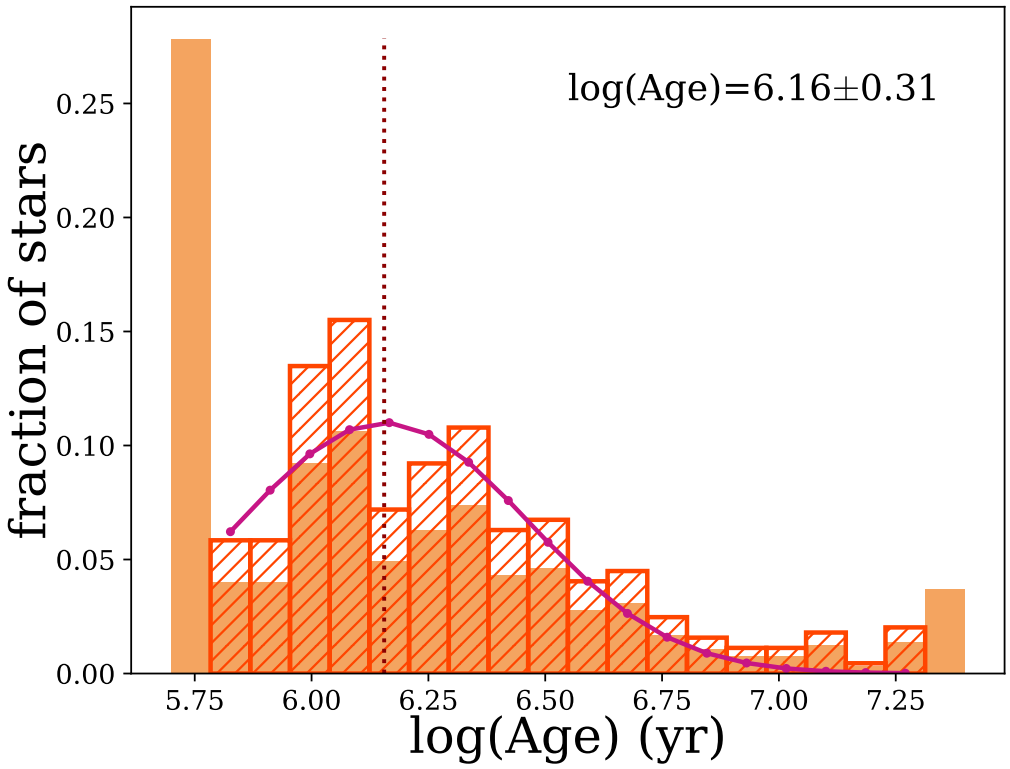

Figure A.13: Fraction of stellar ages derived from HR diagram for stars with $\log(T_{\rm eff}) < 3.73$, analogous to Fig. 4.10 but using tracks from Baraffe et al. (2015) and Siess et al. (2000). Filled orange histogram shows distribution for the whole sample, while hatched red histogram represents the fraction distribution after removing the extreme bars with respect to the total number of stars within the new age range. The normal fit to the probability density distribution converted into the fraction distribution for the visual purposes is shown as a dark violet curve with mean value of $\log(\text{age}) = 6.16 \pm 0.31$ corresponding to the $1.4^{+1.5}_{-0.7}$ Myr

.

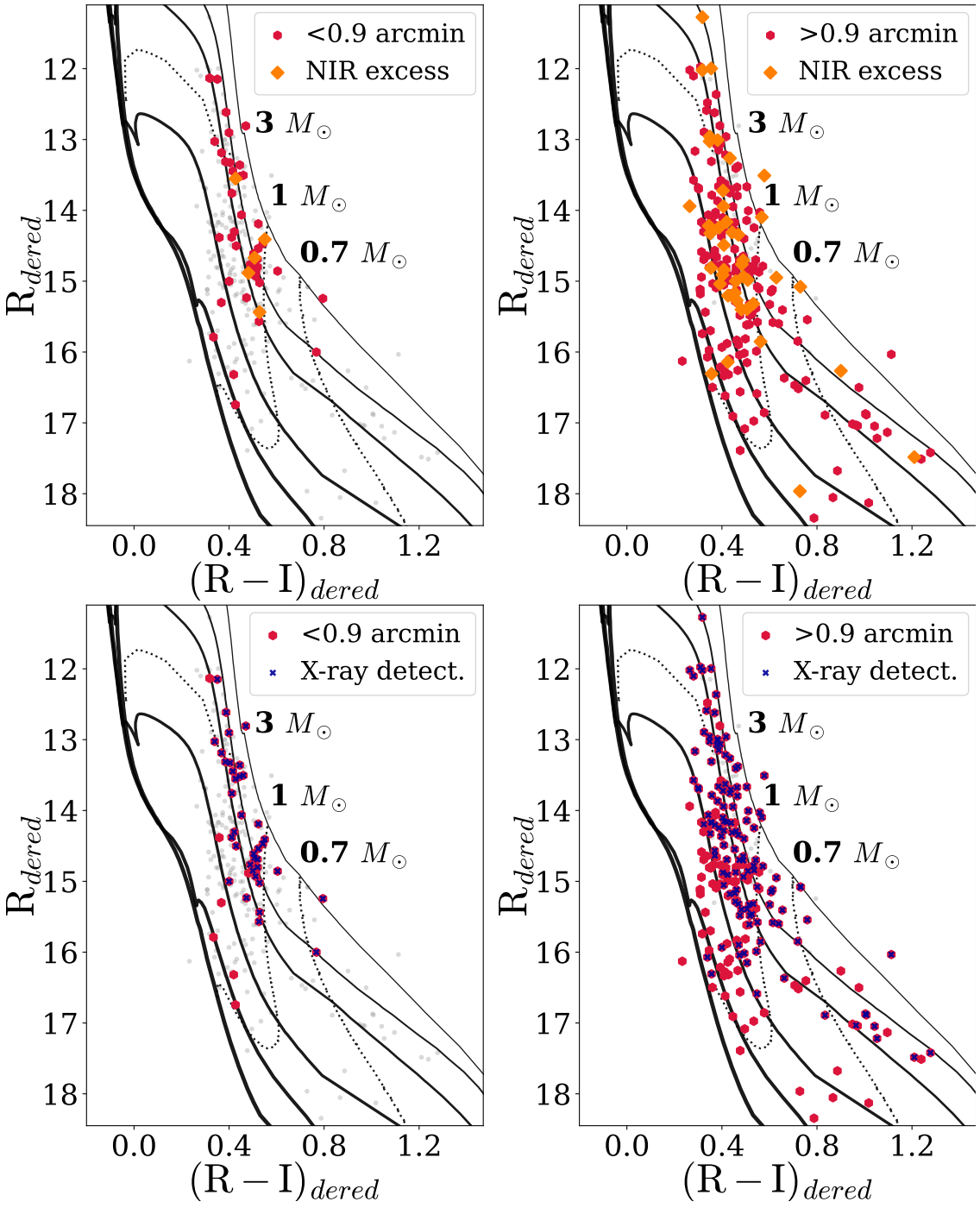

Figure A.14: Colour-magnitude diagrams for de-reddened R and I-band magnitudes from MUSE. Red hexagons mark stars within the core of Tr 14 (left, 0.9′, Kharchenko et al. (2013)) or outside (right). The orange diamonds (top) indicate the NIR excess stars, while the dark blue crosses mark sources with detected X-ray component (bottom, Townsley et al. 2011).

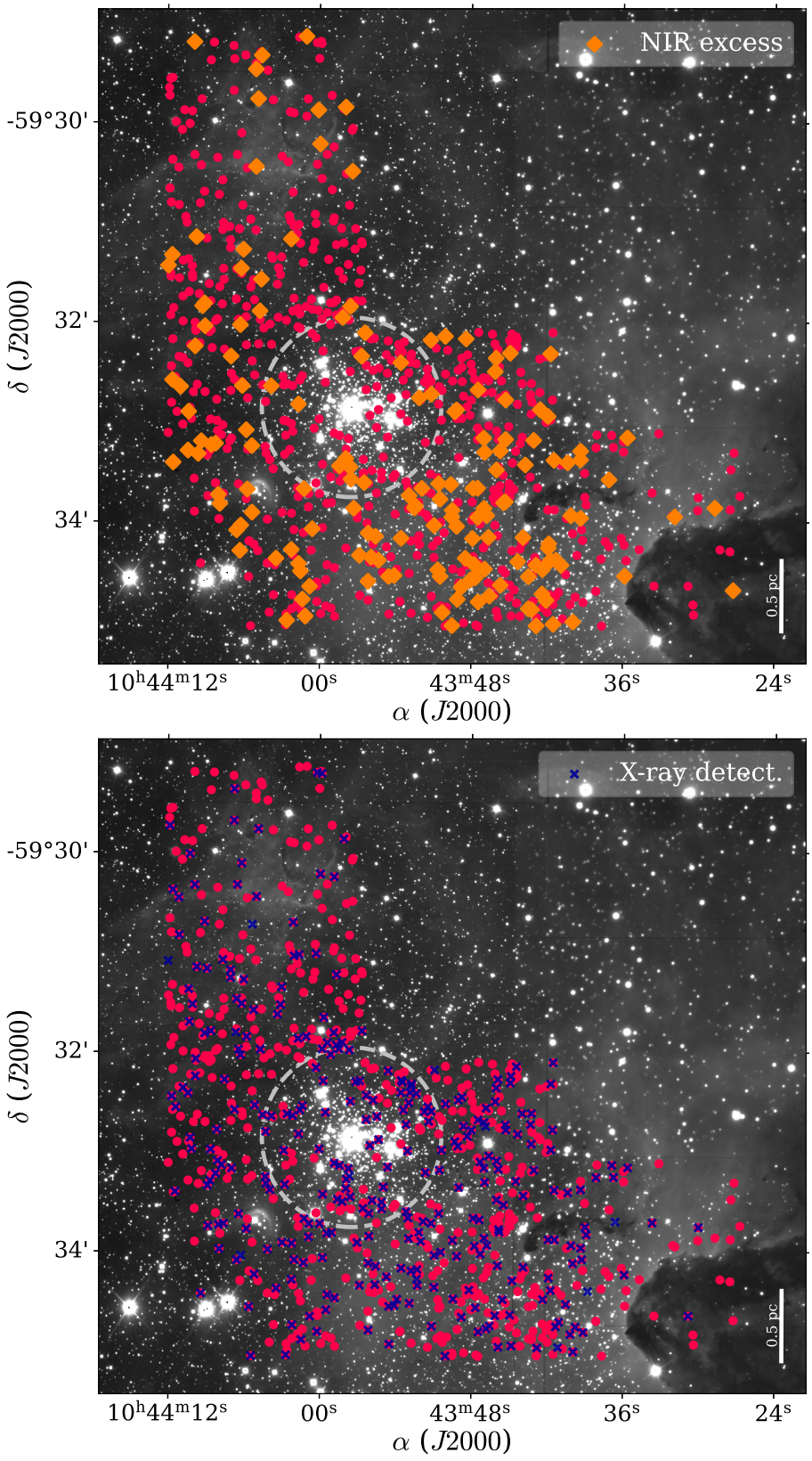

Figure A.15: Locations of the NIR excess stars (orange diamonds, top) and the X-ray detections in Tr 14 (dark blue crosses, bottom). All stars studied here are marked with red dots, as in Fig. 4.1. The dashed circle with radius of 0.9′ shows the core of the Tr 14, as defined by Kharchenko et al. (2013). The background image in grey scale is the *H*-band image from HAWK-I (Preibisch et al. 2011a,b).

Bibliography

Adams, F. C. 2010, ARA&A, 48, 47

Adams, F. C., Hollenbach, D., Laughlin, G., & Gorti, U. 2004, ApJ, 611, 360

Adams, F. C., Ruden, S. P., & Shu, F. H. 1989, ApJ, 347, 959

Akeson, R. L., Boden, A. F., Monnier, J. D., et al. 2005a, ApJ, 635, 1173

Akeson, R. L. & Jensen, E. L. N. 2014, ApJ, 784, 62

Akeson, R. L., Jensen, E. L. N., Carpenter, J., et al. 2019, ApJ, 872, 158

Akeson, R. L., Walker, C. H., Wood, K., et al. 2005b, ApJ, 622, 440

Akiyama, E., Hashimoto, J., Liu, H. B., et al. 2016, AJ, 152, 222

Akiyama, E., Vorobyov, E. I., Liu, H. B., et al. 2019, AJ, 157, 165

Albacete-Colombo, J. F., Damiani, F., Micela, G., Sciortino, S., & Harnden, F. R., J. 2008, A&A, 490, 1055

Alcalá, J. M., Manara, C. F., Natta, A., et al. 2017, A&A, 600, A20

Alcalá, J. M., Natta, A., Manara, C. F., et al. 2014, A&A, 561, A2

Alexander, R., Rosotti, G., Armitage, P. J., et al. 2023, MNRAS, 524, 3948

Alexander, R. D., Clarke, C. J., & Pringle, J. E. 2006, MNRAS, 369, 229

Ali-Dib, M. 2017, MNRAS, 464, 4282

Allard, F., Homeier, D., & Freytag, B. 2012, Philosophical Transactions of the Royal Society of London Series A, 370, 2765

Allington-Smith, J. 2005, in Optics in Astrophysics, ed. R. Foy & F. C. Foy (Dordrecht: Springer Netherlands), 155–180

Allington-Smith, J., Murray, G., Content, R., et al. 2002, PASP, 114, 892

ALMA Partnership, Brogan, C. L., Pérez, L. M., et al. 2015, ApJ, 808, L3

Almendros-Abad, V., Mužić, K., Bouy, H., et al. 2023, arXiv e-prints, arXiv:2305.07158

Almendros-Abad, V., Mužić, K., Moitinho, A., Krone-Martins, A., & Kubiak, K. 2022, A&A, 657, A129

Alves, F. O., Cleeves, L. I., Girart, J. M., et al. 2020, ApJ, 904, L6

Anderson, D. E., Cleeves, L. I., Blake, G. A., et al. 2022, ApJ, 927, 229

Anderson, K. R., Adams, F. C., & Calvet, N. 2013, ApJ, 774, 9

Andre, P., Ward-Thompson, D., & Barsony, M. 1993, ApJ, 406, 122

Andre, P., Ward-Thompson, D., & Barsony, M. 2000, in Protostars and Planets IV, ed. V. Mannings, A. P. Boss, & S. S. Russell, 59

Andrews, S. M. 2020, ARA&A, 58, 483

Andrews, S. M., Rosenfeld, K. A., Kraus, A. L., & Wilner, D. J. 2013, ApJ, 771, 129

Andrews, S. M., Terrell, M., Tripathi, A., et al. 2018, ApJ, 865, 157

Andrews, S. M. & Williams, J. P. 2005, ApJ, 631, 1134

Andrews, S. M., Wilner, D. J., Espaillat, C., et al. 2011, ApJ, 732, 42

Andrews, S. M., Wilner, D. J., Hughes, A. M., Qi, C., & Dullemond, C. P. 2009, ApJ, 700, 1502

Ansdell, M., Haworth, T. J., Williams, J. P., et al. 2020, AJ, 160, 248

Ansdell, M., Williams, J. P., Manara, C. F., et al. 2017, AJ, 153, 240

Ansdell, M., Williams, J. P., Trapman, L., et al. 2018, ApJ, 859, 21

Ansdell, M., Williams, J. P., van der Marel, N., et al. 2016, ApJ, 828, 46

Antokhin, I. I., Rauw, G., Vreux, J. M., van der Hucht, K. A., & Brown, J. C. 2008, A&A, 477, 593

Antoniucci, S., García López, R., Nisini, B., et al. 2014, A&A, 572, A62

Ardizzone, L., Kruse, J., Wirkert, S., et al. 2018, arXiv e-prints, arXiv:1808.04730

Ardizzone, L., Lüth, C., Kruse, J., Rother, C., & Köthe, U. 2019, arXiv e-prints, arXiv:1907.02392

Arsenault, R., Madec, P. Y., Hubin, N., et al. 2008, in Society of Photo-Optical Instrumentation Engineers (SPIE) Conference Series, Vol. 7015, Adaptive Optics Systems, ed. N. Hubin, C. E. Max, & P. L. Wizinowich, 701524

Ascenso, J., Alves, J., Vicente, S., & Lago, M. T. V. T. 2007, A&A, 476, 199

Avenhaus, H., Quanz, S. P., Garufi, A., et al. 2018, ApJ, 863, 44

Avenhaus, H., Quanz, S. P., Meyer, M. R., et al. 2014a, ApJ, 790, 56

Avenhaus, H., Quanz, S. P., Schmid, H. M., et al. 2014b, ApJ, 781, 87

Azevedo, G. M., Chies-Santos, A. L., Riffel, R., et al. 2023, MNRAS, 523, 4680

Bacon, R., Accardo, M., Adjali, L., et al. 2010, in Society of Photo-Optical Instrumentation Engineers (SPIE) Conference Series, Vol. 7735, Ground-based and Airborne Instrumentation for Astronomy III, ed. I. S. McLean, S. K. Ramsay, & H. Takami, 773508

Bae, J., Isella, A., Zhu, Z., et al. 2023, in Astronomical Society of the Pacific Conference Series, Vol. 534, Astronomical Society of the Pacific Conference Series, ed. S. Inutsuka, Y. Aikawa, T. Muto, K. Tomida, & M. Tamura, 423

Ballabio, G., Haworth, T. J., & Henney, W. J. 2023, MNRAS, 518, 5563

Bally, J., Sutherland, R. S., Devine, D., & Johnstone, D. 1998, AJ, 116, 293

Banzatti, A., Pascucci, I., Edwards, S., et al. 2019, ApJ, 870, 76

Banzatti, A., Pontoppidan, K. M., Carr, J., et al. 2023, arXiv e-prints, arXiv:2307.03846

Baraffe, I., Chabrier, G., & Gallardo, J. 2009, ApJ, 702, L27

Baraffe, I., Homeier, D., Allard, F., & Chabrier, G. 2015, A&A, 577, A42

Barenfeld, S. A., Carpenter, J. M., Ricci, L., & Isella, A. 2016, ApJ, 827, 142

Barenfeld, S. A., Carpenter, J. M., Sargent, A. I., Isella, A., & Ricci, L. 2017, ApJ, 851, 85

Basri, G. & Batalha, C. 1990, ApJ, 363, 654

Bate, M. R. 2018, MNRAS, 475, 5618

Beccari, G., De Marchi, G., Panagia, N., et al. 2015, A&A, 574, A44

Beccari, G., Spezzi, L., De Marchi, G., et al. 2010, ApJ, 720, 1108

Beckwith, S. V. W., Sargent, A. I., Chini, R. S., & Guesten, R. 1990, AJ, 99, 924

Benisty, M., Bae, J., Facchini, S., et al. 2021, ApJ, 916, L2

Benisty, M., Dominik, C., Follette, K., et al. 2023, in Astronomical Society of the Pacific Conference Series, Vol. 534, Astronomical Society of the Pacific Conference Series, ed. S. Inutsuka, Y. Aikawa, T. Muto, K. Tomida, & M. Tamura, 605

Benisty, M., Juhasz, A., Boccaletti, A., et al. 2015, A&A, 578, L6

Benisty, M., Natta, A., Isella, A., et al. 2010, A&A, 511, A74

Bergin, E. A., Cleeves, L. I., Gorti, U., et al. 2013, Nature, 493, 644

Berlanas, S. R., Maíz Apellániz, J., Herrero, A., et al. 2023, A&A, 671, A20

Berné, O., Habart, É., Peeters, E., et al. 2022, PASP, 134, 054301

Bertin, E. & Arnouts, S. 1996, Astron. Astrophys. Suppl. Ser., 117, 393

Bertout, C., Basri, G., & Bouvier, J. 1988, ApJ, 330, 350

Beuther, H., van Dishoeck, E. F., Tychoniec, L., et al. 2023, A&A, 673, A121

Birnstiel, T., Dullemond, C. P., Zhu, Z., et al. 2018, ApJ, 869, L45

Blandford, R. D. & Payne, D. G. 1982, MNRAS, 199, 883

Boccaletti, A., Chauvin, G., Mouillet, D., et al. 2020, arXiv e-prints, arXiv:2003.05714

Boccaletti, A., Pantin, E., Ménard, F., et al. 2021, A&A, 652, L8

Böker, T., Arribas, S., Lützgendorf, N., et al. 2022, A&A, 661, A82

Boss, A. P. 1997, Science, 276, 1836

Boss, A. P. 2002, ApJ, 567, L149

Bouvier, M., López-Sepulcre, A., Ceccarelli, C., et al. 2021, A&A, 653, A117

Boyden, R. D. & Eisner, J. A. 2020, ApJ, 894, 74

Brandner, W., Grebel, E. K., Chu, Y.-H., et al. 2000, AJ, 119, 292

Breiman, L. 2001, Machine Learning, 45, 5

Breslau, A., Steinhausen, M., Vincke, K., & Pfalzner, S. 2014, A&A, 565, A130

Bressan, A., Marigo, P., Girardi, L., et al. 2012, MNRAS, 427, 127

Broos, P. S., Townsley, L. K., Feigelson, E. D., et al. 2011, ApJS, 194, 2

Bruderer, S., van Dishoeck, E. F., Doty, S. D., & Herczeg, G. J. 2012, A&A, 541, A91

Cabedo, V., Maury, A., Girart, J. M., & Padovani, M. 2021, A&A, 653, A166

Calvet, N. & Gullbring, E. 1998, ApJ, 509, 802

Calvet, N., Patino, A., Magris, G. C., & D'Alessio, P. 1991, ApJ, 380, 617

Canovas, H., Ménard, F., Hales, A., et al. 2013, A&A, 556, A123

Canovas, H., Perez, S., Dougados, C., et al. 2015, A&A, 578, L1

Cantat-Gaudin, T. & Anders, F. 2020, A&A, 633, A99

Cantat-Gaudin, T., Jordi, C., Vallenari, A., et al. 2018, A&A, 618, A93

Caratti o Garatti, A., Tambovtseva, L. V., Garcia Lopez, R., et al. 2015, A&A, 582, A44

Cardelli, J. A., Clayton, G. C., & Mathis, J. S. 1989, ApJ, 345, 245

Carpenter, J. M., Hillenbrand, L. A., & Skrutskie, M. F. 2001, AJ, 121, 3160

Carraro, G., Romaniello, M., Ventura, P., & Patat, F. 2004, A&A, 418, 525

Carrera, D., Gorti, U., Johansen, A., & Davies, M. B. 2017, ApJ, 839, 16

Carrera, D., Johansen, A., & Davies, M. B. 2015, A&A, 579, A43

Cazzoletti, P., Manara, C. F., Liu, H. B., et al. 2019, A&A, 626, A11

Chabrier, G. 2003, ApJ, 586, L133

Chabrier, G., Baraffe, I., Phillips, M., & Debras, F. 2023, A&A, 671, A119

Chapillon, E., Guilloteau, S., Dutrey, A., Piétu, V., & Guélin, M. 2012, A&A, 537, A60

Chen, Y., Girardi, L., Bressan, A., et al. 2014, MNRAS, 444, 2525

Chevance, M., Krumholz, M. R., McLeod, A. F., et al. 2023, in Astronomical Society of the Pacific Conference Series, Vol. 534, Protostars and Planets VII, ed. S. Inutsuka, Y. Aikawa, T. Muto, K. Tomida, & M. Tamura, 1

Chilcote, J., Konopacky, Q., De Rosa, R. J., et al. 2020, in Society of Photo-Optical Instrumentation Engineers (SPIE) Conference Series, Vol. 11447, Ground-based and Airborne Instrumentation for Astronomy VIII, ed. C. J. Evans, J. J. Bryant, & K. Motohara, 114471S

Choquet, É., Pueyo, L., Hagan, J. B., et al. 2014, in Society of Photo-Optical Instrumentation Engineers (SPIE) Conference Series, Vol. 9143, Space Telescopes and Instrumentation 2014: Optical, Infrared, and Millimeter Wave, ed. J. Oschmann, Jacobus M., M. Clampin, G. G. Fazio, & H. A. MacEwen, 914357

Christiaens, V., Cantalloube, F., Casassus, S., et al. 2019, ApJ, 877, L33

Churchwell, E., Felli, M., Wood, D. O. S., & Massi, M. 1987, ApJ, 321, 516

Cieza, L. A., Olofsson, J., Harvey, P. M., et al. 2013, ApJ, 762, 100

Cieza, L. A., Padgett, D. L., Allen, L. E., et al. 2009, ApJ, 696, L84

Cieza, L. A., Ruíz-Rodríguez, D., Hales, A., et al. 2019, MNRAS, 482, 698

Claes, R. A. B., Manara, C. F., Garcia-Lopez, R., et al. 2022, A&A, 664, L7

Clampin, M., Krist, J. E., Ardila, D. R., et al. 2003, AJ, 126, 385

Clarke, C. J., Gendrin, A., & Sotomayor, M. 2001, MNRAS, 328, 485

Clarke, C. J. & Pringle, J. E. 1993, MNRAS, 261, 190

Claudi, R. U., Turatto, M., Gratton, R. G., et al. 2008, in Society of Photo-Optical Instrumentation Engineers (SPIE) Conference Series, Vol. 7014, Ground-based and Airborne Instrumentation for Astronomy II, ed. I. S. McLean & M. M. Casali, 70143E

Cleeves, L. I., Bergin, E. A., Qi, C., Adams, F. C., & Öberg, K. I. 2015, ApJ, 799, 204

Concha-Ramírez, F., Wilhelm, M. J. C., Portegies Zwart, S., van Terwisga, S. E., & Hacar, A. 2021, MNRAS, 501, 1782

Connelley, M. S., Reipurth, B., & Tokunaga, A. T. 2008, AJ, 135, 2526

Cortes-Rangel, G., Zapata, L. A., Toalá, J. A., et al. 2020, AJ, 159, 62

Costigan, G., Scholz, A., Stelzer, B., et al. 2012, MNRAS, 427, 1344

Costigan, G., Vink, J. S., Scholz, A., Ray, T., & Testi, L. 2014, MNRAS, 440, 3444

Courtes, G. 1982, in Astrophysics and Space Science Library, Vol. 92, IAU Colloq. 67: Instrumentation for Astronomy with Large Optical Telescopes, ed. C. M. Humphries, 123

Cox, A. N. 2000, Allen's astrophysical quantities

Cox, E. G., Harris, R. J., Looney, L. W., et al. 2017, ApJ, 851, 83

Cuello, N., Dipierro, G., Mentiplay, D., et al. 2019, MNRAS, 483, 4114

Cushing, M. C., Rayner, J. T., & Vacca, W. D. 2005, ApJ, 623, 1115

Czekala, I., Chiang, E., Andrews, S. M., et al. 2019, ApJ, 883, 22

D'Alessio, P., Calvet, N., Hartmann, L., Franco-Hernández, R., & Servín, H. 2006, ApJ, 638, 314

Damian, B., Jose, J., Samal, M. R., et al. 2021, MNRAS, 504, 2557

Damiani, F., Klutsch, A., Jeffries, R. D., et al. 2017, A&A, 603, A81

Davies, R., Absil, O., Agapito, G., et al. 2023, arXiv e-prints, arXiv:2304.02343

de Boer, J., Langlois, M., van Holstein, R. G., et al. 2020, A&A, 633, A63

de Boer, J., Salter, G., Benisty, M., et al. 2016, A&A, 595, A114

de Juan Ovelar, M., Kruijssen, J. M. D., Bressert, E., et al. 2012, A&A, 546, L1

De Marchi, G., Panagia, N., & Beccari, G. 2017, ApJ, 846, 110

De Marchi, G., Panagia, N., & Romaniello, M. 2010a, ApJ, 715, 1

De Marchi, G., Panagia, N., Romaniello, M., et al. 2011, ApJ, 740, 11

De Marchi, G., Paresce, F., & Portegies Zwart, S. 2010b, ApJ, 718, 105

DeGioia-Eastwood, K., Throop, H., Walker, G., & Cudworth, K. M. 2001a, ApJ, 549, 578

DeGioia-Eastwood, K., Throop, H., Walker, G., & Cudworth, K. M. 2001b, ApJ, 549, 578

Dent, W. R. F., Thi, W. F., Kamp, I., et al. 2013, PASP, 125, 477

Dobbs, C. L. & Pringle, J. E. 2013, MNRAS, 432, 653

Dong, R., Liu, S.-y., Eisner, J., et al. 2018, ApJ, 860, 124

Draine, B. T. & Lee, H. M. 1984, ApJ, 285, 89

Drążkowska, J. & Alibert, Y. 2017, A&A, 608, A92

Drążkowska, J., Bitsch, B., Lambrechts, M., et al. 2023, in Astronomical Society of the Pacific Conference Series, Vol. 534, Protostars and Planets VII, ed. S. Inutsuka, Y. Aikawa, T. Muto, K. Tomida, & M. Tamura, 717

Duchêne, G. & Kraus, A. 2013, ARA&A, 51, 269

Duchêne, G., Lacour, S., Moraux, E., Goodwin, S., & Bouvier, J. 2018, MNRAS, 478, 1825

Dullemond, C. P., Küffmeier, M., Goicovic, F., et al. 2019, A&A, 628, A20

Dullemond, C. P. & Monnier, J. D. 2010, ARA&A, 48, 205

Dullemond, C. P., Natta, A., & Testi, L. 2006, ApJ, 645, L69

Dupuy, T. J., Kratter, K. M., Kraus, A. L., et al. 2016, ApJ, 817, 80

Eisner, J. A., Arce, H. G., Ballering, N. P., et al. 2018, ApJ, 860, 77

Eisner, J. A., Bally, J. M., Ginsburg, A., & Sheehan, P. D. 2016, ApJ, 826, 16

Eisner, J. A., Chiang, E. I., Lane, B. F., & Akeson, R. L. 2007, ApJ, 657, 347

Eisner, J. A., Hillenbrand, L. A., White, R. J., Akeson, R. L., & Sargent, A. I. 2005, ApJ, 623, 952

Elmegreen, B. G. 2007, ApJ, 668, 1064

Elsasser, H. & Staude, H. J. 1978, A&A, 70, L3

Ercolano, B., Drake, J. J., Raymond, J. C., & Clarke, C. C. 2008, ApJ, 688, 398

Ercolano, B. & Owen, J. E. 2016, MNRAS, 460, 3472

Ercolano, B. & Pascucci, I. 2017, Royal Society Open Science, 4, 170114

Ercolano, B. & Rosotti, G. 2015, MNRAS, 450, 3008

Espaillat, C., Muzerolle, J., Najita, J., et al. 2014, in Protostars and Planets VI, ed. H. Beuther, R. S. Klessen, C. P. Dullemond, & T. Henning, 497–520

Estrada, P. R., Cuzzi, J. N., & Morgan, D. A. 2016, ApJ, 818, 200

Facchini, S., Clarke, C. J., & Bisbas, T. G. 2016, MNRAS, 457, 3593

Fairlamb, J. R., Oudmaijer, R. D., Mendigutía, I., Ilee, J. D., & van den Ancker, M. E. 2015, MNRAS, 453, 976

Fang, M., Kim, J. S., Pascucci, I., & Apai, D. 2021, ApJ, 908, 49

Fang, M., Kim, J. S., Pascucci, I., Apai, D., & Manara, C. F. 2016, ApJ, 833, L16

Fang, Q., Herczeg, G. J., & Rizzuto, A. 2017, ApJ, 842, 123

Favre, C., Cleeves, L. I., Bergin, E. A., Qi, C., & Blake, G. A. 2013, ApJ, 776, L38

Feigelson, E. D., Getman, K. V., Townsley, L. K., et al. 2011, ApJS, 194, 9

Feigelson, E. D. & Montmerle, T. 1999, ARA&A, 37, 363

Feinstein, A., Marraco, H. G., & Muzzio, J. C. 1973, A&AS, 12, 331

Field, G. B., Somerville, W. B., & Dressler, K. 1966, ARA&A, 4, 207

Fiorellino, E., Manara, C. F., Nisini, B., et al. 2021, A&A, 650, A43

Fischer, D. A. & Valenti, J. 2005, ApJ, 622, 1102

Fischer, W., Edwards, S., Hillenbrand, L., & Kwan, J. 2011, ApJ, 730, 73

Fischer, W. J., Hillenbrand, L. A., Herczeg, G. J., et al. 2023, in Astronomical Society of the Pacific Conference Series, Vol. 534, Astronomical Society of the Pacific Conference Series, ed. S. Inutsuka, Y. Aikawa, T. Muto, K. Tomida, & M. Tamura, 355

Fisher, A., Rudin, C., & Dominici, F. 2019, arXiv e-prints, 20, 177

Forgan, D. H., Hall, C., Meru, F., & Rice, W. K. M. 2018, MNRAS, 474, 5036

France, K., Herczeg, G. J., McJunkin, M., & Penton, S. V. 2014, ApJ, 794, 160

Freudling, W., Romaniello, M., Bramich, D. M., et al. 2013, A&A, 559, A96

Freyer, T., Hensler, G., & Yorke, H. W. 2003, ApJ, 594, 888

Fukagawa, M., Hayashi, M., Tamura, M., et al. 2004, ApJ, 605, L53

Fulton, B. J., Rosenthal, L. J., Hirsch, L. A., et al. 2021, ApJS, 255, 14

Furlan, E., Hartmann, L., Calvet, N., et al. 2006, ApJS, 165, 568

Gahm, G. F., Grenman, T., Fredriksson, S., & Kristen, H. 2007, AJ, 133, 1795

Gaia Collaboration, Prusti, T., de Bruijne, J. H. J., et al. 2016, A&A, 595, A1

Gaia Collaboration, Vallenari, A., Brown, A. G. A., et al. 2022, arXiv e-prints, arXiv:2208.00211

Garcia Lopez, R., Tambovtseva, L. V., Schertl, D., et al. 2015, A&A, 576, A84

García-Vázquez, J., Henney, W. J., & Castañeda, H. O. 2023, MNRAS, 523, 4202

Garufi, A., Avenhaus, H., Pérez, S., et al. 2020a, A&A, 633, A82

Garufi, A., Podio, L., Codella, C., et al. 2020b, A&A, 636, A65

Garufi, A., Podio, L., Codella, C., et al. 2022, A&A, 658, A104

Garufi, A., Quanz, S. P., Schmid, H. M., et al. 2014, A&A, 568, A40

Gasman, D., van Dishoeck, E. F., Grant, S. L., et al. 2023, arXiv e-prints, arXiv:2307.09301

Gáspár, A., Wolff, S. G., Rieke, G. H., et al. 2023, Nature Astronomy, 7, 790

Geballe, T. R., Knapp, G. R., Leggett, S. K., et al. 2002, ApJ, 564, 466

Gehrig, L., Steindl, T., Vorobyov, E. I., Guadarrama, R., & Zwintz, K. 2023, A&A, 669, A84

Ghez, A. M., McCarthy, D. W., Patience, J. L., & Beck, T. L. 1997, ApJ, 481, 378

Ginski, C., Facchini, S., Huang, J., et al. 2021, ApJ, 908, L25

Ginski, C., Ménard, F., Rab, C., et al. 2020, A&A, 642, A119

Ginski, C., Stolker, T., Pinilla, P., et al. 2016, A&A, 595, A112

Göppl, C. & Preibisch, T. 2022, A&A, 660, A11

Gorti, U. & Hollenbach, D. 2009, ApJ, 690, 1539

Grady, C. A., Muto, T., Hashimoto, J., et al. 2013, ApJ, 762, 48

Grady, C. A., Polomski, E. F., Henning, T., et al. 2001, AJ, 122, 3396

Grady, C. A., Woodgate, B., Bruhweiler, F. C., et al. 1999, ApJ, 523, L151

Gräfe, C., Wolf, S., Guilloteau, S., et al. 2013, A&A, 553, A69

Grant, S. L., Espaillat, C. C., Wendeborn, J., et al. 2021, ApJ, 913, 123

Grant, S. L., van Dishoeck, E. F., Tabone, B., et al. 2023, ApJ, 947, L6

Green, J. D., Evans, Neal J., I., Jørgensen, J. K., et al. 2013, ApJ, 770, 123

Greene, T. P., Wilking, B. A., Andre, P., Young, E. T., & Lada, C. J. 1994, ApJ, 434, 614

Grenman, T. & Gahm, G. F. 2014, A&A, 565, A107

Gritschneder, M., Burkert, A., Naab, T., & Walch, S. 2010, ApJ, 723, 971

Groff, T. D., Kasdin, N. J., Limbach, M. A., et al. 2015, in Society of Photo-Optical Instrumentation Engineers (SPIE) Conference Series, Vol. 9605, Techniques and Instrumentation for Detection of Exoplanets VII, ed. S. Shaklan, 96051C

Guarcello, M. G., Biazzo, K., Drake, J. J., et al. 2021, A&A, 650, A157

Guarcello, M. G., Drake, J. J., Wright, N. J., et al. 2016, arXiv e-prints, arXiv:1605.01773

Guillot, T. & Hueso, R. 2006, MNRAS, 367, L47

Guilloteau, S., Dutrey, A., Piétu, V., & Boehler, Y. 2011, A&A, 529, A105

Gullbring, E., Hartmann, L., Briceño, C., & Calvet, N. 1998, ApJ, 492, 323

Gundlach, B. & Blum, J. 2015, ApJ, 798, 34

Gupta, A., Miotello, A., Manara, C. F., et al. 2023, A&A, 670, L8

Güttler, C., Blum, J., Zsom, A., Ormel, C. W., & Dullemond, C. P. 2010, A&A, 513, A56

Habart, E., Peeters, E., Berné, O., et al. 2023, arXiv e-prints, arXiv:2308.16732

Habing, H. J. 1968, Bull. Astron. Inst. Netherlands, 19, 421

Haffert, S. Y., Bohn, A. J., de Boer, J., et al. 2019, Nature Astronomy, 3, 749

Haldemann, J., Ksoll, V., Walter, D., et al. 2023, A&A, 672, A180

Hartigan, P., Edwards, S., & Ghandour, L. 1995, ApJ, 452, 736

Hartmann, L. 2001, AJ, 121, 1030

Hartmann, L. 2003, ApJ, 585, 398

Hartmann, L., Calvet, N., Gullbring, E., & D'Alessio, P. 1998, ApJ, 495, 385

Hartmann, L., Herczeg, G., & Calvet, N. 2016, ARA&A, 54, 135

Hartmann, L. & Kenyon, S. J. 1996, ARA&A, 34, 207

Hashimoto, J., Dong, R., Kudo, T., et al. 2012, ApJ, 758, L19

Haworth, T. J. & Harries, T. J. 2012, MNRAS, 420, 562

Haworth, T. J., Kim, J. S., Qiao, L., et al. 2022, MNRAS, 512, 2594

Haworth, T. J., Kim, J. S., Winter, A. J., et al. 2021, MNRAS, 501, 3502

Haworth, T. J. & Owen, J. E. 2020, MNRAS, 492, 5030

Haworth, T. J., Reiter, M., O'Dell, C. R., et al. 2023, MNRAS, 525, 4129

Hayat, M. A., Stein, G., Harrington, P., Lukić, Z., & Mustafa, M. 2021, The Astrophysical Journal Letters, 911, L33

Heiderman, A., Evans, Neal J., I., Allen, L. E., Huard, T., & Heyer, M. 2010, ApJ, 723, 1019

Heller, C. H. 1995, ApJ, 455, 252

Hendler, N., Pascucci, I., Pinilla, P., et al. 2020, ApJ, 895, 126

Henney, W. J., O'Dell, C. R., Meaburn, J., Garrington, S. T., & Lopez, J. A. 2002, ApJ, 566, 315

Herbig, G. H. 1960, ApJS, 4, 337

Herczeg, G. J. & Hillenbrand, L. A. 2008, ApJ, 681, 594

Herczeg, G. J. & Hillenbrand, L. A. 2014, ApJ, 786, 97

Hernández, J., Calvet, N., Briceño, C., Hartmann, L., & Berlind, P. 2004, AJ, 127, 1682

Hester, J. J., Scowen, P. A., Sankrit, R., et al. 1996, AJ, 111, 2349

Hildebrand, R. H. 1983, QJRAS, 24, 267

Hillenbrand, L. A., Strom, S. E., Vrba, F. J., & Keene, J. 1992, ApJ, 397, 613

Hodapp, K. W., Iserlohe, C., Stecklum, B., & Krabbe, A. 2009, ApJ, 701, L100

Hollenbach, D. & Gorti, U. 2009, ApJ, 703, 1203

Holoien, T. W. S., Berger, V. L., Hinkle, J. T., et al. 2023, ApJ, 950, 108

Homma, K. & Nakamoto, T. 2018, ApJ, 868, 118

Huang, J., Andrews, S. M., Pérez, L. M., et al. 2018, ApJ, 869, L43

Hur, H., Lim, B., & Chun, M.-Y. 2023, Journal of Korean Astronomical Society, 56, 97

Hur, H., Sung, H., & Bessell, M. S. 2012, AJ, 143, 41

Husser, T.-O., Kamann, S., Dreizler, S., et al. 2016, A&A, 588, A148

Husser, T. O., Wende-von Berg, S., Dreizler, S., et al. 2013, A&A, 553, A6

Ida, S. & Lin, D. N. C. 2004, ApJ, 616, 567

Iffrig, O. & Hennebelle, P. 2015, A&A, 576, A95

Ilee, J. D., Walsh, C., Jennings, J., et al. 2022, MNRAS, 515, L23

Isella, A., Carpenter, J. M., & Sargent, A. I. 2009, ApJ, 701, 260

Isella, A., Tatulli, E., Natta, A., & Testi, L. 2008, A&A, 483, L13

Itrich, D., Karska, A., Sewiło, M., et al. 2023a, ApJS, 267, 46

Itrich, D., Testi, L., Beccari, G., et al. 2023b, arXiv e-prints, arXiv:2309.14168

Jaehnig, K., Bird, J. C., Stassun, K. G., et al. 2017, ApJ, 851, 14

Jeffries, R. D., Oliveira, J. M., Naylor, T., Mayne, N. J., & Littlefair, S. P. 2007, MNRAS, 376, 580

Jerabkova, T., Beccari, G., Boffin, H. M. J., et al. 2019, A&A, 627, A57

Johansen, A., Blum, J., Tanaka, H., et al. 2014, in Protostars and Planets VI, ed. H. Beuther, R. S. Klessen, C. P. Dullemond, & T. Henning, 547–570

Johnstone, D., Hollenbach, D., & Bally, J. 1998, ApJ, 499, 758

Joncour, I., Duchêne, G., & Moraux, E. 2017, A&A, 599, A14

Kama, M., Bruderer, S., Carney, M., et al. 2016, A&A, 588, A108

Kama, M., Trapman, L., Fedele, D., et al. 2020, A&A, 634, A88

Kamp, I., Henning, T., Arabhavi, A. M., et al. 2023, arXiv e-prints, arXiv:2307.16729

Kang, D. E. 2023, PhD thesis, Heidelberg University

Kang, D. E., Klessen, R. S., Ksoll, V. F., et al. 2023a, MNRAS, 520, 4981

Kang, D. E., Ksoll, V. F., Itrich, D., et al. 2023b, A&A, 674, A175

Kang, D. E., Ksoll, V. F., Itrich, D., et al. 2023c, in prep.

Kang, D. E., Pellegrini, E. W., Ardizzone, L., et al. 2022, MNRAS, 512, 617

Kastner, J. H., Huenemoerder, D. P., Schulz, N. S., Canizares, C. R., & Weintraub, D. A. 2002, ApJ, 567, 434

Kataoka, A., Okuzumi, S., Tanaka, H., & Nomura, H. 2014, A&A, 568, A42

Kennicutt, R. C. & Evans, N. J. 2012, ARA&A, 50, 531

Kenyon, S. J. & Hartmann, L. 1987, ApJ, 323, 714

Kenyon, S. J. & Hartmann, L. 1995, ApJS, 101, 117

Keppler, M., Benisty, M., Müller, A., et al. 2018, A&A, 617, A44

Kharchenko, N. V., Piskunov, A. E., Schilbach, E., Röser, S., & Scholz, R. D. 2013, A&A, 558, A53

Kim, J. S., Clarke, C. J., Fang, M., & Facchini, S. 2016, ApJ, 826, L15

Kingma, D. P. & Dhariwal, P. 2018, arXiv e-prints, arXiv:1807.03039

Kirkpatrick, J. D. 2005, ARA&A, 43, 195

Kirwan, A., Manara, C. F., Whelan, E. T., et al. 2023, A&A, 673, A166

Kobayashi, H. & Ida, S. 2001, Icarus, 153, 416

Köhler, R. & Leinert, C. 1998, A&A, 331, 977

Köhler, R., Neuhäuser, R., Krämer, S., et al. 2008, A&A, 488, 997

Köhler, R., Petr-Gotzens, M. G., McCaughrean, M. J., et al. 2006, A&A, 458, 461

Kokoulina, E., Matter, A., Lopez, B., et al. 2021, A&A, 652, A61

Kolcu, T., Maciejewski, W., Gadotti, D. A., et al. 2023, MNRAS, 524, 207

Komarova, O. & Fischer, W. J. 2020, Research Notes of the American Astronomical Society, 4, 6

Kostov, V. B., Orosz, J. A., Feinstein, A. D., et al. 2020, AJ, 159, 253

Kostov, V. B., Powell, B. P., Orosz, J. A., et al. 2021, AJ, 162, 234

Kratter, K. & Lodato, G. 2016, ARA&A, 54, 271

Kraus, A. L., Ireland, M. J., Martinache, F., & Hillenbrand, L. A. 2011, ApJ, 731, 8

Kraus, S., Preibisch, T., & Ohnaka, K. 2008, ApJ, 676, 490

Krist, J. E., Stapelfeldt, K. R., Ménard, F., Padgett, D. L., & Burrows, C. J. 2000, ApJ, 538, 793

Kruijssen, J. M. D., Schruba, A., Chevance, M., et al. 2019, Nature, 569, 519

Krumholz, M. R., Klein, R. I., & McKee, C. F. 2011, ApJ, 740, 74

Ksoll, V. F., Ardizzone, L., Klessen, R., et al. 2020, MNRAS, 499, 5447

Kuffmeier, M., Dullemond, C. P., Reissl, S., & Goicovic, F. G. 2021, A&A, 656, A161

Kuhn, J. R., Potter, D., & Parise, B. 2001, ApJ, 553, L189

Kurtovic, N. T., Pinilla, P., Long, F., et al. 2021, A&A, 645, A139

Kusakabe, N., Grady, C. A., Sitko, M. L., et al. 2012, ApJ, 753, 153

Kuznetsova, A., Bae, J., Hartmann, L., & Mac Low, M.-M. 2022, ApJ, 928, 92

Kwon, Y. G., Opitom, C., & Lippi, M. 2023, A&A, 674, A206

Lada, C. J. 1987, in Star Forming Regions, ed. M. Peimbert & J. Jugaku, Vol. 115, 1

Lada, C. J. & Lada, E. A. 2003, ARA&A, 41, 57

Lada, C. J. & Wilking, B. A. 1984, ApJ, 287, 610

Lamers, H. J. G. L. M. & Cassinelli, J. P. 1999, Introduction to Stellar Winds (Cambridge University Press)

Lamzin, S. A. 1998, Astronomy Reports, 42, 322

Larkin, J. E., Chilcote, J. K., Aliado, T., et al. 2014, in Society of Photo-Optical Instrumentation Engineers (SPIE) Conference Series, Vol. 9147, Ground-based and Airborne Instrumentation for Astronomy V, ed. S. K. Ramsay, I. S. McLean, & H. Takami, 91471K

Law, C. J., Loomis, R. A., Teague, R., et al. 2021a, ApJS, 257, 3

Law, C. J., Teague, R., Loomis, R. A., et al. 2021b, ApJS, 257, 4

Laws, A. S. E., Harries, T. J., Setterholm, B. R., et al. 2020, ApJ, 888, 7

Lawson, K., Schlieder, J. E., Leisenring, J. M., et al. 2023, AJ, 166, 150

Le Gouellec, V. J. M., Hull, C. L. H., Maury, A. J., et al. 2019, ApJ, 885, 106

Lee, E. J. & Hopkins, P. F. 2020, MNRAS, 495, L86

Leinert, C., van Boekel, R., Waters, L. B. F. M., et al. 2004, A&A, 423, 537

Leinert, C., Zinnecker, H., Weitzel, N., et al. 1993, A&A, 278, 129

Levato, H. & Malaroda, S. 1982, PASP, 94, 807

Li, R. & Youdin, A. N. 2021, ApJ, 919, 107

Lindegren, L. 2018, gAIA-C3-TN-LU-LL-124

Lindegren, L., Bastian, U., Biermann, M., et al. 2021, A&A, 649, A4

Lodato, G., Scardoni, C. E., Manara, C. F., & Testi, L. 2017, MNRAS, 472, 4700

Long, F., Herczeg, G. J., Harsono, D., et al. 2019, ApJ, 882, 49

Long, F., Herczeg, G. J., Pascucci, I., et al. 2018, ApJ, 863, 61

Lovell, J. B., Wyatt, M. C., Ansdell, M., et al. 2021, MNRAS, 500, 4878

Luhman, K. L. 1999, ApJ, 525, 466

Luhman, K. L., Stauffer, J. R., Muench, A. A., et al. 2003, ApJ, 593, 1093

Lynden-Bell, D. & Kalnajs, A. J. 1972, MNRAS, 157, 1

Lynden-Bell, D. & Pringle, J. E. 1974, MNRAS, 168, 603

Maeder, A. & Meynet, G. 2012, Reviews of Modern Physics, 84, 25

Maíz Apellániz, J., Crespo Bellido, P., Barbá, R. H., Fernández Aranda, R., & Sota, A. 2020, A&A, 643, A138

Maíz Apellániz, J., Sota, A., Arias, J. I., et al. 2016, ApJS, 224, 4

Malbet, F., Berger, J. P., Colavita, M. M., et al. 1998, ApJ, 507, L149

Males, J. R., Close, L. M., Guyon, O., et al. 2020, in Society of Photo-Optical Instrumentation Engineers (SPIE) Conference Series, Vol. 11448, Society of Photo-Optical Instrumentation Engineers (SPIE) Conference Series, 114484L

Manara, C. F., Ansdell, M., Rosotti, G. P., et al. 2023, in Astronomical Society of the Pacific Conference Series, Vol. 534, Astronomical Society of the Pacific Conference Series, ed. S. Inutsuka, Y. Aikawa, T. Muto, K. Tomida, & M. Tamura, 539

Manara, C. F., Frasca, A., Alcalá, J. M., et al. 2017, A&A, 605, A86

Manara, C. F., Frasca, A., Venuti, L., et al. 2021, A&A, 650, A196

Manara, C. F., Morbidelli, A., & Guillot, T. 2018, A&A, 618, L3

Manara, C. F., Natta, A., Rosotti, G. P., et al. 2020, A&A, 639, A58

Manara, C. F., Robberto, M., Da Rio, N., et al. 2012, ApJ, 755, 154

Manara, C. F., Rosotti, G., Testi, L., et al. 2016, A&A, 591, L3

Manara, C. F., Tazzari, M., Long, F., et al. 2019, A&A, 628, A95

Manara, C. F., Testi, L., Rigliaco, E., et al. 2013, A&A, 551, A107

Mann, R. K., Andrews, S. M., Eisner, J. A., et al. 2015, ApJ, 802, 77

Mann, R. K., Di Francesco, J., Johnstone, D., et al. 2014, ApJ, 784, 82

Mann, R. K. & Williams, J. P. 2009, ApJ, 694, L36

Mann, R. K. & Williams, J. P. 2010, ApJ, 725, 430

Marmo, C. & Bertin, E. 2008, in Astronomical Society of the Pacific Conference Series, Vol. 394, Astronomical Data Analysis Software and Systems XVII, ed. R. W. Argyle, P. S. Bunclark, & J. R. Lewis, 619

Martin, D. V. 2019, MNRAS, 488, 3482

Massey, P. & Johnson, J. 1993, AJ, 105, 980

McCabe, C., Duchêne, G., & Ghez, A. M. 2002, ApJ, 575, 974

McCaughrean, M. J. & Pearson, S. G. 2023, arXiv e-prints, arXiv:2310.03552

McClure, M. K., Furlan, E., Manoj, P., et al. 2010, ApJS, 188, 75

McGregor, P. J., Hart, J., Conroy, P. G., et al. 2003, in Proceedings of SPIE, Vol. 4841, Instrument Design and Performance for Optical/Infrared Ground-based Telescopes, ed. M. Iye & A. F. M. Moorwood, 178

McKee, C. F. & Ostriker, E. C. 2007, ARA&A, 45, 565

McKee, C. F. & Ostriker, J. P. 1977, ApJ, 218, 148

McLeod, A. F., Dale, J. E., Ginsburg, A., et al. 2015, MNRAS, 450, 1057

Mesa-Delgado, A., Zapata, L., Henney, W. J., Puzia, T. H., & Tsamis, Y. G. 2016, ApJ, 825, L16

Millan-Gabet, R., Malbet, F., Akeson, R., et al. 2007, in Protostars and Planets V, ed. B. Reipurth, D. Jewitt, & K. Keil, 539

Millan-Gabet, R., Schloerb, F. P., & Traub, W. A. 2001, ApJ, 546, 358

Millan-Gabet, R., Schloerb, F. P., Traub, W. A., et al. 1999, ApJ, 513, L131

Miller, G. E. & Scalo, J. M. 1978, PASP, 90, 506

Milli, J., Mouillet, D., Lagrange, A. M., et al. 2012, A&A, 545, A111

Min, M., Hovenier, J. W., & de Koter, A. 2003, A&A, 404, 35

Miotello, A., Bruderer, S., & van Dishoeck, E. F. 2014, A&A, 572, A96

Miotello, A., Kamp, I., Birnstiel, T., Cleeves, L. C., & Kataoka, A. 2023, in Astronomical Society of the Pacific Conference Series, Vol. 534, Astronomical Society of the Pacific Conference Series, ed. S. Inutsuka, Y. Aikawa, T. Muto, K. Tomida, & M. Tamura, 501

Miotello, A., Robberto, M., Potenza, M. A. C., & Ricci, L. 2012, ApJ, 757, 78

Miotello, A., van Dishoeck, E. F., Williams, J. P., et al. 2017, A&A, 599, A113

Moe, M. & Kratter, K. M. 2021, MNRAS, 507, 3593

Mohanty, S., Greaves, J., Mortlock, D., et al. 2013, ApJ, 773, 168

Monga, N. & Desch, S. 2015, ApJ, 798, 9

Monnier, J. D. & Millan-Gabet, R. 2002, ApJ, 579, 694

Mordasini, C., Alibert, Y., & Benz, W. 2009, A&A, 501, 1139

Morrell, N., Garcia, B., & Levato, H. 1988, PASP, 100, 1431

Mouillet, D., Lagrange, A. M., Augereau, J. C., & Ménard, F. 2001, A&A, 372, L61

Mulders, G. D., Pascucci, I., Manara, C. F., et al. 2017, ApJ, 847, 31

Murillo, N. M., van Dishoeck, E. F., Hacar, A., Harsono, D., & Jørgensen, J. K. 2022, A&A, 658, A53

Muzerolle, J., Calvet, N., Hartmann, L., & D'Alessio, P. 2003, ApJ, 597, L149

Muzerolle, J., Hartmann, L., & Calvet, N. 1998, AJ, 116, 455

Nakatani, R., Hosokawa, T., Yoshida, N., Nomura, H., & Kuiper, R. 2018, ApJ, 865, 75

Nanne, J. A. M., Nimmo, F., Cuzzi, J. N., & Kleine, T. 2019, Earth and Planetary Science Letters, 511, 44

Natta, A., Testi, L., Alcalá, J. M., et al. 2014, A&A, 569, A5

Natta, A., Testi, L., Muzerolle, J., et al. 2004a, A&A, 424, 603

Natta, A., Testi, L., Neri, R., Shepherd, D. S., & Wilner, D. J. 2004b, A&A, 416, 179

Natta, A., Testi, L., & Randich, S. 2006, A&A, 452, 245

Nayakshin, S. 2010, MNRAS, 408, L36

Nesvorný, D., Li, R., Youdin, A. N., Simon, J. B., & Grundy, W. M. 2019, Nature Astronomy, 3, 808

Nisini, B., Antoniucci, S., Alcalá, J. M., et al. 2018, A&A, 609, A87

Norman, C. A. & Ferrara, A. 1996, ApJ, 467, 280

Öberg, K. I., Facchini, S., & Anderson, D. E. 2023, Annual Review of Astronomy and Astrophysics, 61, 287

Öberg, K. I., Guzmán, V. V., Walsh, C., et al. 2021, ApJS, 257, 1

Oberg, N., Kamp, I., Cazaux, S., Rab, C., & Czoske, O. 2023, A&A, 670, A74

Oberti, S., Kolb, J., Madec, P.-Y., et al. 2018, in Society of Photo-Optical Instrumentation Engineers (SPIE) Conference Series, Vol. 10703, Adaptive Optics Systems VI, ed. L. M. Close, L. Schreiber, & D. Schmidt, 107031G

O'Dell, C. R. & Wen, Z. 1994, ApJ, 436, 194

O'Dell, C. R., Wen, Z., & Hu, X. 1993, ApJ, 410, 696

O'Dell, C. R. & Wong, K. 1996, AJ, 111, 846

Offner, S. S. R., Moe, M., Kratter, K. M., et al. 2023, in Astronomical Society of the Pacific Conference Series, Vol. 534, Astronomical Society of the Pacific Conference Series, ed. S. Inutsuka, Y. Aikawa, T. Muto, K. Tomida, & M. Tamura, 275

Ohashi, N., Tobin, J. J., Jørgensen, J. K., et al. 2023, ApJ, 951, 8

Oliveira, J. M., Jeffries, R. D., Devey, C. R., et al. 2003, MNRAS, 342, 651

Olofsson, J., Augereau, J. C., van Dishoeck, E. F., et al. 2009, A&A, 507, 327

Oppenheimer, B. R., Kulkarni, S. R., Matthews, K., & van Kerkwijk, M. H. 1998, ApJ, 502, 932

Ossenkopf, V. & Henning, T. 1994, A&A, 291, 943

Ostriker, E. C. 1994, ApJ, 424, 292

Otter, J., Ginsburg, A., Ballering, N. P., et al. 2021, ApJ, 923, 221

Owen, J. E. & Altaf, N. 2021, MNRAS, 508, 2493

Owen, J. E., Clarke, C. J., & Ercolano, B. 2012, MNRAS, 422, 1880

Owen, J. E., Ercolano, B., Clarke, C. J., & Alexander, R. D. 2010, MNRAS, 401, 1415

Panagia, N., Romaniello, M., Scuderi, S., & Kirshner, R. P. 2000, ApJ, 539, 197

Paneque-Carreño, T., Pérez, L. M., Benisty, M., et al. 2021, ApJ, 914, 88

Pantin, E., Waelkens, C., & Lagage, P. O. 2000, A&A, 361, L9

Parker, R. J. 2020, Royal Society Open Science, 7, 201271

Pascucci, I., Cabrit, S., Edwards, S., et al. 2023, in Astronomical Society of the Pacific Conference Series, Vol. 534, Protostars and Planets VII, ed. S. Inutsuka, Y. Aikawa, T. Muto, K. Tomida, & M. Tamura, 567

Pascucci, I., Testi, L., Herczeg, G. J., et al. 2016, ApJ, 831, 125

Pearson, S. G. & McCaughrean, M. J. 2023, arXiv e-prints, arXiv:2310.01231

Penny, L. R., Gies, D. R., Hartkopf, W. I., Mason, B. D., & Turner, N. H. 1993, PASP, 105, 588

Pérez, L. M., Carpenter, J. M., Andrews, S. M., et al. 2016, Science, 353, 1519

Perotti, G., Christiaens, V., Henning, T., et al. 2023, Nature, 620, 516

Perrin, M. D., Duchêne, G., Kalas, P., & Graham, J. R. 2006, ApJ, 645, 1272

Perrot, C., Boccaletti, A., Pantin, E., et al. 2016, A&A, 590, L7

Persson, M. V. 2014, SEDs of the different protostellar evolutionary stages

Peterson, D. E., Megeath, S. T., Luhman, K. L., et al. 2008, ApJ, 685, 313

Pfalzner, S. 2013, A&A, 549, A82

Pfalzner, S., Davies, M. B., Gounelle, M., et al. 2015, Phys. Scr, 90, 068001

Picogna, G., Ercolano, B., Owen, J. E., & Weber, M. L. 2019, MNRAS, 487, 691

Pineda, J. E., Arzoumanian, D., Andre, P., et al. 2023, in Astronomical Society of the Pacific Conference Series, Vol. 534, Protostars and Planets VII, ed. S. Inutsuka, Y. Aikawa, T. Muto, K. Tomida, & M. Tamura, 233

Pineda, J. E., Segura-Cox, D., Caselli, P., et al. 2020, Nature Astronomy, 4, 1158

Pinte, C., Price, D. J., Ménard, F., et al. 2018, ApJ, 860, L13

Pinte, C., Teague, R., Flaherty, K., et al. 2023, in Astronomical Society of the Pacific Conference Series, Vol. 534, Astronomical Society of the Pacific Conference Series, ed. S. Inutsuka, Y. Aikawa, T. Muto, K. Tomida, & M. Tamura, 645

Pittman, C. V., Espaillat, C. C., Robinson, C. E., et al. 2022, AJ, 164, 201

Pollack, J. B., Hollenbach, D., Beckwith, S., et al. 1994, ApJ, 421, 615

Povich, M. S., Maldonado, J. T., Nuñez, E. H., & Robitaille, T. P. 2019, ApJ, 881, 37

Povich, M. S., Smith, N., Majewski, S. R., et al. 2011, ApJS, 194, 14

Powell, D., Gao, P., Murray-Clay, R., & Zhang, X. 2022, Nature Astronomy, 6, 1147

Preibisch, T., Flaischlen, S., Göppl, C., Ercolano, B., & Roccatagliata, V. 2021, A&A, 648, A34

Preibisch, T., Hodgkin, S., Irwin, M., et al. 2011a, ApJS, 194, 10

Preibisch, T., Ratzka, T., Kuderna, B., et al. 2011b, A&A, 530, A34

Preibisch, T., Roccatagliata, V., Gaczkowski, B., & Ratzka, T. 2012, A&A, 541, A132

Preibisch, T., Zeidler, P., Ratzka, T., Roccatagliata, V., & Petr-Gotzens, M. G. 2014, A&A, 572, A116

Qiao, L., Coleman, G. A. L., & Haworth, T. J. 2023, MNRAS, 522, 1939

Qiao, L., Haworth, T. J., Sellek, A. D., & Ali, A. A. 2022, MNRAS, 512, 3788

Quanz, S. P., Amara, A., Meyer, M. R., et al. 2013a, ApJ, 766, L1

Quanz, S. P., Avenhaus, H., Buenzli, E., et al. 2013b, ApJ, 766, L2

Quanz, S. P., Birkmann, S. M., Apai, D., Wolf, S., & Henning, T. 2012, A&A, 538, A92

Quanz, S. P., Schmid, H. M., Geissler, K., et al. 2011, ApJ, 738, 23

Rainot, A., Reggiani, M., Sana, H., Bodensteiner, J., & Absil, O. 2022, A&A, 658, A198

Reipurth, B., Guimarães, M. M., Connelley, M. S., & Bally, J. 2007, AJ, 134, 2272

Reipurth, B. & Zinnecker, H. 1993, A&A, 278, 81

Reiter, M., McLeod, A. F., Klaassen, P. D., et al. 2019, MNRAS, 490, 2056

Ricci, L., Isella, A., Carpenter, J. M., & Testi, L. 2013, ApJ, 764, L27

Ricci, L., Robberto, M., & Soderblom, D. R. 2008, AJ, 136, 2136

Ricci, L., Testi, L., Natta, A., et al. 2010, A&A, 512, A15

Ricci, L., Testi, L., Natta, A., et al. 2014, ApJ, 791, 20

Rice, K., Lopez, E., Forgan, D., & Biller, B. 2015, MNRAS, 454, 1940

Rich, E. A., Monnier, J. D., Aarnio, A., et al. 2022, AJ, 164, 109

Riddick, F. C., Roche, P. F., & Lucas, P. W. 2007, MNRAS, 381, 1067

Rieke, G. H., Wright, G. S., Böker, T., et al. 2015, The mid-infrared instrument for the James Webb Space Telescope, I: Introduction, Technical Report JWST-STScI-000001

Rigliaco, E., Natta, A., Randich, S., & Sacco, G. 2009, A&A, 495, L13

Rigliaco, E., Natta, A., Randich, S., Testi, L., & Biazzo, K. 2011, A&A, 525, A47

Robitaille, T. P., Whitney, B. A., Indebetouw, R., Wood, K., & Denzmore, P. 2006, ApJS, 167, 256

Roccatagliata, V., Preibisch, T., Ratzka, T., & Gaczkowski, B. 2013, A&A, 554, A6

Rochau, B., Brandner, W., Stolte, A., et al. 2011, MNRAS, 418, 949

Roddier, C., Roddier, F., Northcott, M. J., Graves, J. E., & Jim, K. 1996, ApJ, 463, 326

Romaniello, M. 1998, PhD thesis, Scuola Normale Superiore, Pisa, Italy

Romaniello, M., Robberto, M., & Panagia, N. 2004, ApJ, 608, 220

Rosotti, G. P. 2023, New A Rev., 96, 101674

Rosotti, G. P., Booth, R. A., Tazzari, M., et al. 2019, MNRAS, 486, L63

Rosotti, G. P., Clarke, C. J., Manara, C. F., & Facchini, S. 2017, MNRAS, 468, 1631

Rosotti, G. P., Dale, J. E., de Juan Ovelar, M., et al. 2014, MNRAS, 441, 2094

Rowles, J. & Froebrich, D. 2009, MNRAS, 395, 1640

Ruíz-Rodríguez, D., Cieza, L. A., Williams, J. P., et al. 2018, MNRAS, 478, 3674

Sanchis, E., Testi, L., Natta, A., et al. 2021, A&A, 649, A19

Sanchis, E., Testi, L., Natta, A., et al. 2020, A&A, 633, A114

Santos, N. C., Israelian, G., & Mayor, M. 2004, A&A, 415, 1153

Scally, A., Clarke, C., & McCaughrean, M. J. 1999, MNRAS, 306, 253

Schäfer, U., Yang, C.-C., & Johansen, A. 2017, A&A, 597, A69

Schoonenberg, D. & Ormel, C. W. 2017, A&A, 602, A21

Segura-Cox, D. M., Harris, R. J., Tobin, J. J., et al. 2016, ApJ, 817, L14

Segura-Cox, D. M., Schmiedeke, A., Pineda, J. E., et al. 2020, Nature, 586, 228

Sellek, A. D., Booth, R. A., & Clarke, C. J. 2020, MNRAS, 498, 2845

Sellek, A. D., Clarke, C. J., & Ercolano, B. 2022, MNRAS, 514, 535

Sewiło, M., Whitney, B. A., Yung, B. H. K., et al. 2019, ApJS, 240, 26

Shakura, N. I. & Sunyaev, R. A. 1973, A&A, 24, 337

Sharples, R., Bender, R., Agudo Berbel, A., et al. 2013, The Messenger, 151, 21

Sheehan, P. D. & Eisner, J. A. 2017, ApJ, 851, 45

Shull, J. M., Darling, J., & Danforth, C. W. 2021, ApJ, 914, 18

Sicilia-Aguilar, A., Henning, T., & Hartmann, L. W. 2010, ApJ, 710, 597

Siess, L., Dufour, E., & Forestini, M. 2000, A&A, 358, 593

Simon, M. N., Pascucci, I., Edwards, S., et al. 2016, ApJ, 831, 169

Simón-Díaz, S., Herrero, A., Esteban, C., & Najarro, F. 2006, A&A, 448, 351

Sissa, E., Olofsson, J., Vigan, A., et al. 2018, A&A, 613, L6

Smith, M. J. & Geach, J. E. 2023, Royal Society Open Science, 10, 221454

Smith, N. 2002, MNRAS, 337, 1252

Smith, N. 2006, MNRAS, 367, 763

Smith, N., Bally, J., & Morse, J. A. 2003, ApJ, 587, L105

Smith, N. & Brooks, K. J. 2008, in Handbook of Star Forming Regions, Volume II, ed. B. Reipurth, Vol. 5, 138

Somigliana, A., Testi, L., Rosotti, G., et al. 2023, ApJ, 954, L13

Somigliana, A., Toci, C., Lodato, G., Rosotti, G., & Manara, C. F. 2020, MNRAS, 492, 1120

Stauffer, J. R., Prosser, C. F., Hartmann, L., & McCaughrean, M. J. 1994, AJ, 108, 1375

Stelzer, B., Frasca, A., Alcalá, J. M., et al. 2013, A&A, 558, A141

Stelzer, B. & Schmitt, J. H. M. M. 2004, A&A, 418, 687

Stock, C., McGinnis, P., Caratti o Garatti, A., Natta, A., & Ray, T. P. 2022, A&A, 668, A94

Stolker, T., Dominik, C., Avenhaus, H., et al. 2016, A&A, 595, A113

Stolte, A., Hußmann, B., Olczak, C., et al. 2015, A&A, 578, A4

Störzer, H. & Hollenbach, D. 1998, ApJ, 502, L71

Ströbele, S., La Penna, P., Arsenault, R., et al. 2012, in Society of Photo-Optical Instrumentation Engineers (SPIE) Conference Series, Vol. 8447, Adaptive Optics Systems III, ed. B. L. Ellerbroek, E. Marchetti, & J.-P. Véran, 844737

Strom, K. M., Strom, S. E., Edwards, S., Cabrit, S., & Skrutskie, M. F. 1989, AJ, 97, 1451

Sturm, J. A., McClure, M. K., Harsono, D., et al. 2022, A&A, 660, A126

Tabone, B., Bettoni, G., van Dishoeck, E. F., et al. 2023, Nature Astronomy, 7, 805

Tabone, B., Rosotti, G. P., Cridland, A. J., Armitage, P. J., & Lodato, G. 2022, MNRAS, 512, 2290

Tacconi, L. J., Genzel, R., & Sternberg, A. 2020, ARA&A, 58, 157

Tagliaferri, R., Longo, G., Andreon, S., et al. 2003, in Lecture Notes in Computer Science, Vol. 2859, 226–234

Tamura, M. 2009, in American Institute of Physics Conference Series, Vol. 1158, Exoplanets and Disks: Their Formation and Diversity, ed. T. Usuda, M. Tamura, & M. Ishii, 11–16

Tamura, M. 2016, Proceedings of the Japan Academy, Series B, 92, 45

Tannirkulam, A., Monnier, J. D., Millan-Gabet, R., et al. 2008, ApJ, 677, L51

Tapia, M., Roth, M., Vázquez, R. A., & Feinstein, A. 2003, MNRAS, 339, 44

Tazzari, M., Testi, L., Ercolano, B., et al. 2016, A&A, 588, A53

Tazzari, M., Testi, L., Natta, A., et al. 2017, A&A, 606, A88

Tazzari, M., Testi, L., Natta, A., et al. 2021, MNRAS, 506, 5117

Teague, R., Bae, J., Bergin, E. A., Birnstiel, T., & Foreman-Mackey, D. 2018, ApJ, 860, L12

Testi, L. 2009, A&A, 503, 639

Testi, L., Birnstiel, T., Ricci, L., et al. 2014, in Protostars and Planets VI, ed. H. Beuther, R. S. Klessen, C. P. Dullemond, & T. Henning, 339–361

Testi, L., Natta, A., Manara, C. F., et al. 2022, A&A, 663, A98

Testi, L., Natta, A., Scholz, A., et al. 2016, A&A, 593, A111

Thalmann, C., Carson, J., Janson, M., et al. 2009, ApJ, 707, L123

Thatte, N., Tecza, M., Schnetler, H., et al. 2021, The Messenger, 182, 7

Thieme, T. J., Lai, S.-P., Lin, S.-J., et al. 2022, ApJ, 925, 32

Thies, I., Kroupa, P., Goodwin, S. P., Stamatellos, D., & Whitworth, A. P. 2011, MNRAS, 417, 1817

Throop, H. B. & Bally, J. 2005, ApJ, 623, L149

Tielens, A. G. G. M. 2010, The Physics and Chemistry of the Interstellar Medium (Cambridge University Press)

Tobin, J. J., Dunham, M. M., Looney, L. W., et al. 2015, ApJ, 798, 61

Tobin, J. J., Megeath, S. T., van't Hoff, M., et al. 2019, ApJ, 886, 6

Tobin, J. J., Offner, S. S. R., Kratter, K. M., et al. 2022, ApJ, 925, 39

Tobin, J. J., Sheehan, P. D., Megeath, S. T., et al. 2020, ApJ, 890, 130

Tokovinin, A. & Briceño, C. 2020, AJ, 159, 15

Townsley, L. K., Broos, P. S., Corcoran, M. F., et al. 2011, ApJS, 194, 1

Trapman, L., Miotello, A., Kama, M., van Dishoeck, E. F., & Bruderer, S. 2017, A&A, 605, A69

Trapman, L., Zhang, K., van't Hoff, M. L. R., Hogerheijde, M. R., & Bergin, E. A. 2022, ApJ, 926, L2

Tripathi, A., Andrews, S. M., Birnstiel, T., & Wilner, D. J. 2017, ApJ, 845, 44

Tychoniec, Ł., Manara, C. F., Rosotti, G. P., et al. 2020, A&A, 640, A19

Tychoniec, Ł., Tobin, J. J., Karska, A., et al. 2018, ApJS, 238, 19

Uyama, T., Hashimoto, J., Kuzuhara, M., et al. 2017, AJ, 153, 106

Vaidya, K., Chen, W.-P., & Lee, H.-T. 2015, AJ, 150, 195

Valdivia-Mena, M. T., Pineda, J. E., Segura-Cox, D. M., et al. 2022, A&A, 667, A12

Valenti, J. & Fischer, D. 2008, in Astronomical Society of the Pacific Conference Series, Vol. 384, 14th Cambridge Workshop on Cool Stars, Stellar Systems, and the Sun, ed. G. van Belle, 292

van der Marel, N., Birnstiel, T., Garufi, A., et al. 2021, AJ, 161, 33

van der Marel, N. & Mulders, G. D. 2021, AJ, 162, 28

van Dishoeck, E. F., Grant, S., Tabone, B., et al. 2023, arXiv e-prints, arXiv:2307.11817

van 't Hoff, M. L. R., Walsh, C., Kama, M., Facchini, S., & van Dishoeck, E. F. 2017, A&A, 599, A101

van Terwisga, S. E., Hacar, A., van Dishoeck, E. F., Oonk, R., & Portegies Zwart, S. 2022, A&A, 661, A53

van Terwisga, S. E., van Dishoeck, E. F., Cazzoletti, P., et al. 2019, A&A, 623, A150

van Terwisga, S. E., van Dishoeck, E. F., Mann, R. K., et al. 2020, A&A, 640, A27

Vazquez, R. A., Baume, G., Feinstein, A., & Prado, P. 1996, A&AS, 116, 75

Venuti, L., Bouvier, J., Flaccomio, E., et al. 2014, A&A, 570, A82

Veronesi, B., Paneque-Carreño, T., Lodato, G., et al. 2021, ApJ, 914, L27

Vigan, A., Bonavita, M., Biller, B., et al. 2017, A&A, 603, A3

Villenave, M., Ménard, F., Dent, W. R. F., et al. 2020, A&A, 642, A164

Wagner, K., Apai, D., Kasper, M., & Robberto, M. 2015, ApJ, 813, L2

Wahhaj, Z., Milli, J., Romero, C., et al. 2021, A&A, 648, A26

Walborn, N. R. 1973, ApJ, 179, 517

Walborn, N. R. 1995, in Revista Mexicana de Astronomia y Astrofisica Conference Series, Vol. 2, Revista Mexicana de Astronomia y Astrofisica Conference Series, ed. V. Niemela, N. Morrell, & A. Feinstein, 51

Walborn, N. R., Howarth, I. D., Lennon, D. J., et al. 2002, AJ, 123, 2754

Ward-Thompson, D., André, P., Crutcher, R., et al. 2007, in Protostars and Planets V, ed. B. Reipurth, D. Jewitt, & K. Keil, 33

Weilbacher, P. M., Palsa, R., Streicher, O., et al. 2020, A&A, 641, A28

Weinberger, A. J., Becklin, E. E., Schneider, G., et al. 1999, ApJ, 525, L53

White, R. J. & Basri, G. 2003, ApJ, 582, 1109

White, R. J. & Hillenbrand, L. A. 2004, ApJ, 616, 998

Whitworth, A. P. & Zinnecker, H. 2004, A&A, 427, 299

Williams, J. P. & Best, W. M. J. 2014, ApJ, 788, 59

Williams, J. P., Cieza, L., Hales, A., et al. 2019, ApJ, 875, L9

Williams, J. P. & Cieza, L. A. 2011, ARA&A, 49, 67

Williams, T. G., Sun, J., Barnes, A. T., et al. 2022, ApJ, 941, L27

Wilner, D. J., D'Alessio, P., Calvet, N., Claussen, M. J., & Hartmann, L. 2005, ApJ, 626, L109

Winter, A. J., Clarke, C. J., Rosotti, G., & Booth, R. A. 2018a, MNRAS, 475, 2314

Winter, A. J., Clarke, C. J., Rosotti, G., et al. 2018b, MNRAS, 478, 2700

Winter, A. J., Clarke, C. J., Rosotti, G., et al. 2018c, MNRAS, 478, 2700

Winter, A. J. & Haworth, T. J. 2022, European Physical Journal Plus, 137, 1132

Winter, A. J., Kruijssen, J. M. D., Longmore, S. N., & Chevance, M. 2020, Nature, 586, 528

Woitke, P., Kamp, I., & Thi, W. F. 2009, A&A, 501, 383

Wolk, S. J. & Walter, F. M. 1996, AJ, 111, 2066

Wright, N. J., Drake, J. J., Drew, J. E., et al. 2012, ApJ, 746, L21

Xiang-Gruess, M. 2016, MNRAS, 455, 3086

Xie, C., Haffert, S. Y., de Boer, J., et al. 2020, A&A, 644, A149

Xie, C., Haffert, S. Y., de Boer, J., et al. 2021, A&A, 650, L6

Yamamoto, T., Kadono, T., & Wada, K. 2014, ApJ, 783, L36

Yamashita, M., Itoh, Y., & Takagi, Y. 2020, PASJ, 72, 80

Yang, Y.-L., Sakai, N., Zhang, Y., et al. 2021, ApJ, 910, 20

Yasui, C., Kobayashi, N., Tokunaga, A. T., Saito, M., & Tokoku, C. 2010, ApJ, 723, L113

Yen, H.-W., Gu, P.-G., Hirano, N., et al. 2019, ApJ, 880, 69

Youdin, A. N. & Goodman, J. 2005, ApJ, 620, 459

Yusef-Zadeh, F., Biretta, J., & Geballe, T. R. 2005, AJ, 130, 1171

Zagaria, F., Clarke, C. J., Rosotti, G. P., & Manara, C. F. 2022, MNRAS, 512, 3538

Zeidler, P., Preibisch, T., Ratzka, T., Roccatagliata, V., & Petr-Gotzens, M. G. 2016, A&A, 585, A49

Zormpas, A., Birnstiel, T., Rosotti, G. P., & Andrews, S. M. 2022, A&A, 661, A66

Zúñiga-Fernández, S., Bayo, A., Elliott, P., et al. 2021, A&A, 645, A30

Zubko, V. G., Mennella, V., Colangeli, L., & Bussoletti, E. 1996, MNRAS, 282, 1321

Zurlo, A., Cieza, L. A., Pérez, S., et al. 2020, MNRAS, 496, 5089

Zurlo, A., Gratton, R., Pérez, S., & Cieza, L. 2023, European Physical Journal Plus, 138, 411

Acknowledgements

This thesis concludes a certain period of my life. A period full of events, people, discussions, experiences, and (hopefully) also full of a gained knowledge. This journey would not have been possible if not for my supervisor, Leonardo Testi. Thank you for your support, guidance, possibilities, and my personal development. I will always be grateful for this adventure and I do not think I can find the right words to thank you. Grazie mille per tutto!

I would also like to thank people sharing this journey with me. First to my collaborators at ESO, Giacomo Beccari and Carlo Manara, and my LMU supervisor, Thomas Preibisch, for all the discussions, brain storming, and not only scientific conversations. I would like to thank Anna F. Mc Leod for the amazing data, once-in-ESO Megan Reiter for your relentless enthusiasm in discovering the mysteries of the Universe (and Carina), and Thomas Haworth for spreading his honest passion for science. Many thanks to the ECOGAL team, especially to my Heidelberg collaborators: Da Eun and Victor. My growth as a scientist would not be able without the SPF team at ESO. It was amazing to be part of this community, I am sure I will miss you the most. Special thanks to Amelia Bayo for our endless conversations, as well as to many people at ESO with whom I had a countless (and random) discussions on various topics – you made my ESO experience very colourful. Many thanks to my friends who helped me to go through this adventure: Adrian, Alice, Andres, Arseniy, Avinash, Chi Yan, Claudia, Francesco, Haochang, Jolanta, Jianhang, Jiri, Julia, Luca, Łukasz, Michał, Oerd, Paulo, Samuel, Stephen, Tere, and Victor. Thank you all!

Last but not least, I would like to extend my thanks to my family, especially to my parents. You gave me support to go through the life in my own way, you gave me freedom to make my own choices and to discover the world, and you gave me love, the one thing that really matters in life. With all my heart, thank you!

Not all those who wander are lost

— J.R.R. Tolkien